

Zinc anode-based and plasmonic-based electrochromic devices for dynamic light modulation

by

Wu Zhang

A thesis submitted in partial fulfillment of the requirements for the degree of

Doctor of Philosophy

in

Photonics and Plasmas

Department of Electrical and Computer Engineering

University of Alberta

© Wu Zhang, 2024

Abstract

Electrochromism is the phenomenon where the optical transmittance or absorbance of a material changes under an applied electric potential. When a voltage is applied to an electrochromic material, the optical properties of the material are altered in a reversible fashion. Owing to their optical switching behavior, electrochromic materials provide great opportunities for a variety of energy-saving and color-tuning applications, including smart windows, multicolor displays, electronic skins and color-tunable optical elements.

In this thesis, we developed a promising Zinc anode-based electrochromic device (ZECD) platform. The ZECD platform not only reduces the energy consumption during operation, via the energy retrieval functionality, but also exhibits a rapid spontaneous switching behavior due to the high value of redox potential difference between the metal anode and the electrochromic cathode. Furthermore, ZECDs enable independent operation of top and bottom electrochromic electrodes, thus providing additional operation flexibility of the devices through the utilization of dual electrochromic layers under the same or different color states. As such, the color overlay effect can greatly broaden the color palettes via altering the coordinates of the 2D Commission Internationale de l'Eclairage (CIE) color space. Moreover, a dual-mode electrochromic device having both self-coloring and self-bleaching operations is demonstrated via coupling the ZECD platform into a rocking-chair type electrochromic device. By employing a hybrid electrolyte system, the rocking-chair type device is shown to be capable of spontaneously bleaching through the redox potential difference between the anodic and cathodic electrodes.

Furthermore, the demonstrations of the manipulation of plasmonic silver adatoms through reversible metal deposition are presented for dynamic light modulation. The

reversible silver metal deposition on Indium Tin Oxide (ITO) glasses, having tunable nanostructures, along with their localized surface plasmon resonance (LSPR), is considered as a promising strategy for dynamic color displays. The voltage-activated reversible silver nanoparticles deposition enables a wide range of dynamic plasmonic color change of 100 nm, and also facilitates a size and shape control of the grown silver nanoparticles. The silver nanoparticles interact with visible light through LSPR, the size and shape of the particles affect their optical properties. We further demonstrate a novel concept for solar-regulated dynamic windows by depositing thin films of gold on glass substrates to serve as transparent conductive electrodes. By employing a reversible silver metal deposition technique, we develop a dual-band dynamic window capable of independent regulation of visible light and near-infrared radiation. This technique, which permits the targeted adjustment of visible light and near-infrared radiation, opens possibilities for diverse operational modes – bright, light, and dark modes. The developed platform not only has the potential to reduce building energy consumption but also maintains optimal indoor lighting conditions.

The outcomes of this thesis represent novel strategies for fabricating dynamic windows, provide indispensable building blocks for future generations of transparent multicolor displays, as well as open up new areas of research into the development of future electrochromic devices.

Preface

Parts of Chapter 2 consist of work published as invited review articles. The research presented in Chapter 3 and Chapter 4 along with their supporting information is original work.

Chapter 2 involves review articles that have been published as:

1. Zhang, W.; Li, H.; Hopmann, E.; Elezzabi, A. Y. “Nanostructured inorganic electrochromic materials for light applications.” *Nanophotonics*, 10, 825-850 (2021).
2. Zhang, W.; Li, H.; Yu, W. W.; Elezzabi, A. Y. “Emerging Zn anode-based electrochromic devices.” *Small Science*, 1, 2100040 (2021).

Chapter 3 describes work that has been published as:

3. Zhang, W.; Li, H.; Yu, W. W.; Elezzabi, A. Y. “Transparent inorganic multicolor displays enabled by zinc-based electrochromic devices.” *Light: Science & Applications*, 9, 121 (2020).
4. Zhang, W.; Li, H.; Elezzabi, A. Y. “Electrochromic displays having two-dimensional CIE color space tunability.” *Advanced Functional Materials*, 32, 202108341 (2022).
5. Zhang, W.; Li, H.; Elezzabi, A. Y. “A dual-mode electrochromic platform integrating zinc anode-based and rocking-chair electrochromic devices.” *Advanced Functional Materials*, 33, 2300155 (2023).

Chapter 4 describes work that has been published as:

6. Zhang, W.; Li, H.; Elezzabi, A. Y. “Manipulating silver adatoms for aqueous plasmonic electrochromic devices.” *Advanced Materials Interfaces*, 9, 202200021 (2022).
7. Zhang, W.; Li, H.; Elezzabi, A. Y. “Spectral-selective dynamic windows: a new horizon

in light and heat management technologies.” Under Review (2024).

In addition to the above publications, I also first-authored or corresponded three publications (related to electrochromism):

8. Zhang, W.; Li, H.; Firby, C. J.; Al-Hussein, M.; Elezzabi, A. Y. “Oxygen-vacancy-tunable electrochemical properties of electrodeposited molybdenum oxide films.” *ACS Applied Materials & Interfaces*, 11, 20378–20385 (2019).

9. Zhang, W.; Li, H.; Al-Hussein, M.; Elezzabi, A. Y. “Electrochromic battery displays with energy retrieval functions using solution-processable vanadium oxide nanoparticles.” *Advanced Optical Materials*, 8, 1901224 (2020).

10. Zhao, F.; Wang, B.; Zhang, W.; Cao, S.; Liu, L.; Elezzabi, A. Y.; Li, H.; Yu, W. W. “Counterbalancing the interplay between electrochromism and energy storage for efficient electrochromic devices.” *Materials Today*, 66, 431-447 (2023).

Acknowledgment

I would like to express my gratitude to my supervisor, Professor Abdulhakem Elezzabi, for his valuable advice and lessons during my graduate studies. His guidance over the past years has benefited me greatly in different ways. He developed a close relationship with his graduate students and motivated them to continuously grow as a better researcher. I appreciate him for shaping me into the researcher that I have become. I thank him for his support in financing and producing my research work. Without his support, this work would be impossible to complete.

I also want to say thank you to Alberta Innovates, Natural Sciences and Engineering Research Council of Canada, and All Weather Windows Ltd. for their financing support.

I truly appreciate Professor Haizeng Li for his generous instruction during my research. Professor Haizeng Li has taught me a lot of valuable skills, which has had a significant impact on my knowledge. His insightful guidance helped me overcome countless difficulties in my research. Many thanks to him for his instruction and I enjoyed working with him.

I would also like to express my sincere appreciation to my parents and my long-time friends Jackson, Cecilia, Marsha, Alex, Zhen, Jiafei, and Danzhu for their companionship and support. I also want to express my gratitude to my research team members: Brett, Eric, Basem, Curtis and Leo for their advice and assistance. I enjoyed the time spent with each of you. I would like to devote my thesis to all of you and thank you.

Table of Contents

1	Introduction	1
1.1	Research background.....	1
1.2	Research objectives	3
1.3	Thesis overview	3
2	Design of electrochromic devices	5
2.1	Introduction	5
2.2	Electrochromic materials	5
2.2.1	Inorganic electrochromic materials.....	6
2.2.2	Organic electrochromic materials	11
2.2.3	Organic-inorganic hybrid electrochromic materials	13
2.2.4	Nanoparticles and nanostructured plasmonic material.....	17
2.3	Key metrics for electrochromic materials	21
2.3.1	Color and optical contrast	21
2.3.2	Coloring and bleaching switching times	23
2.3.3	Coloration efficiency	25
2.3.4	Cycling stability	26
2.4	Design of nanostructured electrochromic materials	27
2.4.1	Tungsten oxides.....	27

2.4.2	Molybdenum oxides	32
2.4.3	Titanium oxides	35
2.4.4	Vanadium oxides	37
2.4.5	Nickel oxides	38
2.4.6	Cobalt oxides	41
2.5	Complementary electrochromic devices	42
2.6	Major challenges of electrochromic devices	44
3	Zinc anode-based electrochromic devices	46
3.1	Introduction	46
3.2	Transparent inorganic multicolor displays enabled by zinc-based electrochromic devices	49
3.2.1	Introduction	49
3.2.2	Characterization of SVO nanorods	52
3.2.3	Fabrication of SVO electrodes via the bar-coating method	55
3.2.4	Electrochromic performance of the SVO electrodes	58
3.2.5	Electrochromic displays with broadened color palettes	64
3.2.6	Summary	68
3.3	Electrochromic devices having two-dimensional CIE color space tunability	69
3.3.1	Introduction	69
3.3.2	Fabrication of transmissive-type and Fabry-Perot nanocavity	

	reflective-type WO ₃ electrochromic electrode.	73
3.3.3	Electrochromic performance of working electrodes	75
3.3.4	Transparent electrochromic displays with broadened color palettes	79
3.3.5	Reflective electrochromic displays with broadened color palettes	83
3.3.6	Demonstration of a dual-mode prototype transparent-reflective zinc-based electrochromic display	86
3.3.7	Summary	88
3.4	A dual-mode electrochromic platform integrating zinc anode-based and rocking-chair electrochromic devices	89
3.4.1	Introduction	89
3.4.2	Mechanism of the dual-mode electrochromic platform	95
3.4.3	Optimization of the electrochromic electrodes	101
3.4.4	Operation of dual-mode electrochromic devices.....	107
3.4.5	Summary	115
3.5	Summary of zinc anode-based electrochromic devices.....	116
4	Plasmonic-based electrochromic devices	117
4.1	Introduction.....	117
4.2	Manipulating silver adatoms for aqueous plasmonic electrochromic devices.....	118
4.2.1	Introduction	118
4.2.2	Underpotential deposition of Ag nanoparticles.....	120

4.2.3	Size and shape control of Ag nanoparticles	123
4.2.4	Transparent Ag-based plasmonic electrochromic devices	128
4.2.5	Reflective Ag-based plasmonic electrochromic devices	131
4.2.6	Summary	133
4.3	Spectral-selective dynamic windows: a new horizon in light and heat management technologies	134
4.3.1	Introduction	134
4.3.2	Mechanism of selective modulation of visible and NIR lights	137
4.3.3	Three-mode solar-regulated dynamic windows	143
4.3.4	Large-scale dynamic windows	150
4.3.5	Flexible thermal-regulated devices	154
4.3.6	Summary	158
4.4	Summary of plasmonic-based electrochromic devices	159
5	Conclusion and Future Outlook.....	160
5.1	Conclusion	160
5.2	Future Outlook.....	161
	References	163
	Appendices	179
	Appendix A: Characterization of sodium vanadium nanorod films.....	179
	Appendix B: Characterization of tungsten oxide electrochromic electrodes	187

Appendix C: Characterization of dual-mode electrochromic devices	192
Appendix D: Characterization of silver nanoparticle films	197
Appendix E: Characterization of solar-regulated dynamic windows	200

List of Tables

Table 2.1: Summary of the electrochromic properties of nanostructured WO ₃ with different morphologies	32
Table 3.1: Atomic ratio of V ⁴⁺ and V ⁵⁺ in the as-deposited, annealed for 30 mins, annealed for 24 h, reduced (0.2 V) and oxidized (2.0 V) SVO film.....	58
Table 4.1: The sheet resistance versus transmittance in visible and near-infrared regions of the Au/glass electrodes with seven different thicknesses.	139
Table A-1: Diameter and length of the SVO nanorods	182

List of Figures

Figure 2.1: Electrochromic transition metal oxides showing both cathodic and anodic coloration	7
Figure 2.2: Structure, working principle, and application of Zn-PB electrochromic device.....	10
Figure 2.3: Characterization and demonstration of organic electrochromic materials. ..	12
Figure 2.4: Preparation and characterization of organic-inorganic hybrid films.	16
Figure 2.5: Depiction of plasmonic electrochromic nanocrystals and nanostructures. ..	20
Figure 2.6: Demonstration of electrochromic materials having different colors and light spectra.	22
Figure 2.7: Al anode-based electrochromic energy storage windows.	25
Figure 2.8: Structure and Characterization of WO ₃ -based electrochromic films.....	30
Figure 2.9: Structure and characterization of MoO ₃ -based electrochromic films.....	34
Figure 2.10: Structure and characterization of TiO ₂ -based electrochromic films.....	36
Figure 2.11: Structure and characterization of vanadium oxide-based electrochromic displays.	38
Figure 2.12: Characterization of NiO-based electrochromic films.	40
Figure 2.13: Characterization of Co ₃ O ₄ -based electrochromic films.	41
Figure 2.14: Complementary electrochromic devices.....	43
Figure 3.1: Zinc anode-based electrochromic devices	47
Figure 3.2: Schematic illustrations of two different types of electrochromic devices. ...	51
Figure 3.3: Characterization of SVO nanorods	54
Figure 3.4: Fabrication of SVO films via a bar-coating method.....	56
Figure 3.5: The ex-situ XPS survey spectra of the SVO electrode.	60
Figure 3.6: Electrochromic performance of the SVO electrode.	62

Figure 3.7: Design and performance of the Zn-SVO electrochromic displays with broadened color palettes.	66
Figure 3.8: Schematic illustrations of two different types of electrochromic devices and their expected chromaticity coordinate plots in CIE color space.	70
Figure 3.9: Schematic illustrations of two different types of displays and their expected chromaticity coordinate plots in CIE color space	72
Figure 3.10: Transmissive-type and Fabry-Perot nanocavity reflective-type WO ₃ electrochromic electrode	74
Figure 3.11: Characterization of the electrochromic electrodes.....	77
Figure 3.12: Transparent electrochromic display exhibiting broadened color palettes...80	
Figure 3.13: Optical transmittance spectra of the display	82
Figure 3.14: Reflective electrochromic display exhibiting broadened color palettes.	84
Figure 3.15: Optical reflectance spectra of the display	85
Figure 3.16: Color images of the transparent-type displays and the reflective-type displays at different viewing angles	85
Figure 3.17: Demonstration of prototype zinc-based electrochromic displays.....	87
Figure 3.18: Schematic diagram illustrating the rocking-chair type electrochromic devices	92
Figure 3.19: Schematic diagram illustrating the dual-mode operation processes	94
Figure 3.20: Characterization of the electrochromic electrodes in different electrolytes.	97
Figure 3.21: Cyclic voltammetry performance of the WO ₃ electrode at different scanning rates.....	98
Figure 3.22: Cyclic voltammetry performance of the PB electrode at different scanning rates.....	98
Figure 3.23: Digital photograph of the dual-mode device showing an increased OCP ..	101
Figure 3.24: Electrochemical performance of the WO ₃ and PB electrodes.	102
Figure 3.25: Electrochromic performance of the WO ₃ and PB electrodes.....	106

Figure 3.26: Design and performance of the dual-mode electrochromic device.....	108
Figure 3.27: The functionalities of the dual-mode electrochromic device with digital photographs.	110
Figure 3.28: Stability analysis of the dual-mode electrochromic device from PB electrode	113
Figure 3.29: Stability analysis of the dual-mode electrochromic device from WO ₃ electrode.....	114
Figure 4.1: The working mechanism of the Ag-based electrochromic devices.	121
Figure 4.2: Cycling analysis of the Ag-based electrochromic devices.....	123
Figure 4.3: FE-SEM images and the corresponding extinction spectra of the Ag nanoparticles grown on ITO electrode under different applied voltages.	124
Figure 4.4: The LSPR and size distribution of Ag nanoparticles.	127
Figure 4.5: Transparent Ag-based electrochromic device.....	129
Figure 4.6: Round-trip energy consumption of the Ag-based electrochromic devices...	131
Figure 4.7: Reflective Ag-based electrochromic devices	132
Figure 4.8: Schematic diagram illustrating the solar-regulated dynamic window	136
Figure 4.9: Schematic diagram illustrating the selective modulation of the visible and NIR light spectra.....	138
Figure 4.10: FESEM images of the Au films taken at different thicknesses.....	139
Figure 4.11: Visible-near infrared transmittance spectra of the ITO/FTO glasses	141
Figure 4.12: Characterization of Ag-coated stainless-steel mesh (Ag-SSE) mounted on glass	144
Figure 4.13: Performance of the solar-regulated dynamic windows.....	146
Figure 4.14: FESEM images depicting the reversible silver growth and dissolution on Au/glass electrodes and stainless-steel mesh..	147
Figure 4.15: Bistability test of the solar-regulated dynamic windows	148

Figure 4.16: Demonstration of solar energy transferred to thermal radiation.	150
Figure 4.17: Performance of the large-area dynamic windows.....	153
Figure 4.18: The mid-infrared transmittance spectrum of the glass substrates	154
Figure 4.19: Performance of the flexible thermal-regulated devices.	155
Figure 4.20: The mid-infrared transmittance spectrum of the Ag-coated stainless-steel mesh.....	157
Figure A-1: FESEM image of the SVO nanorods.....	182
Figure A-2: FESEM images of the bar-coated and annealed SVO films.....	183
Figure A-3: CV measurement of SVO electrodes	184
Figure A-4: Coloration Efficiency (CE) of the SVO film.....	185
Figure A-5: Cycle performance of the SVO electrode	186
Figure B-1: FESEM images of the sputtered WO ₃ films.	189
Figure B-2: Digital images of the Fabry-Perot nanocavity electrode at different viewing angles with respect to the surface normal.....	189
Figure B-3: Coloration Efficiency (CE) of the sputtered WO ₃ film.....	190
Figure B-4: Cycle performance of the WO ₃ electrode	191
Figure C-1: CV performance of the PB electrode.	194
Figure C-2: Dynamic optical transmittance of the WO ₃ electrode.....	195
Figure C-3: Dynamic optical transmittance of the PB electrode.....	196
Figure D-1: FESEM image of the ITO electrode at 0.5 V.	199
Figure E-1: CV measurement of 5 nm Au/glass electrodes.	202
Figure E-2: Digital image of a large-area dynamic window	203

List of Abbreviations

BF	Bright-field
CE	Coloration efficiency
CIE	International Commission on Illumination
CV	Cyclic voltammetry
DF	Dark-field
DMSO	Dimethyl sulfoxide
ECD	Electrochromic device
FE-SEM	Field emission scanning electron microscopy
FTO	Fluorine doped tin oxide
FTIR	Fourier-transform infrared spectroscopy
ITO	Indium tin oxide
LED	Light-emitting diode
LSPR	Localized surface plasmon resonance
LSV	Linear sweep voltammetry
NIR	Near-infrared
OCP	Open circuit potential
PB	Prussian blue
PE	Polyethylene
RME	Reversible metal deposition
RTEE	Round-trip energy efficiency
SSE	Stainless-steel mesh
SVO	Sodium ion stabilized vanadium oxide
TEM	Transmission electron microscope
TMO	Transition metal oxide
XPS	X-ray photoelectron spectroscopy
XRD	X-ray powder diffraction
ZECD	Zinc anode-based electrochromic device

List of Symbols

Symbol	Meaning	Units
F	Faraday constant	96485 C mol ⁻¹
n	Sample numbers	dimensionless
μ	Average diameter distribution	nm
σ	Standard deviation	nm
T	Transmittance	dimensionless
η	Coloration efficiency	cm ² C ⁻¹
C _A	Capacitance	mF cm ⁻²
ΔT	Optical contrast	dimensionless
ΔOD	Optical density	dimensionless
ΔV	Potential window	V
A	Area	cm ²
R _s	Internal Resistance	Ω
D	Diffusion coefficient	cm ² s ⁻¹
C	Concentration	mol cm ⁻³
v	Scan rate	V s ⁻¹
I	Current	A

Chapter 1

Introduction

1.1 Research background

Electrochromism is an intriguing phenomenon by which electrochemical oxidation and reduction induce a reversible color change in materials.¹ This Phenomenon was first introduced in 1961 by J. R. Platt from the University of Chicago.² In 1969, S. K. Deb explained in detail the electrochromic performance of WO₃ films.³ Since then, researchers in the field of electrochromism discovered numerous electrochromic materials, including transition metal oxides, plasmonic metallic materials, and organic electrochromic materials. This compelling light control technology endows a variety of applications, including electronic skins,^{4,5} transparent displays,^{6,7} optical sensors,⁸ and smart windows.⁹⁻¹¹ For example, Electrochromic technology offers an innovative approach to conserving energy in buildings by allowing for the real-time control of solar radiation and visible light transmission through windows.¹²

Electrochromic films can be deposited on the surface of conductive glass, such as indium tin oxide (ITO) or fluorine-doped tin oxide (FTO) glass. When a voltage is applied to electrochromic films, the photochemical properties of the materials are altered in a reversible fashion.¹³ By applying varying voltage levels or utilizing different types of electrochromic film materials, the color and transparency characteristics of the window can be altered. Additionally, windows can retain their transparency when the applied voltage is switched off. Hence, by regulating the voltage supplied to the electrochromic film, windows can mitigate energy loss resulting from temperature disparities between indoor and outdoor environments and the building's energy consumption is

reduced. Along with light control, an interesting feature of electrochromic devices is their supercapacitive ability to store and release an amount of the utilized electrical energy during the switching process.^{14,15} Notwithstanding, the zero energy consumption advantage results in a slow and complex energy release mechanism. Therefore, to meet the fast switching requirement, an external voltage bias is still required to reverse the colored state of the device.¹⁶⁻¹⁹

Although the current electrochromic devices do not consume energy while maintaining their colored or colorless states, the operation of conventional electrochromic devices requires external voltages to trigger both the coloration/bleaching processes,^{20,21} making the conventional electrochromic devices far from a net-zero energy-consumption technology.

Electrochromic devices with a wide color gamut distribution have long been sought after for non-emissive transparent display technologies. The current state-of-the-art multicolor electrochromic devices utilize a single electrochromic layer.²² Such a configuration restricts their color hues tunability to either a linear or curved segment trajectory on the International Commission on Illumination (CIE) color space. As such, it is highly desirable to have an energy-efficient electrochromic device expressing significantly broadened color palettes. Another significant challenge in the development of electrochromic devices is their limited ability to manage separately visible light radiation and near-infrared radiation (NIR). Beyond just adjusting transparency and opacity, the ability to independently manipulate visible light and near-infrared radiation could introduce a novel device state, specifically designed to modulate NIR radiation alone. This approach has the potential to greatly reduce building energy consumption while still providing adequate indoor lighting.

1.2 Research objectives

The main focus of this thesis is on the design and fabrication of energy-efficient electrochromic devices for multifunctional applications. With recent rapid development of electrochromic technology, there is a pressing demand for high-efficiency, extremely energy-efficient, and multi-colored electrochromic devices to fulfill a range of applications. However, the current state-of-the-art multicolor electrochromic devices utilize a single electrochromic layer, which leads to limited color hues. Moreover, electrochromic devices are unable to independently regulate visible light and near-infrared radiation. The primary goal of this thesis is twofold: first, to offer both theoretical and experimental evidence of multifunctional electrochromic devices that combine high energy efficiency with a broad spectrum of colors. The second goal is to create an electrochromic device capable of precise control over visible light and near-infrared radiation. The approaches explored in this thesis unlock a vast array of possibilities for a wide range of operational modes in dynamic windows.

1.3 Thesis overview

This thesis is organized as follows:

Chapter 1 introduces the research background of electrochromism and highlights the challenges currently faced in this field of study.

Chapter 2 examines the general categorization of electrochromic materials and the essential key metrics used to assess their electrochromic properties. This is followed by in-depth design strategies of electrochromic devices and their underlying working mechanism.

Chapter 3 introduces a Zinc-based electrochromic device (ZECD) platform. In the first section, we

provide a detailed explanation of the working mechanism of ZECs, serving as the foundational knowledge for the subsequent developments. The second part of this chapter focuses on transparent multicolor displays enabled by ZECs. We show that the ZEC platform not only enhances energy efficiency through energy retrieval functionality but also exhibits rapid and spontaneous switching behavior due to the substantial redox potential difference between the metal anode and the electrochromic cathode. The third part of this chapter explores multicolor displays with tunability in the two-dimensional CIE color space, leveraging the color overlay effect to expand the available color palettes by adjusting coordinates in the two-dimensional CIE color space. Lastly, in the fourth section we present a dual-mode electrochromic device capable of both self-coloring and self-bleaching operations, achieved by integrating the ZEC platform into a rocking-chair type electrochromic device.

Chapter 4 presents a plasmonic-based electrochromic device platform that utilizes reversible silver metal deposition on ITO glasses with adjustable nanostructures, combined with their localized surface plasmon resonance (LSPR). This platform showcases a promising approach for dynamic color displays. Additionally, a novel concept for solar-regulated dynamic windows is introduced, achieved by depositing thin films of gold on glass substrates to serve as transparent conductive electrodes. Through precise control of reversible silver metal deposition, a dual-band dynamic window is realized, enabling independent regulation of both visible light and near-infrared radiation.

Chapter 5 Provides a summary of the theoretical and experimental accomplishments within this thesis, as well as offers insights into potential future research areas relevant to the thesis.

Chapter 2

Design of Electrochromic Devices

2.1 Introduction

With recent the rapid development of electrochromic technology, there is an urgent requirement for high efficiency and ultralow energy consumption electrochromic devices for various applications. Comprehensive reviews on electrochromic materials and devices outlining their respective strengths and limitations have served to address some of such challenges. In light of these investigations, this chapter provides a critical comprehensive review focusing on the emerging electrochromic materials and their application in devices. Herein, the general classification of electrochromic materials and the key metrics used in evaluating electrochromic properties are introduced, followed by in-depth design strategies of nanostructured electrochromic materials and correlations between the electrochromic properties and synthetic methods for different nanostructured electrochromic materials. Next, the basic mechanisms, device structures and electrochemical processes involved in the complementary electrochromic devices are presented, followed by discussions on the major advancements, future challenges, and new opportunities in electrochromic technology.

Versions of this chapter have been published in: Zhang, W.; Li, H.; Hopmann, E.; Elezzabi, A. Y. “Nanostructured inorganic electrochromic materials for light applications.” *Nanophotonics*, 10, 825-850 (2021); Zhang, W.; Li, H.; Yu, W. W.; Elezzabi, A. Y. “Emerging Zn anode-based electrochromic devices.” *Small Science*, 1, 2100040 (2021).

2.2 Electrochromic materials

As the core component in an electrochromic device, electrochromic materials, having different optical properties, have been utilized for various electrochromic applications. Correspondingly, the electrochromic materials can be classified into a variety of types, including inorganic electrochromic materials, organic electrochromic materials, inorganic-organic hybrids, and plasmonic materials.

2.2.1 Inorganic electrochromic materials

Inorganic electrochromic materials mainly consist of the oxides of transition metals, which exhibit several different valence states upon reduction. Electron delocalization between the mixed-valence states results in different bandgaps of inorganic materials, thus leading to different absorption of the light and inducing distinct color changes of the material.²³ There are two principally different types of electrochromic transition metal oxides which are classified according to the coloration mechanisms: cathodic electrochromic materials, which are colored under guest ion insertion (reduction process); and anodic electrochromic materials, which are colored under guest cation extraction (oxidation process).²⁴ The transition metals whose oxides possessing electrochromic properties are shown in the periodic table of elements (Figure 2.1).

ELECTROCHROMIC OXIDES:

H																	He
Li	Be											B	C	N	O	F	Ne
Na	Mg											Al	Si	P	S	Cl	Ar
K	Ca	Sc	Ti	V	Cr	Mn	Fe	Co	Ni	Cu	Zn	Ga	Ge	As	Se	Br	Kr
Rb	Sr	Y	Zr	Nb	Mo	Tc	Ru	Rh	Pd	Ag	Cd	In	Sn	Sb	Te	I	Xe
Cs	Ba	La	Hf	Ta	W	Re	Os	Ir	Pt	Au	Hg	Tl	Pb	Bi	Po	At	Rn
Fr	Ra	Ac															

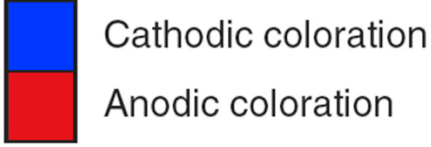


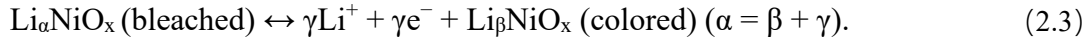
Figure 2.1 Electrochromic transition metal oxides showing both cathodic and anodic coloration. Reproduced with permission from Ref. ²⁴. Copyright 2017, Elsevier Ltd.

As can be inferred from Figure 2.1, WO_3 , TiO_2 , Nb_2O_5 , MoO_3 , and Ta_2O_5 exhibit the cathodic coloration effect, which means that these oxides can be tinted via a reduction or cation intercalation. ²⁵⁻³⁰ These oxides commonly consist of highly distorted MO_6 octahedra crystalline structure, ^{31,32} where M represents the transition metal atom. The layered structure, formed by the edge- and corner-sharing MO_6 octahedra, facilitates ion transport through the conduits or chains of interstitial sites. ³³ Notably, these oxides exhibit similar electronic band structures. Their intrinsically empty *d*-bands become populated upon cathodic charge injection, and thus cause a color change through new intraband transitions. ^{34,35} Among this class of oxides, WO_3 is the most widely studied cathodic electrochromic material, especially used for electrochromic smart windows platforms. The WO_3 layer is transparent in the oxidation state, while it can be tinted to blue as cations are injected into the WO_3 structures via the following reaction,

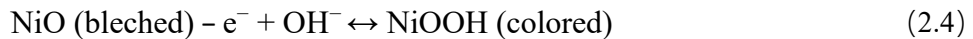


where M^+ can be either H^+ or an alkali metal ion, such as Li^+ , Na^+ , K^+ , Al^{3+} , or the recently reported Zn^{2+} .³⁶ Compared with employed monovalent ions (e.g. H^+ , Li^+ , K^+ and Na^+), multivalent ions (e.g., Mg^{2+} , Al^{3+} , Zn^{2+}) are expected to provide multiple charges to accelerate the redox reactions for fast electrochromic switching times.^{37,38} Another key advantage of multivalent ions, especially the Zn^{2+} , is their compatibility with aqueous electrolytes, which facilitates the formation of newly developed Zn-based electrochromic devices.³⁹

On the other hand, the anodic coloration effect is observed in NiO , IrO_2 , Cr_2O_5 , MnO_2 , FeO_2 , and Co_3O_4 .⁴⁰⁻⁴⁶ Such anodic electrochromic oxides usually serve as a counter electrode which is often used in conjunction with a cathodic electrochromic electrode in a complementary device.^{47,48} The most widely studied anodic electrochromic material is NiO , which is transparent in its reduced state and colored gray in its oxidized state.⁴⁹ The schematic reaction of NiO_x cycled in the Li^+ -ion electrolytes can be summarized as follows,^{50,51}



The irreversible reaction (i.e. eq. 2.2) refers to an activation process in the initial cycling of NiO_x . The reversible reaction, represented by eq.2.3, indicates the color switching processes accompanying the ion insertion/extraction. The insertion/extraction of OH^- can also lead to the oxidation/reduction of nickel oxide owing to the transformation of nickel ions between Ni^{2+} and Ni^{3+} .⁵² This process can be summarized as follows,⁵³



In addition to the above-mentioned cathodic and anodic electrochromic materials, vanadium oxides (e.g., V_2O_3 , V_3O_7 and V_2O_5) are considered to be a type of bi-functional electrochromic

material. This is due to their multicolor change properties under both anodically and cathodically potentials.⁵⁴

Along with the above transition metal oxides, Prussian blue (PB), represented as $\text{Fe}_4[\text{Fe}(\text{CN})_6]_3 \cdot n\text{H}_2\text{O}$ and its analogs (e.g. $\text{KFe}[\text{Fe}(\text{CN})_6]$ and $\text{Na}_2\text{Fe}[\text{Fe}(\text{CN})_6]$) is another important type of inorganic electrochromic material. PB is a type of polynuclear transition metal hexacyanometallates. Similar to the anodic electrochromic transition metal oxides, PB exhibits a blue color in its oxidized state and can be reduced to Prussian white (PW, colorless) via electrochemical redox reactions.⁵⁵⁻⁵⁸ Kang and co-workers deposited quasi-cubic PB particles with diameters of ≈ 450 nm on top of a fluorine-doped tin oxide (FTO) coated glass substrate (Figure 2.2A).⁵⁹ Figure 2.2B depicts an ideal unit cell of PB with guest ions. The PB-based electrochromic device achieved a high optical modulation of 84.9% at 633 nm during the voltage variation from 1.9 to 0.5 V (Figures 2.2C and 2.2D). This PB-based device also exhibited excellent cycling stability for up to 2000 cycles. The feature of PB that stands out, in comparison to transition metal oxides based electrochromic materials, is its fast color response that results from the PB's open framework structures.^{60,61}

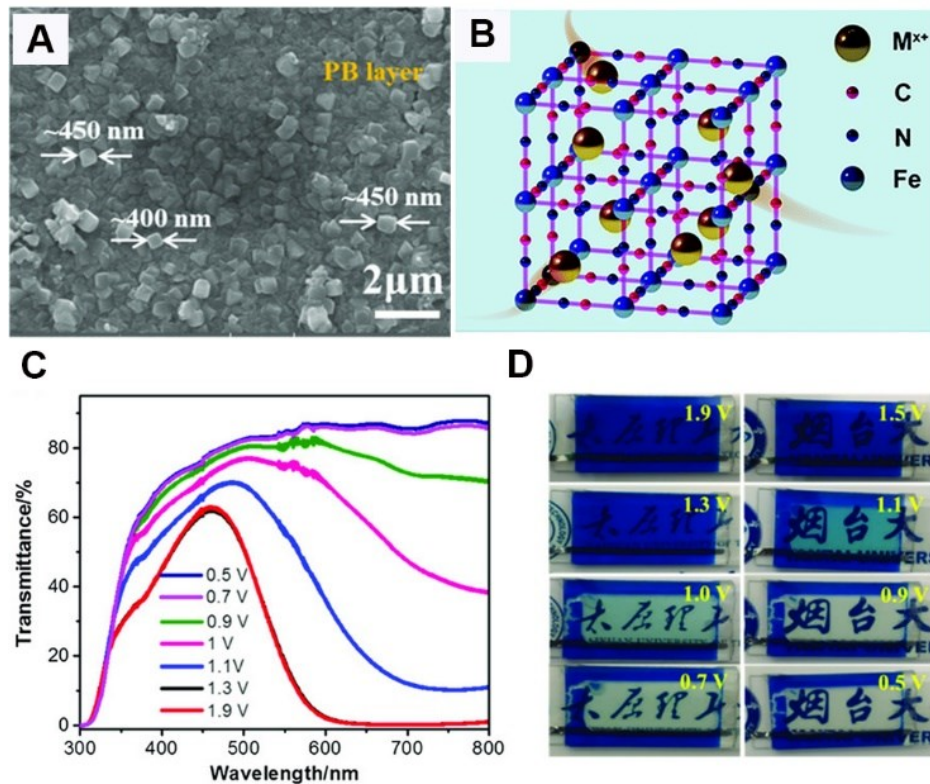


Figure 2.2. Structure, working principle, and application of PB-based electrochromic device. (A) Scanning electron microscope (SEM) image of the PB thin films. (B) A schematic diagram of an ideal PB unit cell. M^{x+} represents guest cations (e.g. Li^+ , Zn^{2+} , K^+ , Al^{3+} , Na^+ and the corresponding hydrated ions). (C) Transmittance spectra of the PB-based device at different discharge voltages from 0.5 to 1.9 V. (D) Photographs of the PB-based electrochromic device at different discharge voltages. (A–D) Reproduced with permission from Ref. ⁵⁹. Copyright 2020, Wiley.

Another class of electrochromic materials that have attracted recent attention is based on MXene. MXenes represent a large family of 2D transition metal carbides and nitrides which have been utilized for energy storage and various optoelectronic applications.⁶² For example, titanium carbide ($Ti_3C_2T_x$) has been shown to exhibit electrochromic properties cycling in 1 M phosphoric acid polyvinyl alcohol gel electrolyte (H_3PO_4/PVA gel).⁶³

2.2.2 Organic electrochromic materials

Electrochromic characteristics are shown by a wide range of organic materials, including organic molecules⁶⁴⁻⁶⁶ and conjugated polymers.⁶⁷⁻⁷⁶ Typically, organic electrochromic materials offer multiple colors under different applied biases, which are highly desired for multicolor displays. Viologens, 1,1'-disubstituted-4,4'-bipyridinium salts, are by far the most intensively investigated small molecule-based electrochromic materials.⁶⁴ Viologens exhibit three reversible redox states: a dication (V^{2+}), a radical cation (V^+) and a neutral form (V), thus yielding differently colored species (Figure 2.3A). The intense color is produced upon reduction of the viologen dication, leading to a strong absorption at its radical cation state. The substitution groups on the nitrogen of the bipyridinium salt mainly control the colors of their reduction states. As illustrated in Figure 2.3B, an ethyl viologen-based electrochromic device exhibits a blue color in its reduced state and a light yellow color in its oxidized state.⁶⁶ The major advantages of Viologens as electrochromic materials reside in their high optical contrast, excellent coloration efficiency, ease in molecular design, and the feasibility for large-area assembly. A successful application is their use by Gentex Corporation as a smart window in Boeing 787 aircraft.⁷⁷

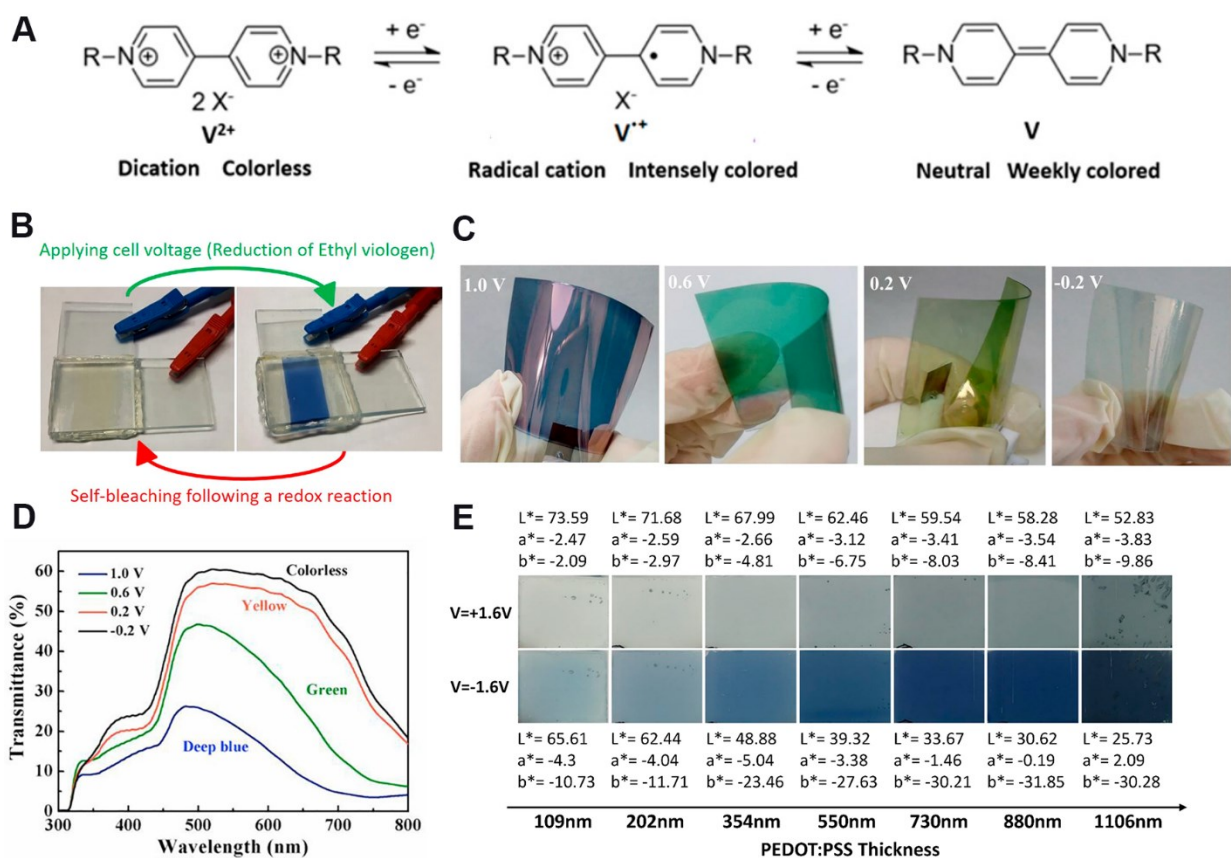


Figure 2.3. Characterization and demonstration of organic electrochromic materials. (A) Different redox states of viologen. (B) The photographs of ethyl viologen-based electrochromic device at bleached and colored states. (A–B) Reproduced with permission from Ref. ⁶⁴. Copyright 2019, Multidisciplinary Digital Publishing Institute. (C) The photographs of the flexible PANI film electrode in its colored state at the different potentials. (D) The corresponding optical transmittance spectra of the flexible PANI film electrode at different potentials. (C–D) Reproduced with permission from Ref. ⁷⁵. Copyright 2018, Elsevier Ltd. (E) Photographs of the electrochromic symmetrical displays built from PEDOT: PSS films with different thicknesses, showing an oxidized state for a potential of +1.6 V and a reduced (colored) state for a potential of –1.6 V. The corresponding measured CIE L*a*b* parameters are labeled. Reproduced with permission from Ref. ⁷³. Copyright 2019, Multidisciplinary Digital Publishing Institute.

Some long-chain polymers, such as polypyrroles,⁶⁷⁻⁶⁹ polythiophenes⁷⁰⁻⁷² and polyanilines^{74,75}, are found to possess electrochromic properties by altering the structures of their π -conjugated systems. Polyaniline (PANI) films exhibit reversible multicolors: transparent \leftrightarrow pale yellow \leftrightarrow green \leftrightarrow blue, as the applied potential is varied.⁷⁸ As shown in Figure 2.3C, PANI films can be prepared on flexible indium tin oxide (ITO)/polyethylene terephthalate (PET) substrates.⁷⁵ The

optical transmission spectra of PANI films at different potentials and color states are shown in Figure 2.3D. The transmittance variation between colorless and blue states can be as high as 49% at 630 nm as the applied potential increased from -0.2 to 1.0 V. Another interesting polymer is poly(3,4-ethylenedioxythiophene) polystyrene sulfonate (abbreviated as PEDOT:PSS). PEDOT:PSS is a conductive polymer which exhibits a blue coloration upon electrochemical reduction. Figure 2.3E depicts a series of images of the electrochromic symmetrical displays built from PEDOT:PSS films of various thickness.⁷³ A clear color gradient was observed with the increase of thickness in reduced (colored) state as distinguished by the CIE $L^*a^*b^*$ color space parameters. Clearly, utilizing PEDOT:PSS as a transparent conducting electrode is promising in applications requiring a stretchable electrochromic platform.^{79,80}

2.2.3 Organic-inorganic hybrid electrochromic materials

Different electrochromic materials have their respective advantages and disadvantages, thus instead of using a single class of electrochromic materials, organic-inorganic electrochromic hybrids can combine the advantages of each platform, thus offering enhanced electrochromic properties. Considerable efforts have been devoted towards the development of organic-inorganic electrochromic nanocomposites, wherein the assembly of the organic polymers into an inorganic porous framework is shown to lead to enhanced electrochromic performance and chemical stability.⁸¹⁻⁸³ For example, the organic polymers PEDOT:PSS can also be introduced into porous nanorod layers of tungsten molybdenum oxide ($W_{0.71}Mo_{0.29}O_3$).⁸² Figures 2.4A and 2.4B schematically illustrate the spray layer-by-layer assembly process used to prepare the $W_{0.71}Mo_{0.29}O_3$ /PEDOT:PSS hybrid electrochromic films. The PEDOT:PSS chains were observed to permeate into the porous nanorod layers of the $W_{0.71}Mo_{0.29}O_3$, forming an interconnected

conductive network (Figures 2.4C and 2.4D). The $W_{0.71}Mo_{0.29}O_3$ /PEDOT:PSS hybrid electrochromic films realized an improved electrochromic performance that is superior to both pure PEDOT:PSS and $W_{0.71}Mo_{0.29}O_3$ films. In the organic-inorganic nanocomposites, the interfacial interactions between the organic and the inorganic phases have a large impact on the properties of the nanocomposites. A good distribution of the introduced materials within the matrix material and their strong interfacial interaction is shown to improve the mechanical and electrochromic properties of structural nanocomposites, due to the synergic effect of these materials.^{84,85} A recent study demonstrated that a class of hybrid electrochromic materials utilizing polythiophenes and tin-doped indium oxide nanoparticles that enabled the independently modulating visible and near-infrared light.⁸⁶ This inorganic-organic hybrid electrochromic film combines polythiophenes to modulate visible light with tin-doped indium oxide nanoparticles that modulate near-infrared light. Such hybrid materials can be operated in three distinct voltage regimes, each of which uniquely modulates visible and near-infrared light. Besides simple physical contact, the strong interfacial interactions between the organic and inorganic components (e.g. covalent bond, coordination bond, electrostatic interaction, hydrogen bond and π - π stacking interaction) are conducive for avoiding structural damage caused by the volume change during the switching process and thus improving the structural stability of the hybrids.⁸⁷⁻⁹⁰ For example, Yang et al. investigated covalently bonded WO_3 /polyvinylimidazole core-shell microspheres.⁸⁸ It is found that the chemical and thermal stabilities of covalently bonded WO_3 /polyvinylimidazole are higher than those of pure WO_3 nanoparticles and noncovalently bonded WO_3 /polyvinylimidazole. The covalent bond ($\sim 100 \text{ kJ mol}^{-1}$ to 500 kJ mol^{-1}) can supply solid strength for the organic/inorganic electrochromic nanocomposites, leading to enhanced electrochemical and electrochromic performances.⁸⁷

Another important example of inorganic-organic hybrids is Metallo-supramolecular polyelectrolytes (MEPEs). This hybrid electrochromic material is based on the metal-to-ligand charge transfer and the intervalence charge transfer.⁹¹⁻⁹³ Through altering the metal ion center or the surrounding organic ligands, MEPE can switch between various colors. As shown in Figure 2.4E, Kurth et al. reported a reversible redox behavior of Fe^{II}/Fe^{III} in FeL2-MEPEs device where a color-switching between the red and the green colors was demonstrated.⁹⁴ Furthermore, electrochromic performance can be observed in Os^{II} -based Metallo-supramolecular polyelectrolytes.⁹⁵ Figure 2.4F illustrates an electrochromic device using linear Os^{II} -based MEPEs, where a distinct color change from yellow-green to pale-pink was observed upon reduction reaction.

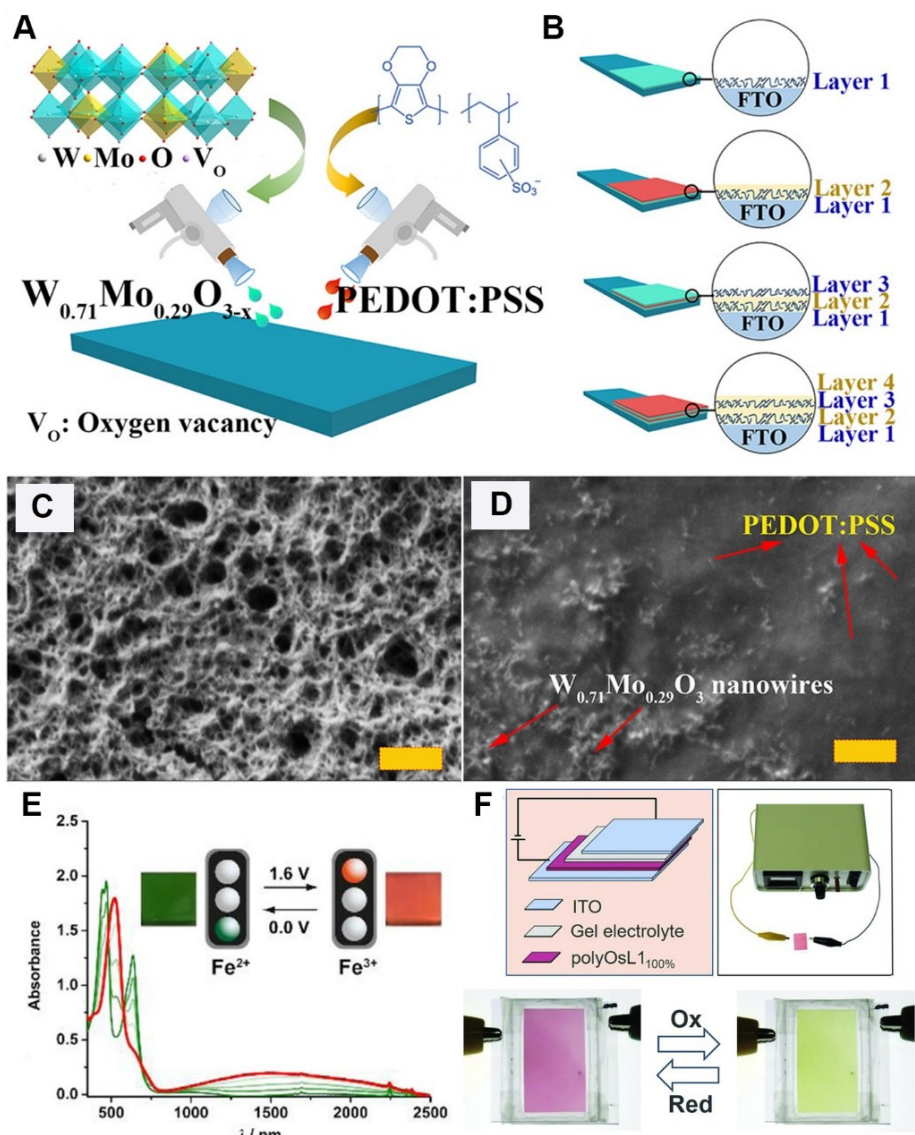


Figure 2.4. Preparation and characterization of organic-inorganic hybrid films. (A) Schematic illustration of the spray layer-by-layer assembly process used to prepare the $W_{0.71}Mo_{0.29}O_3$ /PEDOT:PSS hybrid electrochromic films. (B) Schematic illustration of the evolution of the $W_{0.71}Mo_{0.29}O_3$ /PEDOT:PSS hybrid electrochromic films during the initial four cycles. Layers 1 and 3 depict the porous structure of $W_{0.71}Mo_{0.29}O_3$ material, whereas Layers 2 and 4 depict the PEDOT:PSS material. (C) Field emission scanning electron microscope (FESEM) image of the spray-coated pure $W_{0.71}Mo_{0.29}O_3$ films (D) FESEM image of the spray-coated $W_{0.71}Mo_{0.29}O_3$ /PEDOT:PSS hybrid films (A–D) Reproduced with permission from Ref. ⁸². Copyright 2018, American Chemical Society. (E) Optical absorbance of Fe^{2+} -MEPEs at different potentials with the corresponding photographs of the thin films. Reproduced with permission from Ref. ⁹⁴. Copyright 2017, American Chemical Society. (F) Schematic illustration of linear Os^{II} -based MEPEs electrochromic device. Reproduced with permission from Ref. ⁹⁵. Copyright 2018, Wiley.

2.2.4 Nanoparticles and nanostructured plasmonic material

Plasmonic devices can experience an unconventional electrochromic process, where the color modulation of the electrochromic device is primarily based on dynamically changing the resonance of plasmonic nanostructures. Nanoparticles plasmonic materials are identified as either colloidal metal nanoparticles, which allow for reversible metal deposition, or highly-doped metal oxide nanocrystals that can be electrochemically charged in a capacitive manner due to their extremely small size and high surface area.³⁴ Light couples to the colloidal plasmonic material via the resonant excitation of free charge carriers as localized surface plasmon resonances (LSPRs). Here, LSPR enables a wide range of spectral tunability by changing the nanocrystal size, altering the host environment, or via doping or injection of charges. When the incident electromagnetic radiation frequency matches the natural resonance frequency of collective electron oscillations in the conduction band (or holes in the valence band) of the nanocrystals (Figure 2.5A), light absorption and scattering of nanocrystals are notably enhanced. Although the LSPR frequency of nanocrystals is slightly tunable by their shapes, the doping level, and the nanostructure size, the free electron density plays a key role because it determines the starting position, width, and intensity of the LSPR absorption peak.⁹⁶⁻⁹⁸ Typically, metal-based plasmonic nanostructures exhibit intrinsic free carrier density on an order of 10^{22} cm^{-3} ,⁹⁹ which leads to high energy electronic oscillations resulting in plasmonic resonance frequencies in the visible spectral range. Metal-based electrochromic devices have been demonstrated via reversible electrochemical deposition. Based on the size and shape of the deposited particles, which are strongly dependent on the deposition time, bias voltage, and chemical make up of the solvent, the resonance frequency can be modulated over a wide range. A recent study by Kobayashi et al. demonstrated a multicolor

electrochromic device based on the Ag deposition mechanism.¹⁰⁰ Figure 2.5B illustrates the morphology of Ag deposited on the ITO particle-modified electrode having a diameter size of 21 nm. With the deposition of Ag on the ITO electrode, the LSPRs of Ag nanoparticles result in displaying multicolors (Figure 2.5C).

Highly doped metal oxide nanocrystals exhibit charge carrier densities in the range of 10^{20} - 10^{22} cm^{-3} , which leads to pronounced surface plasmon resonances in the near-infrared spectral range. The resonance of free carriers can be modulated through an electrochemical gating process¹⁰¹. The change in carrier concentration leads to a shift in the LSPR frequency and a change in absorption, giving rise to plasmonic electrochromism.³⁴ Even though this plasmonic electrochromism does not lead to a change in the oxidation state of the material, devices based on metal oxide plasmonic nanostructures show reversible optical transmission changes through electrochemical charge modulation. Figure 2.5D depicts an illustration of the capacitive nature of the plasmonic electrochromic mechanism. The modulation of the electron/hole density is electrochemically controlled by the application of negative and positive potentials to the material. Milliron et al. demonstrated a surface plasmon effect in tin-doped indium oxide (ITO) nanocrystalline film.¹⁰² Figure 2.5E illustrates a transmission electron microscopy (TEM) image of the ITO nanocrystals having varying sizes of 4.1 ± 0.6 nm. When different potentials are applied, the surface plasmon resonance peak of the ITO nanocrystalline film (4.1 nm diameter, 16.8% Sn) was shown to be enhanced and shifts to higher energy (Figure 2.5F).

Additionally, conventional electrochromic materials, such as tungsten oxide or polyaniline, can be used to modulate the LSPR frequency of metallic plasmonic nanostructures. Chumanov et al. utilized a WO_3 -sol on an array of Ag nanoparticles to reversibly modulate the resonance frequency of the Ag particles by changing their dielectric surroundings.¹⁰³ Recently, several

studies have shown the potential of electrochromic modulation of the dielectric environment of metallic nanostructures for a full-color generation.¹⁰⁴⁻¹⁰⁶ In general, these devices make use of the inherent change of the refractive index of an electrochromic material during the intercalation and the deintercalation processes. This change is utilized to shift the resonance frequency of plasmonic nanostructures, such as colloids and nanohole arrays. Hopmann and Elezzabi reported a plasmonic metal-insulator–nanohole cavity based on an electrochromic WO₃ insulator layer. Through intercalation and deintercalation of lithium ions (Li⁺) into the WO₃ film, a broad peak resonance wavelength shift of 64 nm was realized, leading to distinct color reflection (Figure 2.5G).¹⁰⁶

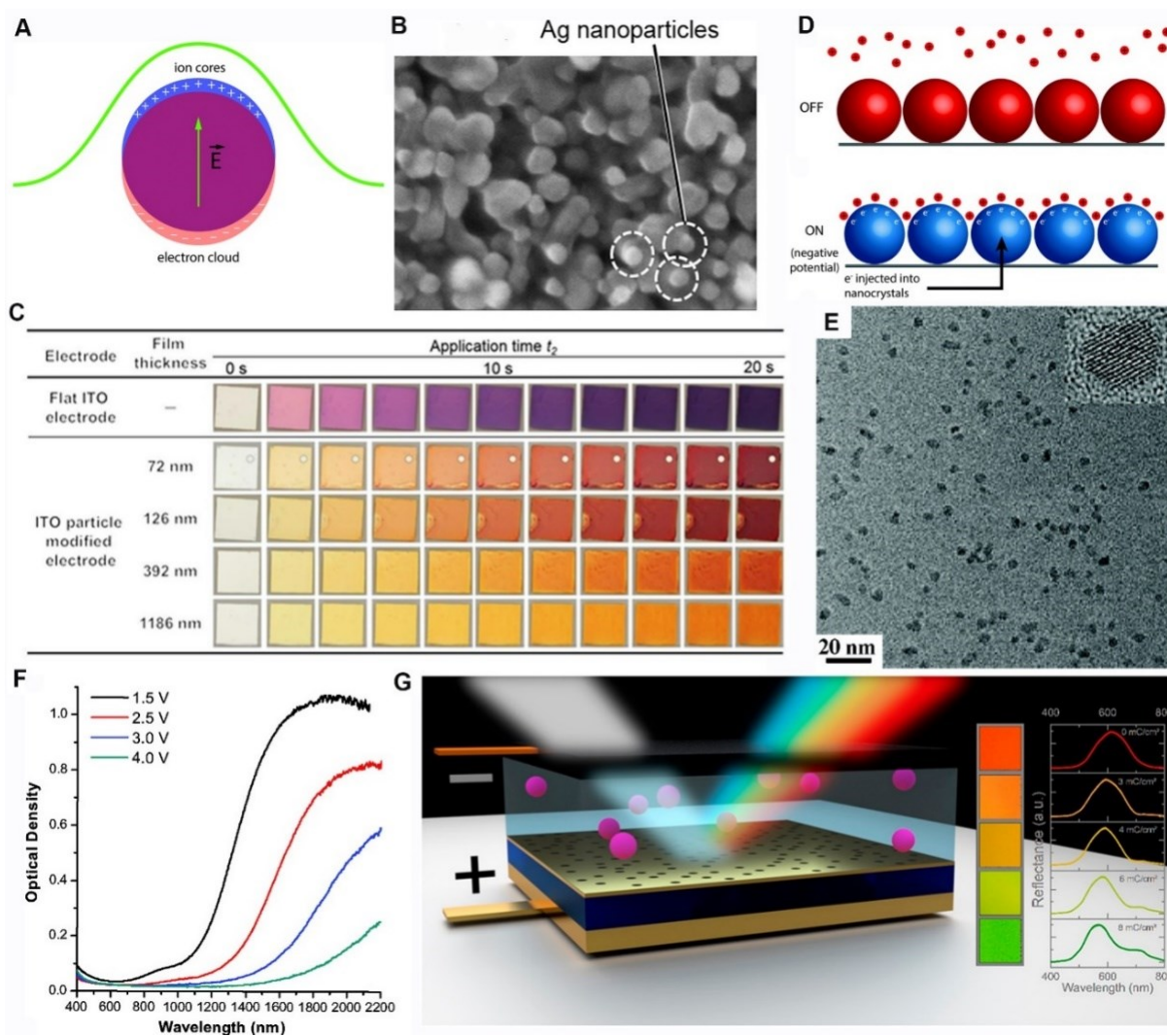


Figure 2.5. Depiction of plasmonic electrochromic nanocrystals and nanostructures. (A) Illustration of a localized surface plasmon in a nanocrystal. Incident electromagnetic radiation displaces the free electron cloud, which then experiences a restoring force exerted by the positively charged ion cores. Reproduced with permission from Ref.³⁴. Copyright 2014, Royal Society of Chemistry. (B) Scanning electron microscope (SEM) image of the Ag nanoparticles deposited on the ITO particle-modified electrode. (C) Photographs of the working electrodes with various ITO film thicknesses during the Ag deposition process. (B–C) Reproduced with permission from Ref.¹⁰⁰. Copyright 2014, American Chemical Society. (D) The mechanism of capacitive electrochromism based on nanocrystal films. In the OFF state, a positive potential is applied to the nanocrystals, no electrons and ions gather at the surface of nanocrystals. In the ON state, a negative potential is applied to the nanocrystals, ions are absorbed to the surface of nanocrystals in order to neutralize the injected electrons. Reproduced with permission from Ref.³⁴. Copyright 2014, Royal Society of Chemistry. (E) TEM image of ITO nanocrystals. (F) Potentials-dependent optical density of a film composed of 4.1 nm diameter, 16.8% Sn ITO nanocrystals. (E–F) Reproduced with permission from Ref.¹⁰². Copyright 2011, American Chemical Society. (G) Schematic of a plasmochromic device based on an electrochromic WO_3 layer and a gold resonator. Reproduced with permission from Ref.¹⁰⁶. Copyright 2020, American Chemical Society.

2.3 Key metrics for electrochromic materials

An electrochromic material alters its optical and electrical properties in response to an external voltage bias. A high-performance electrochromic material must possess fast color switching, reversible light modulations, high color contrast, low energy consumption, and long-term chemical and thermal stabilities. Key performance metrics are introduced and highlighted below.

2.3.1 Color and optical contrast

Color is an important aspect in assessing the performance of electrochromic materials as their applications rely on switching between different colors. The colorimetric analysis is usually performed based on the protocols set out by the International Commission on Illumination (CIE). The CIE 1931 xyY color space is widely used to specify color in practice. As shown in Figure 2.6A, an electrochromic film configured in ultracompact Fabry-Perot nanocavities displays seven distinguished colors.¹⁰⁷ The Fabry-Perot nanocavities utilize partially reflective tungsten metal as the current collector and the reflector layer. As the thickness of the WO₃ thin film changes, various structural colors are generated. These colors cause a significant shift of the CIE color coordinates (Figure 2.6B), forming a circular area with different tints. More interestingly, the Fabry-Perot nanocavity-type electrochromic films exhibit a large variety of multicolor states under different applied potentials (Figure 2.6C). While the 163-nm-thick WO₃/W electrode produces a gradual color change from red to green at different biases (Figure 2.6D), the reflection spectrum displays a drastic shift from 760 to 517 nm in its peak position (Figure 2.6E).

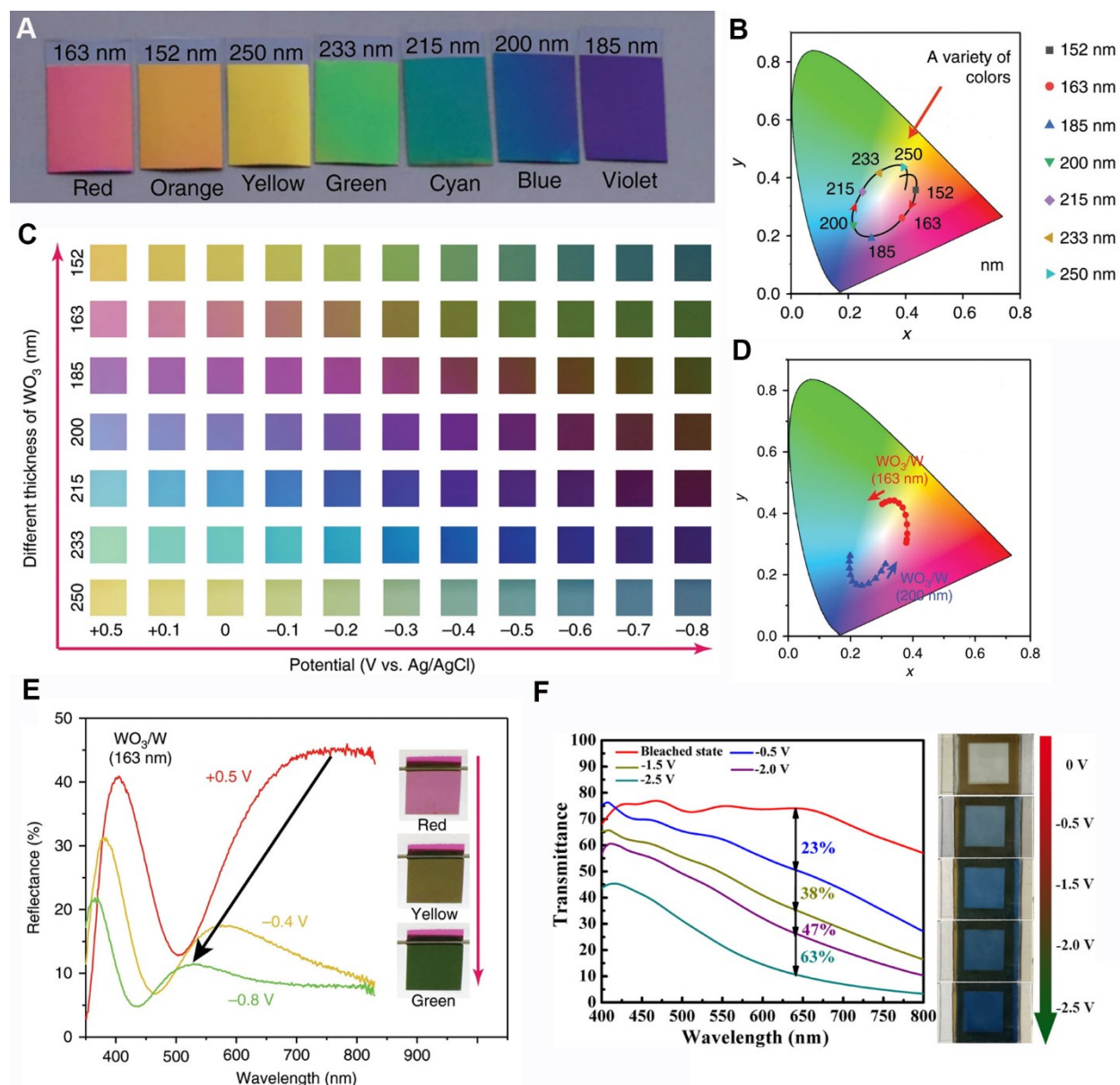


Figure 2.6. Demonstration of electrochromic materials having different colors and light spectra. (A) Photographs of the WO_3/W electrodes having different thicknesses of the WO_3 layer. (B) CIE color coordinates of the WO_3/W electrodes having different thicknesses of the WO_3 layer. (C) Color gallery obtained from the WO_3/W electrodes under different voltage biases. (D) CIE color coordinates of the 163/200-nm-thick WO_3/W electrode under different voltage biases. (E) Reflectance spectra and photographs of the 163-nm-thick WO_3/W electrode under different voltage biases. (A–E) Reproduced with permission from Ref. ¹⁰⁷. Copyright 2020, Nature Publishing Group. (F) Transmittance spectra and photographs of $\text{MoO}_{2+x}\text{-WO}_3$ electrochromic device. Reproduced with permission from Ref. ¹⁰⁸. Copyright 2019, American Chemical Society.

The intensity difference between the colors is an important factor in determining the quality of the electrochromic coloration process. As such, the optical contrast, referring to the degree of optical change during the switching process (intensity change in transmittance (ΔT %), absorbance (ΔA %) or reflectance (ΔR %)), is another metric used in evaluating the electrochromic material performance. However, when describing the optical contrast of electrochromic materials or devices, it is customary to report this parameter at a single wavelength. This wavelength is selected to be either the wavelength at which a maximum absorbance occurs or the wavelength of maximum human visual sensitivity (i.e. 550 nm).³³ Figure 2.6F depicts a WO_3 -based electrochromic device, where a 63% change in transmittance at 633 nm was achieved at an applied voltage of -2.5 V.¹⁰⁸ The choice of the 633 nm wavelength used to calculate the optical contrast is dictated by the maximum absorbance observed at this wavelength. In general, the optical contrast of a material mainly depends on the thickness of the electrochromic layer.¹⁰⁹ As the film thickness increases, the transmittance of both the colored and bleached states will decrease. Typically, the maximum optical contrast is reported at an attained intermediate thickness of a few hundred nanometers.^{110,111} The design of nanostructured electrochromic materials is expected to enhance the electrochromic performance (e.g., optical contrast, switching times, coloration efficiency and cycling stability).¹¹²⁻¹¹⁴ A recent study by Scherer et al. demonstrated that the gyroid-structured vanadium pentoxide films surpass previous inorganic electrochromic materials in all relevant parameters: the switching speed, coloration contrast, and composite coloration efficiency.¹¹⁵

2.3.2 Coloring and bleaching switching times

Switching times, also known as the response times, refer to the times required to switch between the colored/bleached and the bleached/colored states of an electrochromic material or a device.

The coloration and bleaching times are defined as the time required for 90% change in the entire optical modulation.¹¹⁶ As a key parameter when considering the suitability of an electrochromic device for light modulation applications, fast switching between the different color states is highly desirable. Figure 2.7A illustrates an Al anode-based electrochromic energy storage smart window switching between 4V (transparent state), 2.2 V (cool state) and 1.6 V (dark state).¹¹⁷ The switching times of this device were calculated to be 71 s for bleaching and 19 s for coloration at 633 nm, and 56 s for bleaching and 18 s for coloration at 1200 nm (Figures 2.7B and 2.7C). Generally, the switching times of an electrochromic layer will increase as the film thickness increases. Thicker films with a fixed porosity would lead to longer ion-transport pathways to insert into the inner active materials, which results in longer switching times.¹¹⁸⁻¹²⁰ The nanostructured electrochromic materials with large surface active area are promising for fast switching times as the active materials are easy to access for guest ions.^{121,122} For example, rapid switching times of 0.5/0.9 s for the coloration and bleaching processes, respectively, were reported for nanostructured electrochromic materials: core-shell halloysite nanotube (HNT)@inherently conducting polymer (ICP) nanocomposites.¹²¹ Other Parameters, such as the electrolyte properties, counter electrode material composition, substrate sheet resistance and device size, all have a significant effect on the switching times.

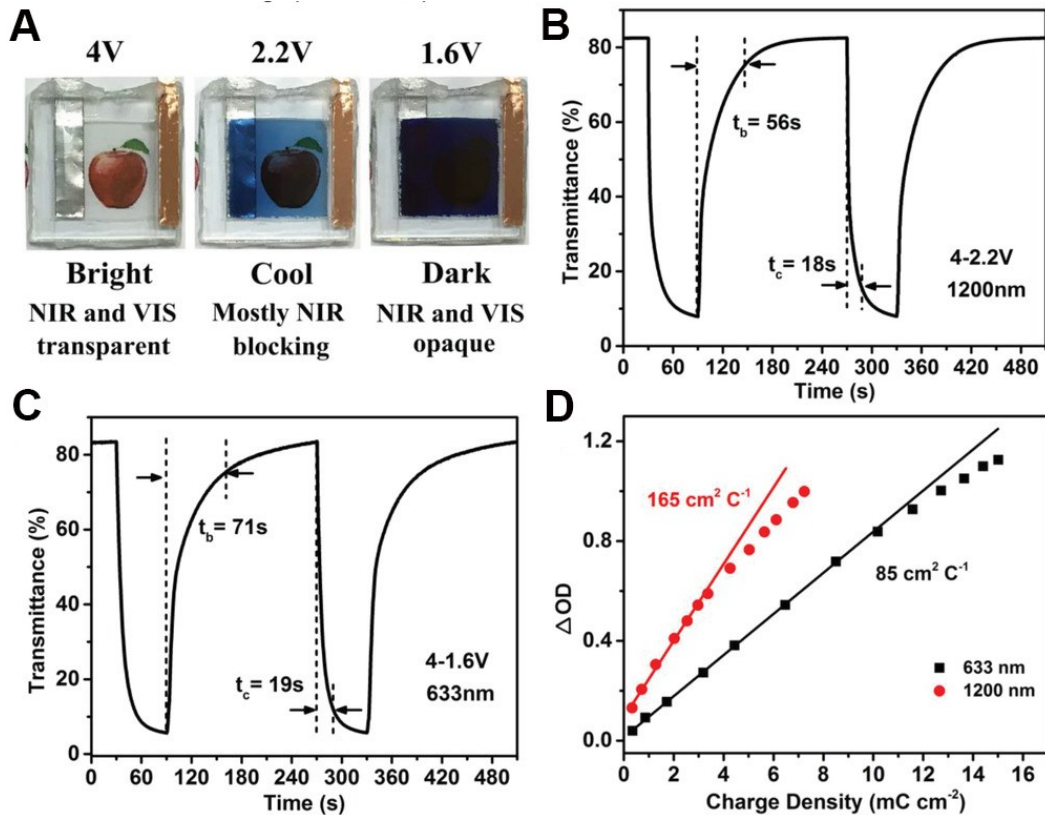


Figure 2.7. Al anode-based electrochromic energy storage windows. (A) Photographs of an Al anode-based electrochromic energy storage window at different applied potentials. (B) The dynamic test of the device between 4-2.2 V at 1200 nm. (C) The dynamic test of the device between 4-1.6 V at 633 nm. (D) Coloration Efficiency of the device switching at 633 nm and 1200 nm. (A-D) Reproduced with permission from Ref. ¹¹⁷. Copyright 2019, Wiley.

2.3.3 Coloration efficiency

An energy-efficient electrochromic material requires a high optical contrast while consuming fewer charges in the process. In this regard, coloration efficiency (CE), representing the change in optical density (ΔOD) per unit of charge intercalated into the electrochromic layer, is proposed to evaluate the energy-related efficiency accordingly,

$$\Delta OD = \log(T_c/T_b) = \eta Q/A, \quad (2.5)$$

where η is coloration efficiency (CE), Q is the charge (C), A is the active area of the electrochromic

material (cm^2), T_c and T_b are the transmittances of electrochromic devices at coloration and bleaching states, respectively. An example of CE value calculation is shown in Figure 2.7D. Here, the Al anode-based electrochromic energy storage window exhibited CE values of $165 \text{ cm}^2 \text{ C}^{-1}$ at 1200 nm and $85 \text{ cm}^2 \text{ C}^{-1}$ at 633 nm, respectively. The coloration efficiency increases as the thickness increases until a maximum value, then the coloration efficiency decreases as the thickness keeps on increasing.^{123,124} The maximum CE value is obtained at an intermediate thickness (~ a few hundred nanometers), which requires rational design and carefully screening several thicknesses of electrochromic films. This phenomenon probably relates to the different ionic/electric resistance of the electrochromic films at various thicknesses.¹²⁵ Since the coloration efficiency is an intrinsic parameter of electrochromic materials and mainly relies on the morphology of the materials,¹²⁶ the design of nanostructured electrochromic materials having large surface active area is required to achieve high CE values. As reported by Ma et al., the CE value of WO_3 nanoflake films film is much higher than the WO_3 nanoparticle/nanorod films.¹²⁷

2.3.4 Cycling stability

Cycling stability is the loss of the optical contrast upon electrochemical cycling and is another important parameter used to evaluate the long-term stability of the electrochromic device.¹²⁸ For practical applications, electrochromic materials are expected to exhibit a cycle life of more than 10^5 cycles. However, in laboratory exploration, cycling stability is often reported for a small area of electrochromic film which is not sufficient for real-world applications. Both physical and chemical stabilities are crucial to the cycling stability of an electrochromic thin film. Generally, as the electrochromic film's thickness increases, the electrochromic film would suffer a poor adhesion to the substrate and thus leading to the significant degradation of the cycle performance due to the peeling of active materials.¹²⁹ A strong interfacial interaction between the film and the

substrate will certainly enhance the cycling stability.¹³⁰ The design of nanostructures is expected to improve both physical and chemical stability of thin films. Nanostructured electrochromic materials can be designed to optimize the contacting area between the film and the substrate and hence providing a strong interfacial adhesion.¹³¹ Furthermore, the volume expansion of nanostructured electrochromic materials during the switching process is supposed to be significantly eliminated as the numerous surface active sites increase the capacitive contribution during the redox reactions.¹³² In other words, nanostructured electrochromic materials possess excellent chemical stability upon cycling. Besides the stability of thin films, the cycling stability of an electrochromic device is influenced by several factors, including the electrolyte properties, the counter electrode material, and the device dimensions.

2.4 Design of nanostructured electrochromic materials

To develop electrochromic materials having high performance, including the above-mentioned metrics for potential real-world applications, a list of recent achievements on the fabrication of promising electrochromic materials is presented. It is hoped that universal strategies for fabricating nanostructured electrochromic materials can be realized to advance the future development of the electrochromism.

2.4.1 Tungsten oxides

The most commonly used cathodic electrochromic materials are based on tungsten oxides (e.g., tungsten oxide, hydrated tungsten oxide and doped tungsten oxide. Naturally, bulk tungsten oxide exhibits intrinsic oxygen deficiencies,¹³³ making the material appear yellowish. In contrast, in a thin film configuration, stoichiometric tungsten oxide is transparent and becomes blue upon

applying a cathodic potential.¹³⁴ Tungsten oxide has a nearly cubic structure formed by WO_6 octahedra that share corners.¹³⁵ The void space inside the cubes provides the accessibility of numerous interstitial sites where guest ions (e.g., protons or alkali cations) can be inserted. The first study on the electrochromic effect in tungsten trioxide was reported in 1969.¹³⁶ Over the past decades, the most promising application of the WO_3 electrochromic coating is as a switchable glazing for smart windows. The color change in WO_3 electrochromic smart windows offers an important energy-efficient module for designing environmentally friendly buildings by reducing the cost of air conditioning, controlling direct sun illumination, and simultaneously improving the indoor living comfort for the occupants.¹⁴

Recently, nanostructured WO_3 films have been realized for practical applications due to their excellent electrochromic performance. A variety of crystallographic and morphological structures of WO_3 films have been reported to exhibit shorter switching time, higher coloration efficiencies, and higher cycling stabilities compared to their bulk counterparts. These nanostructured WO_3 films include nanoparticles,^{53,137} nanowires,¹³⁸ nanosheets,¹³⁹ nanofibers,¹⁴⁰ and hierarchical structures,¹⁴¹ possess a large interfacial contact area with the electrolyte, short ions diffusion pathway, and good structure stability associated with the intercalation/deintercalation of guest ions. These advantages of nanostructured WO_3 give rise to highly-efficient and stable electrochromic performance. Shan et al. reported the first demonstration of tungsten oxide quantum dots (QDs) for electrochromic applications.¹⁴² As shown in Figure 2.8A, since the QDs size is very small (~ 1.6 nm), this yielded a fast electron/ion transport during the coloration/bleaching process. Similarly, Yao et al. reported WO_3 QDs with an average diameter of 1.2 nm (Figure 2.8B).¹⁴³ The cycle stability of WO_3 QDs electrochromic films can reach 20,000 cycles upon the intercalation/deintercalation of Al^{3+} . Moreover, larger WO_3 QD nanocrystals and their inks (~ 4 nm in diameter,

Figures 2.8C and 2.8D) were investigated by Zhang et al. for ink-jet printed flexible electrochromic devices.¹³⁷ The printed tungsten oxide thin films are assembled into a novel electrochromic pseudocapacitive device, which exhibits a relatively high capacity ($\approx 260 \text{ C g}^{-1}$ at 1 A g^{-1}). In addition to the abovementioned QD WO_3 nanocrystalline structures, Zhang et al. reported oxygen-deficient monoclinic tungsten oxide nanowire (m- WO_{3-x} NW) (Figures 2.8E and 2.8F). With efficient Al^{3+} intercalation/deintercalation, the m- WO_{3-x} NWs based electrochromic device delivered not only efficient and independent control of near-infrared and visible light transmittance but also exhibited high coloration efficiency.³⁷ High optical contrast of 93.2%, high coloration efficiency of $121 \text{ cm}^2 \text{ C}^{-1}$, fast switching times of 16/13 s, and good cycling stability (5.5% capacity loss after 2000 cycles) were reported. An interesting form of nanostructured WO_3 films is the hierarchical nest-like $\text{WO}_3 \cdot 0.33\text{H}_2\text{O}$ film (Figure 2.8G). Li and co-workers reported a self-seeded hydrothermal process that eliminates the grain boundaries existing in the nanocrystalline seed layer.¹⁴⁴ This process accelerates electron transport to the FTO glass substrate and promotes electron transfer efficiency. As shown in Figure 2.8H, the prepared $\text{WO}_3 \cdot 0.33\text{H}_2\text{O}$ films have an optical contrast of 40.8% and 57.6% after applying voltages of -0.5 V and -1.0 V, respectively. The response times of $\text{WO}_3 \cdot 0.33\text{H}_2\text{O}$ films are found to be 26 s and 5.5 s under $\pm 3.0 \text{ V}$ bias. Due to the large active surface area, this self-seeded film also exhibits a high CE value of $126.34 \text{ cm}^2 \text{ C}^{-1}$.

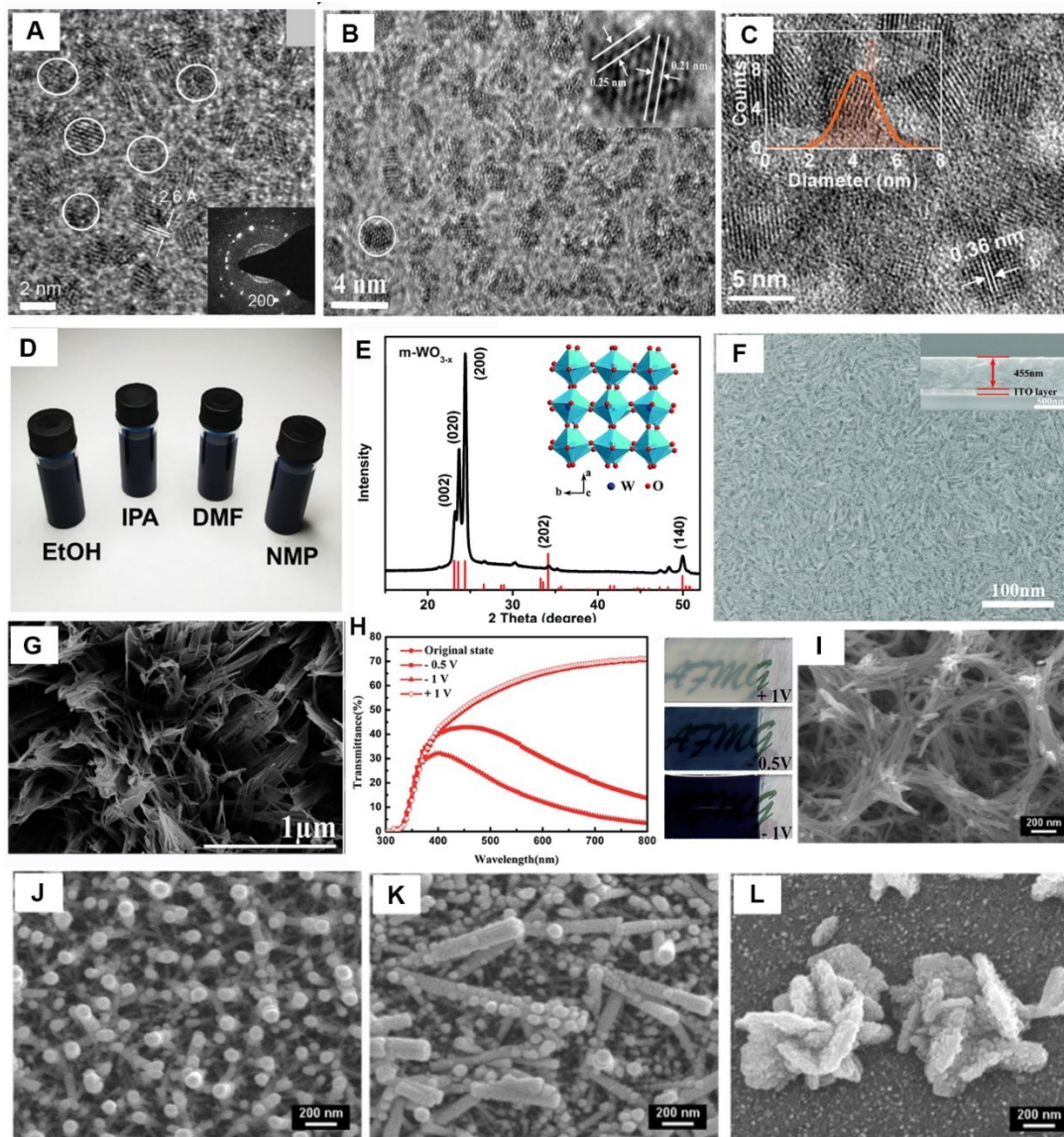


Figure 2.8. Structure and Characterization of WO_3 -based electrochromic films. (A) TEM image of tungsten oxide QDs with average sizes of 1.6 nm. Reproduced with permission from Ref. ¹⁴². Copyright 2014, Wiley. (B) High-resolution TEM image of as-prepared tungsten oxide QDs. Reproduced with permission from Ref. ¹⁴³. Copyright 2020, Elsevier. (C) TEM image of WO_{3-x} nanocrystals. Inset shows the nanocrystals diameter statistics. (D) WO_{3-x} inks based on four different solvents. (C-D) Reproduced with permission from Ref. ¹³⁷. Copyright 2020, Wiley. (E) XRD patterns and crystal structure (inset) of $m\text{-WO}_{3-x}$ NWs. (F) Surface and cross-sectional (inset) SEM images of $m\text{-WO}_{3-x}$ NW films. (E-F) Reproduced with permission from Ref. ³⁷. Copyright 2018, Royal Society of Chemistry. (G) SEM image of self-seeded grown $\text{WO}_3 \cdot 0.33\text{H}_2\text{O}$ electrode with less amount of ethylene glycol. (H) Optical transmittance spectra and photographs of the self-seeded grown $\text{WO}_3 \cdot 0.33\text{H}_2\text{O}$ film measured at different biases. (G-H) Reproduced with permission from Ref. ¹⁴⁴. Copyright 2014, Royal Society of Chemistry. FESEM images of WO_3 films doped with different Ni content: (I) 0%, (J) 0.5%, (K) 1.5% and (L) 2.5%. (I-L) Reproduced with permission from Ref. ⁴⁷. Copyright 2016, Royal Society of Chemistry.

Doping WO_3 with other elements has been realized as an efficient method to tune the nanostructures of WO_3 .⁴⁷ Li and co-workers reported that the molybdenum doping of WO_3 significantly reduces the particle size of the WO_3 . The solution-based fabrication process was simple and inexpensive to allow for large-scale fabrication of electrochromic films.¹¹⁶ Furthermore, a slight increase of the Ni content (from 0% to 2.5%) alters the surface morphology of the WO_3 film (Figures 2.8I-2.8L).⁴⁷ For the undoped WO_3 film (Figure 2.8I), the SEM image shows a porous network structure. Whereas by doping the film with only 0.5% Ni, the Ni- WO_3 grows into vertically-aligned nanorod array structures (Figure 2.8J). As the doping concentration of Ni is increased to 1.5%, the nanorods become randomly distributed nanorods (Figure 2.8K). Once the Ni doping content was increased to 2.5%, nanorods disappeared and nanoflowers composed of clusters of nanoplates appear (Figure 2.8L). For the WO_3 films with 0–1.5% Ni doping, the electrochromic performance is found to be enhanced with the increase of Ni concentration. The optical contrast in both the visible and near-infrared region increases with increasing Ni doping. At a light wavelength of 600 nm, the optical contrast enhanced from 50.9% to 86.0% at 0% and 1.5% Ni concentrations, respectively. Similarly, the coloration efficiency is also higher at $60.5 \text{ cm}^2 \text{ C}^{-1}$ for 1.5% Ni content compared to $20.8 \text{ cm}^2 \text{ C}^{-1}$ for the undoped WO_3 film. Notably, other doping techniques with different elements, such as Nb,¹⁴⁵ Mo,¹⁴⁶ Fe,¹⁴⁷ and Ti,¹⁴⁸ were shown to greatly improve the electrochromic performance of WO_3 films. The most efficient strategy to develop the high-performance electrochromic WO_3 films is the doping method,¹⁴⁹ which requires further investigation from the community. To distinguish the electrochromic properties of different nanostructured WO_3 , Table 2.1 summarizes and compares the key electrochromic metrics.

Table 2.1 Summary of the electrochromic properties of nanostructured WO₃ with different morphologies

Ref.	Nanostructures	Optical Contrast (ΔT)	Switching time (s)	Coloration Efficiency (cm ² C ⁻¹)	Cycling numbers
Yao et al. ¹⁴³	WO ₃ Quantum dots	97.8% at 633 nm	Coloration: 4.5 Bleaching: 4	76.8	20000
Cong et al. ¹⁴²	WO ₃ Quantum dots	94% at 633 nm	Coloration: 0.9 Bleaching: 1.0	154	50
Zhang et al. ¹³⁷	WO _{3-x} Nanocrystals	76% at 633 nm	Coloration: 4.5 Bleaching: 3.7	97.7	1000
Zhang et al. ³⁷	m-WO _{3-x} Nanowires	93.2% at 633 nm	Coloration: 16 Bleaching: 13	121	2000
Azam et al. ¹³⁹	WO ₃ Nanosheets	62.6% at 700 nm	Coloration: 10.7 Bleaching: 6.9	—	1000
Adhikari et al. ¹⁴⁰	WO ₃ Nanofibers	43% at 550 nm	Coloration: 6.5 Bleaching: 4.0	63.15	500
Li et al. ¹⁴¹	WO ₃ Nanotrees	74.7 % at 630 nm	Coloration: 7.3 Bleaching: 2.6	75.35	250
Li et al. ¹⁴⁴	WO ₃ ·0.33H ₂ O Nanonests	57.6 % at 633 nm	Coloration: 26 Bleaching: 5.5	126.34	1000
Zhou et al. ⁴⁷	Ni-doped WO ₃ Nanorods	86% at 600 nm	Coloration: 19 Bleaching: 6.2	60.5	5500
Zhan et al. ¹⁴⁸	Ti-doped WO ₃ Nanoplates	67.6 % at 633 nm	Coloration: ~15 Bleaching: ~5	106.6	3000
Li et al. ¹¹⁶	W _{0.71} Mo _{0.29} O _{3-x} Nanoparticles	42.9 % at 633 nm	Coloration: 10 Bleaching: 7.5	36.3	2000
Li et al. ³⁶	Mo/Ti:WO ₃ Nanowires	76 % at 633 nm	Coloration: 14 Bleaching: ~10	—	100

2.4.2 Molybdenum oxides

Similar to tungsten oxides, molybdenum oxides (e.g., molybdenum oxide, hydrated molybdenum oxide and doped molybdenum oxide) are transparent in their oxidized state and become colored grey-blue upon reduction. The layered crystalline structure of MoO₃ allows it to exist in a quasi-two-dimensional state.¹⁵⁰ The ion intercalation capabilities, bandgap tunability, and various oxidation states allow MoO₃ to be a promising electrochromic material.¹⁵¹ Naturally, MoO₃ exists in three phases: orthorhombic α -MoO₃, monoclinic β -MoO₃, and hexagonal h -MoO₃.¹⁵² The orthorhombic α -MoO₃ is the most stable phase of MoO₃. This phase is constituted by MoO₆ octahedra that share edges and corners. The structure's unique layers parallel to the (010) plane

provide open channels for guest ion intercalation (Figures 2.9A and 2.9B). However, molybdenum oxides suffer inferior cycling stability due to the large-volume expansion during the intercalation/deintercalation processes. As such, nanostructured molybdenum oxides in the form of nanoparticles,¹⁴ nanobelts¹⁵² and nanosheets¹⁵³ have been shown to have improved electrochromic and electrochemical performances. Xie et al. reported on the fabrication of metastable hexagonal MoO₃ nanobelts for electrochromic device applications (Figure 2.9C).¹⁵² The open channel structure of the hexagonal MoO₃ nanobelts favors the efficient insertion of the guest ions (Figure 2.9D). As such, the MoO₃ nanobelt films exhibit a more stable cycling performance compared to orthorhombic α -MoO₃ films. Moreover, the nanohybridization of molybdenum oxide nanoparticles with tungsten molybdenum oxide nanowires offers an interesting electrochromic material platform as it circumvents many of the issues inherent to MoO₃ (e.g. slow ionic transportation efficiency and volume expansion during cycling).¹⁴ Through a solution-processed method, MoO₃ nanocrystals were embedded in the nanopores of W_{0.71}Mo_{0.29}O₃ nanowire film to form a MoO₃-W_{0.71}Mo_{0.29}O₃ nanocomposite film (Figure 9E). The W_{0.71}Mo_{0.29}O₃ nanowires not only serve as a buffer matrix which eliminates the large-volume expansion of MoO₃ during the intercalation/deintercalation of guest ions, but also provides numerous charge transport pathways to enhance transport kinetics. Notably, the MoO₃-W_{0.71}Mo_{0.29}O₃ nanohybrid films show improved cycling stability compared to the intrinsic MoO₃ films.

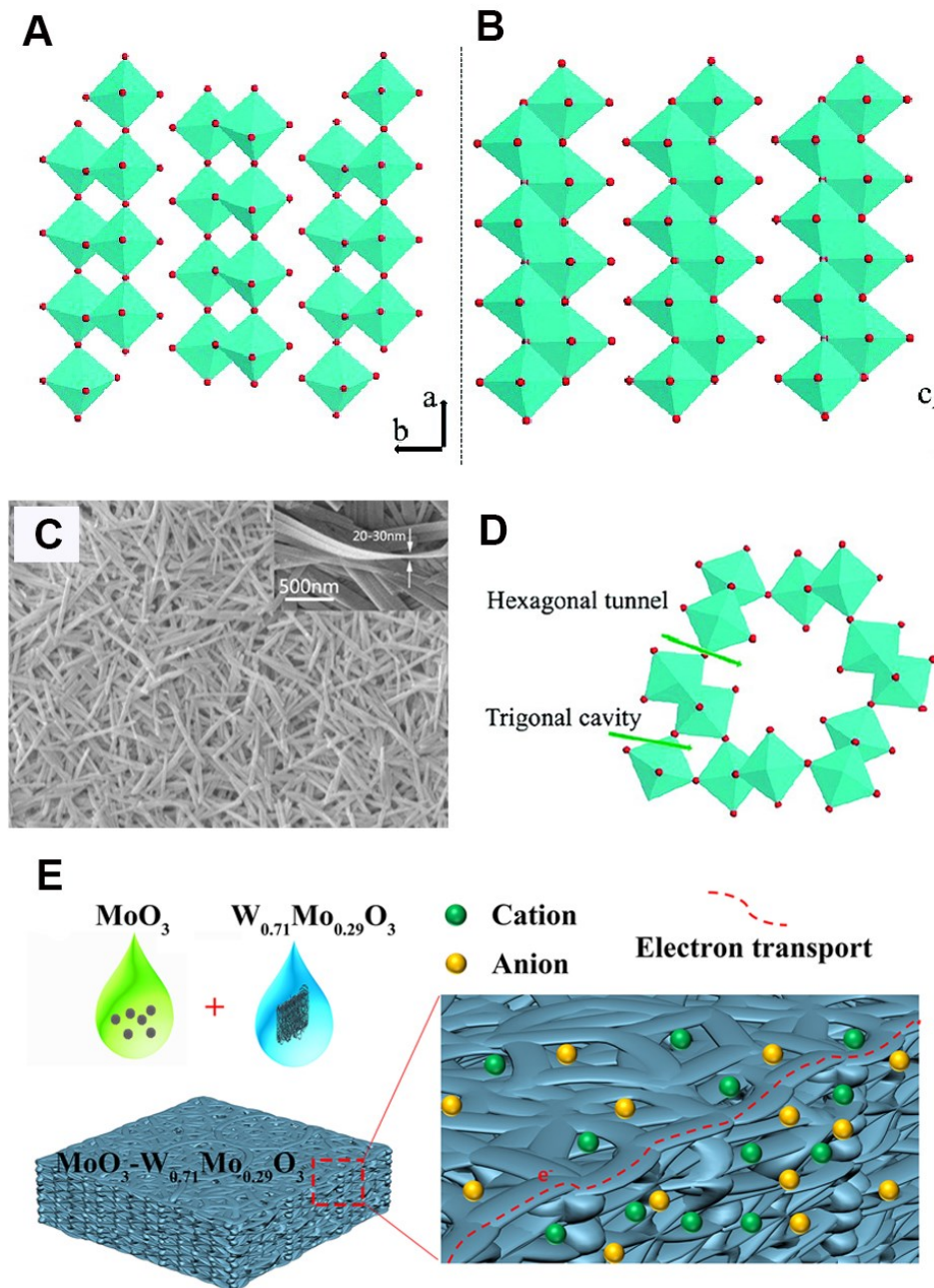


Figure 2.9. Structure and characterization of MoO₃-based electrochromic films. (A-B) Schematic representation of orthorhombic α -MoO₃. (C) SEM image (inset is a cross-section view) of hexagonal MoO₃ nanobelts. (D) Schematic representation of possible intercalation sites in hexagonal MoO₃. (A-D) Reproduced with permission from Ref. ¹⁵². Copyright 2009, American Chemical Society. (E) Schematic illustration of the matrix effect of the W_{0.71}Mo_{0.29}O₃ nanowires. Reproduced with permission from Ref. ¹⁴. Copyright 2018, Elsevier.

2.4.3 Titanium oxides

Titanium oxides (e.g., titanium oxide, hydrated titanium oxide and doped titanium oxide) have been recognized as one of the most promising electrode materials for semiconductor electrochemistry.¹⁵⁴ Naturally, bulk titanium oxide exists in three crystalline phases: rutile, anatase, and brookite.¹⁵⁵ Referring to the crystal structure of titanium oxide, the Ti^{4+} ions are surrounded by six O^{2-} ions creating an $[\text{TiO}_6]$ octahedron, forming large vacant sites to accommodate guest ions. With the intercalation of guest ions, the transmittance of titanium oxide changes from a transparent state to a blue color. However, the electrochromic performance of intrinsic TiO_2 is different from other open structures like WO_3 . A recent report by Tong et al. demonstrated that a TiO_2 mesoporous nanotube film exhibited an optical contrast of 33.5% at 700 nm, which is higher than the bulk TiO_2 films due to the enhanced Li-ion insertion kinetics.¹⁵⁶ Although the optical contrast is enhanced via designing nanotube structures, the electrochromic effect is still lower than other electrochromic materials. This is attributed to the intrinsic moderate electrochromic effect of pure TiO_2 .¹⁵⁷ As such, the aliovalent doping strategy is supposed the most convenient method to attain superior electrochromic effect of TiO_2 -based electrochromic materials.¹⁵⁸ Hence, the focus of titanium oxide research has been shifted towards the synthesis of nanostructured doped- TiO_2 films. Recently, Cao and et al. synthesized Ta-doped TiO_2 nanocrystals¹⁵⁹ (Figures 2.10A and 2.10B). The fabricated Ta-doped TiO_2 thin films showed excellent electrochromic performance in terms of high optical contrast for both the visible and the near-infrared light spectra regions (i.e., 86.3% at 550 nm and 81.4% at 1600 nm). After 2000 cycles, the optical contrasts of Ta-doped TiO_2 thin films slightly decreased by 1.3% and 6.7% at 550 and 1600 nm, respectively, indicating good electrochemical stability. This Ta-doped TiO_2 nanocrystal represents a promising new electrode material for smart windows applications.¹⁵

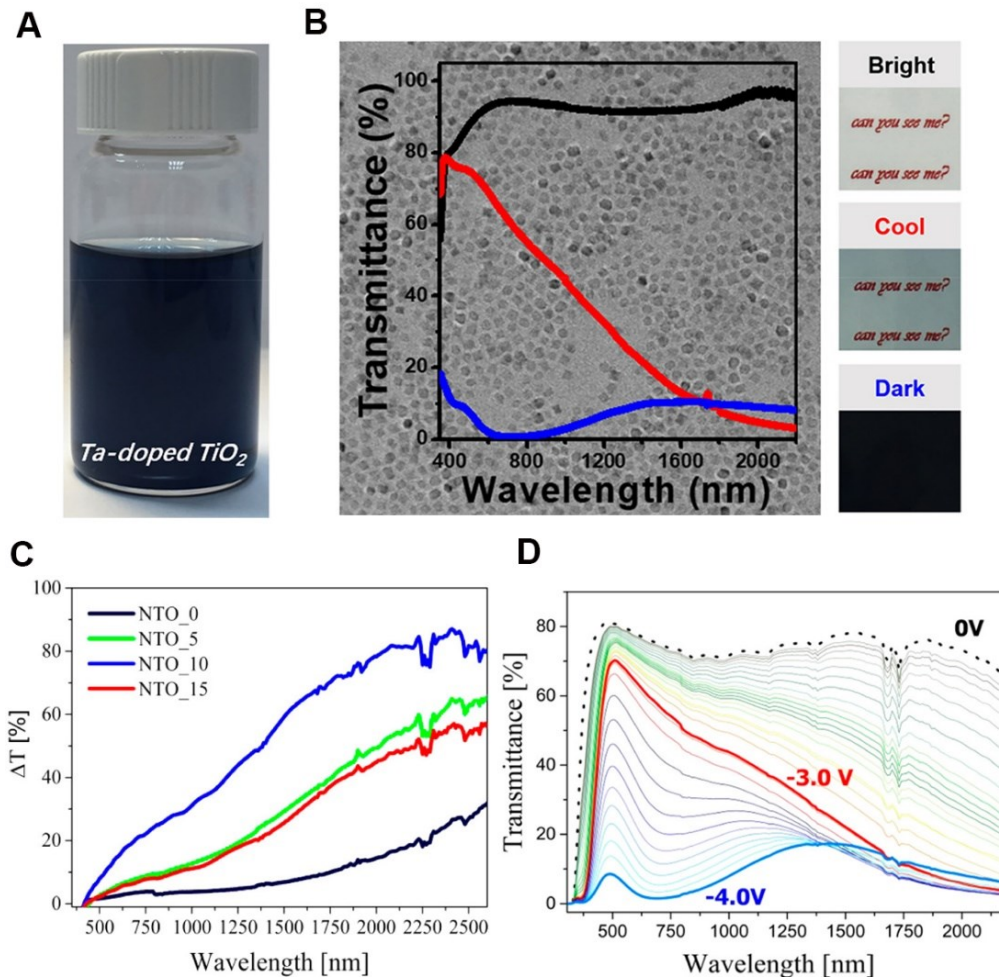


Figure 2.10. Structure and characterization of TiO₂-based electrochromic films. (A) Photograph of Ta-doped TiO₂ nanocrystals dispersion in tetrachloroethylene. (B) Transmittance and corresponding photographs of Ta-doped TiO₂ thin films electrode at different states. (A-B) Reproduced with permission from Ref. ¹⁵⁹. Copyright 2018, American Chemical Society. (C) Spectral variation of the optical transmittance at -1.6 V for four batches of Nb-doped TiO₂ nanocrystal films with different doping levels (from 0% to 15% of niobium content). (D) Transmittance spectra of a device embodying 10%Nb-doped TiO₂ nanocrystals electrode at different bias potentials. Reproduced with permission from Ref. ²⁵. Copyright 2017, American Chemical Society.

Another dopant of TiO₂, reported by Barawi et al.²⁵ to enhance the electrochromic performance of TiO₂, is Nb. Four batches of Nb-doped TiO₂ nanocrystals having different doping levels (from 0% to 15% of niobium content) were used to prepare highly transparent mesoporous electrodes. As shown in Figure 2.10C, the 10% Nb-doped TiO₂ nanocrystals electrode exhibit the

best electrochromic performance in both the visible and near-infrared light spectral regions. A dual-band (i.e., capable of independent control of visible light and near-infrared transmittance) electrochromic device was constructed using a 10% Nb-doped TiO₂ nanocrystals electrode. This dual-band electrochromic device is capable of independent control of visible light and near-infrared transmittance, showing a 67% optical contrast at 2000 nm (Figure 2.10D).

2.4.4 Vanadium oxides

By virtue of their multicolor behaviors, vanadium oxides are regarded as the most favorable inorganic materials for electrochromic displays.^{115,160,161} Vanadium cation exists in V²⁺, V³⁺, V⁴⁺, and V⁵⁺ states in vanadium compounds, thus inducing the associated multicolor characteristics. While VO₂ is known to be a thermochromic material,¹⁶² V₂O₃,¹⁶³ V₃O₇,¹⁶⁴ and V₂O₅¹⁶⁵ are found to have attractive electrochromic properties. The most widely investigated vanadium oxide is V₂O₅. With the intercalation/deintercalation of guest ions, this oxide offers reversible three-color states (i.e. yellow ⇌ green ⇌ blue).¹⁶⁶ However, owing to their low electrical conductivity, significant volume expansion during cycling, and the slow reaction kinetics of bulk, intrinsic unstructured vanadium oxides have not been widely used in electrochromic devices.¹⁶⁷ In recent years, nanostructured vanadium oxides have been studied to mediate these drawbacks since the nanostructures shorten the diffusion paths of ions and provide abundant active sites on the surface. Steiner et al. demonstrated a self-supporting double-gyroid (DG) structure of V₂O₅ (Figure 2.11A).¹⁶¹ The DG nanostructured V₂O₅ possessed a highly-ordered structure having 11 nm wide struts and a high specific surface-to-bulk volume ratio of 161.4 μm⁻¹, leading to a fast and efficient lithium-ion intercalation/extraction process. The assembled electrochromic supercapacitor based

on two opposite DG nanostructured V_2O_5 electrodes is shown in Figure 2.11B, and its three-color displays (i.e. yellow, green, and blue) are presented in Figure 12.1C.

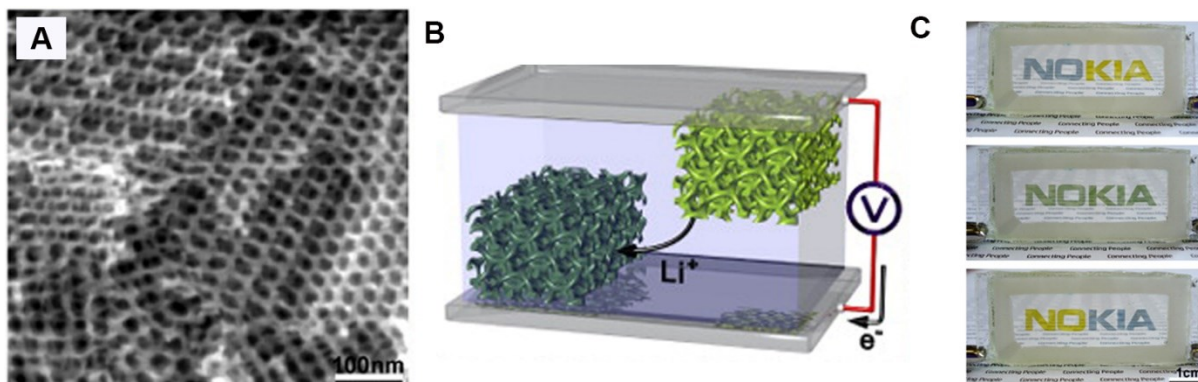


Figure 2.11. Structure and characterization of vanadium oxide-based electrochromic displays. (A) SEM of a mesoporous V_2O_5 double-gyroid film on an FTO substrate (B) Schematic illustration of the electrochromic supercapacitor design based on two laterally offset double-gyroid structured electrodes. (C) Photographs of an electrochromic supercapacitor device displaying color change upon charge and discharge. The letters “NO” form the double-gyroid structured top electrode and “KIA” form the bottom electrode (A-C) Reproduced with permission from Ref. ¹⁶¹. Copyright 2012, American Chemical Society.

2.4.5 Nickel oxides

As typical anodic electrochromic materials, serving as complementary material to tungsten oxides when assembling a device, nickel oxides (e.g., nickel oxide, hydrated nickel oxide and doped nickel oxide) are known for their high coloration efficiency and optical contrast.⁵⁰ In contrast to the cathodic electrochromic materials like WO_3 , the colored state of NiO is caused by electrochemical oxidation, with anion insertion (OH^-) or cation extraction (Li^+).⁴⁹ On the other hand, the NiO films become bleached by electrochemical reduction. The NiO film exhibits a reversible color change that switches between brown color and transparent state.¹⁶⁸ Similar to other intrinsic oxide electrochromic materials, critical issues, such as slow switching speed, low color contrast, and poor cycle durability of NiO limit its practical utility in electrochromic devices.^{169,170}

Enhanced electrochromic performances of NiO thin films have been recently achieved through nanostructured NiO films. Boo et al. reported a nanoporous NiO thin film fabricated by chemical bath deposition (CBD).⁴⁶ The nanoporous NiO thin films having high porosity showed excellent electrochromic properties, with a transmittance change of 77% at 550 nm and a coloration efficiency of $99.5 \text{ cm}^2 \text{ C}^{-1}$. Liou et al. described the growth of NiO nanorods via hot-filament metal-oxide vapor deposition where large-area arrays of one-dimensional NiO nanorods were grown on a conducting ITO film.¹⁷¹ The NiO nanorod films showed excellent electrochromic performance, including high optical transmittance difference (60%), large diffusion coefficient ($\sim 6.33 \times 10^{-8} \text{ cm}^2 \text{ s}^{-1}$) and very fast coloration and bleaching times (1.55 and 1.22 s).

An interesting platform of nanostructured NiO thin films is the one prepared by inkjet printing of NiO nanoparticles.¹⁷² Inkjet printing is a low-cost and efficient technology for patterning and deposition of multi-layered nanostructured materials on various substrates. The printed NiO film, with nine printed layers, exhibited an optical contrast of 64.2% at 550 nm and a coloration efficiency of $136.7 \text{ cm}^2 \text{ C}^{-1}$. Moreover, by doping NiO with other elements, such as Cu,¹⁷³ Al,¹⁷⁴ and Co,¹⁷⁵ the material electrochromic performance was greatly enhanced. As shown in Figures 2.12A-2.12F, with an increase in Co doping (from 0% to 3%), the thickness of the formed NiO film becomes thin and the pore diameter of the nanoflakes decreases.¹⁷⁵ However, nanoflake-shaped NiO films cannot form when the amount of Co doping reaches 3%. This suggests that an optimum Co doping concentration is required for electrochromic applications. In this regard, the 1% Co-doped NiO nanoflake array film exhibited an outstanding optical contrast of 88.3% at 550 nm. Most recently, Liang et al. developed a self-templating method to build up metal-organic framework (MOF)-derived hierarchical-porous carbon-embedded nickel oxide nanoparticle (NiO@C) films for high-performance electrochromism.⁵³ Figure 2.12G illustrates the preparation

procedures of the hierarchical-porous NiO@C electrodes. As a result, the hierarchical-porous NiO@C electrodes with both good ion diffusion and electrical conductivity were achieved. This electrode showed a fast switching speed (0.46/0.25 s for coloring/bleaching), high coloration efficiency ($113.5 \text{ cm}^2 \text{ C}^{-1}$) and excellent cycling stability (90.1% after 20000 cycles).

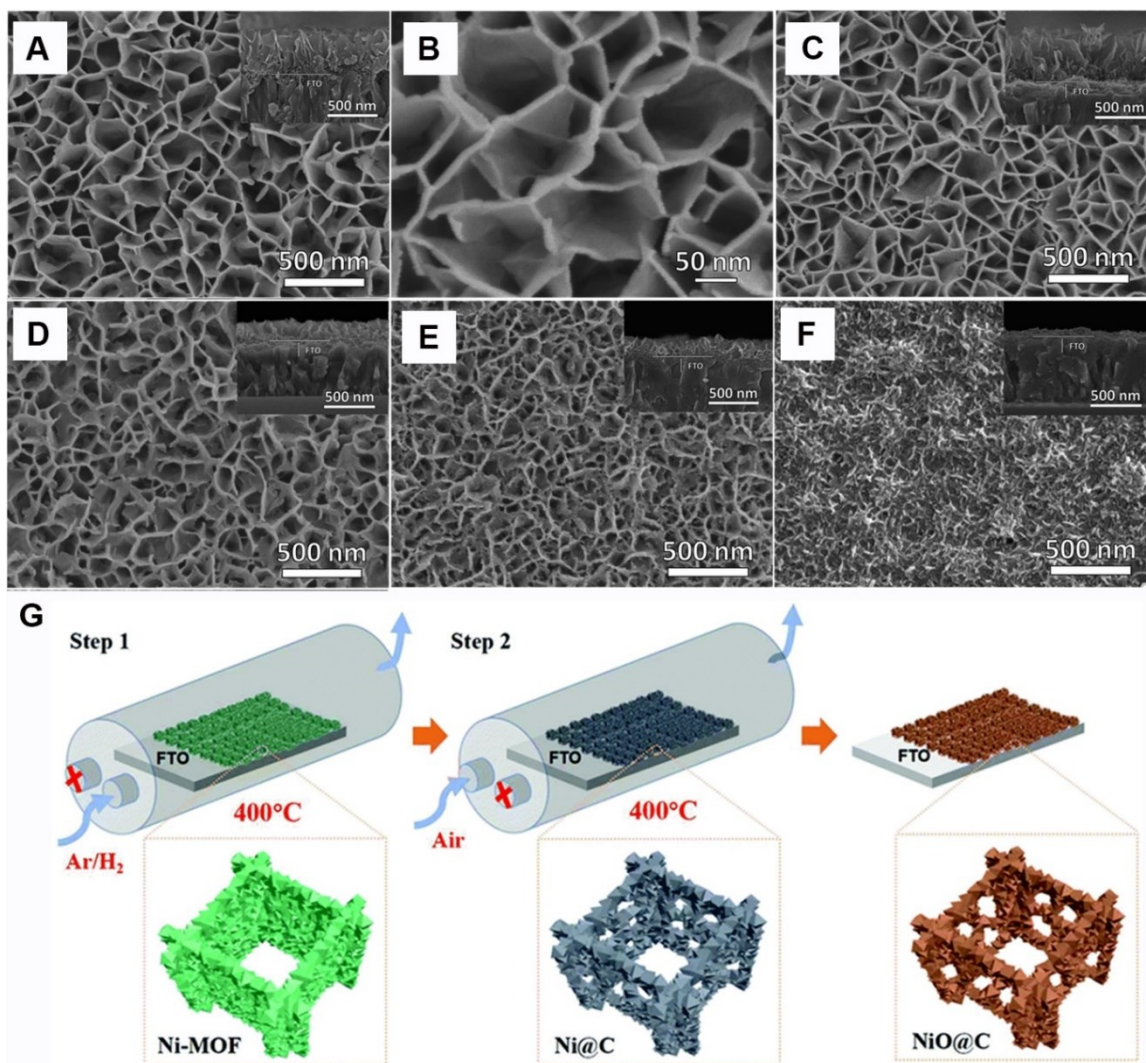


Figure 2.12. Characterization of NiO-based electrochromic films. SEM images of the films: (A and B) undoped NiO, (C) NiO–Co 0.3%, (D) NiO–Co 0.5%, (E) NiO–Co 1% and (F) NiO–Co 3% (cross-sectional view is presented in the inset). Reproduced with permission from Ref.¹⁷⁵. Copyright 2014, Royal Society of Chemistry. (G) Preparation procedures of the hierarchical-porous NiO@C electrode. Reproduced with permission from Ref.⁵³. Copyright 2019, Royal Society of Chemistry.

2.4.6 Cobalt oxides

Cobalt oxide normally exists in three different polymorphs: CoO, Co₃O₄, and Co₂O₃.¹⁷⁶ Among them, the crystalline Co₃O₄ phase has been widely studied because of its thermodynamic stability and electrochemical properties.¹⁷⁷ Co₃O₄ exhibits a reversible color change between a yellow-brown and dark brown under potential cycling.¹⁷⁸ Similar to other metal oxides suffering the large-volume expansion during the coloration and bleaching processes, Co₃O₄ suffers from structural decomposition, poor stability, and cation kinetics. To minimize such shortcomings, several reports described the growth of nanostructured Co₃O₄ thin films for electrochromic applications. Xia et al. demonstrated a facile method for synthesizing ordered bowl-like Co₃O₄ arrays.¹⁷⁹ The as-prepared Co₃O₄ films had a hierarchical porous structure (Figure 2.13A) when annealed at 200 °C, and it exhibits reversible color switchings between dark gray and pale yellow (Figure 2.13B). The coloration efficiency was calculated to be 29 cm² C⁻¹ at 633 nm, with an optical contrast of up to 33%. Notably, due to the microporous structures, the bowl-like Co₃O₄ arrays are found to have good electrochemical stability.

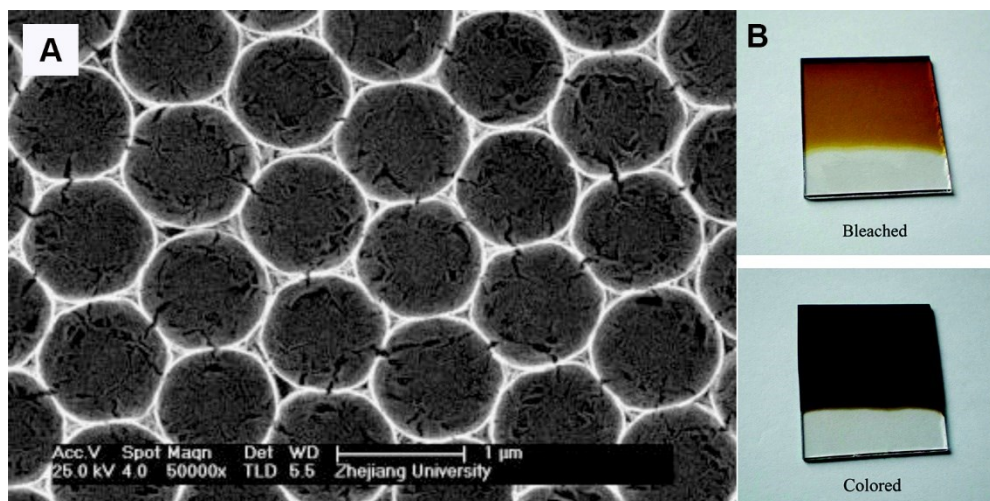


Figure 2.13. Characterization of Co₃O₄-based electrochromic films. (A) SEM images of the Co₃O₄ film annealed at 200 °C for 1 h. (B) Photographs of the Co₃O₄ electrode with a size of 1.5 × 1.5 cm² in the colored and bleached states. Reproduced with permission from Ref.¹⁷⁹. Copyright 2010, American Chemical Society.

The above-mentioned strategies for developing nanostructured electrochromic materials are mainly focused on the solution process techniques. This nanofabrication process has several advantages, such as low-cost, ease of designing nanostructures, and fast switching times which allow the fabrication of electrochromic material having kinetics compared to the vacuum deposition methods. To further enhance their electrochemical stability, future research needs to be focused on the interface engineering of the solution-processed nanostructured films, via strengthening the adhesion between the nanostructured electrochromic layers and the substrates. Notwithstanding, there is still a need for innovative designs of high-performance nanostructured electrochromic films to make the electrochromic device more practical for light control applications.

2.5 Complementary electrochromic devices

A complementary electrochromic device is a “sandwich” structure that contains substrate, transparent conductor, counter-electrode, ion conductor and electrochromic layer (the most important part) as shown below in Figure 2.14A. The substrate is the outer layer of the electrochromic device, which supports the device. It is typically made out of glass. The transparent conductor can be either indium tin oxide (ITO) or fluorine-doped tin oxide (FTO) thin films. The most important function of the transparent conductor is its ability to allow electrons flow. The counter-electrode is also known as the ions store layer. This electrode provides space for ion storage. When the voltage is applied to the electrochromic layer, electrons flow out of the electrochromic layer and enter the counter-electrode. Therefore, the counter-electrode must exhibit high ions storing capacity. The electrochromic layer is the most important part of an electrochromic device. It is also called the working electrode. The coloration and bleaching of

electrochromic material occur in this layer. In general, the optical contrast of a device mainly depends on the thickness of the electrochromic layer.¹⁰⁹ As the film thickness increases, the transmittance of both the colored and bleached states decreases. Typically, the maximum optical contrast is reported at an attained intermediate thickness of a few hundred nanometers.¹¹¹ The ion conductor layer (electrolyte) is used for the transport of ions. Based on the properties of the electrochromic layer, the electrolyte can be either an acid or an alkaline solution. Typically, the ion conductor is in a liquid or gel state, which provides high efficiency in terms of ions transport. Some recent research studies showed that a solid ion conductor can also exhibit high working efficiency.^{172,180,181}

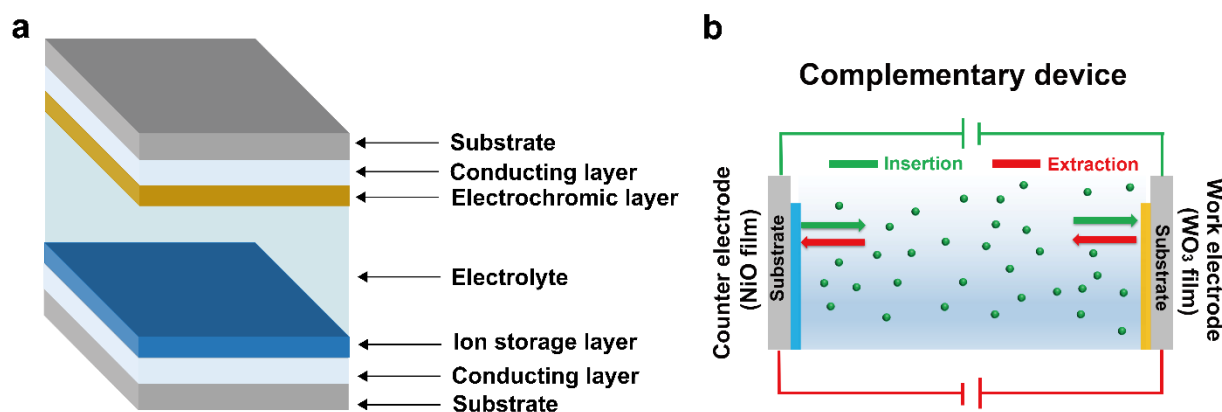


Figure 2.14. Complementary electrochromic devices. (A) Schematic of complementary electrochromic devices. (B) Working principles of a typical complementary electrochromic device.

Usually, anodic electrochromic material serves as a counter electrode which is often used in conjunction with a working electrode (cathodic electrochromic material) in a complementary device. A typical complementary electrochromic device configuration is substrate/WO₃/electrolyte/NiO/substrate (Figure 2.14B). The opposing redox reactions occur at the electrodes in the complementary electrochromic device, while the WO₃ electrode is being oxidized (bleaching) or reduced (coloring), the NiO electrode can be simultaneously reduced

(bleaching) or oxidized (coloring) at the counter electrode. Hence, both NiO and WO₃ can be transformed to a colored state by applying a voltage and reversed to a transparent state by applying an opposite voltage.

2.6 Major challenges of electrochromic devices

In this chapter, the critical components and the system of electrochromism are discussed. The classification of common electrochromic materials is outlined as inorganic, organic, inorganic-organic hybrids, and plasmonic materials. The evaluation metrics for electrochromic materials, including color and optical contrast, coloration efficiency, switching time, and cycling stability are discussed. Electrochromic properties and synthetic methods for different nanostructured electrochromic materials are evaluated based on structure/morphology engineering, doping techniques, and crystal phase designs. The working mechanism and a typically electrochromic device are demonstrated. Although the field of electrochromism has witnessed rapid development and remarkable achievements, there are still some major challenges that hinder the high-performance of electrochromic devices and their real-world applications:

(1) The operation of traditional electrochromic devices requires external voltages to trigger the coloration/bleaching processes, which makes the traditional electrochromic device far from a net-zero energy-consumption technology. It is necessary to develop energy-efficient electrochromic devices. Moreover, the simultaneous redox reactions on both electrodes when operating a complementary electrochromic device restrict the independent operation of a single electrochromic electrode. Such a limitation hindered a single electrochromic electrode to reach its maximum optical contrast. Notably, for a wide scope of applications, it is highly desirable to have an energy-efficient device configuration while also offering precise manipulation of a single

electrode.

(2) The current state-of-the-art multicolor electrochromic devices utilize a single electrochromic layer, which restricts their color tunability within a linear or curved segment scope in International Commission on Illumination (CIE) color space and thus leads to limited color hues. As such, it is highly desirable to have an energy-efficient electrochromic device expressing significantly broadened color palettes.

(3) A significant hurdle faced by electrochromic devices lies in their inability to independently regulate visible light and near-infrared radiation for smart window applications. Beyond mere transparency and opacity modulation, the capacity to independently control visible light and near-infrared radiation could introduce a new device state – one that solely modulates NIR radiation.

This thesis tackles two sets of problems using different electrochromic devices. Problems (1) and (2) are addressed using zinc anode-based electrochromic devices, as detailed in Chapter 3. Problem (3) is tackled through plasmonic-based electrochromic devices, which is the focus of Chapter 4.

Chapter 3

Zinc anode-based electrochromic devices

3.1 Introduction

Although the complementary electrochromic devices can also be used to store energy, the operation of conventional electrochromic devices requires external voltages to trigger both the coloration/bleaching processes. Nevertheless, the majority of the current electrochromic device research has focused on developing electrochromic materials for fast response without paying attention to reducing the consumed energy of the electrochromic devices. In this chapter, a promising Zinc anode-based electrochromic device (ZECD) platform is presented. The ZECD platform not only reduces the energy consumption during operation, via the energy retrieval functionality, but also exhibits a rapid spontaneous switching behavior due to the high value of redox potential difference between the metal anode and the electrochromic cathode. ZECDs that incorporate electrochromic phenomena and energy storage functionalities in a single platform are examples of innovative technologies with great potential.

In a zinc anode-based electrochromic device configuration, a thin metal Zn foil anode is sandwiched between two electrochromic cathodes (Figure 3.1a). When the two electrodes are connected together, the redox potential difference between the anode and cathode acts as a driving force to cause the metal (anode) to be oxidized and the electrochromic material to be reduced (Figure 3.1b). The electrochromic material acquires these electrons and metal ions for the spontaneous color change process. Interestingly, the spontaneous color switching, which is a Gibbs free energy downhill process, is the same as the discharge process in a battery.¹⁸² Conversely,

during the oxidation process (the reverse color switching), metal ions are extracted from the reduced electrochromic cathode and metal atoms are plated onto the anode. This process is also the same as the one taking place during the charging process in a half-cell battery. In other words, this zinc anode-based electrochromic device operates as a secondary device where the guest ions can be de-intercalated during the charging process and spontaneously intercalated during the discharging process. This zinc anode-based electrochromic device is different from those complementary electrochromic devices as it eliminates the need for an external bias needed to reduce the electrochromic cathode and it is efficient in recovering the energy used during the oxidation process. Moreover, such a device configuration enables independent operation of the top and bottom electrochromic electrodes, thus allowing for operation flexibility via precise manipulation of a single electrode.

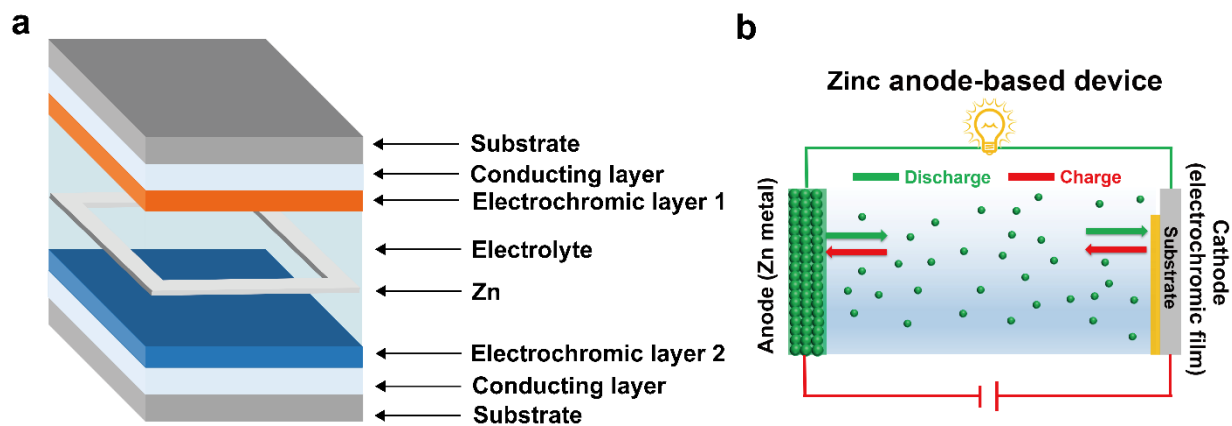


Figure 3.1. Zinc anode-based electrochromic devices. (a) Schematic of zinc anode-based electrochromic devices. (b) Working principles of zinc anode-based electrochromic devices.

To further shed light on the functionalities of ZECDs, three EC platforms are demonstrated in this chapter. The first example shows transparent multicolor displays enabled by ZCEDs. We show that the ZECD platform not only enhances energy efficiency through energy retrieval functionality but also exhibits rapid and spontaneous switching behavior due to the substantial

redox potential difference between the zinc metal anode and the electrochromic cathode. A version of this example has been published in: Zhang, W.; Li, H.; Yu, W. W.; Elezzabi, A. Y. “Transparent inorganic multicolor displays enabled by zinc-based electrochromic devices.” *Light: Science & Applications*, 9, 121 (2020).

The second example explores multicolor displays with tunability in the two-dimensional CIE color space, leveraging the color overlay effect to expand the available color palettes by adjusting coordinates in the two-dimensional CIE color space. A version of this example has been published in: Zhang, W.; Li, H.; Elezzabi, A. Y. “Electrochromic displays having two-dimensional CIE color space tunability.” *Advanced Functional Materials*, 32, 202108341 (2022).

Lastly, in the third example we present a dual-mode electrochromic device capable of both self-coloring and self-bleaching operations, achieved by integrating the ZECD platform into a rocking-chair type electrochromic device. A version of this example has been published in: Zhang, W.; Li, H.; Elezzabi, A. Y. “A dual-mode electrochromic platform integrating zinc anode-based and rocking-chair electrochromic devices.” *Advanced Functional Materials*, 33, 2300155 (2023).

3.2 Transparent inorganic multicolor displays enabled by zinc-based electrochromic devices

3.2.1 Introduction

Due to their zero energy consumption while maintaining either an optically transparent or colored state, electrochromic devices have attracted increased attention for various applications, including smart windows, displays, and color-tuneable optical elements.^{14,15,37} In particular, multicolor electrochromic displays are one of the most versatile applications because they can retain their colored states without the need to supply electrical power. While electrochromic displays based on organic molecules,²¹ polymers⁷³ and metal-organic frameworks¹⁸³ have demonstrated multicolor characteristics, these materials exhibit inferior thermal and chemical stabilities compared to their inorganic electrochromic counterparts. These shortcomings seriously hinder their real-world applications and potential commercialization.¹⁰⁷ Inorganic multicolor electrochromic displays are regarded as a paradigm shift in the field of electrochromic displays.

Recent demonstrations of inorganic multicolor electrochromic displays achieved multicolor functionality from a monochromatic WO_3 film by incorporating either a plasmochromic metal-insulator-nanohole cavity¹⁰⁶ or a photonic Fabry-Perot nanocavity.¹⁰⁷ These platforms enabled multicolor addressing in reflective mode. For a wide scope of applications, it is highly desirable to have a device configuration possessing high optical transparency while also expressing colored states.^{36,91} Notably, in terms of energy efficiency, the aforementioned reflective-mode devices consume electrical energy since an external voltage is needed to trigger the coloration/bleaching processes. Although this field is still in its infancy, electrical energy recovery from multicolor

electrochromic displays will render such a platform highly energy efficient, especially for large-area displays.

In addition to nanocavity-based inorganic multicolor displays, a color overlay strategy can be a simpler approach to broaden the color palette of an inorganic electrochromic device by superimposing layers of different colors (i.e., color overlay). Vanadium oxide (V_2O_5) is regarded as the most promising inorganic material for multicolor electrochromic displays.^{115,160,161} To the best of our knowledge, there are only three colors (yellow \rightleftharpoons green \rightleftharpoons blue) that can be achieved by vanadium oxides using the conventional electrochromic device configuration.¹⁶¹ Simultaneous coloration of the counter layer when operating a conventional electrochromic device restricts the color overlay effects. Since V_2O_5 electrodes can serve as both electrochromic and counter layers, the configuration illustrated in Fig. 3.2a can be used to eliminate the simultaneous coloration effect of the counter V_2O_5 electrode. However, only three colors can be realized under different redox states since the top and bottom V_2O_5 electrodes can only color under inverse redox states when operating the device.

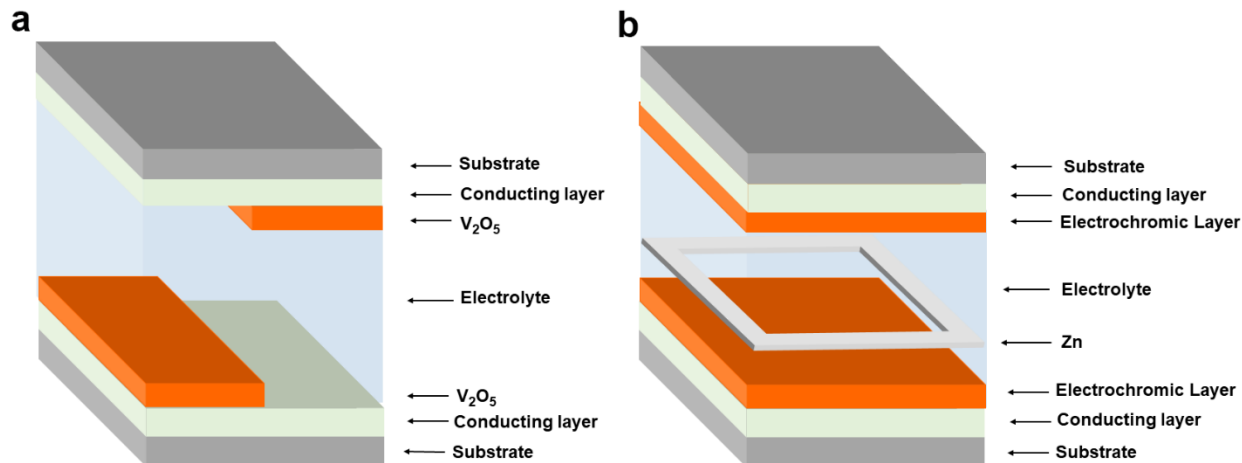


Figure 3.2. Schematic illustrations of two different types of electrochromic devices. (a) A conventional electrochromic device using V_2O_5 films for both electrochromic and ion storage electrodes. Note that in this configuration there is no overlap between the electrochromic layers, as such no color overlay effect and no broadened color palettes are possible. (b) A Zn-based electrochromic device using a Zn foil anode frame. This configuration facilitates color overlay from the two segments of electrochromic electrodes.

On the other hand, the development of Zn-based electrochromic devices with independent color activation of top and bottom electrochromic electrodes is still lacking and needs to be further explored (as depicted in Fig. 3.2b). Specifically, the top and bottom electrochromic electrodes can be independently addressed under the same or different redox states. As such, the color overlay effect can greatly broaden the color palette. Moreover, the operation of conventional electrochromic devices requires external voltages to trigger the coloration/bleaching processes, which makes the conventional electrochromic devices far from a net-zero energy consumption technology. Remarkably, this novel Zn-based electrochromic device architecture is able to self-color via its built-in battery power without external energy input, thus enabling partial retrieval of the electrical energy consumed during the bleaching process. In other words, this Zn-based electrochromic device operates as a secondary device where the device can be bleached during the charging process and spontaneously colored during the discharging process. Hence, to date, this

Zn-based electrochromic device represents the most promising energy-efficient platform for transparent inorganic multicolor display applications.

In this section, a novel concept for transparent inorganic multicolor electrochromic displays by employing sodium ion stabilized vanadium oxide (SVO) nanorods as the electrochromic material is demonstrated. Although the intercalation of sodium ions was shown to improve the electrical conductivity of SVO in zinc-ion batteries¹⁸⁴, to date, there is no report on the utilization of SVO for electrochromic devices. The current state-of-the-art vanadium oxide-based electrochromic display research has focused on developing nanostructured vanadium oxides (e.g., V_2O_3 , V_3O_7 , V_2O_5)^{38,161,163} without paying attention to potential electrochromic materials such as SVO.

3.2.2 Characterization of SVO nanorods

The SVO nanorods were prepared at room temperature using a high yield facile liquid-solid stirring method. Briefly, 100 g of commercial V_2O_5 powder was added into 1.5 L of a NaCl aqueous solution (2 M) at room temperature and stirred for 96 h to form a solution with a brownish suspension. Next, purification was conducted by adding distilled water, followed by centrifugation. The centrifugation process was repeated six times. Afterward, the product was diluted with distilled water to form a precursor solution (15 mg mL^{-1}). Next, the precursor solution was sonicated in an ultrasonic bath until a clear SVO colloid was formed (see Appendix A, the Method section).

To analyze the phase composition of the as-synthesized SVO, the suspension was dried at room temperature and characterized by powder X-ray diffraction (XRD). As shown in Fig. 3.3a,

the diffraction peaks of SVO can be indexed to the monoclinic $\text{NaV}_3\text{O}_8 \cdot 1.5\text{H}_2\text{O}$ (JCPDS No. 00-016-0601) phase. The hydrated sodium ions, inserted between the V_3O_8 layers, act as pillars to stabilize the layered structure (Fig. 3.3b). Figures 3.3c, d show field emission scanning electron microscopy (FESEM) images of the SVO, depicting a homogeneous nanorod morphology. The SVO nanorods range from 0.5-2.0 μm in length and 20–60 nm in diameter (Fig. A-1 and Table A-1). The transmission electron microscopy (TEM) image (Fig. 3.3e) also affirms the high aspect ratio of the SVO nanorod morphology. The high-resolution TEM image (Fig. 3.3e inset) shows crystalline lattice spacings of 2.27 Å and 2.92 Å corresponding to the (-303) and (-211) crystal planes, respectively. The peak of the (-211) crystal plane observed in the HRTEM image is covered by the (111) plane peak in the XRD pattern. As the standard crystal plane peaks from JCPDS No. 00-016-0601 in Fig. 3.3a show, the (-211) crystal plane peak is close to the highly preferred (111) crystal plane peak with a much lower peak intensity. Thus, the (-211) crystal plane peak would be covered by the (111) plane peak in the XRD pattern. The TEM elemental mapping images in Fig. 3.3f illustrate the homogeneous distributions of Na, V, and O elements in the SVO nanorods, thus confirming that the sodium ions have been intercalated into the V_3O_8 interlayers.

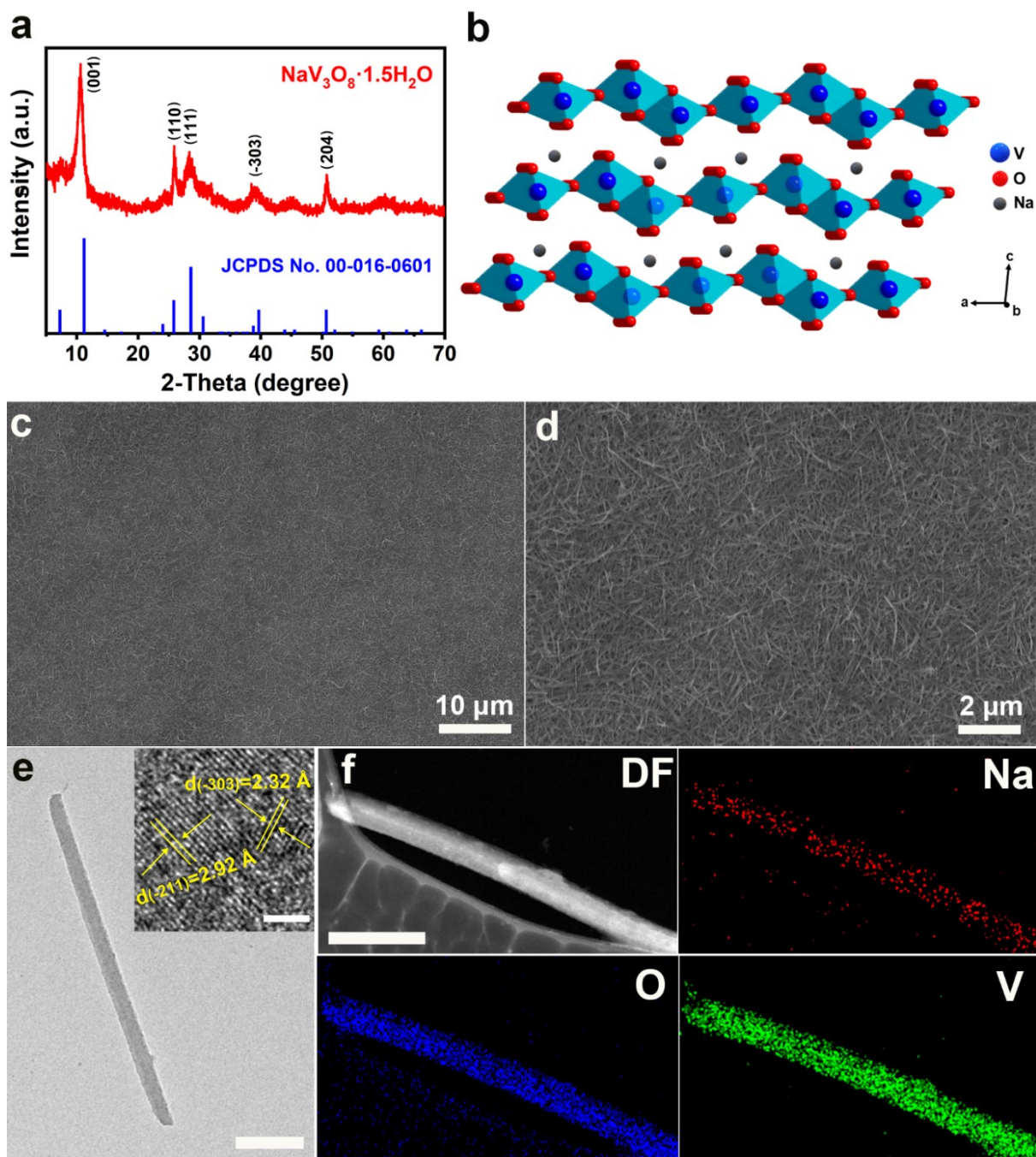


Figure 3.3 Characterization of SVO nanorods. (a) XRD pattern of the SVO nanorods. (b) Crystal structure of SVO nanorods. (c, d) FESEM images of the SVO nanorods. (e) Bright-field (BF) TEM image of a single SVO nanorod (scale bar: 100 nm). Inset: high-resolution TEM image of an SVO nanorod depicting the lattice planes (scale bar: 2 nm). (f) Dark-field (DF) TEM image of an SVO nanorod and the corresponding elemental mapping images of Na, O, V (scale bar: 200 nm).

3.2.3 Fabrication of SVO electrodes via the bar-coating method

The facile bar-coating method is considered a promising candidate to replace the common vacuum-processing techniques due to its great potential for large-scale, rapid, and inexpensive manufacturing.¹⁸⁵ Notwithstanding, the fabrication of electrochromic films via the facile bar-coating process requires a high-quality electrochromic paste. We therefore prepared a SVO paste via the addition of water-soluble and eco-friendly cellulose. To meet the high viscosity requirement for the bar-coating method, 3 g of cellulose was added to 60 mL of the SVO colloid (15 mg mL^{-1}) at $60 \text{ }^\circ\text{C}$ under stirring for 24 h. Prior to deposition, ITO-coated glass substrates were cleaned with ethanol and deionized (DI) water. Next, the SVO/cellulose paste was bar-coated onto an ITO glass substrate ($2 \text{ cm} \times 5 \text{ cm}$), covering an effective area of $1 \text{ cm} \times 4 \text{ cm}$. Cellulose can be uniformly dispersed in the SVO suspension due to its water-soluble property, while it can be easily decomposed at a low temperature due to the oxidation nature of SVO. Complete decomposition of cellulose prevents possible residual dispersion in the aqueous electrolyte system, which may affect the electrical conductivity of the SVO films. Figure 3.4a illustrates a schematic diagram of the bar-coating process that comprises three steps: (i) load the SVO/cellulose paste on one end of the substrate, (ii) spread the SVO/cellulose paste over the substrate through horizontal sliding of a coating bar, and (iii) anneal the bar-coated film at $200 \text{ }^\circ\text{C}$ for 24 h in air to decompose the cellulose. Using this facile bar-coating method, we obtained $\sim 800 \text{ nm}$ thick SVO films as measured by an Alpha-Step probe (IQ -W1-040).

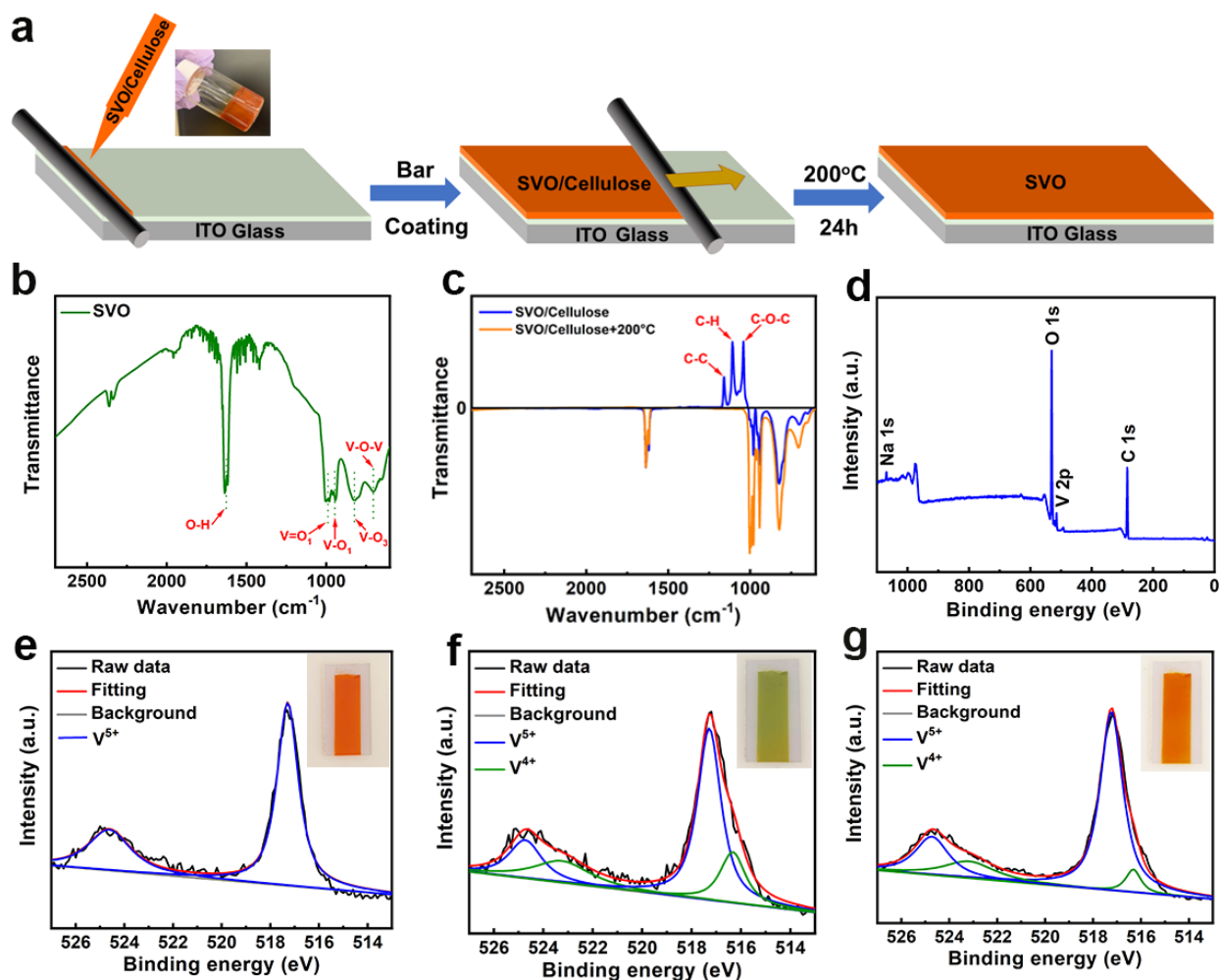


Figure 3.4 Fabrication of SVO films via a bar-coating method. (a) Schematic diagram of the bar-coating process. The inset shows a digital photograph of the SVO/cellulose paste. FTIR spectra of: (b) SVO, (c) SVO/cellulose and the annealed SVO film. (d) XPS survey spectrum of as-prepared SVO/cellulose film. V 2p core-level XPS spectrum of the bar-coated SVO/cellulose film under different annealing states: (e) as-prepared, (f) annealed for 30 mins, and (g) annealed for 24 hrs. Insets in Fig. 3.4e-g illustrate to the color of the corresponding films.

To confirm that the cellulose was fully decomposed from the film after heating, Fourier transform infrared spectroscopy (FTIR) was employed to characterize the SVO nanorods, SVO/cellulose paste and annealed SVO films. As shown in Fig. 3.4b, the absorption bands at approximately 1633 and at 1003, 945, 830 and 714 cm⁻¹ in the SVO film spectrum are assigned to O-H vibrations of water and to stretching vibrations of V=O₁, V-O₁, V-O₃, and V-O-V^{185,186},

respectively. Figure 3.4c shows the FTIR spectra of the as-prepared SVO/cellulose paste and the annealed SVO films. To distinctly reveal the cellulose absorption bands, the FTIR spectra were corrected based on the SVO nanorod spectrum (Fig. 3.4b). In the spectrum of the as-prepared SVO/cellulose film before annealing, the absorption bands at approximately 1158, 1106 and 1042 cm^{-1} are assigned to the stretching vibration of C–C, C-H in-plane bending and stretching vibration of C-O-C, respectively. These absorption bands originate from cellulose, confirming the existence of cellulose in such films.^{187,188} After annealing at 200 °C for 24 h, no functional groups of cellulose are found in the spectrum (Fig. 3.4c), indicating complete decomposition of cellulose in the annealed SVO film.

Ex situ X-ray photoelectron spectroscopy (XPS) measurements were carried out to investigate the valence states of SVO during the heating process. As shown in Fig. 3.4d, the XPS survey spectrum of the as-prepared SVO/cellulose film indicates the presence of Na, V, C and O elements. The intense peaks of C and O elements are attributed to the presence of cellulose.¹⁸⁹ Figures 3.4e-g depict the high-resolution V 2p core-level XPS spectra of the bar-coated SVO/cellulose film under different annealing conditions (as-prepared, annealed for 30 mins and annealed for 24 h). The most intense doublet peaks, located at 517.2 and 524.6 eV, are assigned to V^{5+} .¹⁹⁰ The other pair of peaks centred at 516.2 and 523.2 eV correspond to V^{4+} . In Fig. 3.4e, only V^{5+} peaks exist in the spectrum of the as-prepared film, which is consistent with the valence state of V in SVO. After annealing the bar-coated film for 30 mins (Fig. 3.4f), V^{4+} peaks appear, and the atomic ratio of $\text{V}^{4+}/\text{V}^{5+}$ increases to 0.41 (Table 3.1). The presence of the V^{4+} peaks indicates that SVO serves as an oxidizer to oxidize the cellulose, leading to decomposition of the cellulose at a low temperature. After 24 h of annealing, the spectrum, shown in Fig. 3.4g, shows that the $\text{V}^{4+}/\text{V}^{5+}$ atomic ratio decreases to 0.12 (Table 3.1). This result affirms that the cellulose was fully

decomposed and that the reduced V^{4+} was oxidized to V^{5+} by annealing. Figure A-2 shows FESEM images of the SVO film after the annealing process. The homogenous nanorod morphology is consistent with the morphology of the as-prepared SVO nanorods (i.e., Figs. 3.3c, d).

Table 3.1 Atomic ratio of V^{4+} and V^{5+} in the as-deposited, annealed for 30 mins, annealed for 24 h, reduced (0.2 V) and oxidized (2.0 V) SVO film.

Sample	Atomic percentage of V in different valence states		V^{4+}/V^{5+}
	V^{4+}	V^{5+}	
As-deposited	0.00	1.00	0.00
Annealed for 30 mins	0.29	0.71	0.41
Annealed for 24 h	0.11	0.89	0.12
Reduced (0.2 V)	0.87	0.13	6.69
Oxidized (2.0 V)	0.09	0.91	0.10

3.2.4 Electrochromic performance of the SVO electrodes

The electrochromic performance of the SVO electrodes was characterized via a two-electrode configuration. Here, zinc foil and a SVO electrode were used as the anode and cathode, respectively, and 1 M $ZnSO_4$ was used as the electrolyte solution. The choice of the $ZnSO_4$ solution as the electrolyte is supported by the fact that the SVO electrode is more electrochemically active towards Zn^{2+} (Fig. A-3). To analyze the operation of the Zn-SVO electrochromic display, ex-situ X-ray photoelectron spectroscopy (XPS) measurements were carried out to evaluate the valence state of the V accompanied by Zn^{2+} insertion/extraction. As illustrated in Fig. 3.5a, the ex-situ XPS full survey spectra of the SVO electrode indicate the presence of Na, V, and O elements, without other impurities (excluding C). The presence of Zn 2p peaks in the tinted SVO film (discharging at 0.2 V) confirms the insertion of Zn^{2+} . The weak intensities of Zn 2p peaks in the bleached SVO

film (charging at 2.0 V) indicate that most of the Zn^{2+} cations are extracted from the SVO electrode. The presence of Zn^{2+} residue in the electrode is due to the intercalated Zn^{2+} cations trapped at the “dead Zn^{2+} sites”.¹⁹¹ The trapped Zn^{2+} ions can be extracted from the dead Zn^{2+} sites by applying a high current under a stable voltage window of the electrolyte for real applications.¹⁹² These features are further confirmed by the high-resolution Zn 2p core-level XPS spectra (Fig. 3.5b). Figure 3.5c depicts the high-resolution V 2p core-level XPS spectra of the SVO film under different states (charging/discharging). As expected, the intercalation/deintercalation of Zn^{2+} would induce the valence state change of the V. The most intense doublet peaks, located at 517.2 and 524.6 eV, are assigned to the V^{5+} .³⁸ Another pair of peaks, centered at 516.2 and 523.2 eV, are corresponded to the V^{4+} . The atomic ratio of $\text{V}^{4+}/\text{V}^{5+}$ for the as-annealed SVO film is estimated to be 0.12 (Table 3.1). During the discharging process (0.2 V), the high valence state V^{5+} was partially reduced to V^{4+} and the atomic ratio of $\text{V}^{4+}/\text{V}^{5+}$ increased to 6.69 (Table 3.1). In another part, the $\text{V}^{4+}/\text{V}^{5+}$ atomic ratio of the bleached film (2.0 V) is estimated to be 0.10 (Table 3.1). The switch of $\text{V}^{4+}/\text{V}^{5+}$ ratio during discharging/charging induces the color switch of such Zn-SVO electrochromic device.

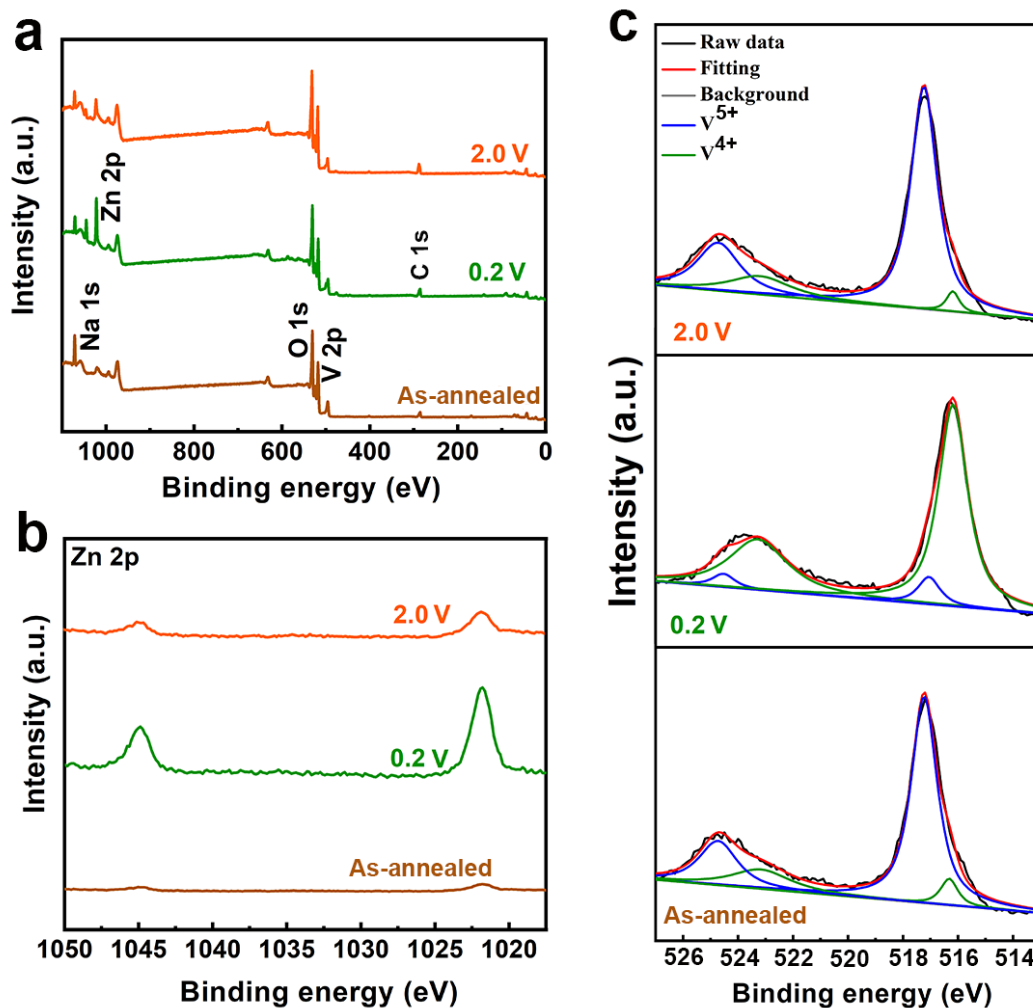


Figure 3.5. The ex-situ XPS survey spectra of the SVO electrode during discharging/charging: (a) Full survey (b) Zn 2p, and (c) V 2p.

Figure 3.6a illustrates a schematic diagram of the working principle of the Zn-SVO electrochromic display. The redox potential difference between the zinc foil and the SVO electrode provides the driving force that activates oxidation of Zn and reduction of the SVO film. Such a process is similar to the discharging process of a secondary battery. During the discharging process, the redox potential difference induces oxidation of the Zn anode ($\text{Zn} \rightarrow \text{Zn}^{2+}$) and intercalation of Zn^{2+} into the SVO cathode. Thus, this discharging process triggers a self-coloration behaviour. In

the charging process, the applied external voltage induces deintercalation of Zn^{2+} from the SVO cathode and reduction of Zn^{2+} ($\text{Zn}^{2+} \rightarrow \text{Zn}$). The charging process, therefore, triggers a bleaching behaviour. As depicted in Fig. 3.6b, the pair of reduction and oxidation peaks (at approximately 0.90/1.25 V) observed in the cyclic voltammetry (CV) curve indicate a single-step intercalation and extraction process of Zn^{2+} through the SVO lattice. Figure 3.5c shows the change in the optical transmittance spectra of the SVO electrode under different applied voltages. The spectroscopy test was conducted with an Ocean Optics USB4000 Spectrometer without subtracting the transmittance loss of ITO glass. Clearly, different colors are realized under different applied voltages. The transmission peak blueshifts as the applied voltage decreases. The processes of Zn^{2+} insertion (self-coloring) and extraction (bleaching) allow the SVO electrode to exhibit reversible color switching (orange \rightleftharpoons yellow \rightleftharpoons green, inset in Fig. 3.6c). Remarkably, the SVO electrode displays different colors while still preserving its high optical transparency of $>50\%$. This key feature can potentially provide access to new applications that are unattainable with reflective-mode electrochromic displays.^{106,107} The gradual color switching from orange to green results in a 73 nm blueshift of the transmission peak from 643 to 570 nm, while achieving a 21% optical contrast at 632.8 nm (without subtracting the transmittance loss of the ITO-coated glass). This gradual color switching is attributed to the cathodic coloration effect of the SVO. To further investigate the self-coloration behaviour (spontaneous color switching from orange to green) of this SVO electrode, the self-coloration process was monitored by applying 0 V for 60 s (equivalent to connecting the Zn and SVO electrodes together, Fig. 3.6d). The self-coloration time (spontaneous color switching time), defined as the time required to achieve 90% of the maximum optical contrast⁸², was measured to be 7.8 s.

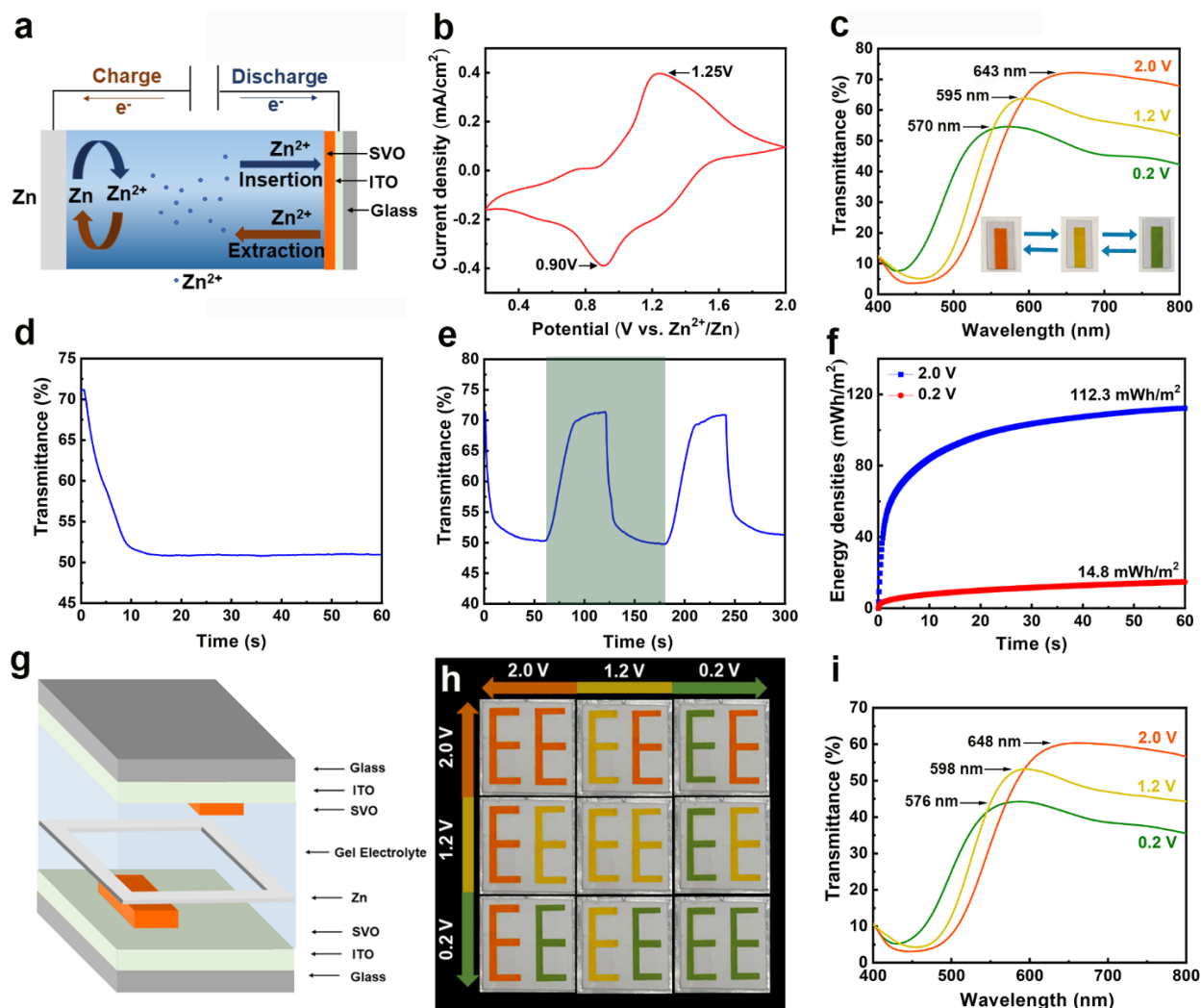


Figure 3.6. Electrochromic performance of the SVO electrode. (a) Schematic illustration of a Zn-SVO electrochromic display platform. (b) CV curve of the SVO electrode at a scan rate of 5 mV/s over a voltage range of 0.2-2.0 V. (c) Visible-near infrared transmittance spectra of the SVO electrode under different voltages for 60 s: green (0.2 V), yellow (1.2V) and orange (2.0 V). Inset: the corresponding photographs of the SVO electrodes under different voltages. (d) In situ self-coloring process (spontaneous color switching from orange to green) of the SVO film. (e) Dynamic test of the SVO film at 632.8 nm in the 0.2-2.0 V window. (f) Round-trip energy density comparison of the SVO electrode during the selected cycle (dark-green region in Fig. 3.6e) of dynamic test. (g) Schematic illustration of a large-scale Zn-SVO electrochromic display having three intrinsic colors. (h) Digital photographs of the large-scale Zn-SVO display under different voltage bias conditions. (i) Visible-near infrared transmittance spectra of the large-scale Zn-SVO display under different voltages: green (0.2 V), yellow (1.2V) and orange (2.0 V).

Furthermore, the dynamic transmittance characteristics of the SVO electrode were tested within the applied voltage window between 0.2 and 2.0 V. The dynamic test was conducted by transmitting a helium-neon laser (632.8 nm) through the samples. A voltage was applied from a Zahner electrochemical workstation, and the photodiode output signal was collected with an oscilloscope. The response times were calculated based on the time required to achieve 90% of the maximum optical contrast. As shown in Fig. 3.6e, the response times are calculated to be 12.6 s for coloration (green) and 25.4 s for bleaching (orange). Notably, this Zn-based SVO electrochromic display eliminates the need for electrical energy to trigger the coloration process, thus making it more energy efficient than existing electrochromic displays.^{106,193,194} Remarkably, the self-coloration (spontaneous color switching) process enables partial retrieval of the energy expended during the bleaching process. An important metric that characterizes our Zn-based SVO electrochromic display performance is the round-trip net energy consumption. The energy densities of both the coloration process and the bleaching process during a selected round-trip cycle in Fig. 3.6e are compared and presented in Fig. 3.6f. Here, the SVO electrode recovers 14.8 mWh m⁻² from 112.3 mWh m⁻² in a selected round-trip cycle (i.e., the round-trip net energy consumption is 97.5 mWh m⁻²). While the amount of retrieved energy can be further increased by operating at higher discharge voltages, such a low discharge voltage is found to be adequate for counterbalancing the interplay between the fast switching time requirement and the energy retrieval capability. Along with the dynamic switching shown in Fig. 3.5e, the coloration efficiency (CE) of the SVO electrode is calculated to be 61.2 cm² C⁻¹ (Fig. A-4). This CE value is higher than the values reported for Li⁺-based vanadium oxide electrochromic films^{195,196}, indicating that Zn²⁺ is efficient and promising in SVO-based electrochromic displays. Moreover, Fig. A-5 shows that the cycling performance of the Zn-SVO electrochromic display is higher than those in published

works^{197,198}, where it maintains 51% of its initial capacity and retains ~62% of the optical contrast after 1000 CV cycles.

The bar-coating method, as expected, can be used to fabricate large-area electrochromic displays with patterns. A 100-cm² display having three intrinsic colors was constructed to demonstrate the scalability of the bar-coated SVO electrode (Fig. 3.6g). The SVO electrodes for the “EE” display were prepared by bar-coating SVO/cellulose paste onto an “EE” shaped cut-out mask on top of an ITO glass substrate (10 cm × 10 cm). The effective area of one “E” letter is 5 cm², and the total effective area of the whole “EE” display is 10 cm². Such a configuration enables independent operation of the top and bottom SVO electrodes, thus providing additional configuration flexibility in displaying patterns (i.e., different color arrays) compared to the device illustrated in Fig. 3.2a. The colors of the two letters “EE”, as depicted in Fig. 3.6h, can also be reversibly switched (orange ⇌ yellow ⇌ green) under different bias conditions. The “EE” patterns exhibit a nine different color array, while the previously reported conventional V₂O₅-based devices (configured as in Fig. 3.2a) only exhibit a three different color array.¹⁶¹ Figure 3.6i shows the change in the optical transmittance spectra of the large-area display under different bias conditions while maintaining an optical transparency of >40%. The reversible color switching between orange and green colors of the display shows an optical transmission difference of 19% at 632.8 nm. The bar-coating method shows great potential for a large-scale, rapid, and inexpensive manufacturing capability, providing an efficient route to the commercialization of electrochromic indicators and tags. For high-resolution electrochromic displays, the inkjet printing method might be a potential approach because of its high-resolution features.¹⁶⁰

3.2.5 Electrochromic displays with broadened color palettes

As previously discussed, our newly established Zn-based electrochromic device enables a compelling color overlay effect for electrochromic displays, which could significantly broaden the color palettes of the displays. To implement such an innovative platform for multicolor Zn-based electrochromic displays, a Zn-SVO device (5 cm × 5 cm) was assembled and is schematically shown in Fig. 3.7a. The Zn-SVO electrochromic displays were constructed by sandwiching a thin Zn square frame between two pieces of SVO electrodes. The SVO electrodes for the display were prepared by bar-coating SVO/cellulose paste onto a 2 cm × 2 cm cut-out square mask on top of an ITO glass substrate (5 cm × 5 cm). A PVA-ZnSO₄ gel was used as the electrolyte, where the gel was prepared by gradually adding 6 g of PVA to 60 mL of a ZnSO₄ solution (0.5 M), which was stirred and heated in a water bath. The color overlay effect is achieved through a combination of two SVO electrode segments to broaden the resultant color palette. Such a device configuration is different from the configuration shown in Fig. 3.6g. To demonstrate the different color arrays attained via the Zn-based electrochromic device, we assembled the device shown in Fig. 3.6g. Here, the device configuration in Fig. 3.7a is used to demonstrate the color overlay of two SVO electrode segments. Since the two SVO electrode segments can be colored and bleached independently, multiple colors can be achieved via the color overlay effect of the three intrinsic colors (i.e., orange, yellow, and green). Figure 3.7b illustrates the color overlay effect obtained by superimposing the orange, yellow, and green colors. Since a single SVO electrode exhibits a three-color behaviour (orange ⇌ yellow ⇌ green, Fig. 3.7c), the device can achieve six colors (i.e., orange, amber, yellow, brown, chartreuse and green). For example, the brown color can be obtained via color overlay of the top orange electrode and the bottom green electrode.

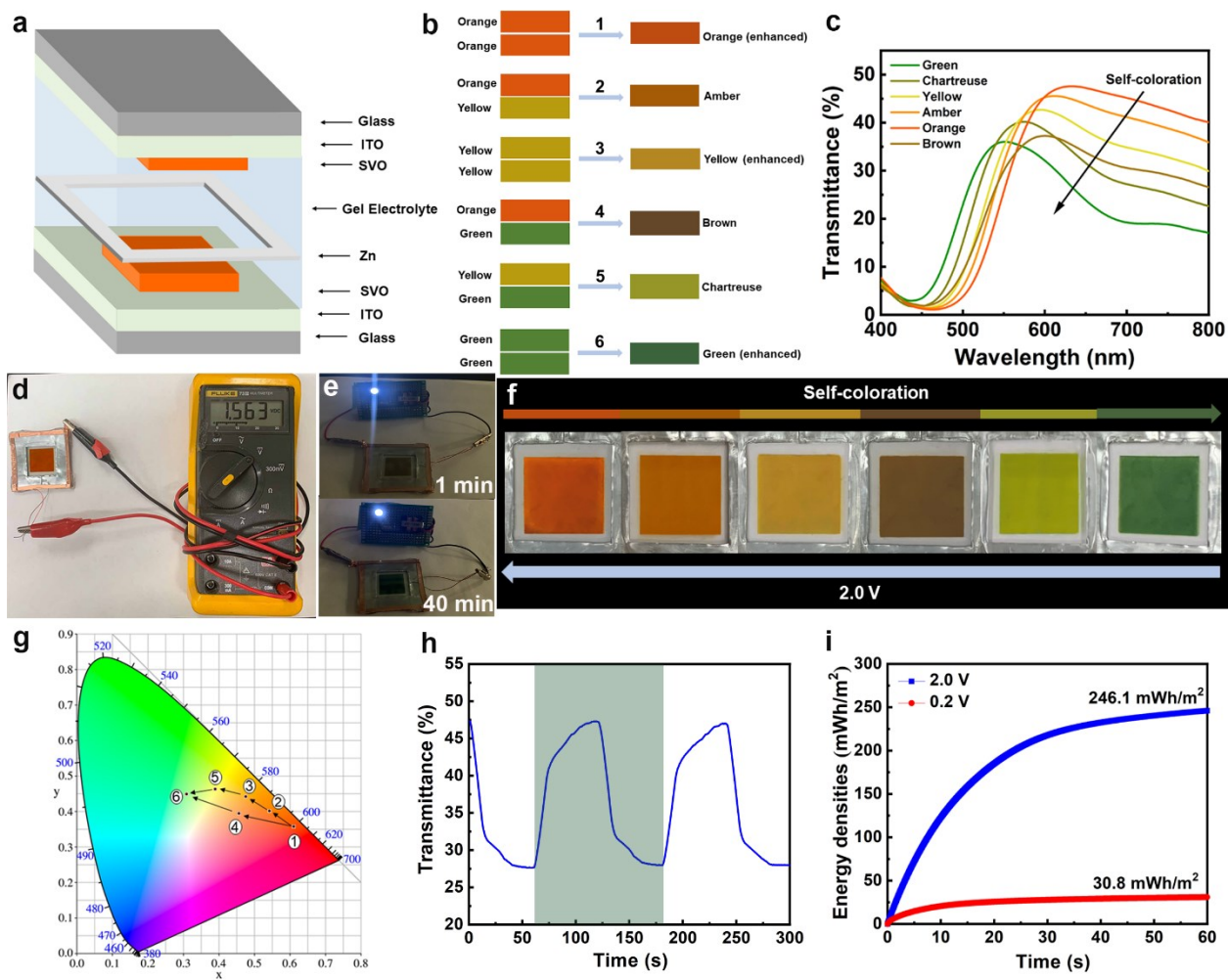


Figure 3.7. Design and performance of the Zn-SVO electrochromic displays with broadened color palettes. (a) Schematic illustration of the Zn-SVO electrochromic display having six colors. (b) Schematic illustration of color overlay effect via the combination of orange, yellow, and green colors. The upper color code represents the color of the top SVO electrode, while the lower one represents the color of the bottom SVO electrode. (c) Visible-near infrared transmittance spectra of the display under different color states. (d) Digital photograph of the display having an orange color, showing an OCP of 1.56 V. (e) Digital photographs of a 0.5 V regulated LED powered by the Zn-SVO electrochromic display at 1 min and 40 mins. (f) Digital photographs of the Zn-SVO display showing six colors obtained through the color overlay effect. (g) CIE color coordinates of the Zn-SVO electrochromic display under different color states. The labeled six numbers are corresponding to the six colors in Fig. 3.7c. (h) Dynamic test of the display at 632.8 nm in the 0.2-2.0 V window. (i) Energy densities comparison during the selected round-trip cycle (dark-green region) in Fig. 3.7h.

Figure 3.7c shows the change in the optical transmittance of the electrochromic display under different color states. There are four intermediate colors between the orange and green colors, which significantly broadens the color palette of the display. The device maintains a semitransparency of >30%, which is a great advantage compared to the recently reported multicolor electrochromic displays using nanocavity structures.^{106,193,194} The gradual color switching from orange to green results in a 76 nm blueshift of the transmission peak from 627 to 551 nm while achieving a 20% optical contrast at 632.8 nm. Interestingly, the orange-colored display possesses an open-circuit potential (OCP) of 1.56 V (Fig. 3.7d) as it is in the fully charged state, which enables a self-coloration behaviour.^{117,199} This OCP stems from the redox potential difference between the zinc foil and the SVO electrode, which provides the driving force that activates oxidation of Zn (i.e., stripping of Zn into the electrolyte) and reduction of the SVO film (i.e., intercalation of Zn^{2+} into SVO). Thus, the built-in voltage allows the display to switch its color from orange to green (including the four intermediate colors) due to the reduction of the SVO film while powering an LED for more than 40 mins (Fig. 3.7e). These vivid colors from the electrochromic display are shown in Fig. 3.7f. Conversely, the green-colored display can be recovered to the orange color via a charging process, wherein Zn is plated onto Zn foil and Zn^{2+} is extracted from the reduced SVO electrode. This charging process leads to bleaching of the SVO electrode. Figure 3.7g illustrates the corresponding chromaticity coordinates of the six colors within the CIE color space. Such brilliant color changes cause a remarkable shift of the CIE color coordinates, forming a circular area from orange to green with different tints. The dynamic transmittance characteristics of the electrochromic display were evaluated in the 0.2-2.0 V window (Fig. 3.7h), where the response times are calculated to be 23.2 s for coloration and 34.8 s for bleaching. The orange color indicates that the device is in the fully charged state, while the green

color indicates that the device is in the fully discharged state. Therefore, a color change between the six displayed colors of the Zn-SVO electrochromic display can be triggered by lighting an LED. Furthermore, the amber, yellow, brown, and chartreuse colors are intermediate color states. As such, the response times of color switching between these colors are faster than the values (23.2 s for coloration, 34.8 s for bleaching) shown in Figure 3.7h. The energy densities during the dynamic switching between the orange state and the green state are shown in Fig. 3.7i, where 30.8 mWh m⁻² is retrieved from the operating 246.1 mWh m⁻².

3.2.6 Summary

In summary, the first demonstration of a transparent inorganic multicolor display, constructed by utilizing zinc-based electrochromic devices, was presented. The SVO electrode was fabricated via a bar-coating method with careful design of an eco-friendly SVO/cellulose paste. Such SVO electrodes deliver reversible color switching (orange \rightleftharpoons yellow \rightleftharpoons green) associated with Zn²⁺ insertion (self-coloring/discharging) and extraction (bleaching/charging) while having a high optical transparency. The three intrinsic orange, yellow, and green colors were utilized as basic colors to develop multicolor Zn-SVO electrochromic displays via the color overlay effect of two segments of the SVO electrodes. The constructed electrochromic display shows switching between the multiple colors (orange, amber, yellow, brown, chartreuse and green). These key properties mark a significant improvement over reported electrochromic displays, making the Zn-SVO electrochromic displays promising for switchable optical filters, electrochromic tuneable micro-optics, and transparent displays. Our platform represents a new paradigm in electrochromic displays that can potentially facilitate new opportunities for the development of next-generation electrochromic displays.

3.3 Electrochromic devices having two-dimensional CIE color space tunability

3.3.1 Introduction

Multicolor electrochromic displays can switch between multiple colors with minimal power requirements and retain their colored states without the need for external electrical power.²⁰⁰ While the color display of conventional electrochromic devices (Figure 3.8a) usually relies on the intrinsic properties of the electrochromic materials, these devices can only switch their colors following a single mode traversing a one-dimensional (1D) trajectory in the CIE color space. That is, the chromaticity coordinate plots of conventional electrochromic devices distribute as a linear or curved segment in the CIE color space (Figure 3.8b).^{7,107,194} Such 1D color space tunability characteristic of the conventional electrochromic devices introduces a major challenge to fabricate multicolor displays as they can only exhibit limited color hues.^{37,107,201} For example, the most commonly reported cathodic electrochromic material, WO_3 , displays only a blue hue, which significantly restricts its application in multicolor displays.

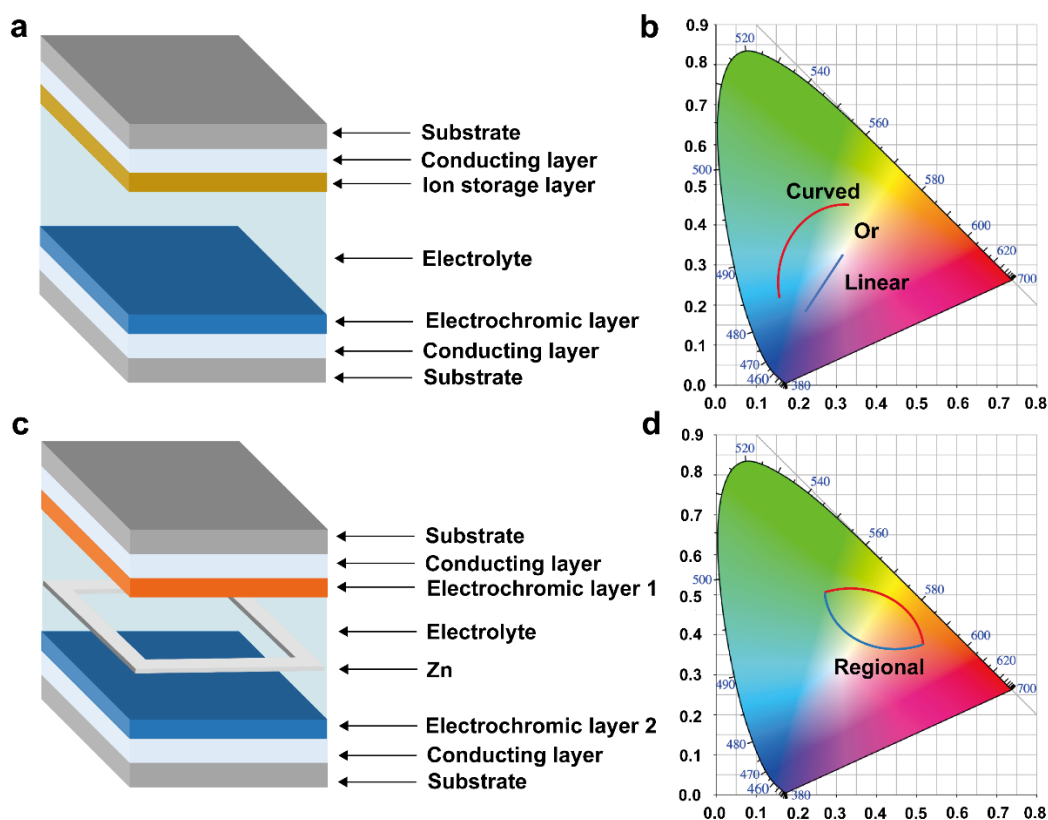


Figure 3.8. Schematic illustrations of two different types of electrochromic devices and their expected chromaticity coordinate plots in CIE color space. (a) Conventional electrochromic device using ion storage electrode and electrochromic electrode. (b) In the configuration of (a), the single variable parameter of the electrochromic layer restricts the color tunability within a linear or curved segment scope in CIE color space and thus leading to limited color hues. (c) Zn-based electrochromic device using various electrochromic layers as two separate variable parameters for generating vivid colors. (d) In the configuration of (c), two different electrochromic layers are incorporated to work independently in an electrochromic device, thus, the two layers act in unison to provide much wider 2D CIE color space tunability for vivid colors.

Recently, electrochromic devices based on asymmetric Fabry-Perot nanocavity-type thin films have been investigated as a means to broaden the color hues of the WO_3 -based electrochromic displays.^{7,107,194} Compared to conventional electrochromic devices, where the optical index of the electrochromic layer is altered through ions intercalation,^{15,38,117,202} asymmetric Fabry-Perot nanocavity-type thin films show a strong optical resonance interference, thus, enabling multiple structural color hues.²⁰³ Although the color hues of the electrochromic WO_3

films are broadened via this unique structure, the chromatic coordinate plots of films are still distributed as a linear or curved segment in the CIE color space. To realize electrochromic displays having 2D CIE color space tunability, the thickness of the asymmetric Fabry-Perot nanocavity-type thin films must be altered.^{7,107,194,204,205} However, thickness physical adjustment is impractical for a viable and configurable color display device. Certainly, the current state-of-the-art electrochromic displays are still suffering from the challenge of overcoming the 1D CIE color space tunability. Although it is reported that using subpixels arranged side by side (i.e., multiple micro electrochromic devices) can attain multicolors (Figure 3.9a),^{206,207} it suffers a costly nanofabrication process for subpixels.²⁰⁴ In addition, the counter electrode for the subpixels arranged side by side should also be divided into small segments to enable every single pixel to be addressed separately. Furthermore, the counter electrode, serving as a charge storage layer, would obstruct a considerable fraction of the incident light and further reduces the brightness of the device. Notwithstanding, the subpixels design requires an expensive nanofabrication process, which would hinder its practical commercialization. Therefore, it is of great importance to identify an electrochromic display platform to reduce the number of subpixels while retaining multicolor features.²⁰⁴

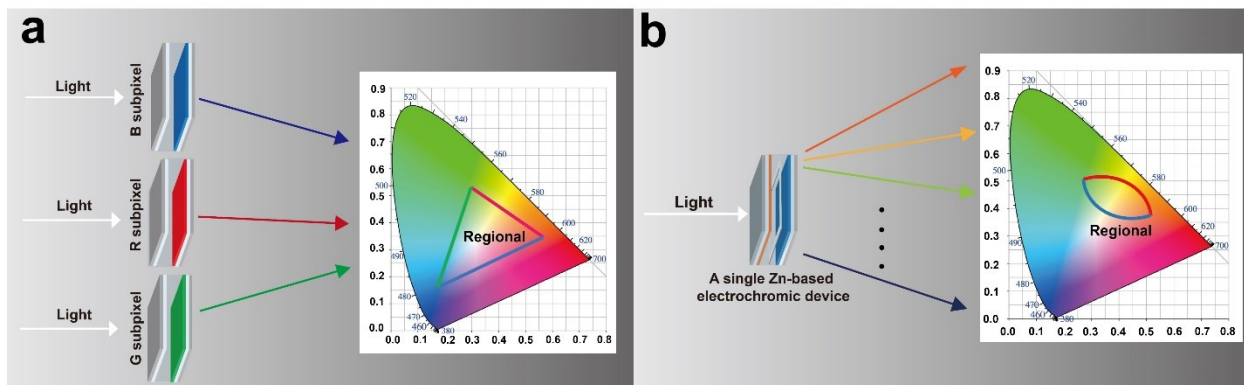


Figure 3.9. Schematic illustrations of two different types of displays and their expected chromaticity coordinate plots in CIE color space. (a) An electrochromic display having three RGB subpixels. R represents red, G represents green and B represents blue. (b) A Zn-based electrochromic display utilizing various electrochromic layers as two separate variable parameters for generating vivid colors.

The 1D CIE color space tunability of the conventional electrochromic devices stems from the single variable parameter of the electrochromic layer. If two different electrochromic layers are incorporated to work independently in an electrochromic device, each of the electrochromic layers serves to display a color hue that traverses a 1D trajectory on the CIE color space map. When combined, the two electrochromic layers act in unison to provide much wider 2D CIE color space tunability for vivid colors (Figures 3.8c and 3.8d). This feature can be demonstrated via Zn-anode-based electrochromic devices consisting of a thin Zn foil anode sandwiched between two different electrochromic electrodes where electrical addressing of the top and the bottom electrochromic layers allowed for vivid 2D CIE color space tunability (Figure 3.9b). Along with such enhanced light performance, this class of electrochromic devices is also energy efficient as it offers compelling electrical energy storage and retrieval functionalities.^{59,137} Consequently, such a device platform architecture is highly attractive for the development of energy-efficient electrochromic displays having significantly broadened color palettes. Also, since the zinc anode-based electrochromic displays are assembled via sandwiching a zinc frame within two pieces of

electrochromic cathodes, there is no big difference in active area between this type of device and the conventional electrochromic displays. The active area is the area having electrochromic material coatings.

In this section, the zinc anode-based electrochromic displays using various electrochromic layers as two separate variable parameters for generating vivid colors are presented. The electrochromic displays having both transmissive and reflective modes of operation are constructed to display multiple colors traversing a 2D CIE regional color space.

3.3.2 Fabrication of transmissive-type and Fabry-Perot nanocavity reflective-type WO₃ electrochromic electrode

Since WO₃ is the most widely studied and commercially-relevant inorganic electrochromic material,^{37,208,209} it is employed as the primary variable parameter for tuning the 2D CIE color space of the zinc-anode-based electrochromic displays. Figure 3.10a illustrates a typical schematic of a transmissive-type electrochromic electrode consisting of a WO₃ thin film as the electrochromic layer and an indium tin oxide (ITO) glass as the current collector. WO₃ thin films (230 nm) are sputtered onto ITO glass using DC sputtering at a power of 125 W. Here, the pressure is set at 20 mTorr and gas flow is set to 20 sccm of Ar and 5 sccm of O₂ (see Appendix B, the Method section). The excellent uniformity of the 230 nm thick WO₃ film sputtered on top of an ITO glass substrate is evidenced by examining the scanning electron microscopy (SEM) images of the electrode (Figure B-1). Shown in Figure 3.10b, the high optical transmittance (~85%) of a WO₃ electrode spanning a wide wavelength range from 400 nm to 800 nm.

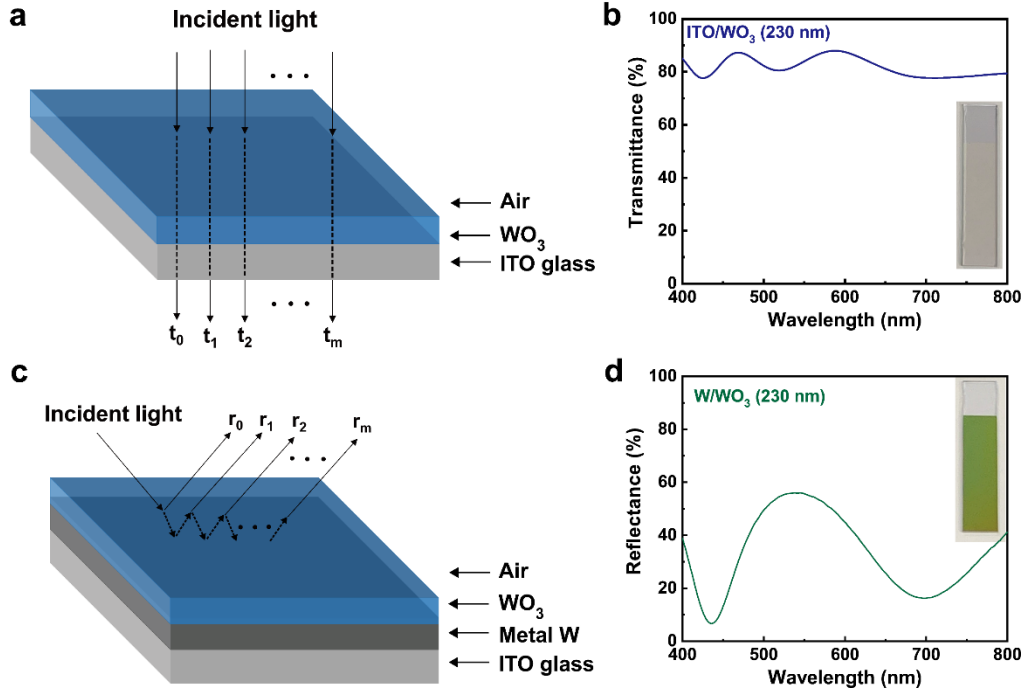


Figure 3.10. Transmissive-type and Fabry-Perot nanocavity reflective-type WO_3 electrochromic electrode. (a) Schematic illustration of a transmissive-type WO_3 electrochromic electrode where t_0, t_1, \dots, t_m are the Fresnel coefficients describing the transmission of light when incident on the air: WO_3 and WO_3 :ITO interfaces (b) Transmittance spectrum of the WO_3 electrode. Inset: Digital image of the WO_3 electrode. (c) Schematic illustration of a reflective-type W/WO_3 electrochromic electrode where r_0, r_1, \dots, r_m are the Fresnel coefficients describing the reflection of light when incident on the air: WO_3 and WO_3 :metal interfaces. (d) Reflectance spectrum of the W/WO_3 electrode. Inset: Digital image of the W/WO_3 electrode having a light green color.

To combine the effects of optical interference and electrochromism into a single structure, Fabry-Perot nanocavities have been developed using WO_3 as the high index of refraction coating, and tungsten (W) metal acting both as a current collector and a reflective layer. As schematically illustrated in Figure 3.10c, this layered structure enables multiple reflections within the tungsten trioxide thin layer and thus, leads to a strong optical interference. A reflective-type W/WO_3 electrochromic electrode is fabricated via layer-by-layer sputtering thin films of metallic W (100 nm) and WO_3 (230 nm) onto the ITO glass substrate. The choice of the 230 nm thick WO_3 layer is beneficial for demonstrating a broad 2D color map of the device. Figure B-2 shows the digital images of the Fabry-Perot nanocavity W/WO_3 (230 nm) electrode at different viewing angles.

There is a small color change up to a large angle (50°), indicating a good angle-independent reflectance behavior. The reflectivity of the W/WO₃ electrochromic electrode is depicted in Figure 3.10d. The reflection spectrum shows a distinct peak having a broad Fabry-Perot resonance centered at 545 nm (green) and having a maximum reflectance of 56%.

3.3.3 Electrochromic performance of working electrodes

The Zn²⁺ intercalation (deintercalation) processes into (from) the WO₃ films were evaluated by cyclic voltammetry in 1 M ZnSO₄ electrolyte. As shown in Figures 3.11a and 3.11b, the presence of the two anodic peaks located at 0.562 V (peak 1) and 0.802 V (peak 2), without the existence of an obvious cathodic peak, suggest a multistep deintercalation and a single-step intercalation process of the Zn²⁺ ions. Figure 3.11c presents the change in the optical transmittance spectra of the WO₃ electrode under different applied voltages. The spectroscopy test for visible light transmittance spectra was conducted with an Ocean Optics USB4000 Spectrometer without subtracting the transmittance loss of ITO glass. The gradual color switching (i.e., from transparent to deep blue while achieving a maximum 63% optical contrast at 632.8 nm) is attributed to the cathodic coloration effect of WO₃ electrodes under different applied voltages. The limited blue hue coloration exhibited by the WO₃ electrode emphasizes the inherent color choice limitations imposed by using a single electrochromic for multi-color display applications.

The switching time response of the WO₃ electrode was tested within the applied voltage window between 0.2-1.4 V. As shown in Figure 3.11d, the response times, defined as the time required for achieving 90% of maximum optical contrast,²¹⁰ are measured to be 14.6 s for coloration (at 0.2 V) and 7.1 s for bleaching (at 1.4 V). These response times are comparable to those reported previously.^{116,144,211} Along with the time switching dynamic test, the coloration

efficiency (CE) of the WO_3 electrode is calculated to be $85.3 \text{ cm}^2 \text{ C}^{-1}$ (Figure B-3). This CE value is much higher than that of previously reported.^{108,212} This is because that the multivalent ions (e.g., Zn^{2+}) provide multiple charges that accelerate the redox reactions which results in high coloration efficiency, compared to the typically employed monovalent ions (e.g., H^+ , Li^+ or K^+).^{37,38}

An interesting feature of the Zn-based electrochromic device platform is that it is different from the conventional electrochromic platforms as it eliminates the need for an applied voltage to reduce the electrochromic cathode. In this regard, this Zn-based electrochromic device platform offers an interesting function where a portion of the consumed electrical energy during the oxidation process can be retrieved. To shed light on the energy cycling efficiency, it is important to measure the round-trip net-energy consumption. The energy densities of both the coloration process and the bleaching processes during a selected round-trip cycle in Figure 3.11d are compared and presented in Figure 3.11e. Here, the WO_3 electrode recovers 13.9 mWh m^{-2} from 108.8 mWh m^{-2} in a selected round-trip cycle (i.e., the round-trip net-energy consumption is 94.9 mWh m^{-2}). Thus, a portion of the consumed electrical energy during the bleaching process is retrieved during the coloration process. Notwithstanding, benefit from the energy retrieval functionality, the round-trip net-energy consumption of 94.9 mWh m^{-2} is less than that of a conventional electrochromic device using TiO_{2-x} as the active electrochromic layer.²⁰² Since a low discharging voltage leads to a large potential difference between the Zn anode and the WO_3 cathode, there is an interplay between rapid color switching and high energy retrieval capability as the low discharging voltage results in a rapid coloration process, but it contrarily reduces the amount of energy retrieved from the device. A proper balance must be struck between the electrochromic switching performance and the energy saving. After 1000 of CV cycling, the Zn- WO_3 electrochromic device, it was shown that the device retains a maximum optical contrast of

34% (Figure B-4). Although such performance is not ideal, the main focus here is to demonstrate proof-of-concept electrochromic displays having vivid colors.

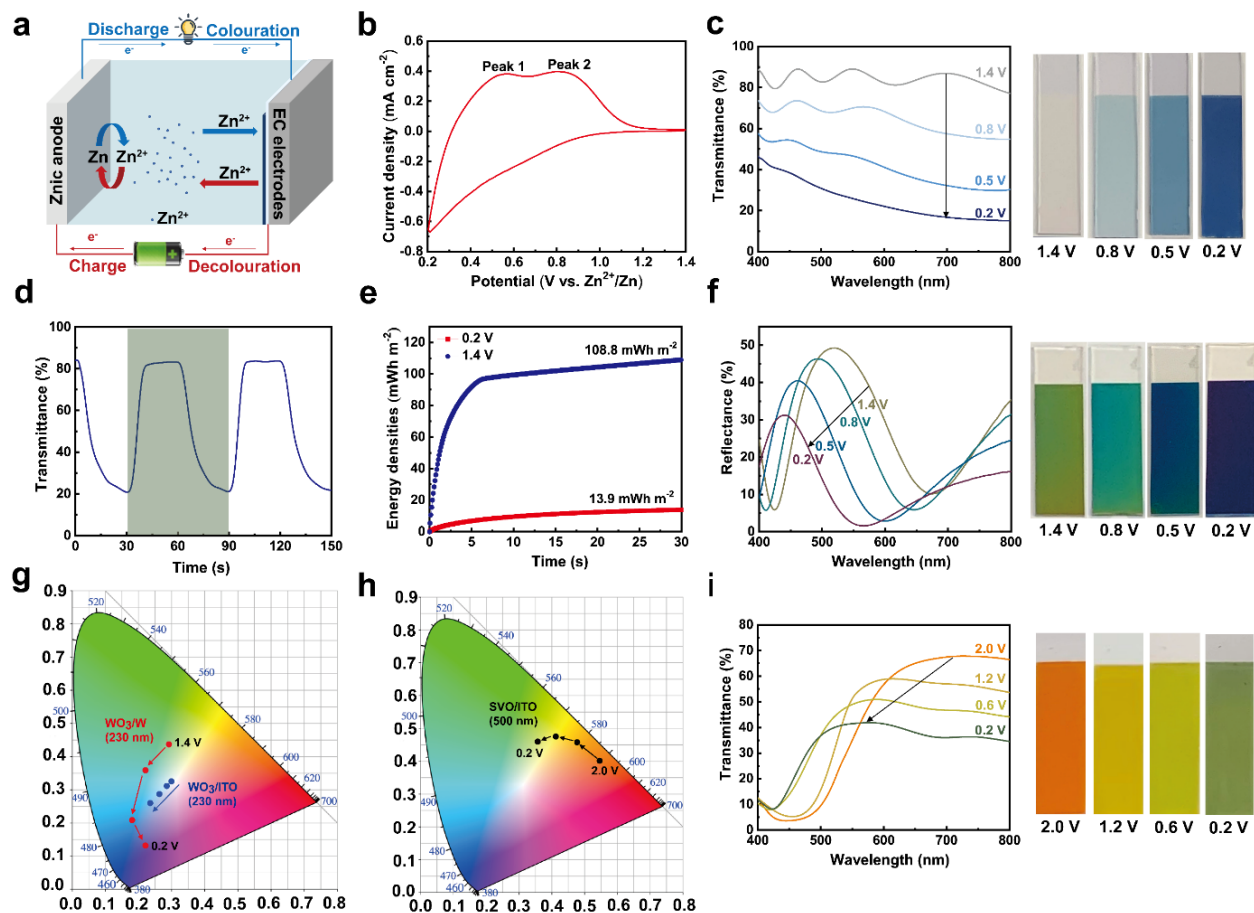


Figure 3.11. Characterization of the electrochromic electrodes. (a) Schematic illustration of the Zn-based electrochromic device platform showing the Zn²⁺ intercalation (deintercalation) processes into (from) the electrochromic electrode. (b) CV curve of the WO₃ electrode taken at a scan rate of 50 mV s⁻¹ over a voltage range of 0.2–1.4 V. (c) Optical transmittance spectra and their corresponding digital images of the WO₃ electrodes under different applied voltages. (d) Dynamic switching times of the WO₃ electrode at 632.8 nm in the 0.2–1.4 V window. (e) Round-trip energy density comparison of the WO₃ electrode during the selected cycle [dark-green shaded region in (d)] of the dynamic test. (f) Optical reflectance spectra and their corresponding digital images of the W/WO₃ electrodes under different applied voltages. (g) CIE color coordinates of the WO₃ electrode and W/WO₃ electrode at different color states. (h) CIE color coordinates of the SVO electrode at different color states. (i) Optical reflectance spectra and their corresponding digital images of the SVO electrodes at different applied voltages.

To investigate the broadened color hues of the Fabry-Perot nanocavity-type W/WO₃ electrochromic electrode, optical reflectance spectra of the W/WO₃ electrode, at 0.2 V-1.4 V, are presented in Figure 3.11f. The spectroscopy test for optical reflectance spectra was conducted with a Hitachi U-3900H Spectrometer. As the voltage decreased from 1.4 V to 0.2 V, the reflectance peak gradually blueshifts while decreasing in amplitude. The gradual color switching from light green to dark purple results in an 80-nm blueshift of the reflectance peak position from 520 to 440 nm. Such an 80-nm blueshift is larger than our previously reported electrochromic displays using a plasmochromic metal-insulator-nanohole cavity structure.¹⁰⁶ When the vivid color changes of the W/WO₃ electrode at different potentials are displayed on chromaticity coordinates in the CIE color space (Figure 3.11g), a curved coordinate line is realized. The presence of the Fabry-Perot nanocavity structure has greatly broadened the blue color hue of the WO₃ electrode. Nonetheless, the chromaticity coordinates plots of the WO₃ electrode and W/WO₃ electrode still distribute within a 1D linear or curved segment in the CIE color space, which limits the diversity of display colors. For a wide scope of applications, it is highly desirable to have an electrochromic display configuration expressing more color hues.

The Zn-anode-based electrochromic device platform enables independent electrochromic activation of top and bottom electrodes, thus providing additional configuration flexibility of the device to span more color states.²² Through the utilization of dual electrochromic layers, a color overlay effect forms a 2D chromaticity coordinate plots distribution within the CIE color space, and thus generating a broadened color palette. To explain the working principles of the dual electrochromic layers, WO₃ and W/WO₃ electrodes are incorporated with our previously fabricated SVO (sodium ion stabilized vanadium oxide) electrodes.²² The zinc-anode-based electrochromic displays possessing 2D CIE color space tunability are demonstrated in both

transmissive and reflective modes. Figures 3.11h and 3.11i display the chromaticity coordinates and the optical transmittance spectra, respectively, of the SVO electrode under different applied voltages. The intercalation of Zn^{2+} into SVO electrodes triggers a gradual color switching from orange to green with a 120 nm blueshift of the transmittance peak position from 690 to 570 nm. Such a bright color change stems from the intrinsic electrochromic properties of the SVO material.

3.3.4 Transparent electrochromic displays with broadened color palettes

As previously discussed, the compelling color overlay effect of the zinc-anode-based electrochromic displays enables the realization of the 2D CIE color space tunability which significantly broadens the color palettes of an electrochromic display. To implement such an innovative platform for transparent multicolor electrochromic displays, an SVO-Zn-WO₃ electrochromic device (5 cm × 5 cm) was assembled as schematically shown in Figure 3.12a. The electrochromic electrodes for the display were prepared by depositing films through a 2.5 cm × 2.5 cm cut-out square mask placed on top of a 5 cm × 5 cm ITO glass substrate. The transparent electrochromic displays were constructed by sandwiching a thin Zn square frame between one piece of SVO electrode and one piece of WO₃ electrode. The PVA-ZnSO₄ gel was used as electrolyte.

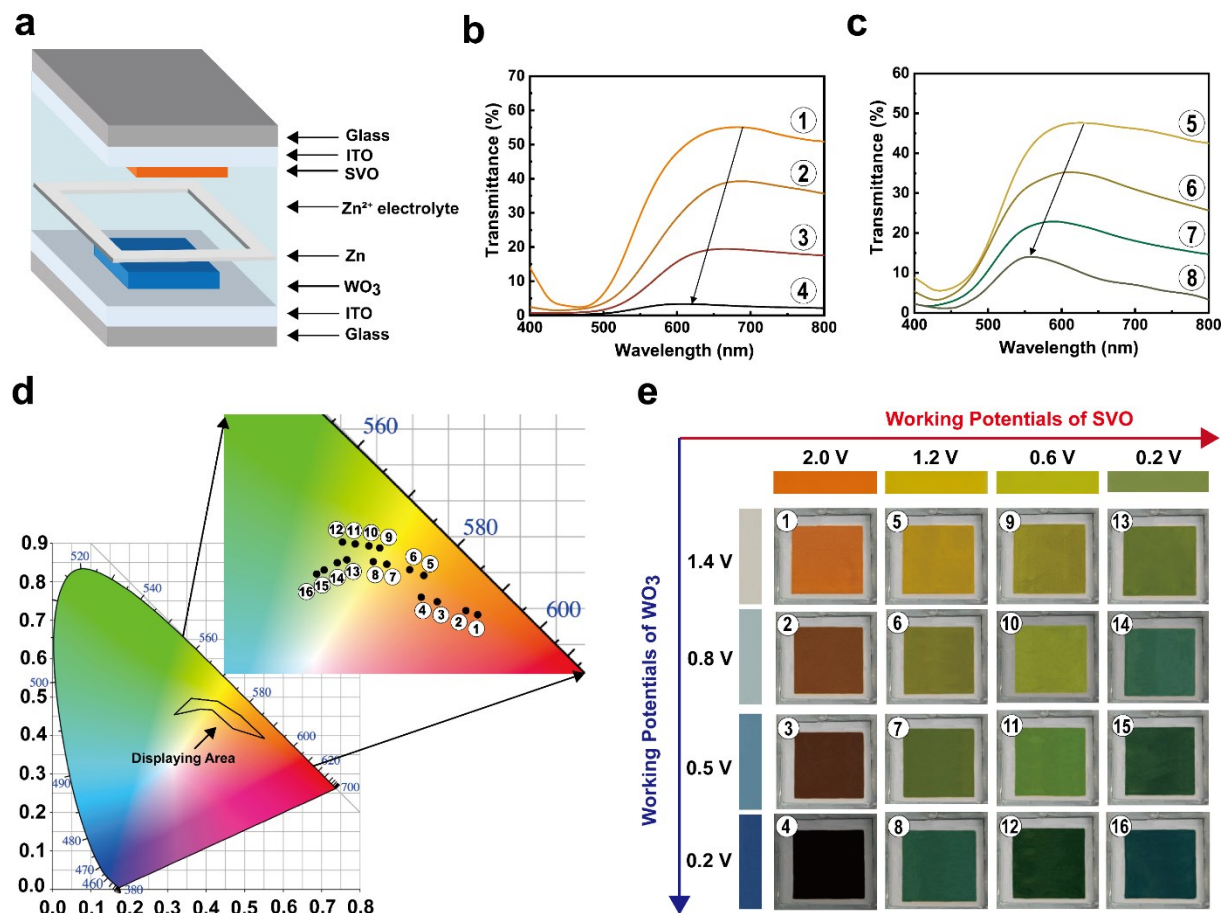


Figure 3.12. Transparent electrochromic display exhibiting broadened color palettes. (a) Schematic illustration of the SVO-Zn-WO₃ electrochromic display. (b) Optical transmittance spectra of the display as the SVO electrode remains fully in a charged state (2.0 V) and the WO₃ electrode tunes its colors under different applied voltages (0.2-1.4 V). (c) Optical transmittance spectra of the display as the SVO electrode remains partially in a charged state (1.2 V) and the WO₃ electrode tunes its colors under different applied voltages (0.2-1.4 V). (d) CIE color coordinates of the SVO-Zn-WO₃ electrochromic display for sixteen different color states which form an enclosed area in CIE color space. (e) Digital images of the SVO-Zn-WO₃ display sixteen colors realized through the color overlay effect.

The color overlay effect was achieved through the combination of an SVO electrode on top of a WO₃ electrode. Since the two electrochromic electrodes can be colored and bleached independently, Figure 3.12b illustrates the optical transmittance spectra of the display as the SVO electrode remains in a fully charged state (2.0 V) and the WO₃ electrode tunes its colors under different applied voltages (0.2-1.4 V). The gradual color switching of the WO₃ electrode results in

a 73 nm blueshift of the transmittance peak position from 681 to 608 nm. As numbered from 1 to 4, four specified color states in Figure 3.12b are displayed on the CIE color space (Figure 3.12d), demonstrating the capability for changing the color hues. Figure 3.12c illustrates the optical transmittance spectra of the display as the SVO electrode remains in a partially charged state (1.2 V) and the WO_3 electrode is color-tuned under different applied voltages. The spectra of the display show a 67 nm blueshift of the transmittance peak position from 624 to 557 nm. Similarly, four specified color states (numbered as 5 to 8) from Figure 3.12c are displayed on CIE color space. Figures 13a and 13b illustrate the change of the optical transmittance spectra of the display as the SVO electrode remains in a partially charged state (0.6 V) or a fully reduced state (0.2 V) and the WO_3 electrode gradually tunes its color states under different applied voltages. Thus, additional eight color states (numbered from 9 to 16) are displayed on the CIE color space (Figure 3.12d). Since the two electrochromic electrodes can be operated independently, while the SVO electrode induces reversible color switching of the display as numbered: $1 \rightleftharpoons 5 \rightleftharpoons 9 \rightleftharpoons 13$; $2 \rightleftharpoons 6 \rightleftharpoons 10 \rightleftharpoons 14$, etc. The reversible color switching of the WO_3 electrode induces different color states as numbered: $1 \rightleftharpoons 2 \rightleftharpoons 3 \rightleftharpoons 4$; $5 \rightleftharpoons 6 \rightleftharpoons 7 \rightleftharpoons 8$, etc. In essence, the SVO-Zn- WO_3 electrochromic device is capable of displaying all color hues within the enclosed area formed by these chromaticity coordinates (Figure 3.12d). While the chromaticity coordinate plots of conventional electrochromic displays form a linear or curved segment in CIE color space (1D CIE color space tunability), the dual electrochromic electrodes of Zn-anode-based electrochromic display is highly versatile as its CIE color space spans a 2D space. Figure 3.12e shows the corresponding digital images of the SVO-Zn- WO_3 electrochromic display under sixteen different representative color states. Since our devices are non-emissive displays, the brightness of colors relies on the intensity of natural light and the thickness of the electrochromic layers.²¹⁰ Some colors appear dark blue

because the total thickness of our electrochromic layers is relatively thick, especially when dual electrochromic layers are applied. The large family of vivid multi-color states attests to the color-tunable characteristic of the device. Notably, it is possible to color or bleach the dual electrochromic layers at the same time for fast switching. The color switching of the display between 1 \rightleftharpoons 6 \rightleftharpoons 11 \rightleftharpoons 16 can also be attained via successively triggering the color evolution of the dual electrochromic layers. The displaying colors of our devices are attributed to the intrinsic colors generated by dual electrochromic layers (e.g., the light absorption of materials). By choosing and incorporating different types of electrochromic materials, different 2D ranges of color can be obtained.

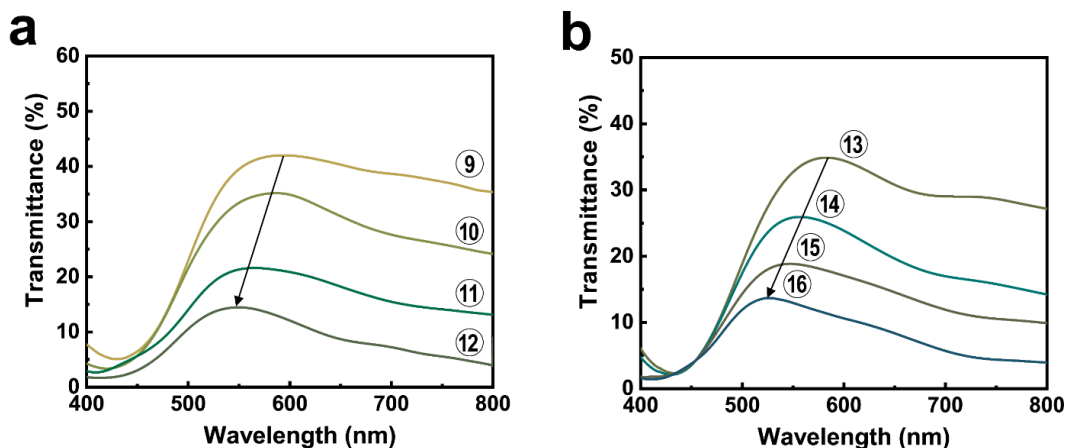


Figure 3.13. (a) Optical transmittance spectra of the display as the SVO electrode remains in a partially charged state (0.6 V) and the WO_3 electrode tunes its colors under different applied voltages (0.2-1.4 V). (b) Optical transmittance spectra of the display as the SVO electrode remains in a fully reduced state (0.2 V) and the WO_3 electrode tunes its colors under different applied voltages (0.2-1.4 V).

3.3.5 Reflective electrochromic displays with broadened color palettes

It is of great importance to realize further versatilities of such an electrochromic display platform through its function as a reflective-type electrochromic display device. As aforementioned, the W/WO₃ Fabry-Perot nanocavity structure can broaden the color hues of the WO₃ electrode. In this regard, a 5 cm × 5 cm reflective-type SVO-Zn-W/WO₃ electrochromic device was assembled through sandwiching a zinc foil between a transmissive SVO electrode and a reflective W/WO₃ electrode (Figure 3.14a). This design architecture enables the color overlay effect while maintaining the reflectivity of the display. Figures 3.14b and 3.14c (and Figures 3.15a and 3.15b) illustrate the optical reflectance spectra of the display as the SVO electrode remains at a specified charged color states (e.g., 2.0 V, 1.2 V, 0.6 V or 0.2 V) and the WO₃ electrode tunes its colors under various applied voltages (0.2-1.4 V). As numbered from 1 to 16, sixteen representative color states are displayed on the CIE color space (Figure 3.14d), demonstrating the excellent capability for changing the color hue of the reflective-type electrochromic device. As such, the dual electrochromic electrodes enable the SVO-Zn-W/WO₃ electrochromic device to display all the color hues within the 2D enclosed area formed by the sixteen representative chromaticity coordinates. Due to the wide color hues modulation of the W/WO₃ Fabry-Perot nanocavity electrode (from light green (520 nm) to dark purple (440nm)), this enclosed area is relatively larger than the area formed by the transparent device (Figure 3.12d). The corresponding digital images of the SVO-Zn-W/WO₃ electrochromic display under sixteen different color states further confirm the compelling function of the color overlay effect (Figure 3.14e).

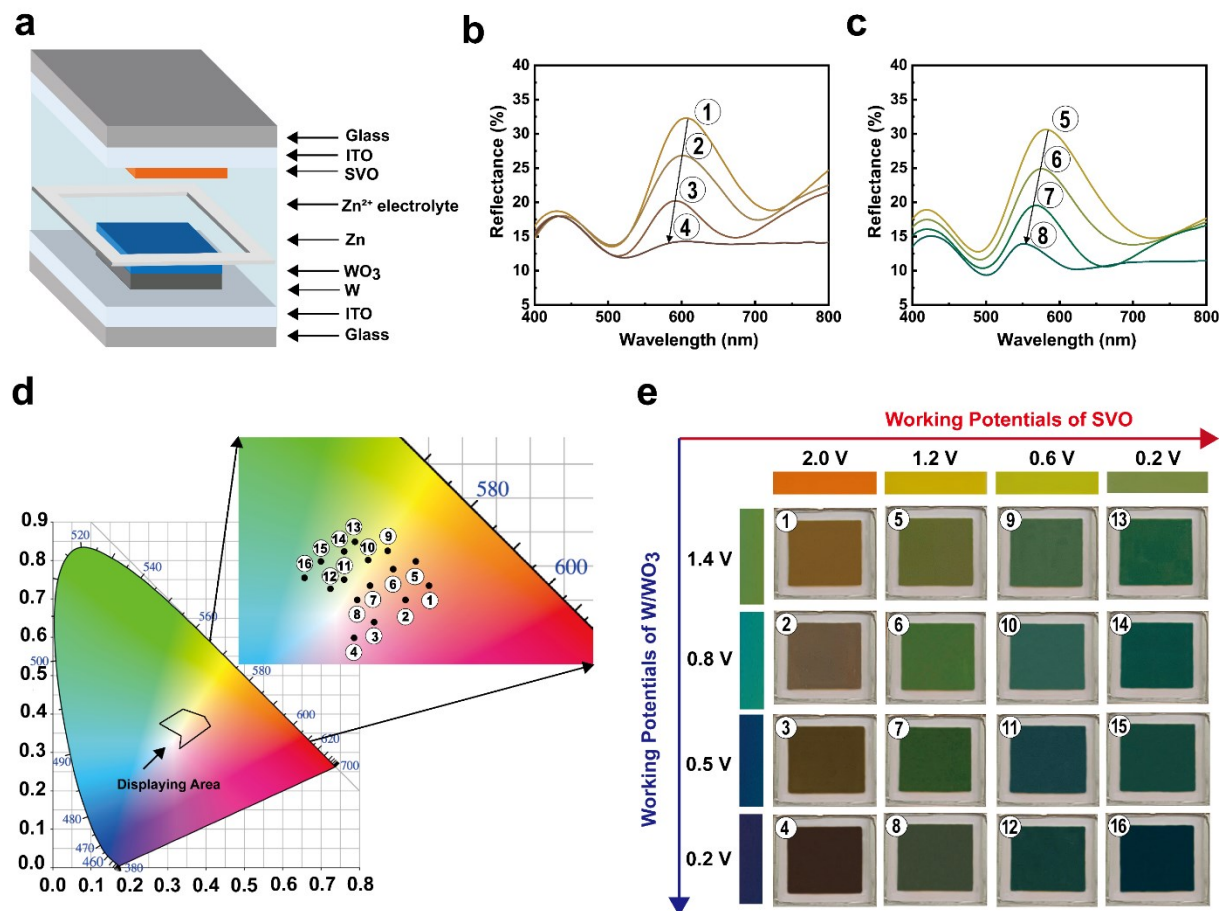


Figure 3.14. Reflective electrochromic display exhibiting broadened color palettes. (a) Schematic illustration of the SVO-Zn-W/WO₃ electrochromic display. (b) Optical reflectance spectra of the display as the SVO electrode remains fully in a charged state (2.0 V) and the W/WO₃ electrode tunes its colors under different applied voltages (0.2-1.4 V). (c) Optical reflectance spectra of the display as the SVO electrode remains partially in a charged state (1.2 V) and the W/WO₃ electrode tunes its colors under different applied voltages (0.2-1.4 V). (d) CIE color coordinates of the SVO-Zn-W/WO₃ electrochromic display under sixteen different color states which form an enclosed area in CIE color space. (e) Digital images of the SVO-Zn-W/WO₃ display showing sixteen colors realized through the color overlay effect.

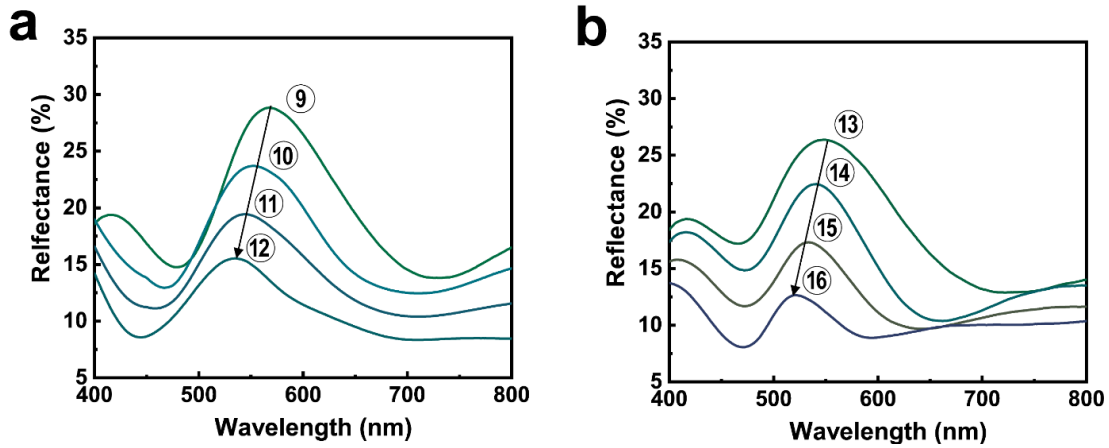


Figure 3.15. (a) Optical reflectance spectra of the display as the SVO electrode remains in a partially charged state (0.6 V) and the W/WO₃ electrode tunes its colors under different applied voltages (0.2-1.4 V). (b) Optical reflectance spectra of the display as the SVO electrode remains in a fully reduced state (0.2 V) and the W/WO₃ electrode tunes its colors under different applied voltages (0.2-1.4 V).

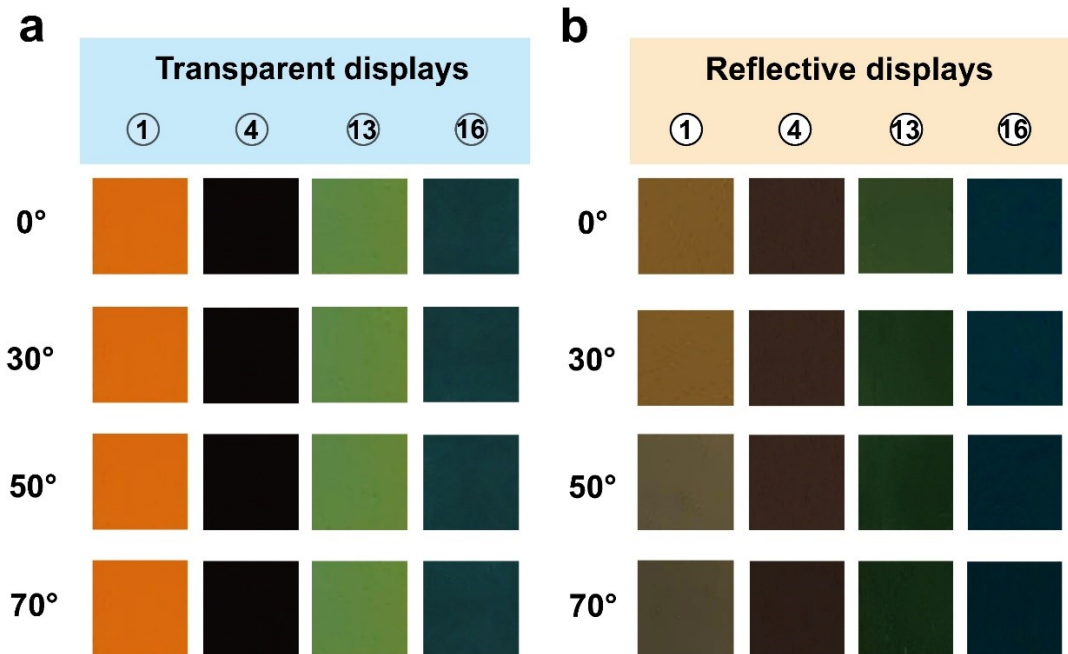


Figure 3.16. Color images of (a) the transparent-type displays and (b) the reflective-type displays at different viewing angles with respect to the surface normal.

Moreover, Figure 3.16 depicts the color images of both the transparent-type and the reflective-type displays at different viewing angles. Four representative color states (#1, 4, 13 and 16) are demonstrated. The transparent-type displays show an excellent angle-independent transmittance behavior as no detectable color change is observed. For the reflective-type displays, there is a slight color change up to a large angle (70°), indicating a good angle-independent reflectance behavior.

3.3.6 Demonstration of a dual-mode prototype transparent-reflective zinc-based electrochromic display

To demonstrate that the zinc-anode-based electrochromic display can be used for electronic shelf labels or optical filters for projectors, a 25-cm² display having a “W” letter pattern was formed and schematically shown in Figure 3.17a. WO₃ film was sputtered onto a W-shaped metallic layer to form a color-changing display pattern. In this way, the assembled display can be addressed by two parts of the structure, namely, the reflective part of the letter “W” and the transmissive part of the remaining surrounding area. Figure 3.17b depicts a schematic illustration of the principle operation of the patterned display where the device can be used as an optical filter for projectors where different colors can be tuned while the pattern remains as a dark background for presenting designed information.

Interestingly, the fully charged display possesses an open circuit potential (OCP) of 1.21 V (Figure 3.17c). This OCP, which stems from the redox potential difference between the zinc foil and the incorporated dual electrochromic electrodes, enables self-coloration behavior and energy retrieval functionality. This display offers an interesting function where a portion of the consumed electrical energy during the oxidation process can be retrieved. That is, the display is able to switch its color from orange to deep green (transmissive region) without the need for applying an external

voltage, while at the same time powering an LED for more than 30 mins (Figure 3.17d). The reflective part (i.e., the letter “W”) of the display exhibits additional color change which varies from brown to deep blue. Figure 3.17e shows the digital images of the display at some representative colors, confirming its great promise for optical filters and projectors. Here, the reversible switching of the display is operated either via powering a 0.5 V regulated LED for the self-coloration/discharging processes or through applying external voltages (2.0 V) for the bleaching/charging processes. Notably, this type of electrochromic display is highly energy efficient as its color change can be triggered by cycling back a portion of the stored electrical energy in the display during the bleaching process.

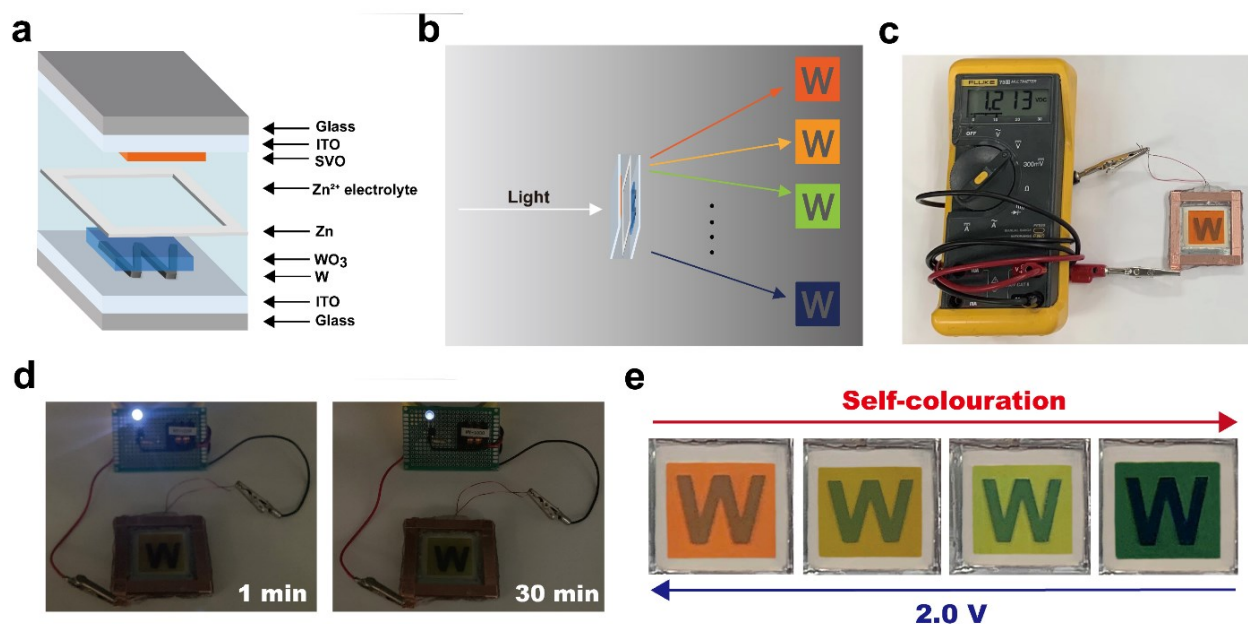


Figure 3.17. Demonstration of prototype zinc-based electrochromic displays. (a) Schematic illustration of a hybrid electrochromic display. (b) Illustration of the prototype device, having an exemplary letter W-shaped pattern. The pattern can be used as an optical filter for projectors, where different colors can be tuned while the pattern remains as a dark background. (c) Digital image of the display for a fully charged state, showing an OCP of 1.21 V. (d) Digital images of a 0.5 V regulated LED powered by the electrochromic display for 1 and 30 min. (e) Digital images of the electrochromic display showing four different color states obtained via lighting an LED.

3.3.7 Summary

To summarize, multi-color electrochromic displays having 2D CIE color tunability were demonstrated via utilizing the Zn-anode-based electrochromic device platform. This novel electrochromic display platform can be addressed to both transmissive-type and reflective-type devices. The device's architecture is configured to have two independent electrochromic electrodes, as such, they can achieve rich color tunability over a wide color gamut distribution via the color overlay effect. As a result, the chromaticity coordinate plots of these displays form a 2D enclosed area in CIE color space, which is rather distinct from those 1D linear curves of conventional electrochromic displays. Our presented Zn-anode-based electrochromic platform is expected to accelerate future electrochromic display technology that brings the full-color tunability in a single electrochromic device within reach.

3.4 A dual-mode electrochromic platform integrating zinc anode-based and rocking-chair electrochromic devices

3.4.1 Introduction

Electrochromic technology platform is typically realized through a device architecture comprised of an electrochromic electrode (i.e., working electrode), a counter electrode and an electrolyte.²¹³ Such a rudimentary electrochromic device is operated in a fashion where cations in the electrolyte are intercalated/extracted and moved back and forth between the electrochromic electrode and the counter electrode as the applied voltage is reversed. By properly matching the cathodically coloring working electrode material and the anodically coloring counter electrode material, both electrodes are able to be colored and bleached in a simultaneity, which offers an optimized optical contrast of this complementary-type electrochromic device. Many pioneer studies on this type of electrochromic device have been reported by matching different electrochromic materials, such as WO_3 and NiO ,^{14,107,214} or TiO_2 and NiO ,^{11,15} or WO_3 and $\text{KFeFe}(\text{CN})_6$ (Prussian blue, PB) or its analogs (PBAs),²¹⁵⁻²¹⁷ etc., which showed low operating potentials and rapid switching speed. However, the performance of the complementary-type electrochromic devices is restricted by the charge balance between the working and counter electrodes, as the different cations storage amount in working and counter electrodes will cause side reactions and thus leading to electrolyte decomposition, poor optical contrast, and low coulombic efficiency. Therefore, the careful design of both electrodes to have a matching electrochemical capacity is critical to achieve an optimized electrochromic performance.

It is well accepted that the complementary-type electrochromic devices are thin film devices possessing low capacity.^{13,15,218} During the charging process, external voltage acts as the driving

force to trigger the cation intercalation into the working electrode, thus, resulting in a corresponding color switching. Conversely, during the discharging process, cations are released from the working electrode and are intercalated into the counter electrode. In this regard, such electrochromic devices are of great interest for their use in energy-efficient optoelectronic devices where the cations stored in the devices can be retrieved while simultaneously having light transparency control. However, not all of the stored cations can be self-retrieved during the discharging process, due to the inherent bistability of electrochromic materials and the low electrode redox potential difference between working and counter electrodes.^{16,218} Most importantly, this class of electrochromic devices cannot be fully switched to its original color state via draining its electrical power through an external load (i.e., via powering external an electronic device). Due to the strong electrostatic interactions between embedded cations and the electrochromic material, even for devices having matching capacity, an external voltage bias is still required to switch the electrochromic device.¹¹ Therefore, the electrode redox potential of the working and the counter electrodes should be tailored for developing self-switching electrochromic devices.²¹⁹

To overcome the limitations (e.g., charge balance, matching electrode potential, and long-term reversibility) imposed by the complementary-type electrochromic devices, zinc anode-based electrochromic devices can be applied.^{22,36,220} Here, the zinc anode acts as the counter electrode, and thus facilitates self-color-switching via the redox potential gradient differences between the zinc anode and the electrochromic cathode.³⁹ Notwithstanding, such devices exhibit only a one-way self-switching mechanism by discharging its voltage similar to a secondary battery. Accordingly, the exploration of reversible electrochromic devices having dual self-switching

functionalities perhaps should be one of the primary tasks to be undertaken by the electrochromic community.

To date, there is no report on the study of tailoring electrode redox potentials of the anodic and cathodic electrodes within a complementary-type electrochromic device. Similar to the zinc anode-based electrochromic devices, where the redox potential gradient differences between the zinc anode and the electrochromic cathode facilitate a self-color-switching behavior, by employing a redox potential gradient difference between the anodic and the cathodic electrodes, the complementary electrochromic device is able to inherently self-discharge and thus facilitating a self-color-switch. As shown in Figure 3.18, during the discharging process, the redox potential gradient difference between the anodic and cathodic electrodes triggers a self-color-switch of both electrodes in a simultaneity (according to the redox potentials of two electrodes, this self-color-switch process may lead to a bleaching of the device ($E_{\text{cathodic}} < E_{\text{anodic}}$) or a coloration of the device ($E_{\text{cathodic}} > E_{\text{anodic}}$)). On the other hand, during the charging process, both electrodes return to the initial optical states by applying an external potential between the two electrodes. Consequently, this type of device, where the flow of cations back and forth between anodic and cathodic electrodes can be triggered by its built-in voltage, is operated in a rocking-chair fashion (i.e., rocking-chair type electrochromic devices). Notably, this rocking-chair type electrochromic device platform is highly manipulative as it exhibits a self-color-switch. As such, by coupling the zinc anode-based electrochromic platform and the rocking-chair type electrochromic platform into a single platform, the coming age of electrochromic devices having dual self-switching functionalities is appearing on the near horizon.

Rocking-chair type electrochromic devices

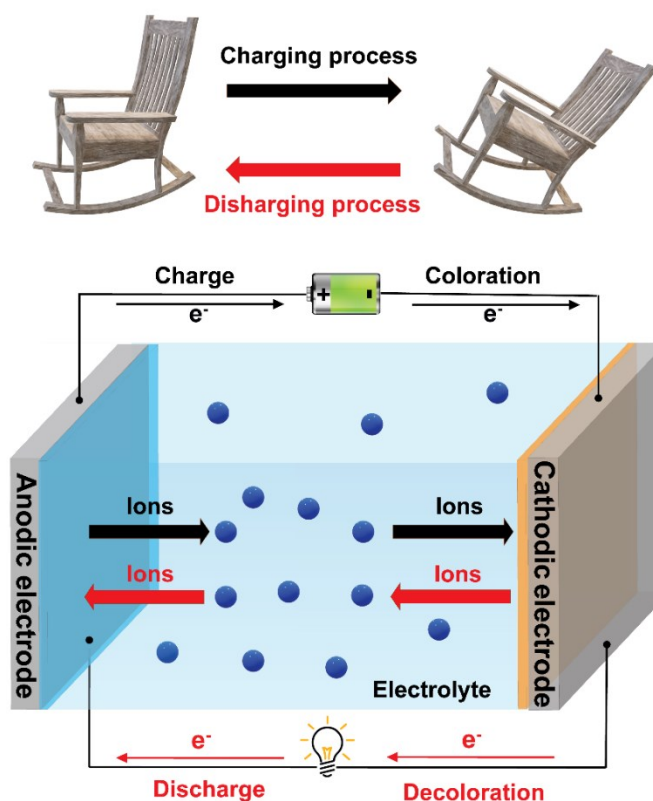


Figure 3.18. Schematic diagram illustrating the rocking-chair type electrochromic devices. During the discharging process, both the anodic and cathodic electrodes can self-bleach (or self-color) in a simultaneity due to the redox potential gradient difference between the two electrodes. By applying an external potential between the two electrodes, during the charging process, both electrodes return to the initial optical states.

In the following section, we investigate a novel dual-mode electrochemically reversible platform enabled by sandwiching a Zn metal anode within a PB-WO₃ rocking-chair type electrochromic device, by virtue of utilizing a well-designed hybrid electrolyte system to tailor the redox potential difference between the WO₃ and the PB electrodes (Figure 3.19a). To prepare the WO₃ electrode, the W powder (1.8 g) was added to 60 mL of H₂O₂ solution (30%) and stirred for 12 h to form a yellow peroxotungstic acid colloid. Next, the sediments were filtered to obtain a clear colloid. The clear colloid was electrodeposited onto a cleaned ITO glass substrate at -0.3 V for 180 s to obtain a WO₃ electrode. To prepare the PB electrode, the K₃[Fe(CN)₆] (10mM),

$\text{FeCl}_3 \cdot 6\text{H}_2\text{O}$ (10 mM), and KCl (50 mM) were dissolved in distilled water under stirring. Next, the electrodeposition was performed at a constant current density (-0.05 mA/cm^2 , 240 s) onto a cleaned ITO glass substrate to obtain a PB electrode (see Appendix C, the Method section).

Such a WO_3 -Zn-PB device configuration enables independent operation of the WO_3 and the PB electrodes, thus providing additional operation flexibility (e.g., self-coloring/self-bleaching) in addition to offering precise manipulation of a single electrode. We show that the redox potential differences between the zinc anode and the WO_3 /PB electrodes endow the self-color-switching of these electrodes (Mode I shown in Figure 3.19b). By further altering the redox potential difference between the WO_3 and the PB electrodes through the utilization of a well-designed hybrid electrolyte system, we demonstrate a rocking-chair type electrochromic device having spontaneous self-bleaching functionality for the first time (i.e., a rocking-chair type electrochromic device, Mode II shown in Figure 3.19c). As such, the full utilization of the redox potential differences between the three electrodes enables dual-mode operations, which is a highly promising function for electrochromic devices having dynamic light control.

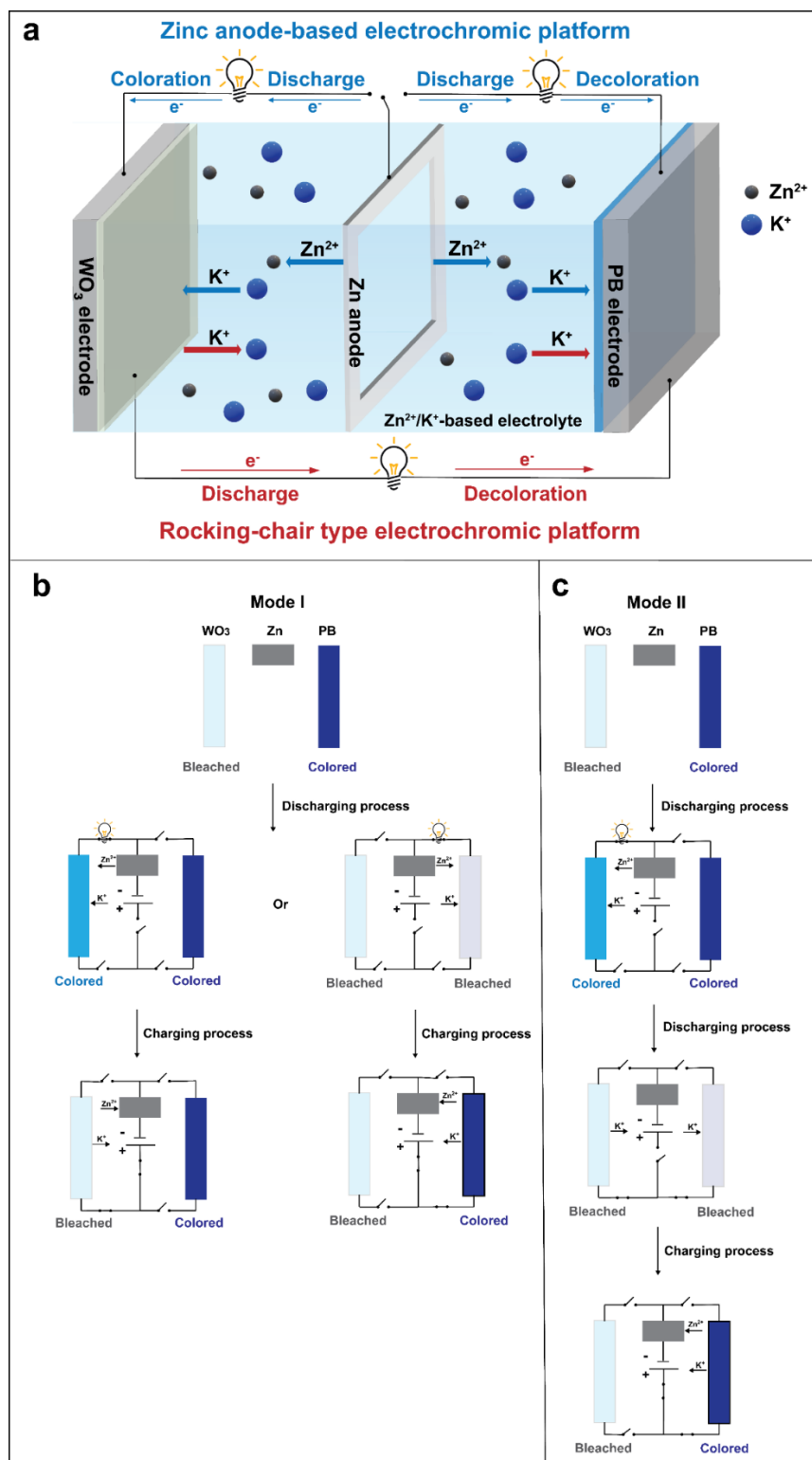


Figure 3.19. Schematic diagram illustrating the dual-mode operation processes. a) Schematic diagram illustrating the basic operation of a reversible dual-mode electrochromic device having a self-switching functionality. b) Schematic diagram illustrating the Mode I operation processes. c) Schematic diagram illustrating the Mode II operation processes.

3.4.2 Mechanism of the dual-mode electrochromic platform

To better elucidate the basic operating mechanism of this dual-mode electrochromic device platform, it is important to examine the energy level transition diagrams for WO_3 , Zn, and PB shown in Figure 3.20a,b. While the large redox potential difference between Zn and PB/ WO_3 electrodes ($\sim 1.12/1.06$ V) is expected to serve as a driving potential to trigger the spontaneous color switching process, the similar redox potentials between WO_3 (0.30 V)³⁶ and PB (0.36 V)²²⁰ brings great challenges to realize a PB- WO_3 rocking-chair type electrochromic device having spontaneous self-color switching. Therefore, to realize a dual-mode electrochromic platform having self-coloring and self-bleaching functionalities, it is critical to alter the redox potential difference between the WO_3 and the PB electrodes. This can be accomplished by coupling the zinc anode-based electrochromic device and the aforementioned PB- WO_3 rocking-chair type electrochromic device with a well-designed electrolyte into a single platform as illustrated in Figure 3.19a. In such a configuration, the first operating mode (i.e., Mode I, Figure 3.19b) is realized by electrically connecting the Zn anode to either the WO_3 or equivalently to the PB cathode, wherein, the redox potential difference between the Zn anode and the WO_3 (or the PB) cathode allows the Zn metal to be oxidized and the WO_3 (or the PB) electrochromic layer to be reduced. During this discharging process, the Zn anode is oxidized and releases Zn^{2+} and, at the same time, the K^+ from the KCl-ZnSO_4 electrolyte are intercalated into the WO_3 (or the PB) electrochromic cathode. This discharging process triggers a spontaneous color-switching of the WO_3 (or the PB) electrochromic electrode where the WO_3 layer changes its color state from being transparent to a light blue color (or when the Zn anode is connected to the PB, the PB layer changes its color from dark blue to be transparent). To return to the initial color state(s), the direct electrical contact between the Zn anode and the WO_3 (or the PB) cathode is disconnected, and an external

potential (1.0 V or 1.8 V) is applied between the Zn anode and the WO₃ cathode (or between the Zn anode and the PB cathode). During this charging process, the Zn²⁺ are reduced and plated onto the Zn anode and the K⁺ are de-intercalated from the WO₃ (or the PB) electrochromic cathode.

The second operating mode (i.e., Mode II, Figure 3.19c) requires taking advantage of the redox potential difference between the WO₃ and PB electrodes. During the discharging process, the Zn anode and the WO₃ electrode are connected, thus inducing the oxidation of the Zn anode ($\text{Zn} \rightarrow \text{Zn}^{2+}$) and the reduction of the WO₃ electrode (due to the K⁺ intercalation). When this process is followed by a direct electrical contact between the WO₃ and the PB electrodes, the K⁺ are extracted from the reduced WO₃ electrode and intercalated into the PB electrode. This discharging process triggers a spontaneous color-switching process of both the WO₃ electrode (i.e., from light blue color to transparent) and the PB electrode (i.e., from dark blue color to transparent). On the other hand, during the charging process, the WO₃-Zn-PB device returns to its initial color state. Here, the Zn²⁺ are reduced and plated onto the Zn anode while the K⁺ are de-intercalated from the PB electrode by applying an external potential of 1.8 V between the Zn anode and the PB electrode.

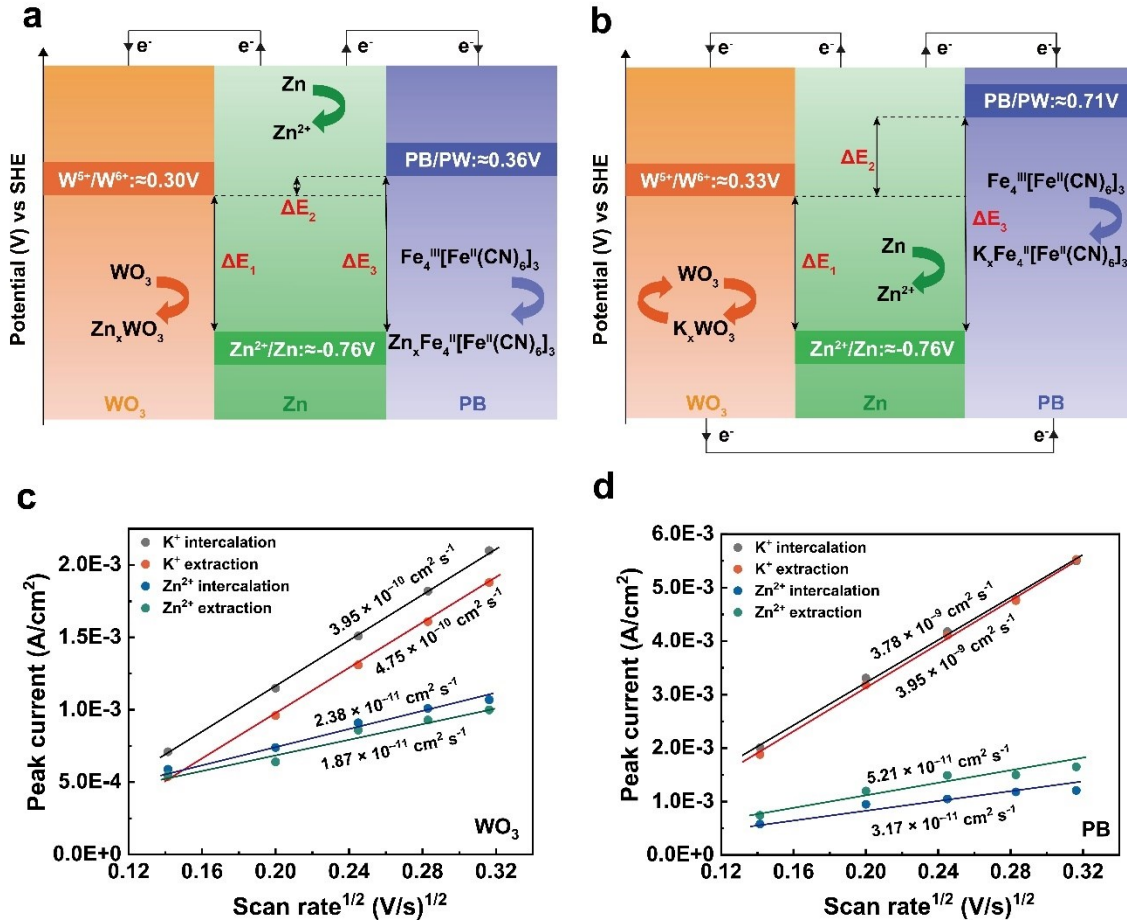


Figure 3.20. Characterization of the electrochromic electrodes in different electrolytes. The energy level transition diagram of WO_3 , Zn, and PB in: a) 1M ZnSO_4 and b) 1 M KCl - 0.1 M ZnSO_4 electrolyte system. c) The diffusion coefficients of the WO_3 electrode. d) The diffusion coefficients of the PB electrode.

To realize the operating Mode II, it is important to tailor the redox potential difference between the WO_3 and PB electrodes. Therefore, it is critical to properly alter the electrolyte composition to tailor the redox potential difference between the WO_3 and the PB electrodes according to the Nernst equation (i.e. Eq. (3.1)),^{221,222}

$$E_{cell} = E_{cell}^{\theta} - \frac{RT}{nF} \ln \left(\frac{a_{red}}{a_{ox}} \right) \quad (3.1)$$

Where E_{cell} is the cell potential of interest, E_{cell}^{θ} is the standard cell potential, R is the universal gas constant, T is the temperature (K), F is the Faraday constant, n is the number of electrons

transferred in the cell, and a is the chemical activity for the relevant species (i.e., a_{red} is the chemical activity of the reduced product and a_{ox} is the chemical activity of the oxidized product).

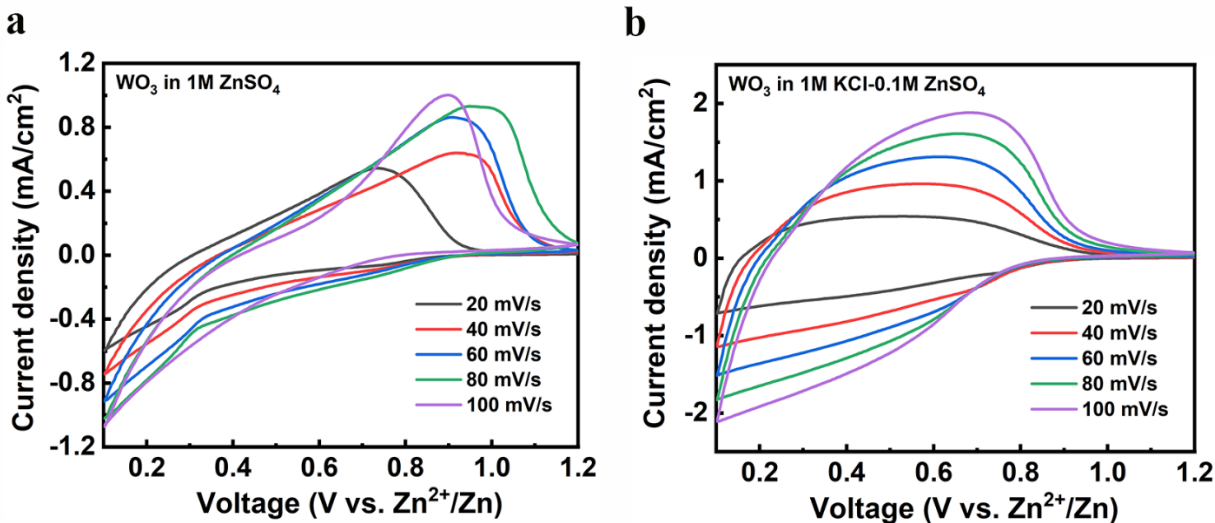


Figure 3.21. Cyclic voltammetry (CV) performance of the WO_3 electrode at different scanning rates: a) 1M ZnSO_4 and b) 1M KCl - 0.1M ZnSO_4 .

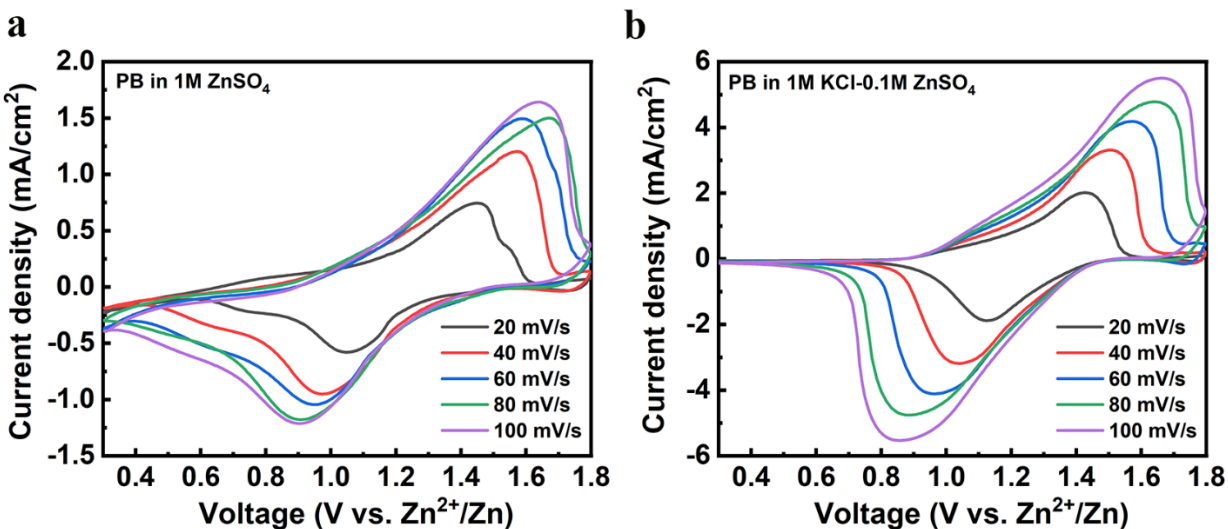


Figure 3.22. Cyclic voltammetry (CV) performance of the PB electrode at different scanning rates: a) 1M ZnSO_4 and b) 1M KCl - 0.1M ZnSO_4 .

Of particular importance, when investigating the cell potential of electrochromic devices, it is able to have the flexibility to modify the redox potential through the chemical activity for the relevant species within the cell. The chemical activity is related to the efficiency of gaining/losing electrons,²²² as such, the redox potential difference between the WO₃ and the PB electrodes can be tailored by selecting the types of cations used in the electrolyte solution. Figures 3.21a and 3.22a depict the cyclic voltammetry (CV) curves for the WO₃ and the PB electrodes in a 1 M ZnSO₄ solution measured at different scan rates. Here, the diffusion coefficient of Zn²⁺ for intercalation and extraction can be estimated from the measured peak current, I_p (Amps) (Eq. (3.2)),¹⁰⁸

$$I_p = 2.69 \times 10^5 AC \sqrt{Dvn^3} \quad (3.2)$$

Where n is the number of electrons transferred, A is the contact area (cm²), D is the diffusion coefficient of the cation ions (cm² s⁻¹), C is the concentration of the cation ions in the electrolyte solution (mol cm⁻³), and v is the scan rate (V s⁻¹). Accordingly, the diffusion coefficients of Zn²⁺ for intercalation and extraction of the WO₃ electrode are calculated to be 2.38×10^{-11} cm² s⁻¹ and 3.17×10^{-11} cm² s⁻¹, respectively (Figure 3.20c); whereas for the PB electrode are 1.87×10^{-11} cm² s⁻¹ for intercalation and 5.21×10^{-11} cm² s⁻¹ for extraction as depicted in Figure 3.20d. Interestingly, since there is no significant difference between the diffusion coefficient values of the WO₃ and the PB electrodes, they must exhibit a very similar electrochemical activity, and, thus, the PB-WO₃ cell potential is close to their standard cell potential. This is further confirmed in a device platform, where the open circuit potential (OCP) of the PB-WO₃ cell is measured in a 1 M ZnSO₄ solution, to be 0.076 V (Figure 3.23a), which is nearly the same as the standard cell potential of 0.06 V shown in Figure 3.20a. As discussed, since the presence of the Zn²⁺ is necessary for the stripping/plating of the Zn anode in the zinc anode-based electrochromic devices,²¹⁸ a hybrid electrolyte is needed for the dual-mode electrochromic operation. As such, it is important to select

the proper cation to intercalate and extract the PB electrode. It is well-known that the intercalation of K^+ into PB structures is a highly reversible and fast kinetics process due to the ease of diffusion of the K^+ into the open-framework atomic structure of PB lattice.^{199,223} Thus, a hybrid electrolyte consisting of Zn^{2+} and K^+ is suitable to tailor the redox potential difference between the WO_3 and the PB electrodes. Figures 3.21b and 3.22b depict the cyclic voltammetry (CV) curves for the WO_3 and the PB electrodes in a 1 M KCl-0.1 M $ZnSO_4$ solution measured at different scan rates. As shown in Figure 3.20c,d, the diffusion coefficients of K^+ into the WO_3 electrode are calculated to be $3.95 \times 10^{-10} \text{ cm}^2 \text{ s}^{-1}$ (for intercalation) and $4.75 \times 10^{-10} \text{ cm}^2 \text{ s}^{-1}$ (for extraction) and for the PB electrode are $3.78 \times 10^{-9} \text{ cm}^2 \text{ s}^{-1}$ (for intercalation) and $3.95 \times 10^{-9} \text{ cm}^2 \text{ s}^{-1}$ (for extraction). In our experiments, we determined that the measured diffusion coefficients of K^+ into the PB electrode are much higher than those diffusion coefficients into the WO_3 electrode. These results confirm that the K^+ is an excellent choice for the hybrid electrolyte since it can be easily extracted from the WO_3 electrode and efficiently intercalated into the PB electrode. Notably, since there is a significant difference between the diffusion coefficient values of the WO_3 and the PB electrodes, the differentiation of electrochemical activities of the two electrodes is created. As such, the redox potential difference between the WO_3 and PB electrodes is increased in the hybrid electrolyte. In order to put all our aforementioned findings into practice, a hybrid electrolyte, consisting of 1 M KCl-0.1 M $ZnSO_4$, was used as the ion-conducting layer of the dual-mode electrochromic device. In this system, the OCP of the PB- WO_3 cell is found to increase from 0.076 to 0.376 V (Figure 3.23b). Such a relatively high OCP is critical for the self-bleaching process of the PB- WO_3 electrodes.

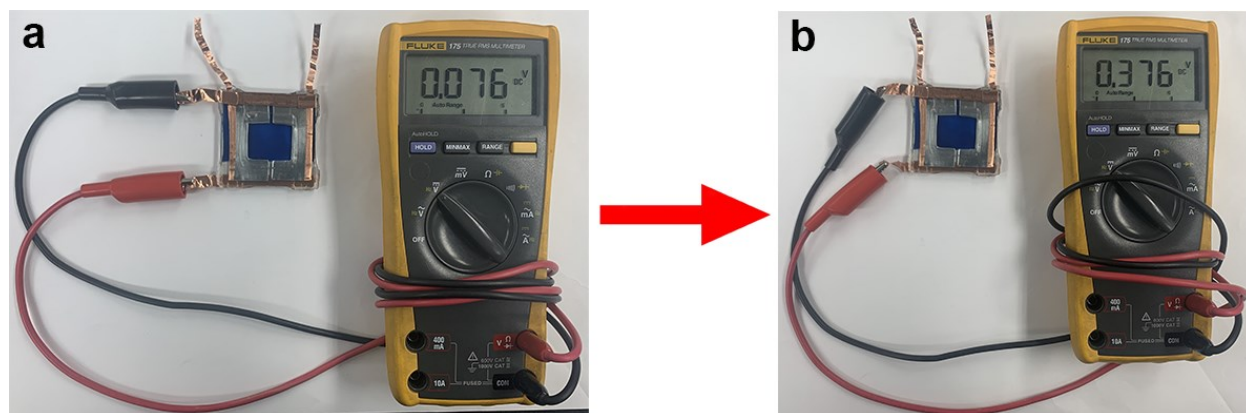


Figure 3.23. Digital photograph of the dual-mode device showing an increased OCP of 0.376 V between the WO_3 electrode and the PB electrode in a 1M KCl - 0.1M ZnSO_4 electrolyte system (b), compared to 0.076 V in the 1M ZnSO_4 electrolyte system (a).

3.4.3 Optimization of the electrochromic electrodes

It is important to further show that the inclusion of the K^+ into the electrolyte makes the WO_3 and PB electrodes more electrochemically active, compared to a pure Zn^{2+} electrolyte. Figure 3.24a,b depicts the cyclic voltammetry (CV) scans of the WO_3 and the PB electrodes in 1M ZnSO_4 and in the hybrid 1 M KCl - 0.1 M ZnSO_4 electrolyte. As indicated in Figure 3.24a,b, the Zn^{2+} intercalation/extraction in pure Zn^{2+} electrolyte is a relatively slow kinetic process (i.e., smaller enclosed area of CV), compared to the K^+ intercalation/extraction process in hybrid K^+ - Zn^{2+} electrolyte. This is attributed to the fact that the multivalent Zn^{2+} cations lead to a large lattice distortion, due to the strong electrostatic interactions, hence, resulting in a drastic depreciation in current densities during successive cycling (Figure C-1a).^{199,224} For the PB electrode, a pair of well-defined redox peaks (at 1.1 and 1.5 V, Figure 3.24b) is observed in the hybrid electrolyte. These peaks are attributed to the reduction/oxidation processes of low-spin $\text{Fe}^{\text{II}}/\text{Fe}^{\text{III}}$ coupling to the C atoms via the intercalation/extraction of K^+ .¹⁹⁹ Remarkably, the redox peaks of the PB film in the hybrid electrolyte remain almost unchanged during cycling (Figure C-1b), suggesting a highly reversible redox reaction is taking place during cycling.

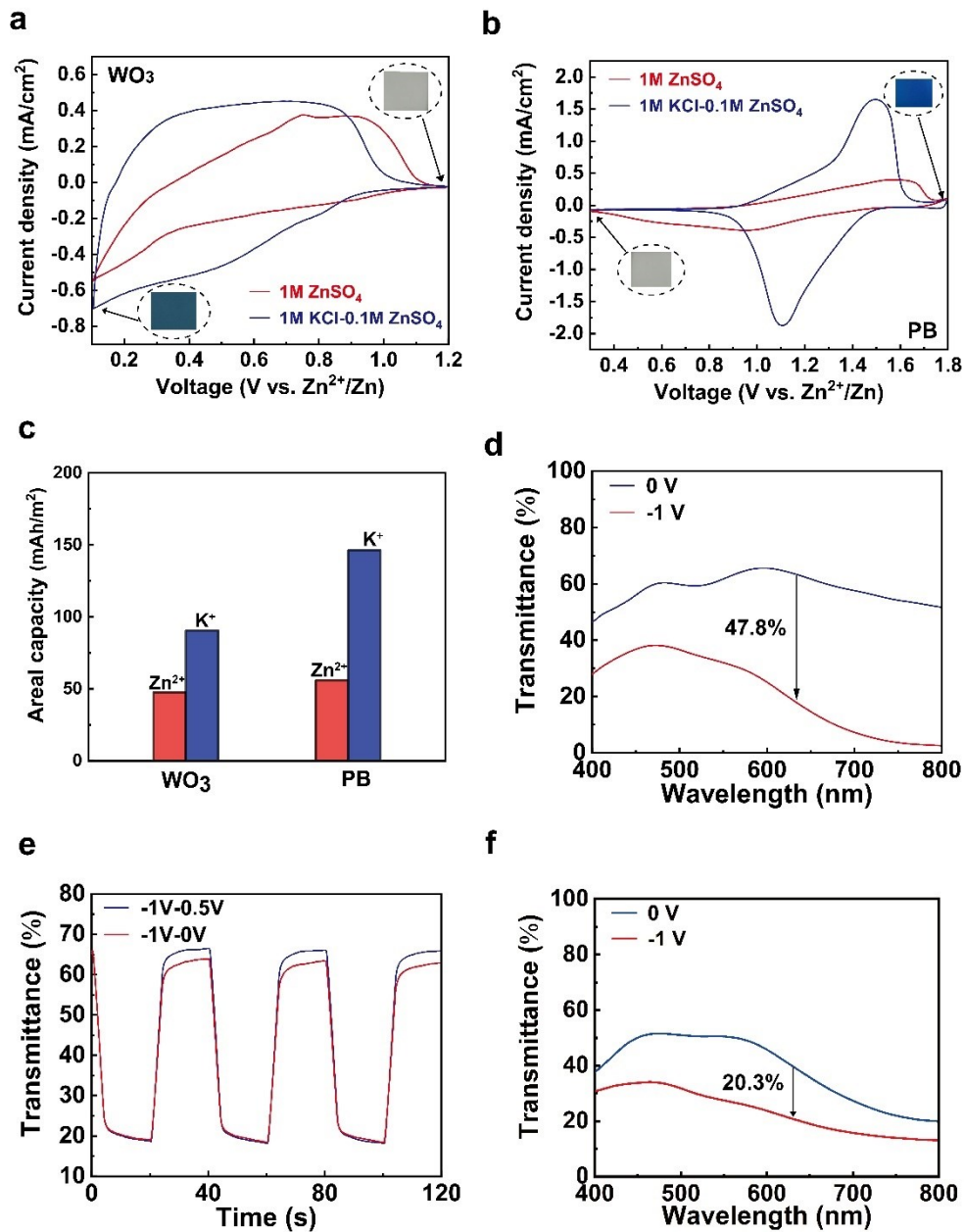


Figure 3.24. a) The CV scan of the WO₃ electrode taken at a scan rate of 20 mV s⁻¹ over a voltage range of 0.1 V–1.2 V. The insets show the WO₃ electrode displays a transparent state in its oxidized state and can be reduced to a blue state via the intercalation of K⁺. b) The CV scan of the PB electrode taken at a scan rate of 20 mV s⁻¹ over a voltage range of 0.3 V–1.8 V. The insets show the PB electrode displays a blue state in its oxidized state and can be reduced to a transparent state via the intercalation of K⁺. c) The areal capacities of the WO₃ electrode and the PB electrode. d) Visible-near infrared transmittance spectra of the PB-WO₃ device under different voltages by using the hybrid electrolyte. e) Dynamic of 632.8 nm optical transmittance of the PB-WO₃ device in two voltage ranges of -1.0 V-0 V and -1.0 V-0.5 V. f) Visible-near infrared transmittance spectra of the PB-WO₃ device in 1M ZnSO₄ electrolyte system.

The redox reactions induce color variations of both the WO₃ and the PB electrodes. As presented in the insets in Figure 3.24a, the WO₃ electrode exhibits a transparent color in its oxidized state and a blue color via the intercalation of the K⁺. On the other hand, the PB electrode exhibits a blue color in its oxidized state and a transparent color when intercalated with the K⁺ (insets in Figure 3.24b). The color behaviors of PB and WO₃ electrodes are consistent with the classification of anodic and cathodic electrochromic materials, respectively.²¹⁰

The areal capacities of the PB and the WO₃ electrodes when intercalated with the Zn²⁺ and the hybrid K⁺/Zn²⁺ are evaluated and compared in Figure 3.24c. Both the PB and the WO₃ electrodes show relatively high capacities of 147 mAh/m² and 92 mAh/m², respectively in the K⁺/Zn²⁺ hybrid electrolyte compared to the capacities (i.e., 56 mAh/m² (for PB) and 47 mAh/m² (for WO₃)) measured in the pure Zn²⁺ electrolyte. The 2.6 times increase in the PB electrode capacity and the 1.9 times increase in the WO₃ electrode capacity further confirm the higher activity of the K⁺ intercalation/extraction process. Notably, since the capacity of the PB electrode is slightly higher than that of the WO₃ electrode, fully self-bleaching of the reduced WO₃ electrode can be easily achieved by electrically coupling the WO₃ and the PB electrodes. As shown in Figure 3.24d,e, the optical transmittances of the PB-WO₃ rocking-chair type device for the two voltage values of -1V and 0V are demonstrated. Clearly, a relatively high 47.8% optical contrast is observed when using the hybrid 1 M KCl-0.1 M ZnSO₄ electrolyte in comparison to the 20.3% achieved with the 1M ZnSO₄ electrolyte (Figure 3.24f). Although such a PB-WO₃ rocking-chair device enables self-bleaching of the WO₃ and PB electrodes due to the redox potential gradient difference, this moderate optical contrast (47.8%) of the PB-WO₃ device is not satisfactory for high-performance dynamic light control applications. A major source of this limitation is due to the insufficient charging/discharging of the PB electrode, where the charge imbalance between

two electrodes (i.e., different capacities) impedes the device from achieving its optimal performance. Nonetheless, a fully bleaching and coloration of the PB electrode can be realized by increasing the capacity of the WO_3 electrode (by increasing the thickness) or decreasing the capacity of the PB electrode (by decreasing the thickness), and thus, matching the charge balance of both electrodes. In this way, the optical contrast of the PB- WO_3 device is supposed to increase but cannot achieve its maximum value. To achieve the maximum optical contrast of the device, a single electrochromic electrode must express its maximum optical contrast; however, the optical contrast of a single electrochromic electrode is also determined by the thickness of the electrode film, as such, critical choice of the film thickness is required. In spite of that, the optimum film thickness for maximum optical contrast may not be the same as the thickness needed for the charge balance. To overcome such a limitation, the zinc anode is sandwiched between the PB and the WO_3 electrodes to offer independent coloration/bleaching of the PB and the WO_3 electrodes to maximize the optical contrast of each electrode.

To determine optimum operating voltages for real-world applications of the dual-mode electrochromic devices, the electrochromic performance of the WO_3 and the PB electrodes at various voltage activations are investigated and presented in Figure 3.25. Figure 3.25a,b depicts the optical transmittances of the WO_3 and PB electrodes in a 1 M KCl -0.1 M ZnSO_4 electrolyte, respectively. The WO_3 electrode is transparent when it is charged to 1.0 V and colors blue when discharged at 0.1 V. It is worth noting that the maximum optical transmittance change (defined as the transmittance difference between the charged and discharged states³⁷) of the WO_3 electrode, is 71.5% (Figure 3.25a, without subtracting the transmittance loss of an ITO/glass substrate), which is higher than those previously reported values.^{144,225} On the contrary, the PB electrode is blue colored when it is charged to 1.6 V and bleached when it is discharged to 0.8 V. The optical

transmittance change of the PB electrode is 76.8% (Figure 3.25b), which is higher than those of previous reports.^{58,226}

While high optical contrast is highly sought after in electrochromic devices, it is same important to have fast color switching times. To highlight the fast-switching times of the device, the switching times between the different optical states (colored and bleached) were determined from transmittance changes at a specific wavelength (i.e., 632.8 nm) in real time. Figure 3.25c shows a coloration time, t_c , of 3.2 s at 0.1 V and a bleaching time, t_b , of 2.6 s at 1.0 V for the WO_3 electrode. As a comparison, at a midpoint voltage value of 0.5 V, $t_c = 5.5$ s, which is slower than the coloration time of 3.2 s at 0.1 V. The voltage dependency of t_c is attributed to the initial charging voltage of the electrode. The low discharging voltage accelerates the ion intercalation process, thus resulting in a shorter switching time.²²⁷ Similar to the WO_3 electrode, the PB electrode also exhibits a relatively fast bleaching time $t_b = 3.6$ s at 0.8 V, compared to 6.7 s at 1.0 V, while the coloration time $t_c = 4.3$ s at 1.6 V (Figure 3.25d). Interestingly, the switching t_c and t_b times in the hybrid KCl-ZnSO₄ electrolyte system are much faster than the switching times ($t_c = 8.5$ and $t_b = 7.8$ for the WO_3 electrode, and $t_c = 8.2$ and $t_b = 7.9$ for the PB electrode) in the pure 1 M ZnSO₄ electrolyte system (Figures C-2 and C-3). These faster switching times further confirm that the K^+ intercalation/extraction process is more electrochemically active, compared to that of Zn^{2+} .

Along with the high optical modulations and the fast-switching times exhibited by the K^+/Zn^{2+} electrolyte system, the coloration efficiency (CE), defined as the change in optical density (ΔOD) per unit of charge intercalated into the electrochromic layer at a particular wavelength,¹⁴⁴ is calculated to be 101.6 cm²/C for the WO_3 electrode and 129.9 cm²/C for the PB electrode in such a hybrid electrolyte system (Figure 3.25e,f).

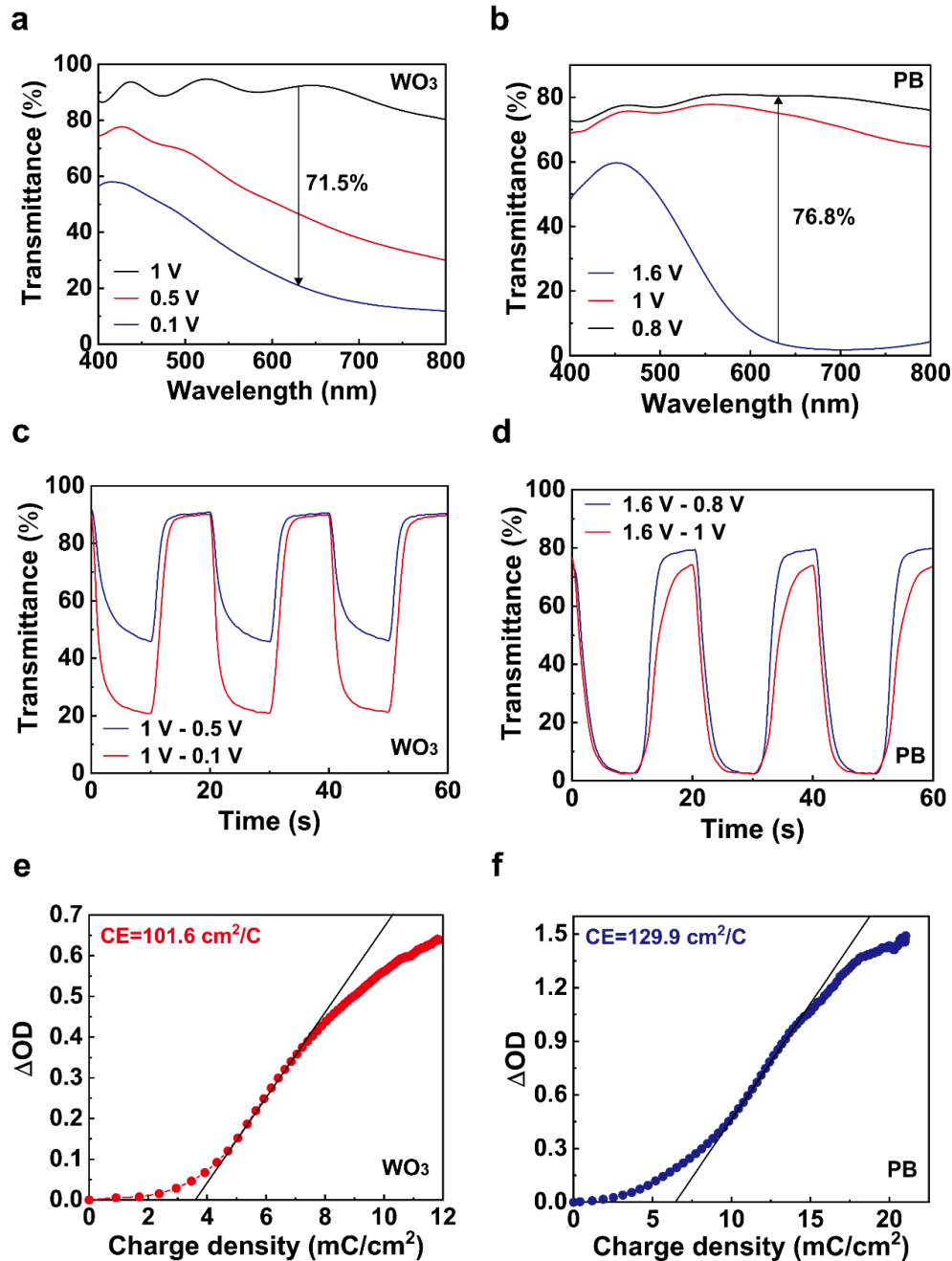


Figure 3.25. Electrochromic performance of the electrodes. a) Visible-near infrared transmittance spectra of the WO₃ electrode taken at 0.1 V, 0.5 V, and 1.0 V. b) Visible-near infrared transmittance spectra of the PB electrode at different voltages of 0.8 V, 1.0 V and 1.6 V. c) Dynamic of 632.8 nm optical transmittance of the WO₃ electrode at two voltage ranges of 0.1 V–1.0 V and 0.5 V–1.0 V. d) Dynamic of 632.8 nm optical transmittance of the PB electrode at two voltage ranges of 1.6 V–0.8 V and 1.6 V–1.0 V. e) Coloration efficiency of the WO₃ electrode in a hybrid K⁺/Zn²⁺ electrolyte. f) Coloration efficiency of the PB electrode in a hybrid K⁺/Zn²⁺ electrolyte.

3.4.4 Operation of dual-mode electrochromic devices

The next step is to investigate the device performance of the dual-mode electrochromic platform. Here, a 5 cm × 5 cm WO₃-Zn-PB electrochromic device is assembled as depicted in Figure 3.19a and Figure 3.26a. As previously discussed, the redox potential difference (built-in voltage, 1.467 V between Zn anode and PB cathode allows the device to switch its color while simultaneously supplying electrical power to light an LED, as shown in Figure 3.26a. The demonstrated self-color-switching feature points out the fact that this electrochromic device platform is energy efficient and operation flexible.

The optical transmittance spectra of the device, taken at different color states (fully colored, fully bleached, PB colored, and WO₃ colored), are shown in Figure 3.26b. At a wavelength of 632.8 nm, the maximum optical modulation of 72.6% (without subtracting the transmittance loss of the ITO-glass substrates) is higher than most of the electrochromic devices reported to date.^{209,228-231} As a key parameter when considering the suitability of the device for practical applications, fast switching between the different color states is highly desirable. Figure 3.26c,d shows the dynamic at 632.8 nm optical transmittance of the device along with the color switching of the WO₃ and PB electrodes. The response times, defined as the time required to achieve 90% of the maximum optical contrast,²² are measured to be 4.0 s for coloration (at 0.1 V) and 3.8 s for bleaching (at 1.0 V) along with the color switching of the WO₃ electrode (Figure 3.16c). Comparable response times of 4.4 s for coloration (at 1.6 V) and 3.6 s for bleaching (at 0.8 V) are obtained, along with the color switching of the PB electrode (Figure 3.26d). These response times are shorter than those previously reported electrochromic devices.^{15,117,159}

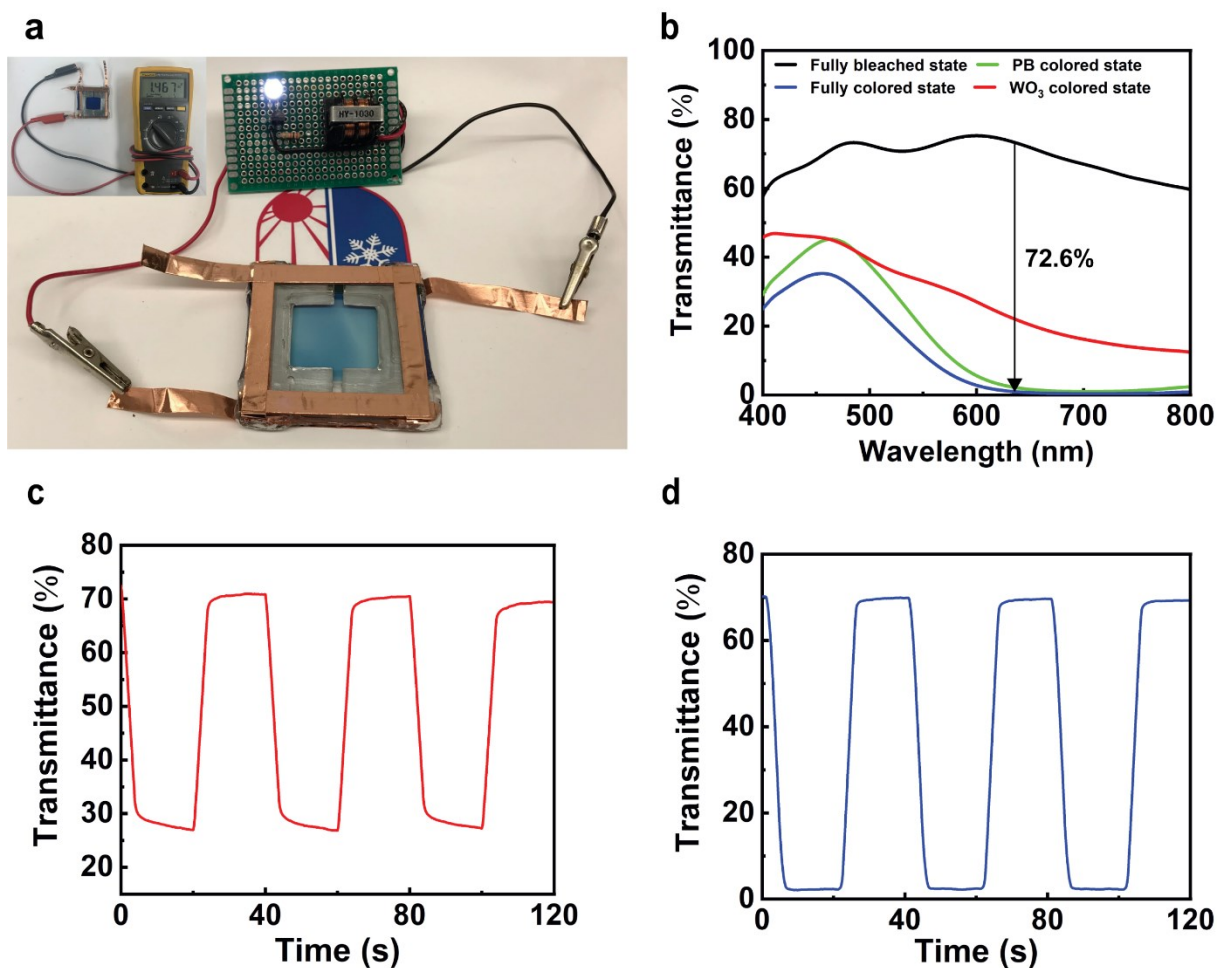


Figure 3.26. Design and performance of the dual-mode electrochromic device. a) Digital photographs of a 0.5 V regulated LED powered by the dual-mode electrochromic device. b) Visible-near infrared transmittance spectra of the dual-mode device at different color states. c) Dynamic of 632.8 nm optical transmittance at a voltage range of 0.1 V–1.0 V along with the color switching of the WO_3 electrode. d) Dynamic of 632.8 nm optical transmittance at a voltage range of 0.8 V–1.6 V along with the color switching of the PB electrode.

Figure 3.27 depicts the reversible color switching processes between four different color states (fully colored, fully bleached, PB colored and WO_3 colored) of the dual-mode electrochromic devices. These color states are realized either via powering a 0.5 V regulated LED or by directly connecting the colored WO_3 and PB electrodes for the discharging process, or through applying an external voltage for the charging process. For example, the device displaying a PB-colored state at the initial state (a combination of colored PB electrode and bleached WO_3

electrode), can be self-colored (via discharging) to a fully colored state via connecting the Zn and WO₃ electrodes to power a 0.5 V regulated LED. Hence after, the fully colored device is able to self-bleach itself to a fully transparent state via connecting the PB-WO₃ and the Zn-PB subsequently. Through applying an external voltage of 1.8 V between the PB and Zn electrodes, the device switches to the initial PB-colored state. Interestingly, as such a device configuration enables independent operation of the WO₃ and PB electrodes, the PB-colored device can self-bleach to a fully bleached state via directly connecting the Zn anode and the PB electrode. Although the choice of WO₃ and PB results in a blue color of the device, the design of PB analogs (e.g., cobalt hexacyanoferrate) is considered a promising platform for electrochromic devices having color neutrality.²³²

Notably, the operation processes shown in Figure 3.27 are highly flexible and effective as their color change (discharging process) can be triggered by powering external electronics. Even though the external biases are still required for operations, such an approach is more effective and reliable for real-world electrochromic devices, thus offering a promising platform for multifunctional electrochromic devices.

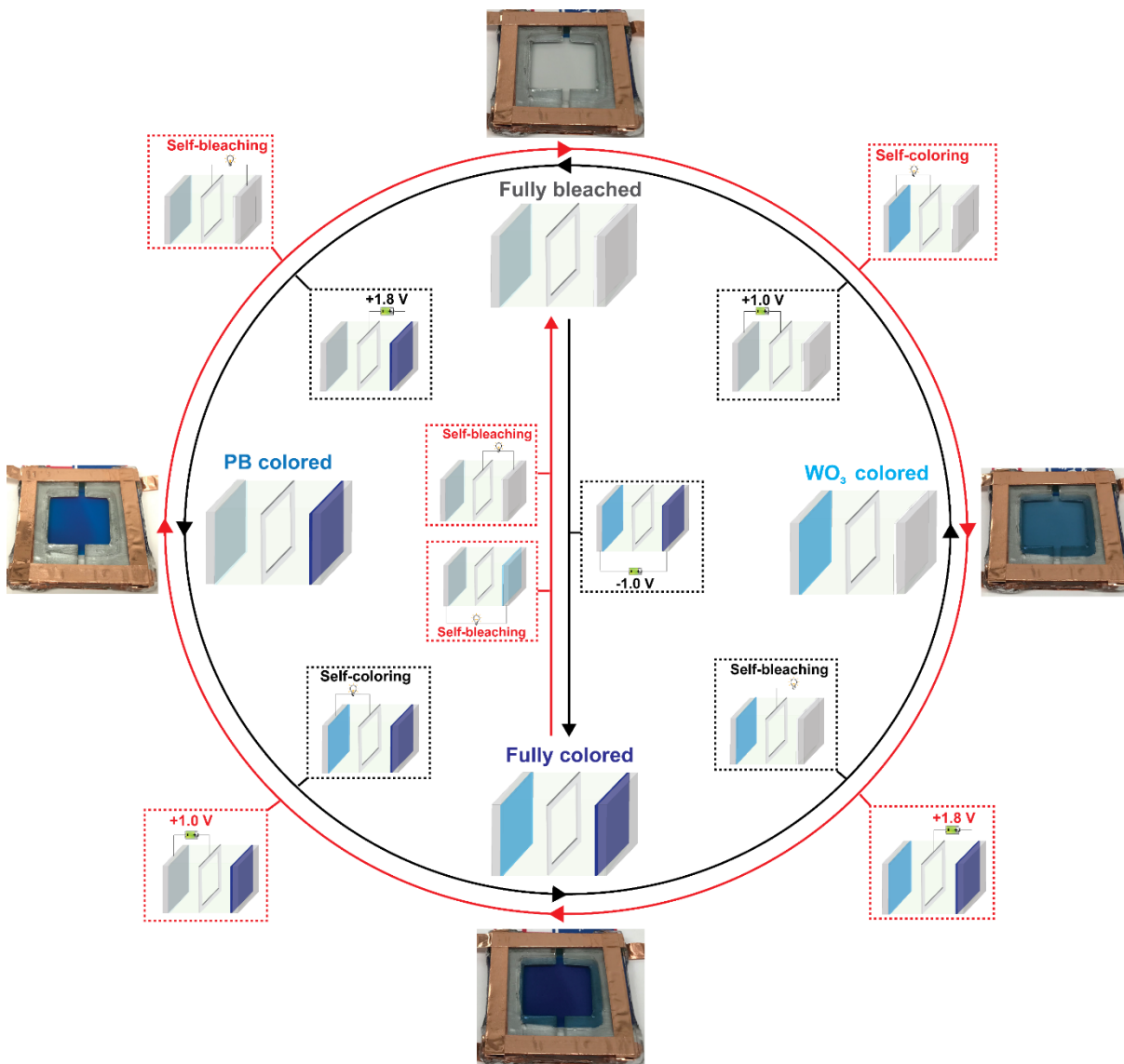


Figure 3.27. The functionalities of the dual-mode electrochromic device with digital photographs. The reversible switching of the device (fully colored, fully bleached, PB colored and WO₃ colored) is operated via powering a 0.5 V regulated LED or directly connecting the colored WO₃ and PB electrodes for the discharging process, or through applying an external voltage for the charging process.

Along with the exciting self-coloration and self-bleaching characteristics of the dual-mode electrochromic devices, an additional advantage offered is the enhanced device bistability, featuring a zero-energy consumption while maintaining a colored or colorless state. Such an attribute is a key function of an electrochromic device.²¹ Figure 3.28a and Figure 3.29a depict the optical transmittance change of the PB and WO₃ electrodes, respectively, during 420 s under the open circuit conditions (off voltage after the operation). At a fully discharged state, the optical transmittance contrast is increased by 18.8% for the WO₃ electrode and decreased by 16.2% for the PB electrode, while showing no apparent change for both electrodes at the fully charged state. This self-charging characteristic is a common phenomenon for inorganic electrochromic materials as the intercalated guest ions (e.g., Zn²⁺, K⁺) can be spontaneously extracted from the materials and diffuse into the electrolyte.^{230,233} As such, a conventional complementary type electrochromic device cannot maintain its colored/colorless state after turning off the power supply for a long time.²³⁴ On the other hand, the zinc anode-based electrochromic device platform exhibits a spontaneous color-switching behavior (i.e., discharging property) due to the high value of redox potential difference between the zinc metal anode and the electrochromic cathode. In other words, the extracted guest Zn²⁺ or K⁺ ions can be spontaneously re-intercalated into the electrochromic electrode by simply connecting the Zn anode with the electrochromic cathode (Figure 3.28b and Figure 3.29b). Thus, the zinc anode-based electrochromic device platform is able to firmly maintain a fully discharged state without the need for external power input and it can also power an external electronic device. To further shed light on the device bistability, the open circuit potentials (OCP) between the Zn anode and the WO₃/PB cathodes were measured and displayed in Figure 3.28c and Figure 3.29c, respectively. As shown in Figure 3.29c, in a bleached state (WO₃ charged state), the high OCP value between the Zn anode and the WO₃ cathode provides the

driving potential that activates the oxidation of Zn (i.e., stripping of Zn into the electrolyte) and the reduction of the WO_3 electrode (i.e., intercalation of K^+ into WO_3), and through this color-switching mechanism, electrical energy is spontaneously supplied. On the other hand, in the colored state (WO_3 discharged state), the OCP value gradually increases with time. It is realized by the intercalated guest ions (e.g., K^+) that are spontaneously extracted from the WO_3 electrode and diffuse into the electrolyte, thus increasing OCP. By connecting the Zn anode with the electrochromic cathode, the dual-mode device is able to maintain its discharged color state and also supply electrical energy to an external load (Figure 3.28b and Figure 3.29b). While the aforementioned results are remarkable for electrochromic devices, they warrant further investigation of the cycling durability of this device. As depicted in Figure 3.28d and Figure 3.29d, the capacity of the PB electrode (in a device platform) remained nearly constant for 1000 cycles, while the WO_3 electrode maintains 50.5% of its initial capacity after 1000 cycles.

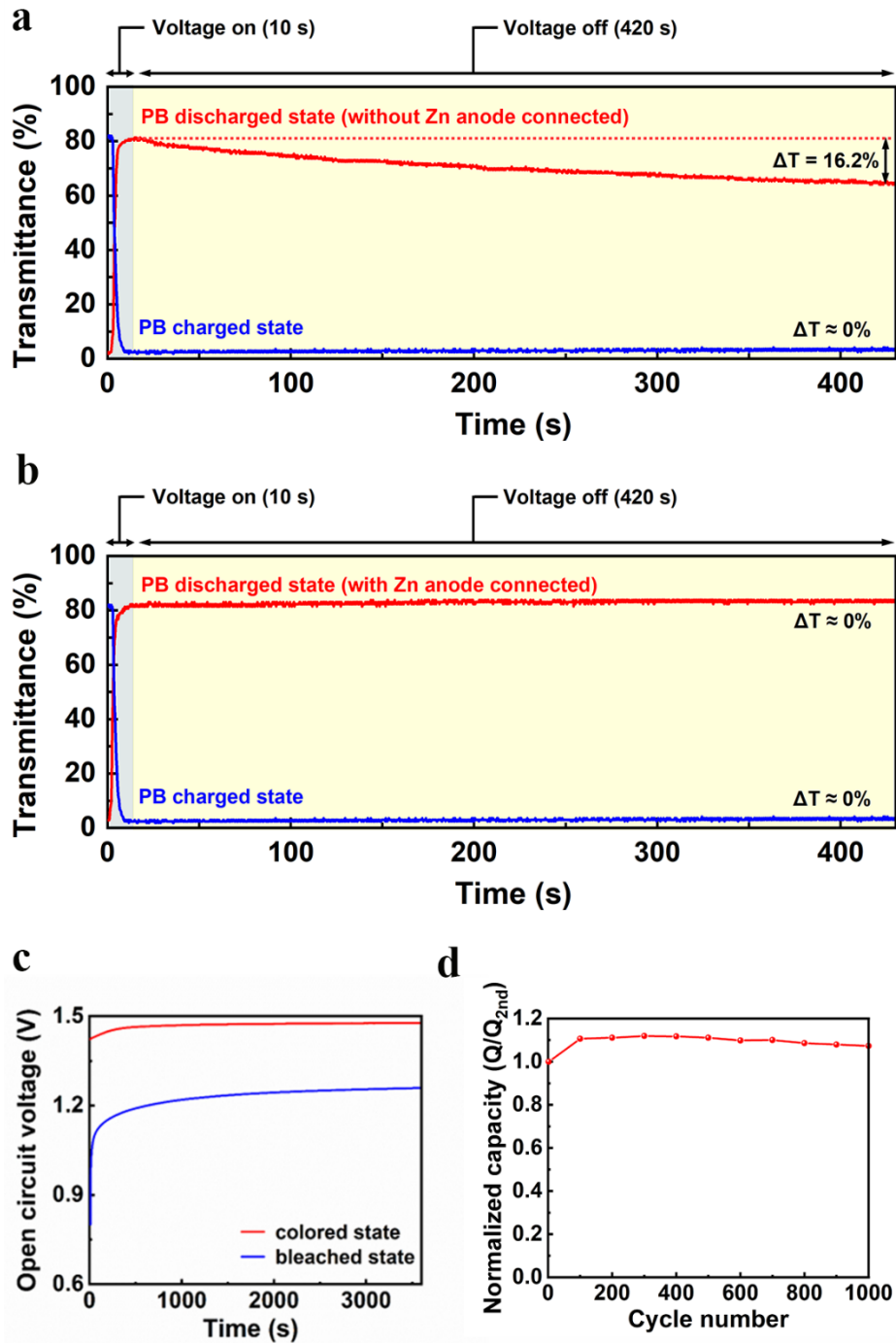


Figure 3.28. Optical transmittance changes of the PB electrode monitored at a wavelength of 632.8 nm during open-circuit conditions after being operated at 1.6 V and 0.8 V for 10 s, respectively, a) without Zn anode connected after cut-off and b) with Zn anode connected after cut-off. c) Open circuit potential between the Zn anode and the PB electrode at different color states. d) Cycle performance of the PB electrode in a device platform.

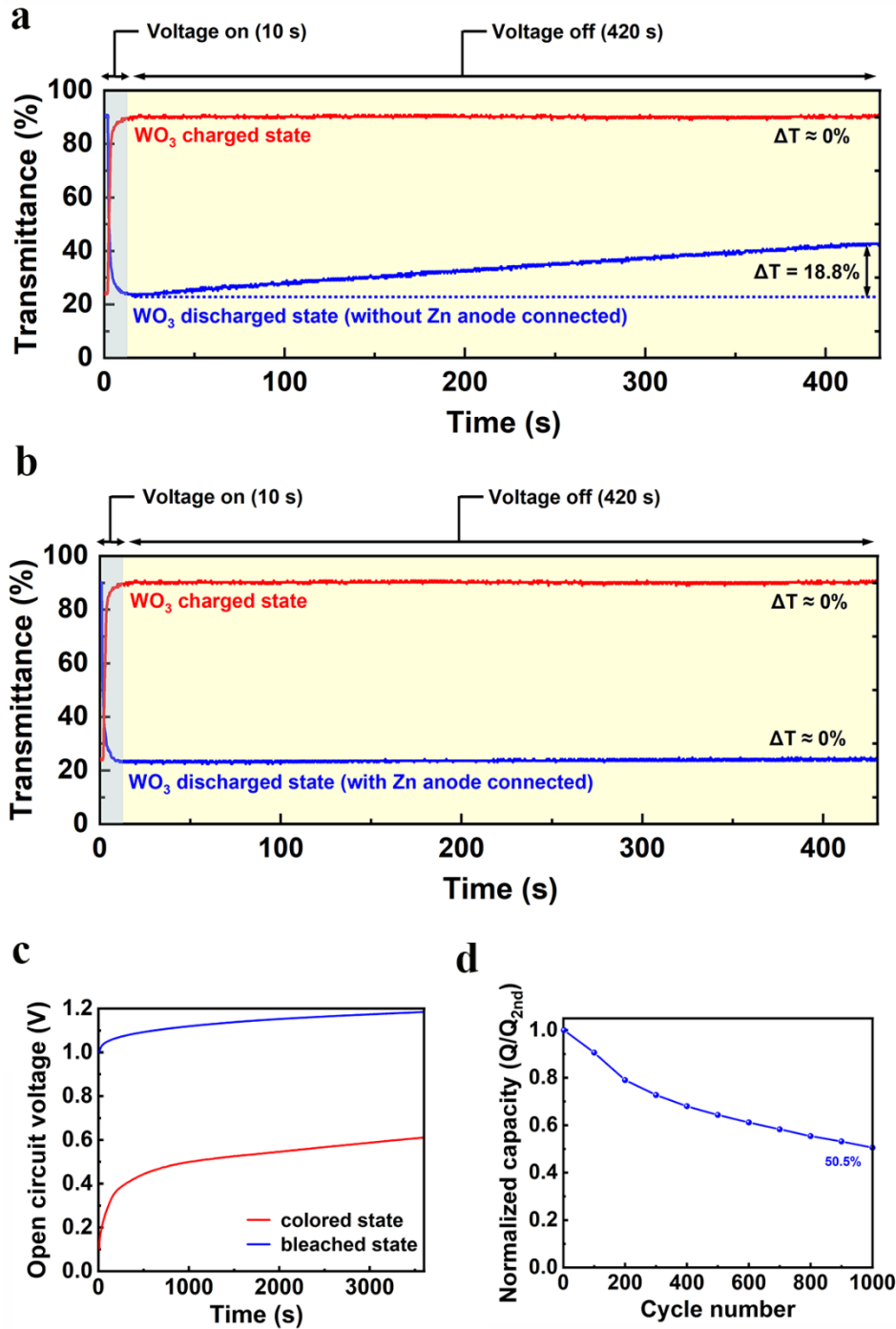


Figure 3.29. Light transmittance changes of the WO₃ electrode monitored at a wavelength of 632.8 nm during open-circuit conditions after being operated at 1.0 and 0.1 V for 10 s, respectively, (a) without Zn anode connected after cut off and (b) with Zn anode connected after cut off. c) Open circuit potential between the Zn anode and the WO₃ electrode at different color states. d) Cycle performance of the WO₃ electrode in a device platform.

3.4.5 Summary

In summary, a dual-mode electrochromic device having both self-coloring and self-bleaching operations is demonstrated via coupling the zinc anode-based electrochromic platform into a rocking-chair type electrochromic device. It is demonstrated that the zinc anode-based electrochromic platform induces a self-color-switching behavior, reduces the energy consumption during operation, enables the independent operation of a single electrochromic electrode, also augments the bistability of the devices. By employing a hybrid electrolyte system of $\text{Zn}^{2+}/\text{K}^+$, the colored PB- WO_3 rocking-chair type device is shown to be capable of spontaneously bleaching by utilizing the redox potential difference between the anodic and cathodic electrodes. Such a dual-mode light-control strategy enables the electrochromic devices to possess four distinct optical states exhibiting a high optical contrast of 72.6% and fast switching times (less than 5 s for the bleaching/coloration processes).

3.5 Summary of zinc anode-based electrochromic devices

In this chapter, the critical components and the system of zinc anode-based electrochromic devices are discussed. Compared to complementary electrochromic devices, ZECs exhibit a rapid spontaneous switching behavior due to the high value of redox potential difference between a metal anode and an electrochromic cathode, thus enabling an energy retrieval functionality. Moreover, ZECs enable multicolor displays with tunability in the two-dimensional CIE color space, leveraging the color overlay effect to expand the available color palettes by adjusting coordinates in the two-dimensional CIE color space. Furthermore, a dual-mode electrochromic device having both self-coloring and self-bleaching operations is demonstrated via coupling the zinc anode-based electrochromic platform into a rocking-chair type electrochromic device. It is demonstrated that the ZEC platform induces a self-color-switching behavior, reduces the energy consumption during operation, enables the independent operation of a single electrochromic electrode, also augments the bistability of the devices.

Chapter 4

Plasmonic-based electrochromic devices

4.1 Introduction

In this chapter, the demonstrations of the manipulation of plasmonic silver adatoms through reversible metal deposition are presented for dynamic light modulation. The voltage-activated reversible silver nanoparticles deposition enables a wide range of dynamic plasmonic color change, and also facilitates a size and shape control of the grown silver nanoparticles. The silver nanoparticles interact with visible light through localized surface plasmon resonance (LSPR), the size and shape of the particles affect their optical properties. This platform showcases a promising approach for dynamic color displays. A version of this concept has been published in: Zhang, W.; Li, H.; Elezzabi, A. Y. “Manipulating silver adatoms for aqueous plasmonic electrochromic devices.” *Advanced Materials Interfaces*, 9, 202200021 (2022).

We further demonstrate a novel concept for solar-regulated dynamic windows by depositing thin films of gold on glass substrates to serve as transparent conductive electrodes. Through precise control of reversible silver metal deposition, a dual-band dynamic window is realized, enabling independent regulation of both visible light and near-infrared radiation. The developed platform not only has the potential to reduce building energy consumption but also maintains optimal indoor lighting conditions. A version of this concept has been prepared in: Zhang, W.; Li, H.; Elezzabi, A. Y. “Spectral-selectively modulation of solar heat and light through dynamic windows coupled ultrathin Au film with reversible Ag electrodeposition.” Under Review (2024).

4.2 Manipulating silver adatoms for aqueous plasmonic electrochromic devices

4.2.1 Introduction

Amongst the electrochromic devices, those that incorporate plasmonic nanomaterials are by far the most intriguing. Through electrochemical control from the application of voltage stimuli, dynamic color displays, generated by noble metal nanoparticles (e.g., Ag, Au), have been realized in a variety of platforms.^{100,235-237} This class of electrochromic devices not only can switch between multiple colors but also retains their colored states without the need for external electrical power.²³⁸⁻²⁴¹ While the electrochromic displays, based on organic molecules,^{242,243} polymers,²⁴⁴⁻²⁴⁶ or transition metal oxides,^{15,37,108,247} have demonstrated multicolor characteristics, these devices exhibit inferior cycling stability compared to reversible metal deposition (RME).²⁴⁸⁻²⁵⁰ Such a limitation hindered their practical applications and their potential commercialization. With the advancement of nanofabrication processes of various plasmonic metal nanostructures, the coming age of electrochromic RME plasmonic high-resolution color displays is appearing on the near horizon.²⁵¹⁻²⁵³

Recently, Ag nanoparticles, having tunable nanostructures, along with their localized surface plasmon resonance (LSPR), have been investigated for multicolor electrochromic films.^{100,238,254} Compared to the nonmetallic-based electrochromic materials, whose optical indices are altered through ions intercalation or redox reactions,^{7,181,204} various LSPR color bands are tuned by manipulating the size and shape of the Ag nanoparticles.^{239,255} However, to realize stable and reversible Ag nanoparticles electrodeposition, these LSPR-based electrochromic displays are administered in non-aqueous electrolyte environments that require high electrodeposition

voltage.^{100,238,239} As such, this platform is far from being energy-efficient and reliable, especially when considering large-area displays.²² Notably, for a wide scope of applications, it is highly desirable to have a dynamically reconfigurable plasmochromic device operating at a safe low voltage window (i.e., aqueous electrolyte compatible platform)^{256,257} while also offering precise manipulation of Ag adatoms to prevent nucleation and growth on the displaying substrate.

To circumvent these challenges, an underpotential metal electrodeposition process (UPMD) needs to be explored as a candidate to precisely manipulate the growth of Ag atoms at the interface between a substrate and the electrolyte. The UPMD process occurs as a result of the strong adatom/substrate adsorption between the electrodeposited metal and the solid substrate.²⁵⁸ The reduction of a metal cation can be achieved at a low voltage, where metal adatoms and adlayers are formed on the solid substrate at a potential that is positive relative to the metal's equilibrium (i.e., Nernst) reduction potential.^{258,259} When compared to the high deposition voltage in a non-aqueous electrolyte, the low voltage of the underpotential deposition is compatible with aqueous electrolytes, as such, underpotential deposition of Ag is highly desirable for operational safety, low production costs, and rapid switching speeds of plasmonic electrochromic devices.

In this section, we investigate an aqueous Ag plasmonic electrochromic device based on the manipulation of Ag adatoms through a reversible plasmonic silver underpotential deposition. We show that size-tunable Ag nanostructures can be grown onto a conducting indium tin oxide (ITO) glass substrate at an operation voltage as low as -0.5 V and can be efficiently dissolved at 0.5 V. Furthermore, we demonstrate that the ITO electrode is able to display various plasmonic colors resulting from the resonant interactions between light and the Ag nanostructures which can be manipulated via voltage-induced size and shape control.

4.2.2 Underpotential deposition of Ag nanoparticles

To elucidate the basic operation of this Ag-based electrochromic device platform, its working principle is illustrated in Figure 4.1a. Here, the Ag foil serves as an anode, while an ITO glass substrate serves as a cathode. During the coloration process, the Ag anode is oxidized ($\text{Ag} \rightarrow \text{Ag}^+$) and the Ag^+ ions are reduced and grown onto the surface of the ITO electrode, forming a thin film of Ag nanoparticles. As a result, the grown Ag thin film on the ITO electrode triggers a coloration of the device due to the LSPR of Ag nanoparticles. Conversely, during the bleaching process, the Ag nanoparticles are dissolved from the ITO electrode and the Ag^+ ions are plated onto the Ag anode ($\text{Ag}^+ \rightarrow \text{Ag}$). The processes of plasmonic Ag nanoparticles growing (coloring) and dissolving (bleaching) allow the ITO electrode to exhibit reversible color switching.

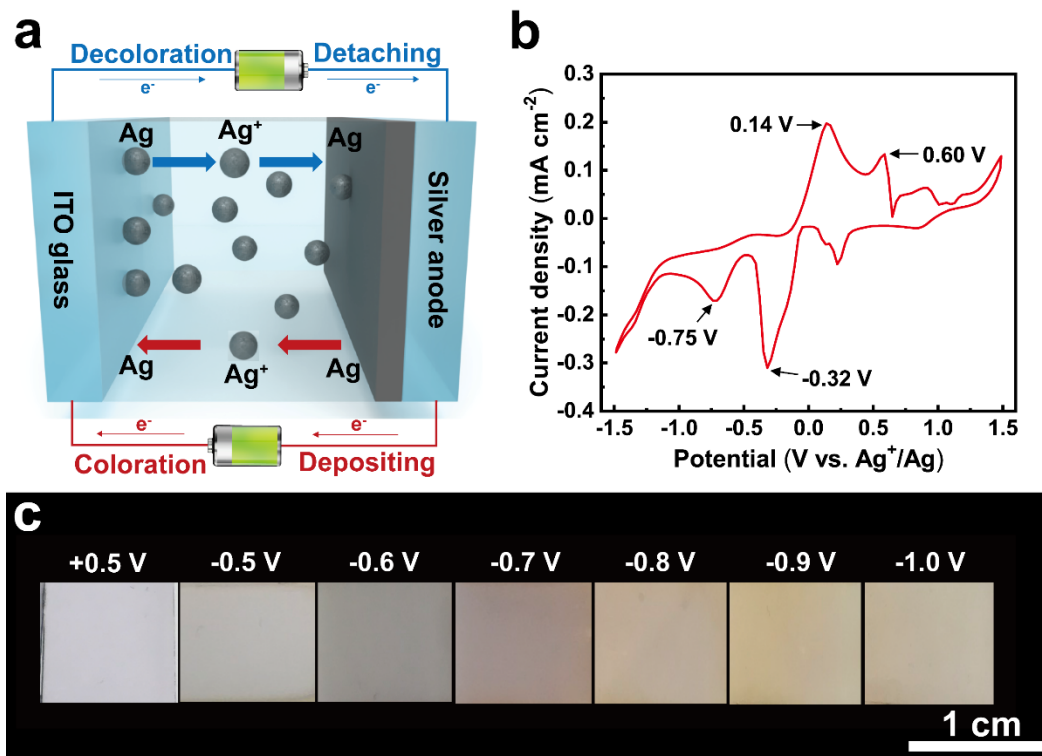


Figure 4.1. The working mechanism of the Ag-based electrochromic devices. (a) Schematic illustration of the Ag-based electrochromic device platform showing the Ag nanoparticles growing (dissolving) processes onto (from) the ITO electrode. (b) CV curve of the ITO electrode taken at a scan rate of 20 mV s^{-1} over a voltage range of $-1.5 - 1.5 \text{ V}$. (c) Digital images of the ITO electrodes under different applied voltages.

To facilitate the underpotential deposition of Ag nanoparticles onto the ITO electrode, we developed an electrodeposition method using an electrolyte solution consisting of 1 mM AgNO_3 and 50 mM LiClO_4 in distilled water (see Appendix D, the Method section). The Ag nanoparticles growing (dissolving) processes onto (from) the ITO electrode were evaluated by cyclic voltammetry (CV) in the modified electrolyte. As shown in Figure 4.1b, the primary pair of reduction and oxidation peaks (at -0.32 and 0.14 V) observed in the CV curve are signatures of the reversible growing/dissolving processes of the Ag nanoparticles. Remarkably, the -0.32 V , required for the growth of Ag nanoparticles, is 2.5 times less than the Nernst potential for the reduction of Ag^+ (i.e., -0.8 V), as such confirming the underpotential deposition of Ag

nanoparticles. The second reduction peak appears at -0.75 V. This -0.75 V is close to the Nernst potential for the reduction of Ag^+ (i.e. -0.8 V). Thus, this peak is due to the standard reduction of Ag^+ . When the applied negative voltage is larger than -1.0 V, Ag nanoparticles are deposited onto the substrate surface in a fast manner. However, the -1.0 V is unfavorable for the growth of uniform nanoparticles (A detailed discussion for the formation of Ag nanoparticles under various applied voltages is demonstrated in section 4.2.3). For the oxidation process, the peaks are almost paired to the peaks during the reduction process. These peaks correspond to the plating of Ag^+ ions onto the Ag anode and the detachment of Ag nanoparticles from the ITO electrode. In a controlled electrodeposition process (i.e., without the LiClO_4 additive), the CV curve (Figure 4.2a) exhibits no obvious reduction peak. However, the addition of a trace amount of LiClO_4 to the electroplating solution facilitates the underpotential deposition of Ag nanoparticles (Figure 4.1b). This is attributed to the fact that LiClO_4 serves as a supporting electrolyte that enhances the ionic conductivity of the electrolyte.²⁶⁰ Figure 4.1c shows digital images of the ITO electrode activated at different applied voltages. The various plasmonic colors obtained at different depositing voltages (from -0.5 V to -1.0V) are attributed to the formation of the different size Ag nanoparticles. The marked high stability and reversibility of such an underpotential deposition process is supported by the unchanged shape and enhanced capacitance of the CV curves for 1000 CV cycles (Figure 4.2b). The enhancement of capacitance during CV cycling is a result of increased Ag^+ concentration in the electrolyte as the Ag leaches from the abundant Ag anode.²⁶¹

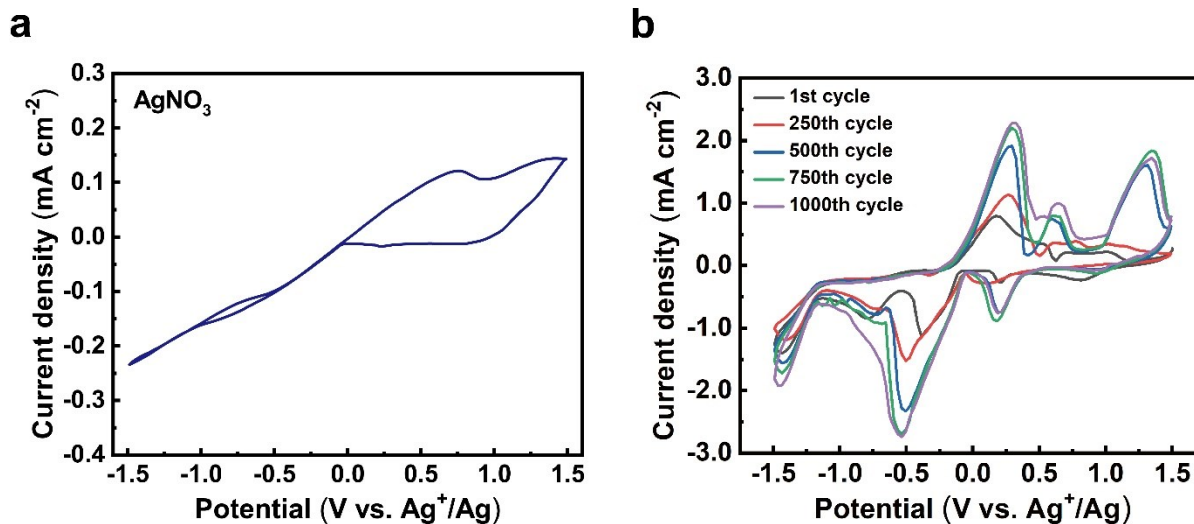


Figure 4.2. (a) Cyclic voltammetry (CV) performance of the ITO electrode at a scanning rate of 20 mVs^{-1} in 1 mM AgNO_3 (b) CV of the ITO electrode at a scanning rate of 50 mV s^{-1} for 1000 cycles.

4.2.3 Size and shape control of Ag nanoparticles

To shed light on the generation of the observed plasmonic colors at various voltage activations (i.e., -0.5 V to -1.0 V), Field Emission Scanning Electron Microscopy (FE-SEM) images and the corresponding extinction spectra of the ITO electrode, are presented in Figure 4.3. When the applied negative voltage is increased from -0.5 V to -0.8 V (Figure 4.3(a-d)), the Ag nanoparticles shrink in size and grow uniformly on the ITO substrate. The size shrinkage is due to the fact that the slightly larger deposition voltage (but less than the Nernst potential for the reduction of Ag^+) allows for more nucleation sites to be formed and, thus, leading to a relatively high density of the Ag nanoparticles.²³⁹ The uniform growth of the nanoparticles under an appropriate deposition voltage is caused by the underpotential deposition of Ag where the low applied voltage suppresses adatoms aggregation.²⁶² That is, decreasing the applied potential results in a lower flux of the adatoms deposited onto the substrate surface and fewer small nucleation sites are formed. This results in a slow formation of the Ag nanoclusters by decreasing the probability of adatom

aggregation.^{263,264} On the other hand, as the applied negative voltage is increased from -0.8 to -1.0 V (Figure 4.3(d-f)), the Ag nanoparticles begin to cluster to form larger Ag nanoparticles while having a sparse distribution of small Ag nanoparticles. This is attributed to the fact that the high applied voltages (i.e., higher than the Nernst potential for the reduction of Ag metal of -0.8 V) are unfavorable for the growth of uniform nanoparticles. That is, increasing the applied potential results in a higher flux of adatoms deposited onto the substrate surface which leads to a fast formation of clusters where adatoms aggregate to form larger particles.^{263,264}

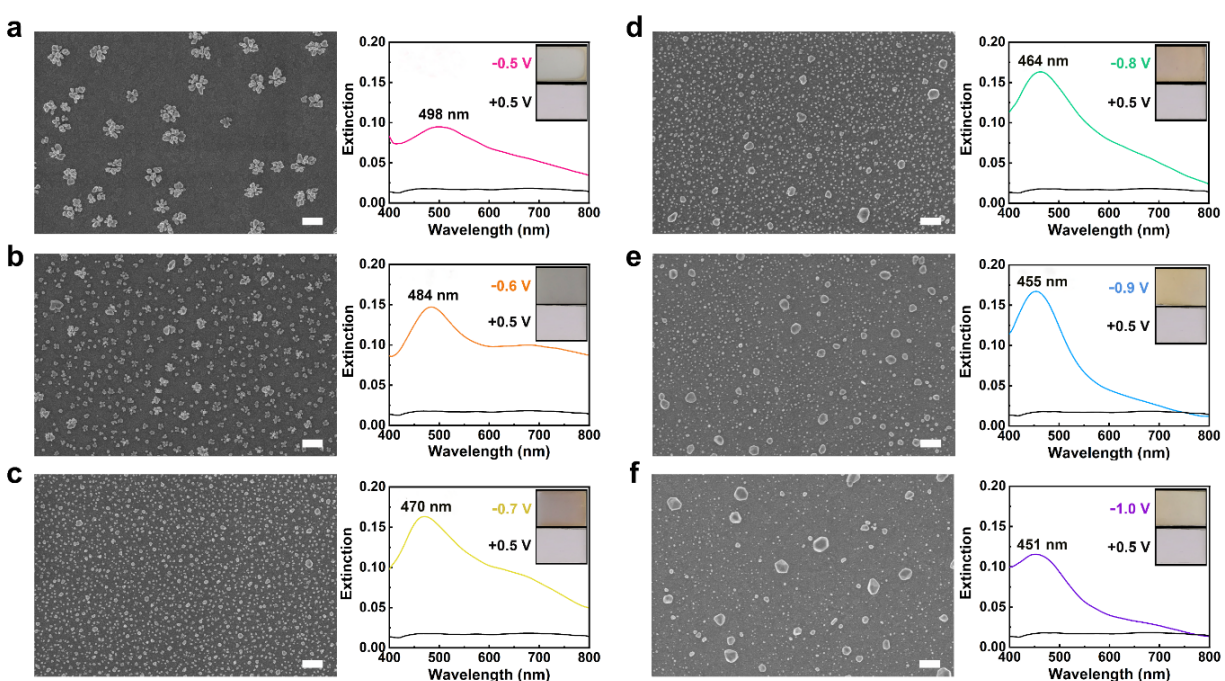


Figure 4.3. FE-SEM images and the corresponding extinction spectra of the Ag nanoparticles grown on ITO electrode under different applied voltages: (a) -0.5 V (b) -0.6 V (c) -0.7 V (d) -0.8 V (e) -0.9 V and (f) -1.0 V. The inset panels are digital images of ITO electrodes under corresponding applied voltages, where the Ag nanoparticles are grown on ITO electrodes under different applied voltages (top) and released of the ITO electrodes at +0.5 V (bottom). Scale bars: 400 nm.

Meanwhile, the corresponding extinction spectra of the ITO electrode activated from -0.5 V to -0.1 V (Figure 4.3(a-f)) reveal the blue-shift of LSPR peaks. A clear blueshift of 47 nm (i.e., from 498 nm to 451 nm) for the LSPR peak of the Ag nanoparticles is observed as the voltage is

tuned from -0.5 V to -1.0 V. Along with the formation of the Ag nanoparticles under different applied voltages, the extinction band arising from LSPR shift results in multiple plasmonic colors. To further understand the effect of the applied voltage on the LSPR peaks, Figure 4.4a illustrates the combined extinction spectra of the ITO electrode at different applied voltages. Along with the blueshift of LSPR peak under different applied voltages (Figure 4.4b), the peak extinction contrasts gradually increase from 0.077 to 0.145 as the voltage is tuned from -0.5 V to -0.8 (Figure 4.4c). This is consistent with the Ag nanoparticle distributions (Figure 4.3(a-d)) where the Ag nanoparticles shrink in size and grow uniformly as the voltage is tuned from -0.5 V to -0.8 V. The observed uniform and homogenous growth of Ag nanoparticles makes the absorption of the LSPR bands relatively narrower, thus, leading to a relatively high color purity and high peak extinction contrasts of the films. Interesting, although the Ag nanoparticles begin to cluster to form larger Ag nanoparticles as the voltage is tuned from -0.8 V to -0.9 V (Figure 4.3(d,e)), there is a slight peak extinction increase from 0.145 to 0.150. This is attributed to the formation of more nucleation sites at high applied voltages. As the voltage is tuned from -0.8 V to -0.9 V, more nucleation sites formed and more Ag nanoparticles grew, although the Ag nanoparticles begin to form slightly larger Ag nanoparticles, the overall performance of Ag nanoparticles leads to a relatively high peak extinction of 0.150 at -0.9 V. However, due to the growth of larger nanoparticles while also having a sparse distribution of small Ag nanoparticles, the observed non-uniform growth of Ag nanoparticles at -1.0 V affects the plasmonic color purity of the films, making the absorption of the LSPR bands relatively broad.²³⁸ Thus, there is a dramatical peak extinction contrast drop at -1.0 V (from 0.150 to 0.100) and no obvious plasmonic color change can be noticed from visible images (Figure 4.3(e,f)).

In comparison to the obvious LSPR peaks of the colored samples shown in Figure 4.3, as a positive 0.5 V was applied, the Ag nanoparticles dissolve from the ITO substrate and the samples exhibit a flat spectrum. As depicted in the FE-SEM image of the ITO electrode at 0.5 V (Figure D-1), the electrodeposited Ag nanoparticles are detached from the ITO electrode, confirming the reversibility of Ag underpotential deposition. Since 0.5 V is a critical voltage within the range between the primary oxidation peak (0.14 V, Figure 4.1b) and the secondary oxidation peak (0.60 V), the choice of 0.5 V allows for a fast and a stable operation of detaching the Ag nanoparticles. In addition, since the 0.5 V potential is within the electrochemical window of aqueous electrolytes, it prevents the decomposition of the aqueous electrolytes.

Ag nanoparticles interact with visible light through LSPR, the size and shape of the particles affect their optical properties. As shown in Figure 4.3(a-f), there is a visible size and shape change of the Ag nanoparticles under different applied voltages. Seen from the SEM images (Figure 4.3(a-f)), most Ag nanoparticles are close to a circular shape in a top view, thus, to statistically evaluate the size and shape change of the Ag nanoparticles, Ag nanoparticles were assumed to be ideal spheres. The average diameter distribution (μ) and the standard deviation (σ) of the nanoparticles were evaluated and shown in Figure 4.4(d-i). The sample numbers (n) of Ag nanoparticles were counted in a random $1 \mu\text{m} \times 1 \mu\text{m}$ area of Ag nanoparticle films. The average diameter distribution and the standard deviation of the Ag nanoparticles were evaluated in Excel. Two-sided confidence intervals (CI) of 68.3% were determined by $\mu \pm \sigma$. The average diameter of Ag nanoparticles gradually decreased from 68.9 nm to 23.6 nm as the applied voltage changed from -0.5 V to -1.0 V. This trend is in good agreement with the extinction spectra where the extinction band arising from LSPR shifts to shorter wavelengths as the Ag nanoparticles decrease in size (Figure 4.4(a,b)).

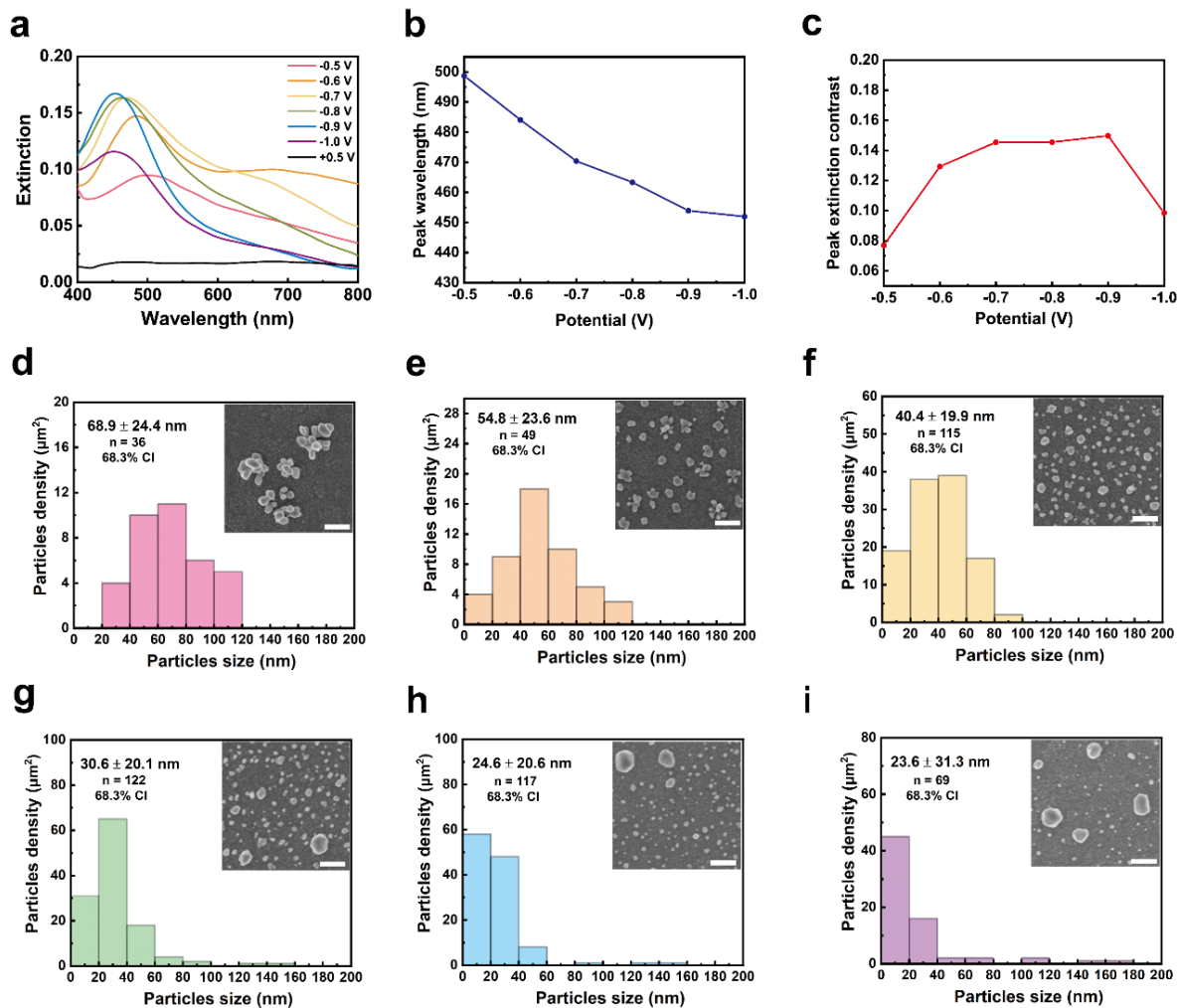


Figure 4.4. The LSPR and size distribution of Ag nanoparticles. (a) Extinction spectra of the Ag nanoparticles grown on ITO electrodes under different applied voltages. (b) Peak wavelength of the extinction spectra from (a) as a function of the applied voltage. (c) Peak extinction contrast of the extinction spectra from (a) as a function of the applied voltage. Distribution of Ag nanoparticles diameter and the standard deviation under different applied voltages: (d) -0.5 V (e) -0.6 V (f) -0.7 V (g) -0.8 V (h) -0.9 V and (i) -1.0 V. Sample numbers (n). Confidence interval (CI): 68.3%. The inset scale bars: 200 nm.

Moreover, as the particles were assumed to be ideal spheres, the diameter's standard deviation, σ , is an important indicative metric of the color purity of the grown films. The high σ of 31.3 nm, as the applied voltage increased to -1.0 V, is consistent with the nonuniform growth of the Ag nanoparticles and a relatively broad LSPR band (Figure 4.3f), whereas at -0.7 V, $\sigma = 19.9$ nm, a

uniform thin film and a relatively narrow LSPR band were observed (Figure 4.3c). Clearly, the underpotential deposition (i.e., voltage < -0.8 V) of the Ag nanoparticles not only reduces the power consumed during operation, but it also facilitates uniform size control of the grown Ag nanoparticles compared to high deposition voltages (> -0.8 V). As such, the precise manipulation of Ag adatoms underpotential deposition enables a relatively high color purity in comparison to the high voltage-induced electrodeposition technique. However, as shown in the SEM images (Figure 4.3(a-f)), the Ag nanoparticles are not identical (same size and shape) at a certain applied voltage. Thus, the colors created by Ag nanoparticles are not absolute pure colors.

4.2.4 Transparent Ag-based plasmonic electrochromic devices

To implement such an innovative Ag-based platform for a dynamic plasmonic color display, a transparent Ag-ITO electrochromic device ($5\text{ cm} \times 5\text{ cm}$) was assembled by combining one piece of a flat ITO glass as cathode and one piece of an Ag anode (Figure 4.5a). A $1\text{ }\mu\text{m}$ thick Ag anode was prepared on a commercial glass substrate and formed as a square frame around the glass substrate by the sputtering/masking techniques. The $\text{AgNO}_3\text{-LiClO}_4$ solution was used as the electrolyte.

Figure 4.5b illustrates the CV curve of the device, where reduction and oxidation peaks are observed at -0.26 V and 0.20 V, respectively. These peaks are signatures of the reversible growing/dissolving of the Ag nanoparticles onto/from the ITO glass. The slight differences from the primary reduction and oxidation peaks (i.e., -0.32 and 0.14 V) observed in the CV curve of a electrochemical measurement utilizing an Ag wire as a counter electrode (Figure 4.1b) is attributed to the area of the counter electrode.²⁶⁵ The Ag underpotential deposition is sensitive to the area of the Ag counter electrode, slight variations in the area can lead to reduction and oxidation peak

shifts. The optical transmittance spectra of the device, taken at different applied voltages, are shown in Figure 4.4c. The spectroscopic measurements for optical transmittance spectra were conducted using an Ocean Optics USB4000 spectrometer, without subtracting the transmission loss due to the substrate. As the applied negative voltage increases from -0.5 V to -1 V, the transmission trough is shown to blueshift from 535 to 460 (i.e., 75 nm shift). The voltage-dependent blueshift is also accompanied by significant optical contrast of 46% at 460 nm.

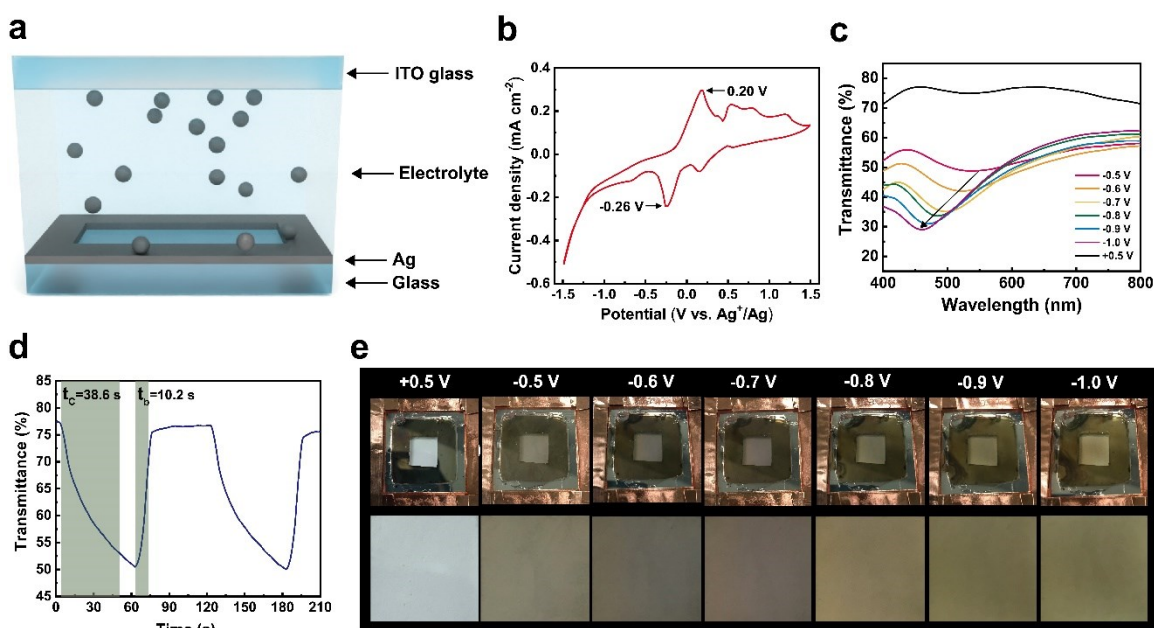


Figure 4.5. Transparent Ag-based electrochromic device. (a) Schematic illustration of the transparent Ag-ITO electrochromic device. (b) CV curve of the ITO electrode taken at a scan rate of 20 mV s^{-1} over a voltage range of -1.5–1.5 V. (c) Optical transmittance spectra of the device at different applied voltages. (d) Dynamic switching times of the device at 632.8 nm in the -1.0-0.5 V window. (e) Digital images of the transparent Ag-ITO electrochromic device at different applied voltages: the full-size device image (top) and the enlarged image (bottom).

The switching times of the device were measured within an applied voltage range between -1.0 V to 0.5 V. As a key parameter when considering the suitability of the device for color display applications, fast switching between the different color states is highly desirable. As shown in Figure 4.5d, the response times, defined as the time required for achieving 90% of maximum

optical contrast,²¹⁰ are measured to be 38.6 s for coloration (at -1.0 V) and 10.2 s for bleaching (at 0.5 V). These response times are comparable to those previously reported electrochromic devices based on metal deposition.^{266,267} Remarkably, the round-trip energy consumption required to switch the device is very low (28.8 mWh m⁻², see Figure 4.6a), which is much lower than that of previously reported electrochromic devices (e.g., ~120 mWh m⁻²).^{11,15,229} This high energy-efficiency of the underpotential deposition process favors such emerging technology for color displays.

Figure 4.5e displays digital images of the transparent Ag-ITO electrochromic device at different applied voltages ranging from -0.5 V to -0.8 V. Following the images in Figure 4.5e from left to right, both the full-size device image (top) and the enlarged image (bottom) attest to the device's color spatial uniformity and tunable characteristic. Notably, when the voltage is increased from -0.8 V to -1.0 V and the corresponding transmittance trough shifts by 20 nm, there is no obvious plasmonic color change. This is attributed to the nonuniform growth of the Ag nanoparticles at high applied voltages (Figure 4.3f), where the plasmonic LSPR absorption becomes broad.

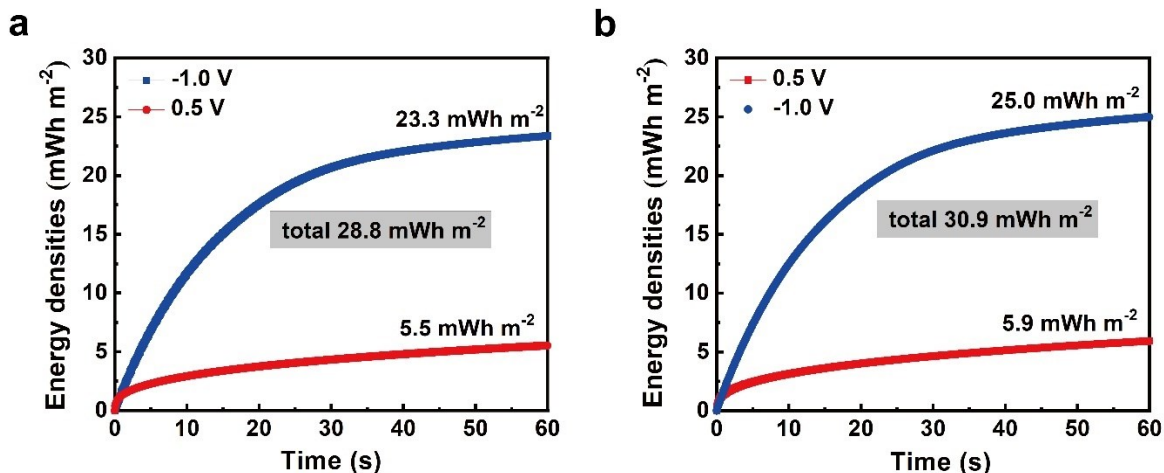


Figure 4.6. (a) Round-trip energy consumption of the transparent-type Ag-based electrochromic devices. (b) Round-trip energy consumption of reflective-type Ag-based electrochromic devices.

4.2.5 Reflective Ag-based plasmonic electrochromic devices

It is of great interest to explore further capabilities of Ag-based platform as a reflective-type electrochromic device. Here, a 5 cm × 5 cm reflective-type Ag-ITO electrochromic device was assembled by incorporating a transmissive ITO cathode and a reflective Ag anode (Figure 4.7a). The Ag anode was prepared on a commercial glass substrate by sputtering 1 μm thick Ag film. The AgNO₃-LiClO₄ solution was used as the electrolyte.

Figure 4.7b illustrates the optical reflectance spectra of the device at various applied voltages. Interestingly, as the applied negative voltage increases from -0.6 V to -1.0 V, the reflectance peak gradually blueshifts from 780 to 680 nm while increasing in amplitude. The 100-nm blueshift of the reflectance peak position is higher than the 75-nm blueshift observed from the transparent device. This increase arises from the uniformity of the electrical field spatial distribution between the planer reflective surface of the Ag anode and the ITO cathode which allows for spatially uniform electrodeposition of Ag nanoparticles.²⁴⁹ Depicted in Figure 4.7c, digital images of the device illustrating representative strong plasmonic colors activated at +0.5 V, -0.6 V, -0.8 V, and

-1.0 V. It is important to note that since these colors are triggered by the underpotential deposition of Ag nanoparticles, the reflective-type Ag-ITO electrochromic device is also energy efficient since device consuming only 30.9 mWh m^{-2} in a round-trip energy (e.g., Figure 4.6b).

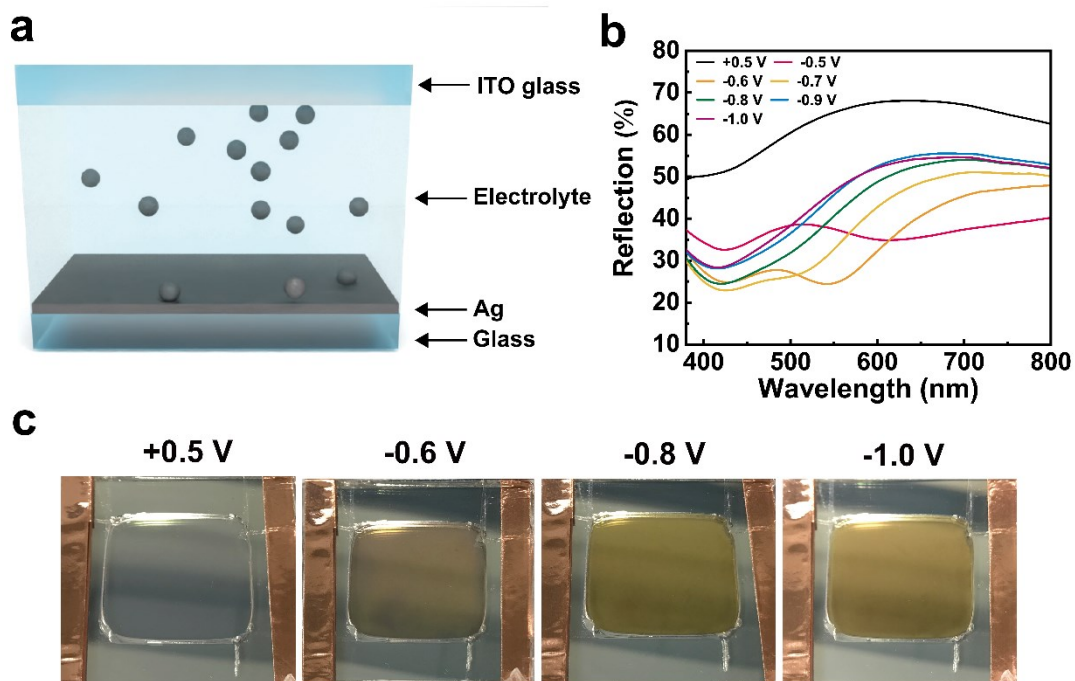


Figure 4.7. Reflective Ag-based electrochromic devices. (a) Schematic illustration of the reflective Ag-ITO electrochromic device. (b) Optical reflectance spectra of the device at different applied voltages. (c) Digital images of reflective Ag-ITO electrochromic device at different applied voltages.

4.2.6 Summary

In summary, for the first time, an energy-efficient aqueous-based multicolor plasmonic electrochromic devices were demonstrated via manipulating silver adatoms through an underpotential deposition technique. The underpotential deposition technology not only reduces the energy consumption during operation, but also facilitates a uniform size control of the grown Ag plasmonic nanoparticles. Such a strategy enables wavelength color shift of ~100 nm for both transmissive-type and reflective-type devices. The underpotential deposition is easily adaptable for fabricating different sizes of plasmonic Ag nanoparticles, which provides a novel platform for rapid, scalable, and green preparation of plasmonic nanoparticles.

4.3 Spectral-selective dynamic windows: a new horizon in light and heat management technologies

4.3.1 Introduction

Keeping indoor temperatures at a comfortable level demands a lot of energy. This results in a considerable amount of energy usage nationwide. For example, in the United States, about 20% of the total energy consumption is for this purpose, and in other developed countries, it can be as high as 40%.²⁶⁸ Notably, windows constitute a substantial fraction of a building's external surface, making them a key source of energy loss. In the colder months, a significant amount of heat is lost through windows. This loss accounts for approximately 25% to 30% of total heat loss in the US and between 40% to 50% in northern China.²⁶⁹ Conversely, in warmer months, windows allow unwanted near-infrared solar energy to penetrate, thus, burdening the cooling systems. The combined energy demands of heating, ventilating, and air conditioning (HVAC) systems account for around 50% of building energy consumption.²⁷⁰ To address these losses, dynamic windows have emerged as a promising avenue for research and development over the past few decades, aiming to enhance energy efficiency and occupant comfort.

Dynamic windows offer a potential energy-saving solution, boasting an average of 20% reduction in energy consumption through adjustable tint that decreases lighting, heating, and cooling requirements.²⁷¹ Unlike passive technologies, such as low-emissivity coatings and radiative coolers, which can curtail energy usage under specific conditions but lack adaptability to dynamic (diurnal and seasonal) variations,^{272,273} dynamic windows are well-suited for future energy-efficient building envelopes. Among these, electrochromic smart windows stand out as one of the most advanced and effective technologies. Leveraging redox reactions, these smart windows

enable reversible control of optical transmission through ion accumulation or depletion in the active layer, responding to an electric field between two transparent conductive electrodes.^{1,12} Notably, the reversible metal electrodeposition (RME) approach, where a solid metal thin film grows on a transparent electrode and metal ions dissolve into an electrolyte,^{274,275} has proven its superiority in overcoming cost, contrast, scale, and durability challenges that have hindered wider adoption of other electrochromic technologies based on transition metal oxides,^{15,39,276} polymers²⁷⁷ or small molecules.²¹

However, despite these advancements, the majority of RME research has concentrated on modulating dynamic windows' transmission within the visible light range (typically 400 to 800 nm),^{249,278} primarily involving transitions between transparent and opaque states. Furthermore, the widespread application of these windows for regulating near-infrared (NIR) light proves challenging due to commonly employed transparent conductive electrodes such as ITO (indium tin oxide) or FTO (fluorine-doped tin oxide) glasses.^{7,36} Unfortunately, both ITO and FTO films strongly absorb near-infrared radiation,^{279,280} rendering such windows platforms incapable of entire solar spectrum control. Previous attempts to address this challenge have explored replacing ITO/FTO glasses with polymer-based conductive electrodes,^{281,282} but such substrates sacrifice the durability of glass inherent in dynamic windows. Furthermore, a significant hurdle faced by RME-based dynamic windows lies in their inability to independently regulate visible light and near-infrared radiation. Beyond mere transparency and opacity modulation, the ability to independently control visible light and near-infrared radiation could introduce an additional window state – one that solely modulates NIR radiation. If put into practice, this method could reduce energy consumption in buildings while preserving indoor lighting. Despite efforts, the RME dynamic windows developed to date have yet to show dual-band modulation of visible and near-infrared

transmittances across the solar spectrum, largely due to limitations posed by the transparent conductive substrates and the electrolytes.

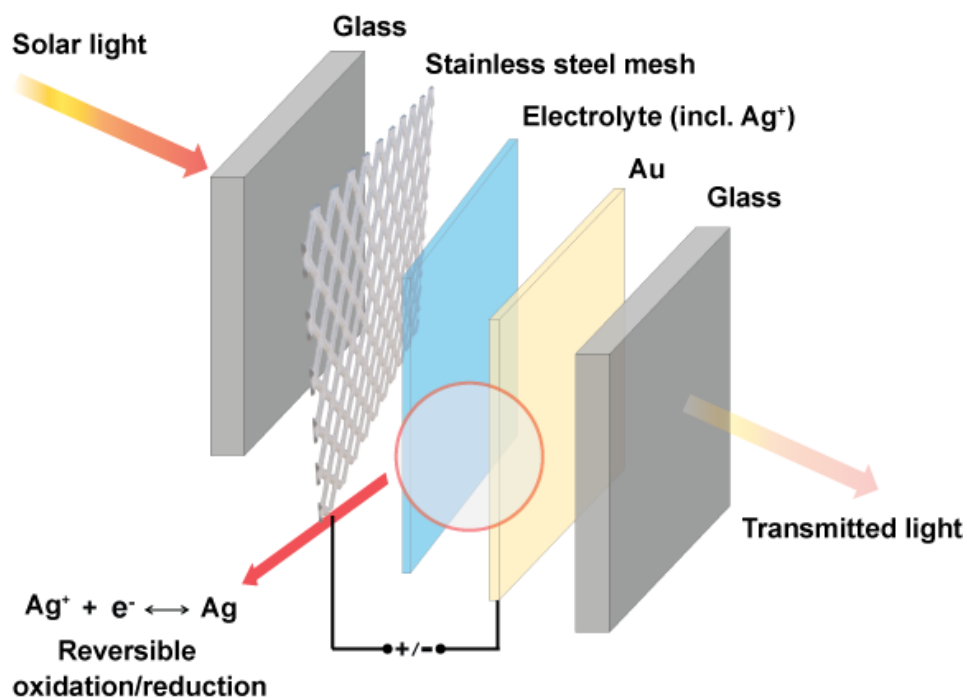


Figure 4.8. Schematic diagram illustrating the solar-regulated dynamic window basic components. The gel electrolyte containing Ag^+ is sandwiched between an Au-coated glass electrode and a stainless-steel-mesh (SSE) mounted glass electrode. During the electrodeposition process, by applying a cathodic potential between the two electrodes, a solid thin Ag film of plates on the Au/glass electrode and blocks light. Conversely, by applying an anodic potential, Ag dissolves back into the electrolyte and the window is bleached.

In the realm of research and technology, gold emerges as an especially important metal due to its chemical inertness, high conductivity, high work function, and noteworthy plasmonic properties.^{181,283} With the advancement of thin-film deposition methods that allow for ultra-thin thickness control,²⁸³ there has been considerable technological interest in creating ultra-thin gold films on glass substrates and understanding their optical behaviour. This interest extends to applications, such as transparent electrical contacts, optical metamaterials, and nanoplasmonic devices.^{181,284} Consequently, the notion of depositing thin films of gold on glass substrates to serve

as transparent conductive electrodes for creating exceptional dynamic windows has gained traction (see Fig. 4.8). However, the chemical inertness of gold impedes the potential for reversible metal deposition. In a similar vein, silver emerges as a noteworthy plasmonic material that has garnered considerable attention for photonic applications.^{238,284} Unlike gold, the RME of silver can be controlled within a low voltage range, owing to silver's low standard redox potential (-0.8 V).²⁸⁵ Moreover, gold can serve as a catalyst to surmount kinetic barriers to the reduction of Ag⁺ ions, thus, facilitating the electrodeposition of silver.²⁸⁶

In this section, we investigate a novel concept for solar-regulated dynamic windows by depositing thin films of gold on glass substrates to serve as transparent conductive electrodes. By employing a reversible silver metal deposition technique, we present a dual-band dynamic window capable of independent regulation of visible light and near-infrared radiation. This versatility allows for operation in three distinct modes: bright mode, light mode, and dark mode.

4.3.2 Mechanism of selective modulation of visible and NIR lights

To elucidate the operation of this solar-regulated dynamic window, thin films of gold of varying thicknesses are deposited on glass substrates. A deposition rate of about 0.2 Å/s and a base pressure of around 2×10^{-6} mbar were used. The thickness during deposition was recorded with a calibrated QCM (quartz crystal microbalance) detector (see Appendix E, the Method section). In this study, we describe in detail the initial growth phases of ultrathin Au films through scanning transmission electron microscopy (SEM) observations, and we identified the structural evolution from quasi-zero-dimensional (0D) nanodroplets to quasi-2D thin films in the initial growth stage (Fig. 4.9a,b). The ideal initial growth of Au thin films on glass substrates follows four stages (Fig. 4.9a): stage

I, nanodroplet nucleation and lateral growth; stage II, coalescence; stage III, film with irregular holes, and stage IV, homogenous film.

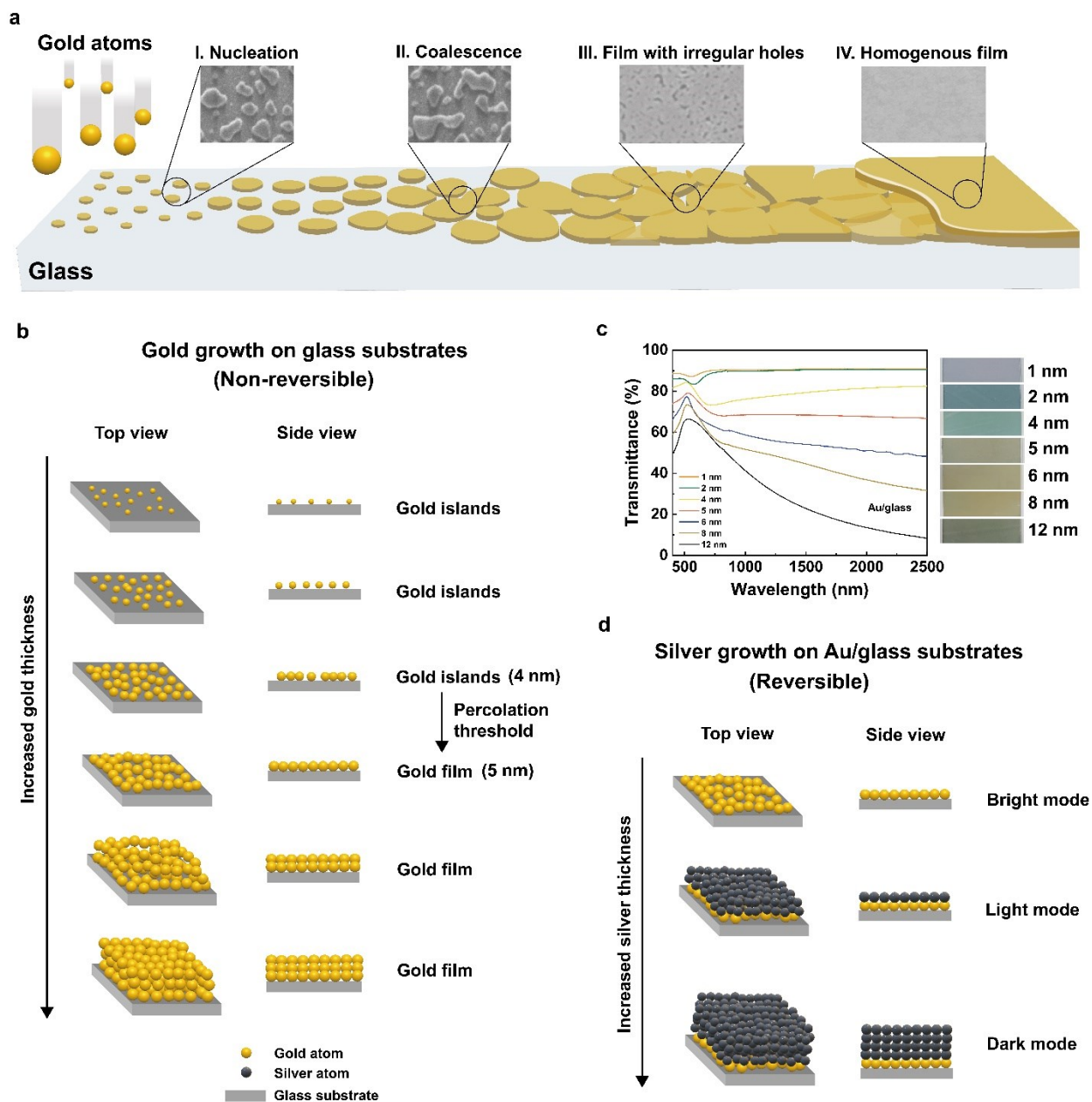


Figure 4.9. Schematic diagram illustrating the selective modulation of the visible and NIR light spectra. (a) Series of schematic diagrams of the structural evolution from quasi-zero-dimensional nanodroplets to a quasi-two-dimensional film. (b) Schematic diagram illustrating the growth of Au on glass substrates (non-reversible). (c) Visible-near infrared transmittance spectra and digital images of the Au/glass electrodes for seven different thicknesses. (d) Schematic diagram illustrating the growth of Ag on 5 nm Au/glass substrates (reversible) which is presented for three distinct operational modes for dynamic windows – bright, light, and dark modes.

Figure 4.9b also illustrates the growth of gold on glass substrates with increasing film thickness. At a deposition thickness below 5 nm, the Au film is composed of small, isolated gold nano-islands. These are tiny isolated clusters of gold atoms, often in the nanometer scale, dispersed across a substrate, rendering the Au film to be nonconductive. The Au nano-islands slightly absorb visible light which appear as a dip in wavelength between 600 and 700 nm due to their LSPR, along with a negligible or slight decrease in NIR transmittance (Fig. 4.9c). Transition to the film's continuity occurs as more Au is deposited and these nano-islands begin to grow and eventually coalesce, or merge. At a film thickness of 4.4 nm marks a transition to a point of the percolation threshold, where there is just enough connectivity between these islands to allow for the continuous flow of electrons across the entire Au film. Beyond the thickness of ~ 5 nm, the film forms a continuous metallic network. This network still retains some of the characteristics of the original nano-islands, like LSPRs, but also exhibits properties typical of bulk gold, such as high electrical conductivity and reflectivity.

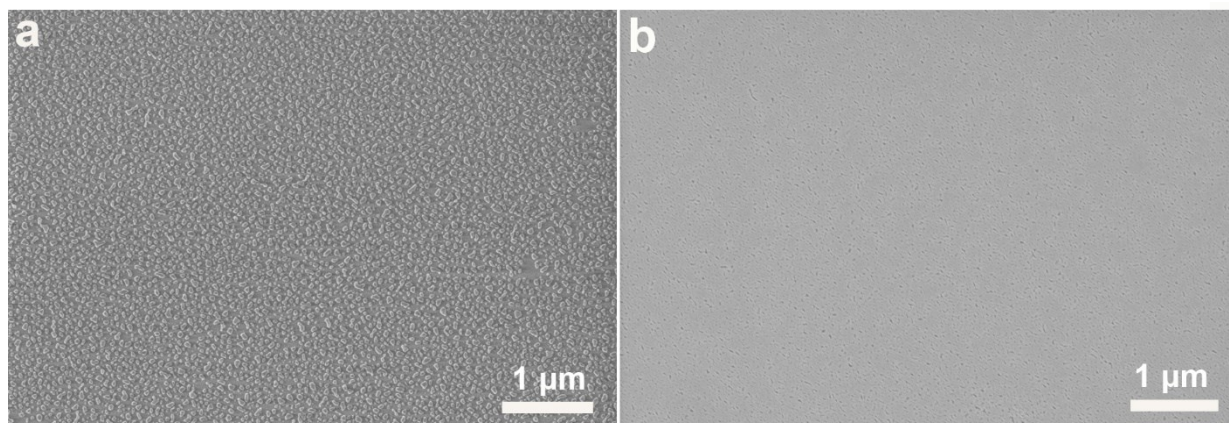


Figure 4.10. FESEM images of the Au films taken at (a) 4 nm and (b) 5 nm.

Table 4.1. Sheet resistance versus transmittance in visible and near-infrared regions of the Au/glass electrodes with seven different thicknesses.

Au (nm) on glass electrodes	Sheet resistance (ohm/sq)	Visible transmittance (632.8 nm)	NIR transmittance (1550 nm)
1	N/A	0.89	0.90
2	N/A	0.85	0.90
4	584	0.76	0.80
5	34.7	0.72	0.68
6	28.6	0.67	0.54
8	23.4	0.64	0.42
12	18.6	0.63	0.21

This transition is observable in the FESEM images of gold films taken at 4 and 5 nm (Fig. 4.10), where discontinuous gold islands evolve into a gold film with irregular holes. This transition is also evident in the sheet resistance measurements of Au films (Table 4.1), indicating a significant decrease in sheet resistance from 584 to 34.7 ohm/sq as the film's thickness increases from 4 to 5 nm, respectively. The sheet resistance of various electrodes was measured by a four-probe resistivity measurement system Pro4 4000. Consequently, the formation of a continuous Au network film leads to flat NIR transmittance (Fig. 4.9c). Figure 4.9c depicts the transmittance spectra of Au/glass electrodes for seven thicknesses, over the wavelength range of 0.4–2.5 μm . The visible-infrared transmittance spectra within a wavelength range of 0.4 to 2.5 μm were measured using a Perkin-Elmer NIR-UV spectrometer. As expected, there is a consistent pattern at NIR wavelengths, namely the transmittance decreases progressively with increasing film thickness. For example, the NIR transmittance decreases from 90% to 23% (at 1550 nm) as the film thickness is increased from 1 nm to 12 nm. This decrease is primarily attributed to the high reflectance of the Au films within the NIR range, along with their morphological transition from being isolated Au nano-islands to cohesive metallic network films.^{283,287} On the other hand, while there is a minor drop in transmittance within the visible light range with increasing film thickness,

the Au/glass electrodes retain a relatively high level of transparency (the visible transmittance decreases from 88% to 63% at 632.8 nm as the film thickness is increased from 1 nm to 12 nm). Since the size of the Au nano-islands (or nanoparticles) varies with the film's thickness, these Au films exhibit wavelength-specific absorptions seen in Fig. 4.9c, due to LSPR absorption. For a comparison, the transmittance spectra of ITO/FTO glasses were also measured in the wavelength range of 0.4–2.5 μm (Fig. 4.11). Notably, the ITO and FTO films absorb heavily in the NIR spectral region, rendering them unsuitable for controlling NIR wavelengths. Notably, for Au film thickness above 5 nm, the NIR transmittance decreases progressively with increasing film thickness, driven by enhanced reflection of gold films in NIR range.²⁸⁷ The findings reveal that the processes of reversible deposition and detachment of Au on glass substrates can effectively regulate the transmittance of solar light within the NIR range while maintaining a notable visible transparency. However, the inherent inertness of Au presents a limitation for its use in reversible metal electrodeposition (RME), hindering its potential in this application.

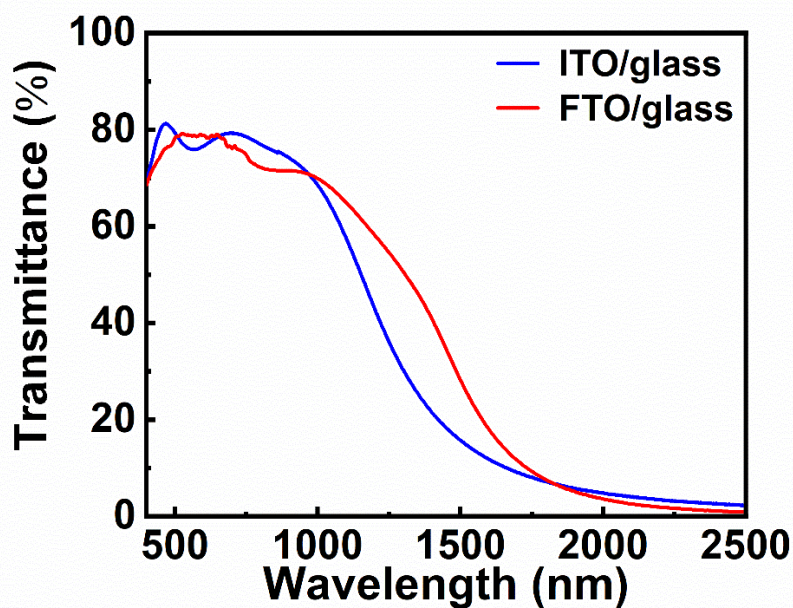


Figure 4.10. Visible-near infrared transmittance spectra of the ITO/FTO glasses.

Unlike gold, the electrodeposition of silver can be controlled within a low voltage range, owing to silver's low standard redox potential (-0.8 V). On the other hand, gold can serve as a catalyst to surmount kinetic barriers to the reduction of Ag^+ ions, facilitating the electrodeposition of silver.²⁸⁶ Therefore, it is expected that the reversible metal electrodeposition (RME) of silver on gold-coated glass electrodes will be a highly effective approach for dynamically regulating the transmission of solar light in the near-infrared (NIR) range. As illustrated in Fig. 4.9d, a thin 5 nm Au film is deposited on the glass substrates, thus providing transparent conductive electrodes for dynamic windows. This 5 nm Au/glass electrode exhibits a sheet resistance of 34.7 ohm/sq (Table 4.1) due to the high electrical conductivity of metallic Au, which is comparable to the sheet resistance of ITO/FTO glasses (typically 10 to 20 ohm/sq). Since both the visible and NIR radiation are transmitted through the glass, this operating condition is known as the bright mode. While it is feasible to apply a thicker Au film (e.g., 6 nm), where the relatively lower sheet resistance of 28.6 ohm/sq at 6 nm facilitates the electrodeposition of silver; however, this comes as a cost of decreasing NIR transmittance. By employing a reversible Ag metal deposition, a thin layer of Ag can be deposited onto this Au/glass electrode, effectively blocking most NIR light. As a result, a new window state is created, called 'Light mode', which specifically adjusts the intensity of the NIR radiation. Intriguingly, as the deposition of the Ag metal is prolonged, the Ag film becomes thicker, effectively blocking most of the visible and near-infrared (NIR) radiation. This results in a dark mode for the dynamic windows. Through precise control of the reversible Ag metal deposition, solar-regulated dynamic windows can switch between these three modes (bright, light and dark modes), allowing for selective modulation of the visible and the NIR light spectrum.

4.3.3 Three-mode solar-regulated dynamic windows

To implement such an innovative three-mode platform for dynamic window applications, a 10 cm × 10 cm window was assembled. This window utilized a 5 nm Au-coated glass as the working electrode and a Ag-coated stainless-steel mesh (Ag-SSE) mounted on glass as the counter electrode (Fig. 4.12a). The gel electrolyte used in the dynamic window was prepared by adding 10 wt% polyvinyl butyral (PVB) in DMSO solution containing 0.05 M AgNO₃ and 0.25 M LiBr. To avoid short-circuiting between the working and counter electrodes, a 2 mm thick 3M double-sided tape was placed as a spacer. The spacer provides the volume for the gel electrolyte. The stainless-steel mesh (50 Mesh, 0.0012" Wire Diameter) was purchased from TWP Inc. The Ag-coated stainless-steel mesh was prepared via an electrodeposition method using a two-electrode configuration, where a piece of Ag foil serves as an anode and the stainless-steel mesh serves as a working electrode. The electroplating solution was prepared by mixing 0.05 M AgNO₃ and 0.25 M LiBr in dimethyl sulfoxide (DMSO). The half-cell was then discharged at a constant voltage of -0.8 V for 3 mins. The Ag-SSE mounted on glass exhibits an optical transmittance of around 83% in the wavelength range of 0.4–2.5 μm (Fig. 4.12b). This low haze and high optical transparency mesh electrode balances the charge flow of the RME and facilitates a uniform electric field spatial distribution between the counter and the working electrodes, which is crucial for the consistent and uniform switching processes in dynamic windows.¹²

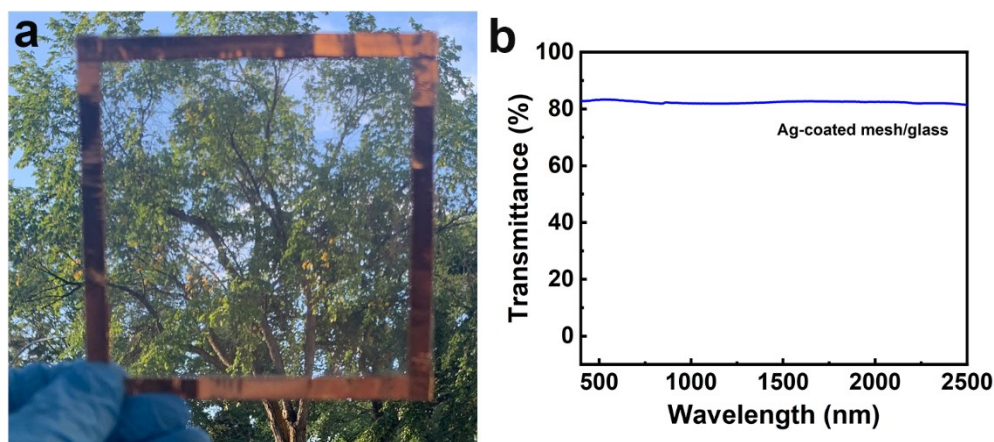


Figure 4.12. (a) Digital image of an Ag-coated stainless-steel mesh (Ag-SSE) mounted glass. (b) Visible-near infrared transmittance spectrum of the Ag-SSE mounted on glass.

Figures 4.13a,b depict the reversible switching processes between the bright, the light and the dark modes of a dynamic window. This window possesses initial transparencies of around 60% across the visible and NIR spectral range (Fig. 4.13c, black line). In this mode, representing the bright mode setting, the visibility through the dynamic window is so clear that even intricate patterns, such as 'Alberta,' can be distinctly observed. Upon applying an external voltage of -1.2 V to the window, the NIR transmission (at 1550 nm) rapidly decreases from 61% to $\sim 10\%$ within 10 seconds (Fig. 4.13c, blue line) while maintaining a satisfactory level of visible transmittance, about 50% at 632.8 nm, the window transitions to the light mode. In this mode, due to the adequate visible transmittance, the pattern 'Alberta' continues to be clearly visible. Interestingly, extending the application of -1.2 V to the window for 60 seconds resulted in a transition to the dark mode where the window completely blocks both the visible and the NIR radiation. In the dark mode, the window's near-infrared (NIR) transmission drops to less than 1%, and its visible transmittance reduces to 2% (Fig. 4.13c, red line). For a more accurate evaluation of the dynamic window's performance for solar irradiation modulation, the solar irradiance is calculated at different operating modes (Figure 4.13d). In the light mode, the window effectively blocks approximately

85% of the solar irradiance in the NIR region while still maintaining favorable visible irradiance. On the other hand, in the dark mode, nearly all solar irradiance (98%) is blocked. To confirm the reversibility of different modes, the dynamic responses of the window were measured at 1550 nm (Fig. 4.13e) and 632.8 nm (Fig. 4.13f). Clearly, when a voltage of 1.2 V is applied, the window is able to quickly revert to its original transparency within 60 seconds. This fast and reversible characteristic due to the growth and dissolution of Ag, is further corroborated by a cyclic voltammetry scan of the device (Fig. E-1) and observed through FESEM images of Au/glass and Ag-SSE electrodes taken at different modes (Fig. 4.14). We next assessed the durability of the solar-regulated dynamic windows. Figure 4.13g illustrates the maximum and minimum transmission of the dynamic window at 632.8 nm during switching over 2500 cycles between the bright and the dark modes. This extended cycle life is credited to the exceptional electrochemical reversibility of Ag growth on the film, achieved by varying the applied voltages. During cycling, the applied deposition voltages were incrementally increased by 0.05 V per 500 cycles (from -1.2 V to -1.5 V) to sustain a stable contrast ratio, while during the reverse process, the applied stripping voltage is kept fixed at 1.2 V. It is important to highlight that the gel-type electrolyte plays a significant role in enhancing the device's stability as the potentials increase. The window's switching speed remained constant at a 60-second deposition time and a 60-second stripping time.

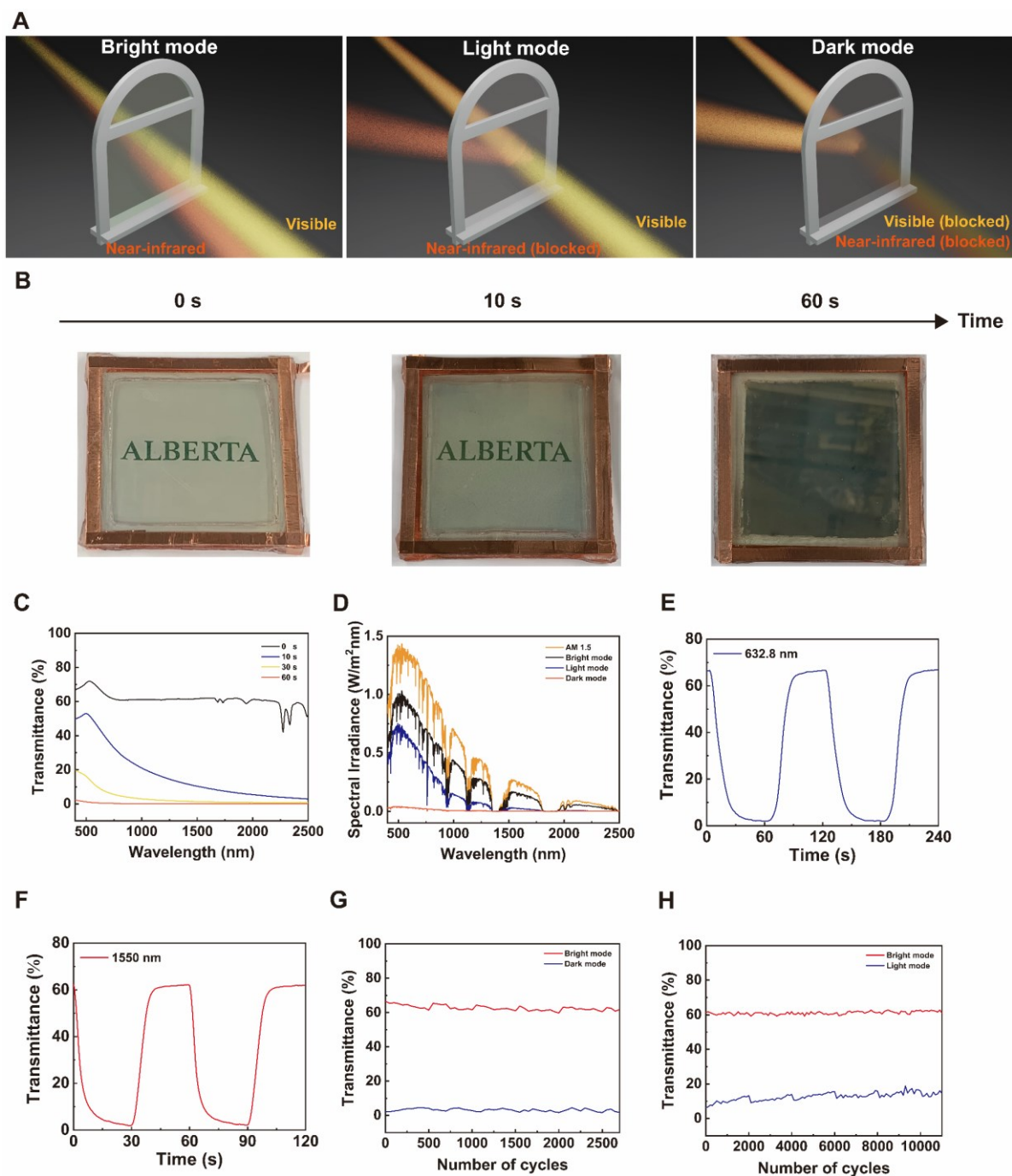


Figure 4.13. Performance of the solar-regulated dynamic windows. The (a) schematic illustrations and (b) digital images of dynamic windows in three distinct modes: bright, light and dark. (c) Visible-near infrared transmittance spectra of the dynamic window under an applied potential of -1.2 V for 0 s (black), 10 s (blue), 30 s (yellow) and 60 s (red). (d) Solar irradiance spectra at three distinct modes. Real-time transmittance changes measured at (e) 632.8 nm and (f) 1550 nm in a voltage range of -1.2 V to 1.2 V. The maximum and minimum transmission of the dynamic window at (g) 632.8 nm and (h) 1550 nm during switching over 2500 cycles and 10,000 cycles, respectively.

Similarly, the durability of the solar-regulated dynamic windows was also examined between bright mode and light mode at 1550 nm, where the applied deposition voltages were increased by 0.05 V per 2000 cycles and the switching speeds of the window were kept constant at a 10-second deposition time and a 10-second stripping time. Remarkably, the dynamic window exhibits an enduring switching capability, maintaining performance over an impressive 10,000 cycles as shown in Fig. 4.13h. To further shed light on the window's bistability, optical transmittance changes at 632.8 nm were monitored over an hour under open circuit conditions (off voltage after the operation, Fig. 4.15.) The dynamic window displays a remarkable bistability, indicating that it does not require additional energy to remain in any of its operating modes.

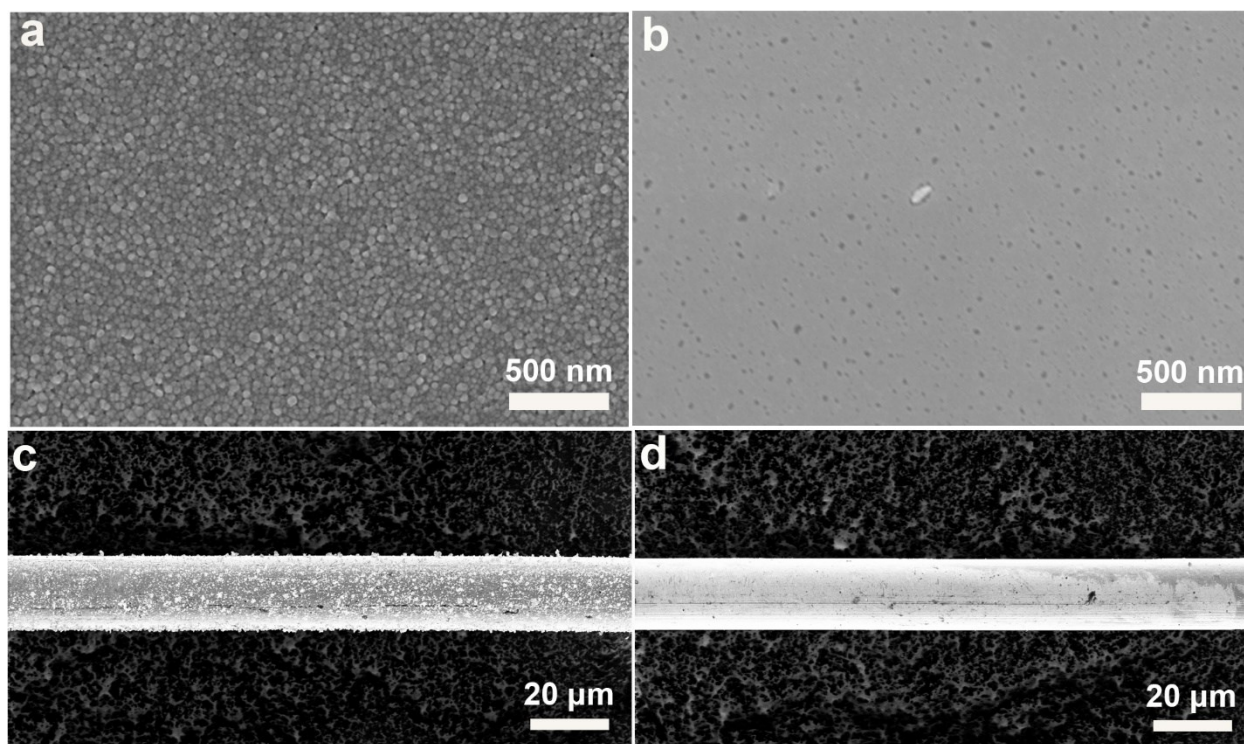


Figure 4.14. FESEM images depicting the reversible silver growth and dissolution on (a,b) Au/glass electrodes and (c,d) stainless-steel mesh.

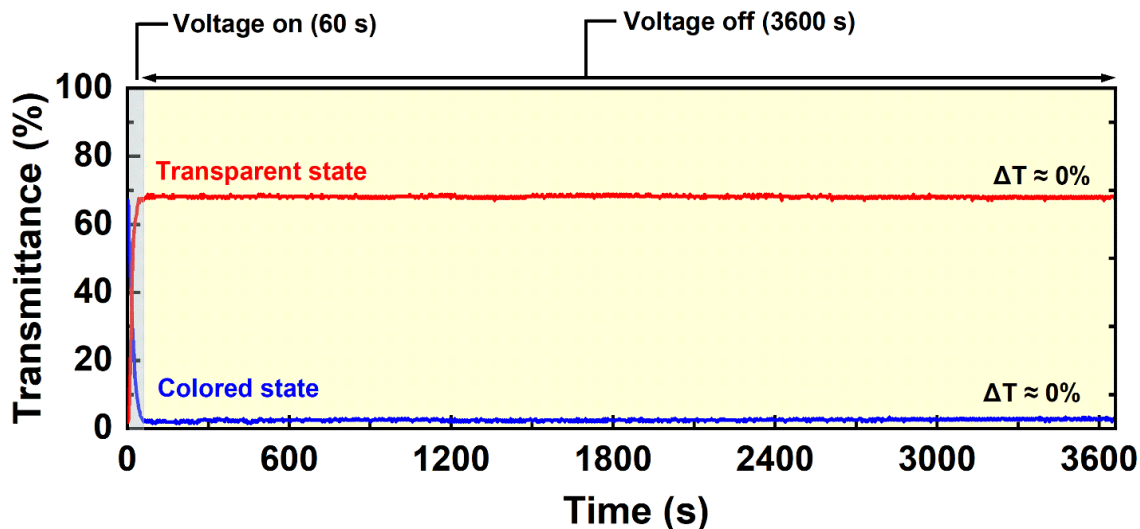


Figure 4.15. Optical transmittance changes of the solar-regulated dynamic windows monitored at 632.8 nm over an hour under open circuit conditions (off voltage after operation).

To demonstrate the modulation of solar energy by the dynamic windows, we devised an experimental setup aimed at visualizing the temperature fluctuations across the various operating modes of an object made of carbon fibres (Figure 4.16a,b). Here, a solar simulator replicated solar illumination, while a thermal camera observed object temperature during the three modes of operation. To prevent undesired thermal interference, we introduced a heat shield, constructed from paperboard layered with thick aluminum foil, to shield excess thermal radiation from the solar simulator's housing. The dynamic window was placed between the object and the solar simulator to prevent additional convective heating or cooling of the object while modulating the transmitted solar light. As depicted in Fig. 4.16c, the thermal camera recorded the object's temperature fluctuations at 45-second intervals for the three modes. After an illumination duration of approximately 180 seconds, the object's temperature stabilized, registering a rise of 4°C under the bright mode condition and a 2.3°C increase during the light mode as shown in Fig. 4.16d.

Remarkably, during the dark mode, the temperature remains consistently stable and perfectly aligned with the room's ambient temperature range of 21 to 22°C. These observed temperature variations are consistent with the calculated spectral irradiance of the dynamic window (Fig. 4.13d). Specifically, the dynamic window obstructs solar irradiation in the dark mode, selectively hinders NIR irradiance while maintaining effective solar irradiation in the visible spectrum during the light mode, and enables significant solar irradiation transmission under bright mode conditions. It is essential to emphasize that in this experiment, although the dynamic window transmits 2% in the visible range during the dark mode, this level of transmitted solar energy does not induce a noticeable temperature increase in the object due to the object's thermal radiative properties.

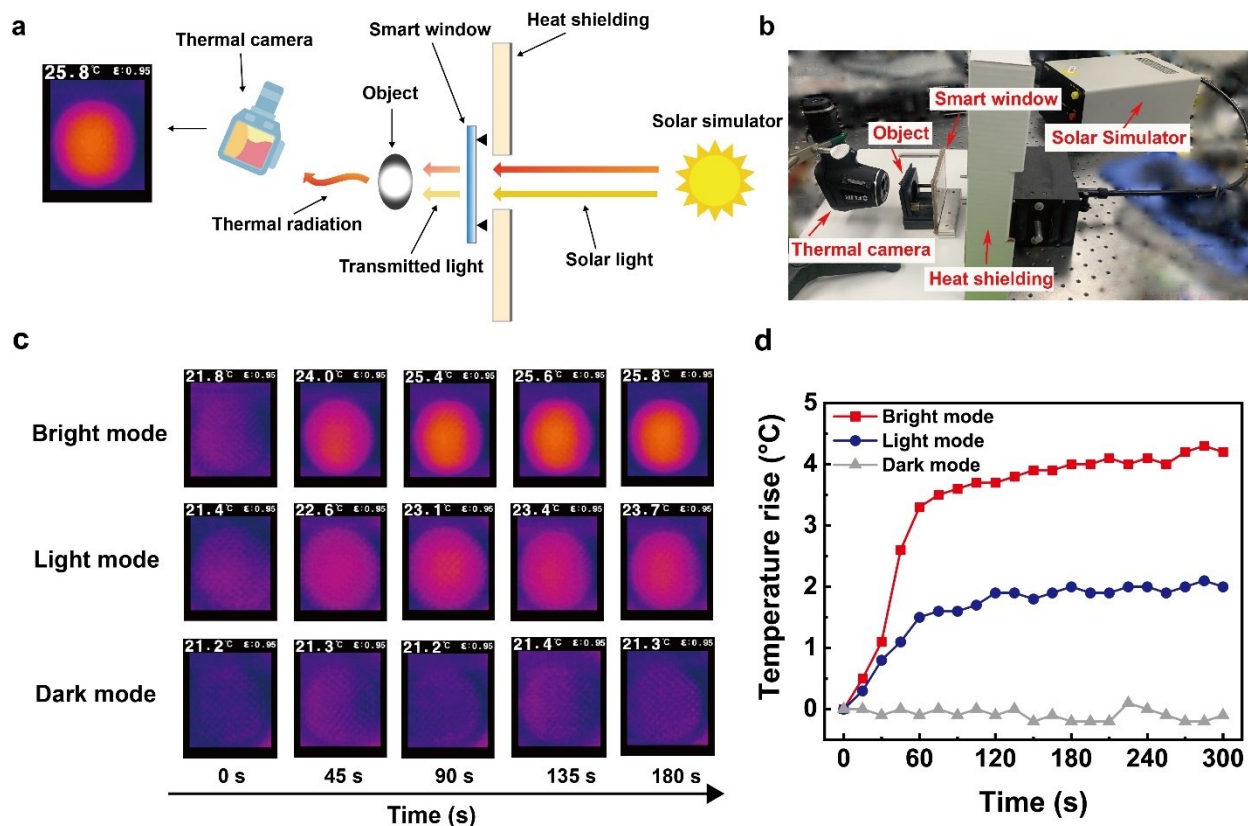


Figure 4.16. Demonstration of solar energy transferred to thermal radiation. (a) Experimental setup used to measure temperature increase in an object. (b) A dynamic window was positioned between the object and the simulator, effectively modulating the transmission of solar light. To capture the temperature variations, a thermal camera was utilized, enabling simultaneous temperature measurements in three distinct modes: bright mode, light mode, and dark mode, all tracked over time. (c) Measured time-dependent temperatures of the object in three different modes. (d) Calculated time-dependent temperature rises in the three different modes.

4.3.4 Large-scale dynamic windows

A large-area dynamic window (30.4 cm × 30.4 cm) was fabricated to showcase the scalability of this three-mode platform. The transmittance data recorded at the centre of the device emphasizes the applicability of selective modulation for visible and NIR lights in a large-scale dynamic window (Fig. 4.17a). Similar to a 100 cm² window, this large window initially exhibits around 60% transparency across the visible and NIR spectra (Fig. 4.17a, black line), making it distinctly discernible to the naked eye (Fig. E-2). Through applying an external voltage of -1.2 V to the

large-area window for 10 seconds, the NIR transmission (at 1550 nm) diminishes to about 18% (Fig. 4.17a, blue line) while maintaining a high visible transmittance (about 54% at 632.8 nm). In comparison, the 100 cm² window experiences a decrease in transmission of about 10% at 1550 nm and 50% at 632.8 nm within the 10-second interval (Fig. 4.13c). These findings suggest that despite the nine-fold increase in window's area, the reduction in device switching speed is only marginal. This observation is further supported by measuring the dynamic responses of the large-area windows at 1550 nm and 632.8 nm (Fig. 4.17c,e), where the switching speed at the window's centre is only slightly slower than at the corners by ~4 seconds. It is worth noting that due to the resistance induced voltage drop across the conducting electrodes, differing switching times at various locations (centre and edge) of the large-area window are common.²⁷⁵ In our device design, the Ag-SSE mounted glass electrode establishes a uniform electric field spatial distribution between the counter and the working electrodes, which greatly promotes the uniform switching in large-area windows.¹²

Upon applying -1.2 V to the window for 60 seconds, the NIR transmission of the large-area window decreases to < 1% and the visible transmittance reduces to ~ 5% (Fig. 4.17a, red line). Such a transmittance profile also aligns with the solar transmittance record of a 100 cm² window (Fig. 4.3c). Further application of -1.2 V to the window for an extended duration of 180 seconds results in the dynamic window transitioning to a completely opaque state, with both visible and NIR transmittances falling below 1% (Fig. 4.17a, green line). As the Ag metal film grows, the reflection of the dynamic windows gradually changes (Fig. 4.17b). When the dynamic window shifts to a fully opaque state (via a 180-second application of -1.2 V), the high reflection (~90%) transforms the window into a reflective state, effectively rendering the dynamic window to be a mirror-like (see Fig. 4.17d, f). The opaque state can be reversed to its original transparency within

180 seconds by applying a voltage of 1.2 V. It is important to note that the dark mode of the dynamic window has already demonstrated the capability to block nearly all of the solar irradiation, as evidenced in Fig. 4.16. The reflective state (or mirror state) of the dynamic window holds promise for specific requirements where the window is intended to obstruct all visible and NIR light or function as a mirror.

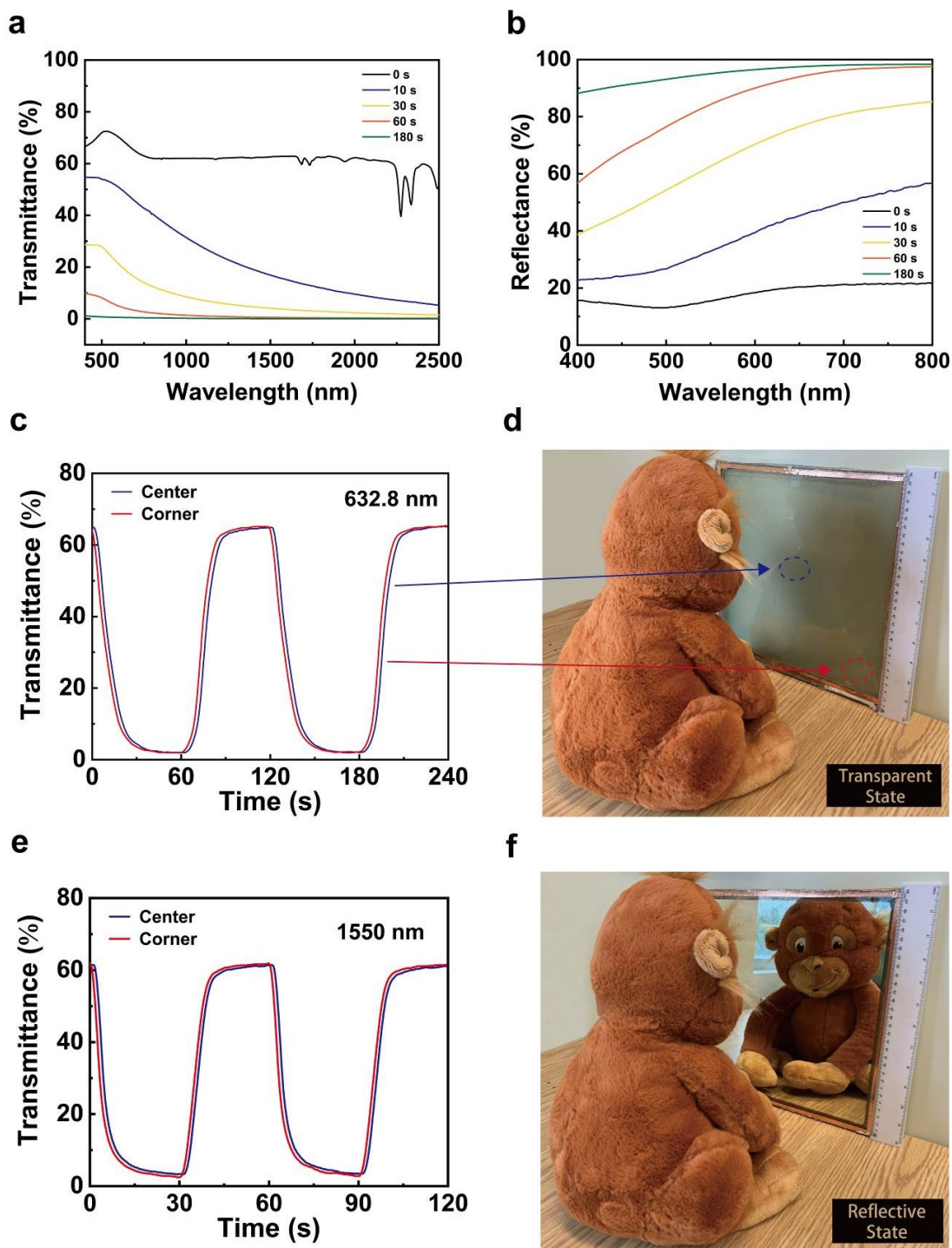


Figure 4.17 Performance of the large-area dynamic windows. The (a) visible-near infrared transmittance and (b) reflection spectra of the large-area window under an applied potential of -1.2 V for 0 s (black), 10 s (blue), 30 s (yellow), 60 s (red) and 180 s (green). Real-time transmittance changes measured at (c) 632.8 nm and (e) 1550 nm in a voltage range of -1.2 V to 1.2 V. The digital photographs of the large-area dynamic window at (d) transparent state (applying 1.2 V for 180 s) and (f) reflective state (applying -1.2 V for 180 s).

4.3.5 Flexible thermal-regulated devices

As previously discussed, our newly presented solar-regulated dynamic window platform enables a three-mode operation for selective modulation of the visible and the NIR light spectra. This has prompted a keen interest in exploring the versatility of this dual-band platform within the mid-infrared region. However, the challenge lies in the fact that mid-infrared light cannot penetrate the glass substrates (as shown in Fig. 4.18). Consequently, the potential application of dynamic windows across the broader mid-infrared range is limited.

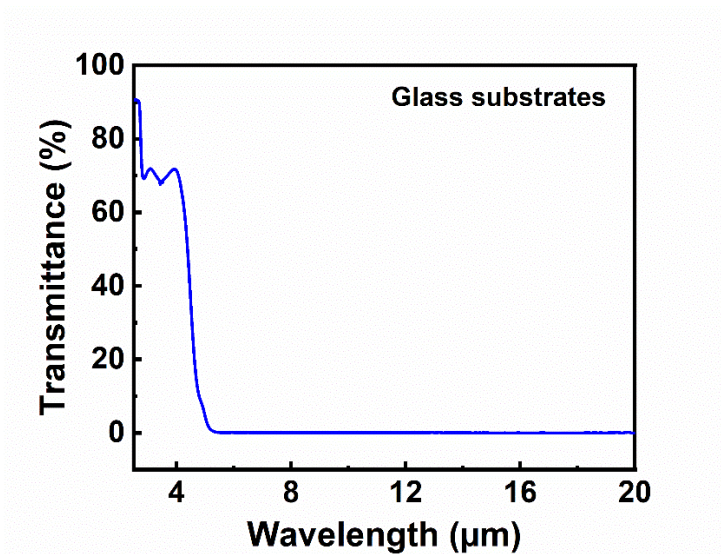


Figure 4.18. The mid-infrared transmittance spectrum of the glass substrates.

However, polyethylene (PE) membrane possesses exceptional optical transmittance within the 0.4–20 μm wavelength range, rendering it a suitable substitute for glass substrates. This enables the dual-band platform to fulfill its solar and radiative heat management capabilities. Remarkably, the Ag-SSE exhibits high transparency within the mid-infrared wavelength range (around 87%, Fig. 4.19), making it an ideal candidate for a counter electrode within this thermal-regulated device.

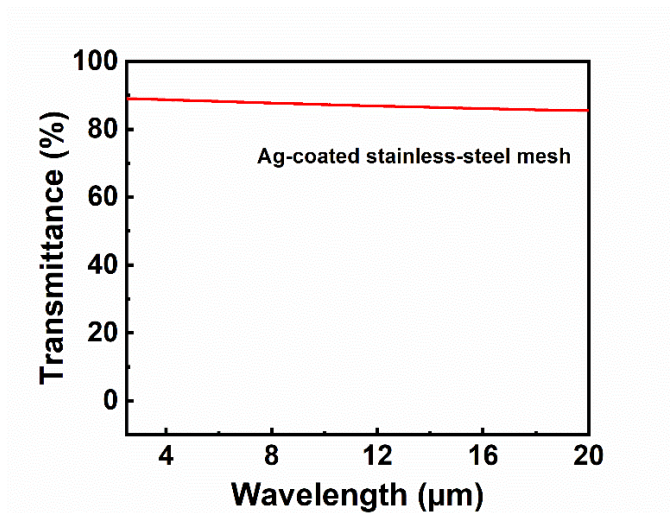


Figure 4.19. The mid-infrared transmittance spectrum of the Ag-coated stainless-steel mesh.

To this end, a flexible thermal-regulated device has been assembled by replacing the glass substrates with PE substrates (Fig. 20a). The collected transmittance data, spanning the 0.4–20 μm wavelength range, underscores the applicability of selective light modulation for this thermal-regulated device (Fig. 4.20b,c). In its initial state, the device exhibits an initial transparency of around 67% across visible and NIR spectra (Fig. 4.20b, black line), signifying the bright mode. Interestingly, the thermal-regulated device also exhibits an initial transparency of around 60% in the mid-infrared region (Fig. 4.20c, black line). The presence of diverse absorption bands and line shapes in this wavelength range is marked by the strong intrinsic absorption of DMSO and PE substrates. For example, the absorption bands at 3.4, 7.2, and 13.9 μm in the spectrum are assigned to stretching vibrations of CH_2 , CH_3 and CH_2 rocking, respectively. Through applying an external voltage of -1.2 V to the device for 10 seconds, the mid-infrared transmission of the device decreases to around 3% (Fig. 4.20c, blue line), along with a decrease in the NIR transmission (at 1550 nm) to 35% (Fig. 4.20b, blue line). Notably, the visible transmittance at 632.8 nm remains relatively high at around 60%, effectively shifting the device into a light mode. Extending the

application of -1.2 V to the device for 60 seconds prompts a transition to a dark mode, effectively blocking the majority of visible and infrared radiation. In dark mode, both the NIR and the mid-infrared transmission drop to $< 1\%$, while the visible transmittance of the window decreases to about 3% (Fig. 4.20b,c, red lines). The light modulation modes are visually confirmed through digital photographs of the flexible devices taken for the three different operating modes (Fig. 4.20d). To verify the reversibility of these distinct modes, the dynamic responses of the thermal devices were measured at 632.8 nm (Fig. 4.20e) and 1550 nm (Fig. 4.20f). Evidently, the thermal device quickly returns to its original transparency state within 60 seconds when a voltage of 1.2 V is applied.

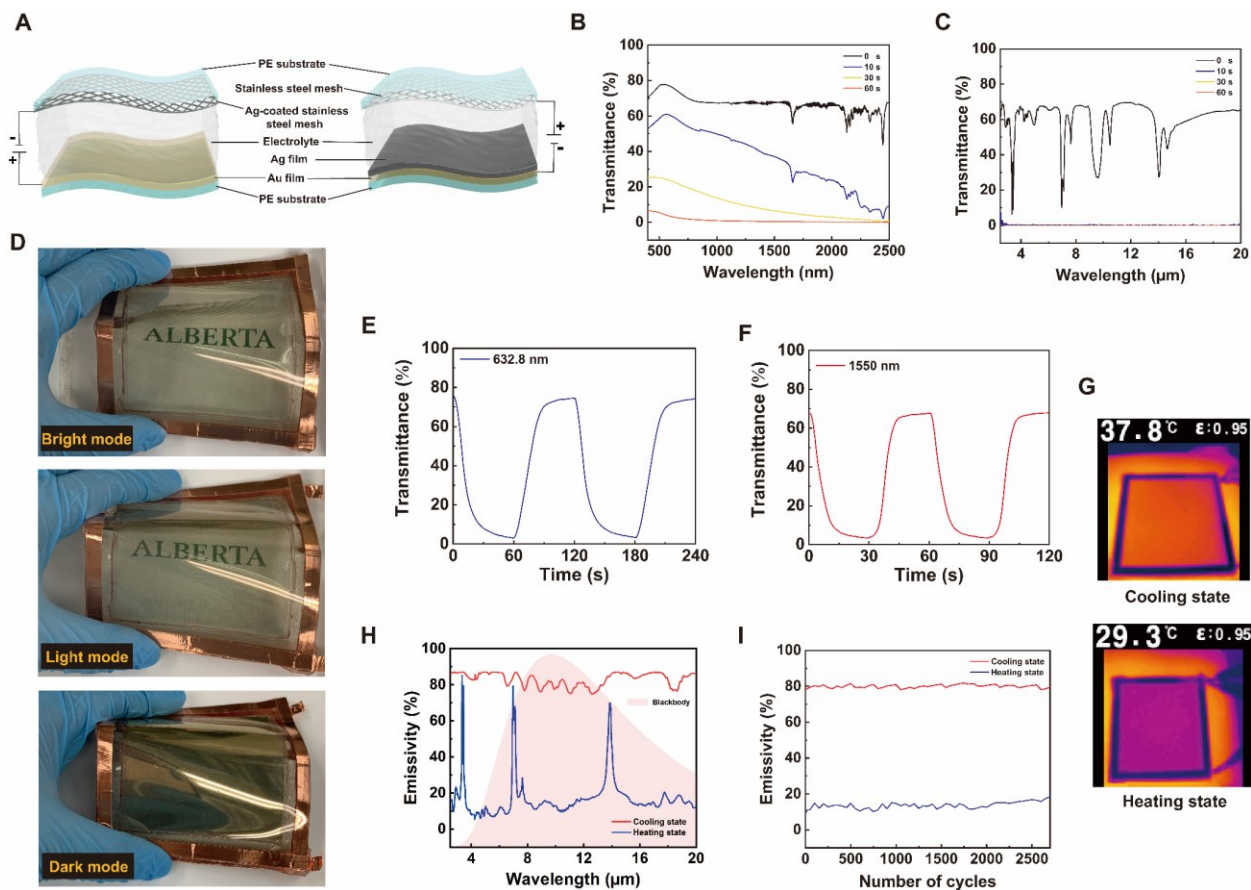


Figure 4.20. Performance of the flexible thermal-regulated devices. (a) Schematic diagram of the flexible thermal-regulated devices featuring reversible silver metal deposition. The (b) visible-near infrared and (c) mid-infrared transmittance spectra of the device under an applied potential of -1.2 V for 0 s (black), 10 s (blue), 30 s (yellow) and 60 s (red). (d) Digital images of the device captured in three different modes (bright, light and dark). Real-time transmittance changes of the device measured at (e) 632.8 nm and (f) 1550 nm in a voltage range of -1.2 V to 1.2 V. (g) Thermal images of the device taken during heating and cooling states. (h) Emissivity spectra of the device in heating and cooling states. (i) The maximum and minimum emissivity of the device at 10 μm during switching over the course of 2500 cycles.

Furthermore, in the context of thermal management considerations, an evaluation of the emissivity of this thermal-regulated device was undertaken (Fig. 4.20h). Within the mid-infrared tuning range (i.e. 2.5–20 μm wavelength range), this thermal-regulated device can effectively adjust its emissivity (i.e. weighted average by 300 K blackbody radiation) between 0.17 and 0.85. This 68% emissivity contrast is achieved by transitioning the thermal-regulated device between

cooling and heating states where in the cooling state Ag film is deposited by applying -1.2 V for 60 seconds, while in the heating state the Ag film is tripped by applying 1.2 V for 60 seconds. The effectiveness of this heat management approach is visually confirmed through thermal images captured during the heating and cooling states (Fig. 4.20g), showing a noticeable temperature difference of 8.5 °C.

The durability of the thermal-regulated device underwent further investigation. Figure 4.20i illustrates the emissivity of the device at 10 μm during 2500 cycles of switching between heating and cooling states. Throughout the cycling process, the switching speed of the thermal device remains consistent with 60-second deposition and stripping times. However, the deposition voltages experience a gradual increment of 0.05 V per 500 cycles (ranging from -1.2 V to -1.5 V) to ensure a stable contrast ratio, while the stripping voltages remain at 1.2 V.

4.3.6 Summary

In summary, we presented a ground breaking solar-regulated dynamic window platform. This innovative window architecture is achieved through Ag-based reversible metal deposition onto a thin layer of Au film. This ingenious technique permits the targeted adjustment of visible light and near-infrared radiation, opening up possibilities for diverse operational modes – bright, light, and dark modes. This strategy not only has the potential to reduce building energy consumption but also maintains optimal indoor lighting conditions. Furthermore, the ingenuity of this device design extends to its adaptability with flexible substrates, facilitating dynamic control of solar and radiative heat emission up to a wavelength of 20 micrometers. Our device design represents a new paradigm in electrochromism, potentially unlocking novel avenues for the advancement of next-generation dynamic windows and innovative thermal management solutions.

4.4 Summary of plasmonic-based electrochromic devices

In this chapter, we demonstrated the manipulation of silver adatoms through reversible metal deposition for dynamic light modulation. The reversible silver metal deposition on ITO glasses, having tunable nanostructures, along with their localized surface plasmon resonance, is presented as a promising strategy for dynamic color displays. We also presented a novel technology for solar-regulated dynamic windows. This innovation involves the operation of a window through Ag-based reversible metal deposition onto a thin layer of Au film. This ingenious technique permits the targeted adjustment of visible light and near-infrared radiation, opening up possibilities for diverse operational modes of dynamic windows. This approach not only holds the promise of decreasing building energy consumption but also ensures optimal indoor lighting conditions are upheld.

Chapter 5

Conclusion and Future Outlook

5.1 Conclusion

This thesis presents recent efforts in developing energy-efficient electrochromic devices for the applications of transparent displays and smart windows. We demonstrate a novel design of zinc anode-based electrochromic devices (ZECsDs). Compared to complementary electrochromic devices, ZECsDs exhibit a rapid spontaneous switching behavior due to the high value of redox potential difference between a metal anode and an electrochromic cathode, thus providing the most energy-efficient consumption during operation. Moreover, ZECsDs enable independent operation of top and bottom electrochromic electrodes, thus providing additional configuration flexibility for the devices through the utilization of dual electrochromic layers under the same or different color states. As such, the color overlay effect can greatly broaden the color palettes via altering the coordinate of the 2D CIE color space. Furthermore, a dual-mode electrochromic device having both self-coloring and self-bleaching operations is demonstrated via coupling the zinc anode-based electrochromic platform into a rocking-chair type electrochromic device. It is demonstrated that the ZECsD platform induces a self-color-switching behavior, reduces the energy consumption during operation, enables the independent operation of a single electrochromic electrode, also augments the bistability of the devices. The advances of ZECsDs detailed in this thesis are expected to accelerate future dynamic light control technology for self-powered smart windows, colorful displays, spatial light modulators, optical sensors and optoelectronic devices.

Moreover, a plasmonic-based electrochromic device is demonstrated via manipulating silver adatoms through an electrochemical deposition technique. The electrochemical deposition technology not only reduces the energy consumption during operation, but also facilitates a uniform size control of the grown silver plasmonic nanoparticles. This thesis also presents a ground breaking platform for solar-regulated dynamic windows. This innovation involves the operation of a window through silver-based reversible metal deposition onto a thin layer of gold film. This novel technique permits the targeted adjustment of visible light and near-infrared radiation, opening up possibilities for diverse operational modes – bright, light, and dark modes of smart windows. This strategy not only has the potential to reduce building energy consumption but also maintains optimal indoor lighting conditions.

5.2 Future Outlook

Future research on ZECs should be more focused on the assembly of high-performance electrochromic devices for practical use. Notwithstanding, like any newly emerging technology, there are still some challenges that hinder the development of high-performance ZECs for real-world applications. Examples of such challenges include: 1) the energy retrieval functionality is currently poorly understood. A better understanding of this intriguing process will assist in designing more energy-efficient ZECs that can reclaim back more of the consumed energy. 2) The ion intercalation mechanism is still not clear, especially for hybrid electrolyte systems and further investigation is needed to optimize such a process. 3) The ZECs also suffer from dendrite growth of anodes that degrade the device's performance. 4) Practical use of ZECs requires long-term stability and excellent light modulation. As such, a better understanding for both of the electrochromic material and the electrolytes involved is critical to promote performance and to

enhance overall device stability. Although such drawbacks need to be remedied, the extraordinary functionalities of ZECDs make them very promising for the future development of electrochromic devices. It is expected that the ZECDs platform will be broadly incorporated in transparent batteries, durable smart windows, multicolor displays, and variable optical devices.

Furthermore, the color-changing mechanism in plasmonic-based electrochromic devices differs from that of ZECDs. In plasmonic-based electrochromic devices, the color change is initiated by metal deposition, whereas in ZECDs, it is triggered by ion intercalation. Therefore, combining metal deposition and ion intercalation in a single device holds great promise for multifunctional applications. Conducting further research on electrochromic devices that leverage this dual color-changing mechanism could represent a compelling direction for future studies.

References

- 1 Korgel, B. a. Materials Science: Composite for Smarter Windows. *Nature* **500**, 278-279 (2013).
- 2 Platt, J. R. Electrochromism, A Possible Change of Color Producible in Dyes by an Electric Field. *J. Chem. Phys.* **34**, 862-863 (1961).
- 3 Deb, S. K. A novel electrophotographic system. *Appl. Opt. Suppl.* **8**, 192-195 (1969).
- 4 Chou, H. H. *et al.* A chameleon-inspired stretchable electronic skin with interactive colour changing controlled by tactile sensing. *Nat. Commun.* **6**, 8011 (2015).
- 5 An, T. C. *et al.* A Wearable Second Skin-Like Multifunctional Supercapacitor with Vertical Gold Nanowires and Electrochromic Polyaniline. *Adv. Mater. Technol.* **4**, 1800473 (2019).
- 6 Cho, S. I. *et al.* Nanotube-based ultrafast electrochromic display. *Adv. Mater.* **17**, 171-175 (2005).
- 7 Chen, J. *et al.* Mimicking Nature's Butterflies: Electrochromic Devices with Dual-Sided Differential Colorations. *Adv. Mater.* **33**, 2007314 (2021).
- 8 Xu, W., Fu, K. Y. & Bohn, P. W. Electrochromic Sensor for Multiplex Detection of Metabolites Enabled by Closed Bipolar Electrode Coupling. *ACS Sens.* **2**, 1020-1026 (2017).
- 9 Cheng, W. *et al.* Photodeposited Amorphous Oxide Films for Electrochromic Windows. *Chem* **4**, 821-832 (2018).
- 10 Yeh, M. H., Lin, L., Yang, P. K. & Wang, Z. L. Motion-Driven Electrochromic Reactions for Self-Powered Smart Window System. *ACS Nano* **9**, 4757-4765, (2015).
- 11 Zhang, S. L., Cao, S., Zhang, T. R. & Lee, J. Y. Plasmonic Oxygen-Deficient $\text{TiO}_{(2-x)}$ Nanocrystals for Dual-Band Electrochromic Smart Windows with Efficient Energy Recycling. *Adv. Mater.* **32**, 2004686 (2020).
- 12 Li, H., Zhang, W. & Elezzabi, A. Y. Transparent zinc-mesh electrodes for solar-charging electrochromic windows. *Adv. Mater.* **32**, 2003574 (2020).
- 13 Yang, P. H., Sun, P. & Mai, W. J. Electrochromic energy storage devices. *Mater. Today* **19**, 394-402 (2016).
- 14 Li, H. Z., McRae, L., Firby, C. J., Al-Hussein, M. & Elezzabi, A. Y. Nanohybridization of molybdenum oxide with tungsten molybdenum oxide nanowires for solution-processed fully reversible switching of energy storing smart windows. *Nano Energy* **47**, 130-139 (2018).
- 15 Cao, S., Zhang, S. L., Zhang, T. R., Yao, Q. F. & Lee, J. Y. A Visible Light-Near-Infrared Dual-Band Smart Window with Internal Energy Storage. *Joule* **3**, 1152-1162 (2019).
- 16 Kim, Y., Han, M., Kim, J. & Kim, E. Electrochromic capacitive windows based on all conjugated polymers for a dual function smart window. *Energy Environ. Sci.* **11**, 2124-2133, (2018).
- 17 Shen, L. X. *et al.* Flexible electrochromic supercapacitor hybrid electrodes based on tungsten oxide films and silver nanowires. *Chem. Commun.* **52**, 6296-6299, (2016).
- 18 Wang, K., Wu, H. P., Meng, Y. N., Zhang, Y. J. & Wei, Z. X. Integrated energy storage and electrochromic function in one flexible device: an energy storage smart window. *Energy Environ. Sci.* **5**, 8384-8389, (2012).

- 19 Wang, S. M., Kim, Y., Kim, B., Han, M. & Kim, E. Ultrathin Polyoxometalate Coating as the Redox Shuttle for Acid-Free Electrochromic Polymer Capacitive Windows. *Adv. Funct. Mater.* **29**, 1806590 (2019).
- 20 Zhang, S. L. *et al.* Monoclinic oxygen-deficient tungsten oxide nanowires for dynamic and independent control of near-infrared and visible light transmittance. *Mater. Horiz.* **5**, 291-297, (2018).
- 21 Wang, Y. Y. *et al.* A multicolour bistable electronic shelf label based on intramolecular proton-coupled electron transfer. *Nat. Mater.* **18**, 1335-1342 (2019).
- 22 Zhang, W., Li, H., Yu, W. W. & Elezzabi, A. Y. Transparent inorganic multicolour displays enabled by zinc-based electrochromic devices. *Light Sci. Appl.* **9**, 121, (2020).
- 23 Jittiarporn, P., Badilescu, S., Al Sawafta, M. N., Sikong, L. & Truong, V. V. Electrochromic properties of sol-gel prepared hybrid transition metal oxides - A short review. *J. Sci. Adv. Mater. Devices* **2**, 286-300, (2017).
- 24 Patel, K. J., Bhatt, G. G., Ray, J. R., Suryavanshi, P. & Panchal, C. J. All-inorganic solid-state electrochromic devices: a review. *J. Solid State Electrochem.* **21**, 337-347, (2017).
- 25 Barawi, M. *et al.* Dual Band Electrochromic Devices Based on Nb-Doped TiO₂ Nanocrystalline Electrodes. *ACS Nano* **11**, 3576-3584 (2017).
- 26 Che, X. Q. *et al.* Properties of all-thin-film glass/ITO/WO₃:H/Ta₂O₅/NiO_x/ITO electrochromic devices prepared by magnetron sputtering. *Thin Solid Films* **662**, 6-12 (2018).
- 27 Dong, W. J. *et al.* Bifunctional MoO₃-WO₃/Ag/MoO₃-WO₃ Films for Efficient ITO-Free Electrochromic Devices. *ACS Appl. Mater. Interfaces* **8**, 33842-33847 (2016).
- 28 Ong, G. K. *et al.* Electrochromic Niobium Oxide Nanorods. *Chem. Mater.* **32**, 468-475 (2020).
- 29 Zhang, X. *et al.* Preparation and performances of all-solid-state variable infrared emittance devices based on amorphous and crystalline WO₃ electrochromic thin films. *Sol. Energy Mater. Sol. Cells* **200**, 109916 (2019).
- 30 Zhao, Q. *et al.* Printing of WO₃/ITO nanocomposite electrochromic smart windows. *Sol. Energy Mater. Sol. Cells* **194**, 95-102 (2019).
- 31 Granqvist, C. G. Electrochromic Materials - Microstructure, Electronic Bands, and Optical-Properties. *Appl. Phys. A* **57**, 3-12 (1993).
- 32 Cong, S., Geng, F. & Zhao, Z. Tungsten Oxide Materials for Optoelectronic Applications. *Adv. Mater.* **28**, 10518-10528, (2016).
- 33 Li, X. F., Perera, K., He, J. Z., Gumyusenge, A. & Mei, J. G. Solution-processable electrochromic materials and devices: roadblocks and strategies towards large-scale applications. *J. Mater. Chem. C* **7**, 12761-12789 (2019).
- 34 Runnerstrom, E. L., Llordes, A., Lounis, S. D. & Milliron, D. J. Nanostructured electrochromic smart windows: traditional materials and NIR-selective plasmonic nanocrystals. *Chem. Commun.* **50**, 10555-10572 (2014).
- 35 Granqvist, C. G. Electrochromics for smart windows: Oxide-based thin films and devices. *Thin Solid Films* **564**, 1-38 (2014).
- 36 Li, H. Z., McRae, L., Firby, C. J. & Elezzabi, A. Y. Rechargeable Aqueous Electrochromic Batteries Utilizing Ti-Substituted Tungsten Molybdenum Oxide Based Zn²⁺ Ion Intercalation Cathodes. *Adv. Mater.* **31**, 1807065 (2019).
- 37 Zhang, S. L., Cao, S., Zhang, T. R., Fisher, A. & Lee, J. Y. Al³⁺ intercalation/deintercalation-enabled dual-band electrochromic smart windows with a high optical

- modulation, quick response and long cycle life. *Energy Environ. Sci.* **11**, 2884-2892 (2018).
- 38 Zhang, W., Li, H. Z., Al-Hussein, M. & Elezzabi, A. Y. Electrochromic Battery Displays with Energy Retrieval Functions Using Solution-Processable Colloidal Vanadium Oxide Nanoparticles. *Adv. Opt. Mater.* **8**, 1901224 (2020).
- 39 Li, H. Z., Firby, C. J. & Elezzabi, A. Y. Rechargeable Aqueous Hybrid Zn²⁺/Al³⁺ Electrochromic Batteries. *Joule* **3**, 2268-2278 (2019).
- 40 Bulja, S. *et al.* Tuneable dielectric and optical characteristics of tailor-made inorganic electro-chromic materials. *Sci. Rep.* **7**, 13484 (2017).
- 41 Gillaspie, D. T., Tenent, R. C. & Dillon, A. C. Metal-oxide films for electrochromic applications: present technology and future directions. *J. Mater. Chem.* **20**, 9585-9592 (2010).
- 42 Majeed, S. A. *et al.* Evaluation of the Intramolecular Charge-Transfer Properties in Solvatochromic and Electrochromic Zinc Octa(carbazolyl)phthalocyanines. *Inorg. Chem.* **56**, 11640-11653 (2017).
- 43 Nam, Y. S. *et al.* Virus-templated iridium oxide-gold hybrid nanowires for electrochromic application. *Nanoscale* **4**, 3405-3409 (2012).
- 44 Ren, Y., Zhou, X. G., Zhang, H., Lei, L. & Zhao, G. Y. Preparation of a porous NiO array-patterned film and its enhanced electrochromic performance. *J. Mater. Chem. C* **6**, 4952-4958 (2018).
- 45 Sakai, N., Ebina, Y., Takada, K. & Sasaki, T. Electrochromic films composed of MnO₂ nanosheets with controlled optical density and high coloration efficiency. *J. Electrochem. Soc.* **152**, E384-E389 (2005).
- 46 Yang, H., Yu, J. H., Seo, H. J., Jeong, R. H. & Boo, J. H. Improved electrochromic properties of nanoporous NiO film by NiO flake with thickness controlled by aluminum. *Appl. Surf. Sci.* **461**, 88-92 (2018).
- 47 Zhou, J. L., Wei, Y. X., Luo, G., Zheng, J. M. & Xu, C. Y. Electrochromic properties of vertically aligned Ni-doped WO₃ nanostructure films and their application in complementary electrochromic devices. *J. Mater. Chem. C* **4**, 1613-1622 (2016).
- 48 Liu, L. *et al.* High-temperature adaptive and robust ultra-thin inorganic all-solid-state smart electrochromic energy storage devices. *Nano Energy* **62**, 46-54, (2019).
- 49 Guo, J. J. *et al.* Mechanistic Insights into the Coloration, Evolution, and Degradation of NiO_x Electrochromic Anodes. *Inorg. Chem.* **57**, 8874-8880 (2018).
- 50 Liu, Q. R. *et al.* In situ electrochromic efficiency of a nickel oxide thin film: origin of electrochemical process and electrochromic degradation. *J. Mater. Chem. C* **6**, 646-653 (2018).
- 51 Ma, D., Shi, G., Wang, H., Zhang, Q. & Li, Y. Hierarchical NiO microflake films with high coloration efficiency, cyclic stability and low power consumption for applications in a complementary electrochromic device. *Nanoscale* **5**, 4808-4815, (2013).
- 52 Bouessaya, I. *et al.* Electrochromic degradation in nickel oxide thin film: A self-discharge and dissolution phenomenon. *Electrochim. Acta* **50**, 3737-3745 (2005).
- 53 Liang, H. *et al.* Regulation of carbon content in MOF-derived hierarchical-porous NiO@C films for high-performance electrochromism. *Mater. Horiz.* **6**, 571-579 (2019).
- 54 Kang, W. *et al.* Green synthesis of nanobelt-membrane hybrid structured vanadium oxide with high electrochromic contrast. *J. Mater. Chem. C* **2**, 4727-4732, (2014).
- 55 Wang, J. M. *et al.* A bi-functional device for self-powered electrochromic window and

- self-rechargeable transparent battery applications. *Nat. Commun.* **5**, 4921 (2014).
- 56 Yue, Y. *et al.* High-performance complementary electrochromic device based on $\text{WO}_3 \cdot 0.33\text{H}_2\text{O}$ /PEDOT and prussian blue electrodes. *J. Phys. Chem. Solids* **110**, 284-289, (2017).
- 57 Qian, J. H., Ma, D. Y., Xu, Z. P., Li, D. & Wang, J. M. Electrochromic properties of hydrothermally grown Prussian blue film and device. *Sol. Energy Mater. Sol. Cells* **177**, 9-14, (2018).
- 58 Wang, Z. *et al.* Using Intrinsic Intracrystalline Tunnels for Near-Infrared and Visible-Light Selective Electrochromic Modulation. *Adv. Opt. Mater.* **5**, 1700194 (2017).
- 59 Wang, B. *et al.* A Long-Life Battery-Type Electrochromic Window with Remarkable Energy Storage Ability. *Sol. RRL* **4**, 1900425 (2020).
- 60 Wessells, C. D., Huggins, R. A. & Cui, Y. Copper hexacyanoferrate battery electrodes with long cycle life and high power. *Nat. Commun.* **2**, 550 (2011).
- 61 Wessells, C. D., Peddada, S. V., McDowell, M. T., Huggins, R. A. & Cui, Y. The Effect of Insertion Species on Nanostructured Open Framework Hexacyanoferrate Battery Electrodes. *J. Electrochem. Soc.* **159**, A98-A103 (2012).
- 62 Anasori, B., Lukatskaya, M. R. & Gogotsi, Y. 2D metal carbides and nitrides (MXenes) for energy storage. *Nat. Rev. Mater.* **2**, 16098 (2017).
- 63 Salles, P. *et al.* Electrochromic Effect in Titanium Carbide MXene Thin Films Produced by Dip-Coating. *Adv. Funct. Mater.* **29**, 1809223 (2019).
- 64 Shah, K. W., Wang, S. X., Soo, D. X. Y. & Xu, J. W. Viologen-Based Electrochromic Materials: From Small Molecules, Polymers and Composites to Their Applications. *Polymers* **11**, 1839 (2019).
- 65 Dmitrieva, E., Rosenkranz, M., Alesanco, Y. & Vinales, A. The reduction mechanism of p-cyanophenylviologen in PVA-borax gel polyelectrolyte-based bicolor electrochromic devices. *Electrochim. Acta* **292**, 81-87 (2018).
- 66 Gelinias, B., Das, D. & Rochefort, D. Air-Stable, Self-Bleaching Electrochromic Device Based on Viologen-and Ferrocene-Containing Triflimide Redox Ionic Liquids. *ACS Appl. Mater. Interfaces* **9**, 28726-28736 (2017).
- 67 Camurlu, P. Polypyrrole derivatives for electrochromic applications. *Rsc Adv.* **4**, 55832-55845 (2014).
- 68 Ghoorchian, M., Tavoli, F. & Alizadeh, N. Long-term stability of nanostructured polypyrrole electrochromic devices by using deep eutectic solvents. *J. Electroanal. Chem.* **807**, 70-75 (2017).
- 69 Neo, W. T., Ye, Q., Chua, S. J. & Xu, J. W. Conjugated polymer-based electrochromics: materials, device fabrication and application prospects. *J. Mater. Chem. C* **4**, 7364-7376 (2016).
- 70 Gomes, L. *et al.* Increasing the electrical conductivity of electrochromic PEDOT:PSS films - A comparative study. *Sol. Energy Mater. Sol. Cells* **144**, 631-640 (2016).
- 71 Hu, F. *et al.* PEDOT nanoparticles fully covered on natural tubular clay for hierarchically porous electrochromic film. *Sol. Energy Mater. Sol. Cells* **199**, 59-65 (2019).
- 72 Yun, T. G. *et al.* All-Transparent Stretchable Electrochromic Supercapacitor Wearable Patch Device. *ACS Nano* **13**, 3141-3150 (2019).
- 73 Levasseur, D., Mjejri, I., Rolland, T. & Rougier, A. Color Tuning by Oxide Addition in PEDOT:PSS-Based Electrochromic Devices. *Polymers* **11**, 179 (2019).
- 74 Chen, X. L. *et al.* Electrochromic Fiber-Shaped Supercapacitors. *Adv. Mater.* **26**, 8126-

- 8132 (2014).
- 75 Zhou, K. L. *et al.* Polyaniline films with modified nanostructure for bifunctional flexible multicolor electrochromic and supercapacitor applications. *Chem. Eng. J.* **345**, 290-299 (2018).
- 76 Lu, Q. *et al.* Donor–acceptor conjugated polymers containing isoindigo block for novel multifunctional materials for electrochromic, resistance memory, and detector devices. *Sol. Energy Mater. Sol. Cells* **200**, 109979 (2019).
- 77 Wang, Z., Wang, X. Y., Cong, S., Geng, F. X. & Zhao, Z. G. Fusing electrochromic technology with other advanced technologies: A new roadmap for future development. *Mater. Sci. Eng. R* **140**, 100524 (2020).
- 78 Zhang, L. *et al.* Further understanding of the mechanisms of electrochromic devices with variable infrared emissivity based on polyaniline conducting polymers. *J. Mater. Chem. C* **7**, 9878-9891, (2019).
- 79 Jensen, J. *et al.* Fast Switching ITO Free Electrochromic Devices. *Adv. Funct. Mater.* **24**, 1228-1233 (2014).
- 80 Singh, R., Tharion, J., Murugan, S. & Kumar, A. ITO-Free Solution-Processed Flexible Electrochromic Devices Based on PEDOT:PSS as Transparent Conducting Electrode. *ACS Appl. Mater. Interfaces* **9**, 19427-19435 (2017).
- 81 Kang, W. B., Yan, C. Y., Foo, C. Y. & Lee, P. S. Foldable Electrochromics Enabled by Nanopaper Transfer Method. *Adv. Funct. Mater.* **25**, 4203-4210 (2015).
- 82 Li, H. Z., McRae, L. & Elezzabi, A. Y. Solution-Processed Interfacial PEDOT:PSS Assembly into Porous Tungsten Molybdenum Oxide Nanocomposite Films for Electrochromic Applications. *ACS Appl. Mater. Interfaces* **10**, 10520-10527 (2018).
- 83 Ling, H., Liu, L., Lee, P. S., Mandler, D. & Lu, X. H. Layer-by-Layer Assembly of PEDOT:PSS and WO₃ Nanoparticles: Enhanced Electrochromic Coloration Efficiency and Mechanism Studies by Scanning Electrochemical Microscopy. *Electrochim. Acta* **174**, 57-65 (2015).
- 84 Ling, H. *et al.* One-pot sequential electrochemical deposition of multilayer poly(3,4-ethylenedioxythiophene):poly(4-styrenesulfonic acid)/tungsten trioxide hybrid films and their enhanced electrochromic properties. *J. Mater. Chem. A* **2**, 2708-2717 (2014).
- 85 Ma, D. Y., Shi, G. Y., Wang, H. Z., Zhang, Q. H. & Li, Y. G. Controllable growth of high-quality metal oxide/conducting polymer hierarchical nanoarrays with outstanding electrochromic properties and solar-heat shielding ability. *J. Mater. Chem. A* **2**, 13541-13549 (2014).
- 86 Barile, C. J., Slotcavage, D. J. & McGehee, M. D. Polymer–Nanoparticle Electrochromic Materials that Selectively Modulate Visible and Near-Infrared Light. *Chem. Mater.* **28**, 1439-1445, (2016).
- 87 Xiong, S. X. *et al.* Organic/inorganic electrochromic nanocomposites with various interfacial interactions: A review. *Mater. Sci. Eng. B* **221**, 41-53 (2017).
- 88 Yang, Z. L., Pu, H. T. & Yin, J. L. Preparation and electrochromic property of covalently bonded WO₃/polyvinylimidazole core-shell microspheres. *J. Colloid Interface Sci.* **292**, 108-112 (2005).
- 89 DeLongchamp, D. M. & Hammond, P. T. Multiple-color electrochromism from layer-by-layer-assembled polyaniline/Prussian Blue nanocomposite thin films. *Chem. Mater.* **16**, 4799-4805 (2004).
- 90 Liu, W. S. *et al.* Electrochromic properties of organic-inorganic composite materials. *J.*

- Alloy Compd.* **718**, 379-385 (2017).
- 91 Lahav, M. & van der Boom, M. E. Polypyridyl Metallo-Organic Assemblies for Electrochromic Applications. *Adv. Mater.* **30**, 1706641 (2018).
- 92 Maier, A., Rabindranath, A. R. & Tieke, B. Coordinative Supramolecular Assembly of Electrochromic Films Based on Metal Ion Complexes of Polyiminofluorene with Terpyridine Substituent Groups. *Chem. Mater.* **21**, 3668-3676 (2009).
- 93 Motiei, L., Lahav, M., Freeman, D. & van der Boom, M. E. Electrochromic Behavior of a Self-Propagating Molecular-Based Assembly. *J. Am. Chem. Soc.* **131**, 3468-3469 (2009).
- 94 Pai, S., Moos, M., Schreck, M. H., Lambert, C. & Kurth, D. G. Green-to-Red Electrochromic Fe(II) Metallo-Supramolecular Polyelectrolytes Self-Assembled from Fluorescent 2,6-Bis(2-pyridyl)pyrindine Bithiophene. *Inorg. Chem.* **56**, 1418-1432 (2017).
- 95 Bera, M. K., Chakraborty, C., Rana, U. & Higuchi, M. Electrochromic Os(II)-Based Metallo-Supramolecular Polymers. *Macromol. Rapid Commun.* **39**, 1800415 (2018).
- 96 Gordon, T. R. *et al.* Shape-Dependent Plasmonic Response and Directed Self-Assembly in a New Semiconductor Building Block, Indium-Doped Cadmium Oxide (ICO). *Nano Lett.* **13**, 2857-2863 (2013).
- 97 Kanehara, M., Koike, H., Yoshinaga, T. & Teranishi, T. Indium Tin Oxide Nanoparticles with Compositionally Tunable Surface Plasmon Resonance Frequencies in the Near-IR Region. *J. Am. Chem. Soc.* **131**, 17736-17737 (2009).
- 98 Liu, Y., Liu, M. & Swihart, M. T. Plasmonic Copper Sulfide-Based Materials: A Brief Introduction to Their Synthesis, Doping, Alloying, and Applications. *J. Phys. Chem. C* **121**, 13435-13447 (2017).
- 99 Agrawal, A. *et al.* Localized Surface Plasmon Resonance in Semiconductor Nanocrystals. *Chem. Rev.* **118**, 3121-3207 (2018).
- 100 Tsuboi, A., Nakamura, K. & Kobayashi, N. Multicolor Electrochromism Showing Three Primary Color States (Cyan Magenta Yellow) Based on Size- and Shape-Controlled Silver Nanoparticles. *Chem. Mater.* **26**, 6477-6485 (2014).
- 101 Tandon, B., Ghosh, S. & Milliron, D. J. Dopant Selection Strategy for High-Quality Factor Localized Surface Plasmon Resonance from Doped Metal Oxide Nanocrystals. *Chem. Mater.* **31**, 7752-7760 (2019).
- 102 Garcia, G. *et al.* Dynamically Modulating the Surface Plasmon Resonance of Doped Semiconductor Nanocrystals. *Nano Lett.* **11**, 4415-4420 (2011).
- 103 Wang, Z. C. & Chumanov, G. WO₃ sol-gel modified Ag nanoparticle arrays for electrochemical modulation of surface plasmon resonance. *Adv. Mater.* **15**, 1285-1289 (2003).
- 104 Peng, J. L. *et al.* Scalable electrochromic nanopixels using plasmonics. *Sci. Adv.* **5**, eaaw2205 (2019).
- 105 Gugole, M. *et al.* High-Contrast Switching of Plasmonic Structural Colors: Inorganic versus Organic Electrochromism. *ACS Photonics* **7**, 1762-1772 (2020).
- 106 Hopmann, E. & Elezzabi, A. Y. Plasmochromic Nanocavity Dynamic Light Color Switching. *Nano Lett.* **20**, 1876-1882, (2020).
- 107 Wang, Z. *et al.* Towards full-colour tunability of inorganic electrochromic devices using ultracompact fabry-perot nanocavities. *Nat. Commun.* **11**, 302 (2020).
- 108 Zhang, W., Li, H. Z., Firby, C. J., Al-Hussein, M. & Elezzabi, A. Y. Oxygen-Vacancy-Tunable Electrochemical Properties of Electrodeposited Molybdenum Oxide Films. *ACS*

- Appl. Mater. Interfaces* **11**, 20378-20385 (2019).
- 109 Lim, J. Y., Ko, H. C. & Lee, H. Systematic prediction of maximum electrochromic contrast of an electrochromic material. *Synth. Met.* **155**, 595-598 (2005).
- 110 Padilla, J., Osterholm, A. M., Dyer, A. L. & Reynolds, J. R. Process controlled performance for soluble electrochromic polymers. *Sol. Energy Mater. Sol. Cells* **140**, 54-60 (2015).
- 111 Padilla, J., Seshadri, V., Sotzing, G. A. & Otero, T. F. Maximum contrast from an electrochromic material. *Electrochem. Commun.* **9**, 1931-1935 (2007).
- 112 Ju, X. Q., Yang, F., Zhu, X. & Jia, X. L. Zinc Ion Intercalation/Deintercalation of Metal Organic Framework-Derived Nanostructured NiO@C for Low-Transmittance and High-Performance Electrochromism. *ACS Sustain. Chem. Eng.* **8**, 12222-12229 (2020).
- 113 Wang, M. H., Chen, Y., Gao, B. W. & Lei, H. Electrochromic Properties of Nanostructured WO₃ Thin Films Deposited by Glancing-Angle Magnetron Sputtering. *Adv. Electron. Mater.* **5**, 1800713 (2019).
- 114 Ayrançi, R. *et al.* Enhanced optical and electrical properties of PEDOT via nanostructured carbon materials: A comparative investigation. *Nano Struct. Nano Objects* **11**, 13-19, (2017).
- 115 Scherer, M. R. J., Li, L., Cunha, P. M. S., Scherman, O. A. & Steiner, U. Enhanced Electrochromism in Gyroid-Structured Vanadium Pentoxide. *Adv. Mater.* **24**, 1217-1221 (2012).
- 116 Li, H. Z. *et al.* Spray coated ultrathin films from aqueous tungsten molybdenum oxide nanoparticle ink for high contrast electrochromic applications. *J. Mater. Chem. C* **4**, 33-38 (2016).
- 117 Zhang, S. L. O. *et al.* Overcoming the Technical Challenges in Al Anode-Based Electrochromic Energy Storage Windows. *Small Methods* **4**, 1900545 (2020).
- 118 Dalavi, D. S. *et al.* Nanoporous nickel oxide thin films and its improved electrochromic performance: Effect of thickness. *Appl. Surf. Sci.* **257**, 2647-2656 (2011).
- 119 Tahtali, G., Has, Z., Doyranli, C., Varlikli, C. & Koyuncu, S. Solution processable neutral state colourless electrochromic devices: effect of the layer thickness on the electrochromic performance. *J. Mater. Chem. C* **4**, 10090-10094 (2016).
- 120 Wen-Cheun Au, B., Chan, K.-Y. & Knipp, D. Effect of film thickness on electrochromic performance of sol-gel deposited tungsten oxide (WO₃). *Opt. Mater.* **94**, 387-392, (2019).
- 121 Hu, F. *et al.* Constructing spraying-processed complementary smart windows via electrochromic materials with hierarchical nanostructures. *J. Mater. Chem. C* **7**, 14855-14860 (2019).
- 122 Zhang, W. *et al.* Pulsed electrodeposition of nanostructured polythiothene film for high-performance electrochromic devices. *Sol. Energy Mater. Sol. Cells* **219**, 110775 (2021).
- 123 Sahu, D. R., Wu, T. J., Wang, S. C. & Huang, J. L. Electrochromic behavior of NiO film prepared by e-beam evaporation. *J. Sci. Adv. Mater. Devices* **2**, 225-232 (2017).
- 124 Sorar, I., Pehlivan, E., Niklasson, G. A. & Granqvist, C. G. Electrochromism of DC magnetron-sputtered TiO₂: Role of film thickness. *Appl. Surf. Sci.* **318**, 24-27 (2014).
- 125 Wu, C. G., Lu, M. I., Chang, S. J. & Wei, C. S. A solution-processable high-coloration-efficiency low-switching-voltage electrochromic polymer based on polycyclopentadithiophene. *Adv. Funct. Mater.* **17**, 1063-1070 (2007).
- 126 Ma, D., Shi, G., Wang, H., Zhang, Q. & Li, Y. Morphology-tailored synthesis of vertically aligned 1D WO₃ nano-structure films for highly enhanced electrochromic

- performance. *J. Mater. Chem. A* **1**, 684-691, (2013).
- 127 Ma, D., Wang, H., Zhang, Q. & Li, Y. Self-weaving WO₃ nanoflake films with greatly enhanced electrochromic performance. *J. Mater. Chem.* **22**, 16633–16639 (2012).
- 128 Arvizu, M. A. *et al.* Electrochromic WO₃ thin films attain unprecedented durability by potentiostatic pretreatment. *J. Mater. Chem. A* **7**, 2908-2918 (2019).
- 129 Peres, R. C. D., Juliano, V. F., Depaoli, M. A., Panero, S. & Scrosati, B. Electrochromic Properties of Dodecylbenzenesulfonate Doped Poly(Pyrrole). *Electrochim. Acta* **38**, 869-876 (1993).
- 130 Hao, L. P., Wang, W., Niu, H. J. & Zhou, Y. Grafting triphenylamine groups onto polysiloxanes to improve interaction between the electrochromic films and ITO. *Electrochim. Acta* **246**, 259-268 (2017).
- 131 Jiao, Z. H., Sun, X. W., Wang, J. M., Ke, L. & Demir, H. V. Hydrothermally grown nanostructured WO₃ films and their electrochromic characteristics. *J. Phys. D Appl. Phys.* **43**, 285501 (2010).
- 132 Ye, T. T. *et al.* Long-term-stable, solution-processable, electrochromic carbon nanotubes/polymer composite for smart supercapacitor with wide working potential window. *J. Mater. Chem. A* **6**, 18994-19003 (2018).
- 133 Berak, J. M. & Sienko, M. J. J. o. S. S. C. Effect of oxygen-deficiency on electrical transport properties of tungsten trioxide crystals. *J. Solid State Chem.* **2**, 109-133 (1970).
- 134 Su, L. Y., Zhang, L. G., Fang, J. H., Xu, M. H. & Lu, Z. H. Electrochromic and photoelectrochemical behavior of electrodeposited tungsten trioxide films. *Sol. Energy Mater. Sol. Cells* **58**, 133-140 (1999).
- 135 Somani, P. R. & Radhakrishnan, S. Electrochromic materials and devices: present and future. *Mater. Chem. Phys.* **77**, 117-133 (2003).
- 136 Deb, S. J. A. O. A novel electrophotographic system. *Appl. Opt.* **8**, 192-195 (1969).
- 137 Zhang, L. *et al.* Flexible Pseudocapacitive Electrochromics via Inkjet Printing of Additive-Free Tungsten Oxide Nanocrystal Ink. *Adv. Energy Mater.* **10**, 2000142 (2020).
- 138 Zhang, J., Tu, J. P., Xia, X. H., Wang, X. L. & Gu, C. D. Hydrothermally synthesized WO₃ nanowire arrays with highly improved electrochromic performance. *J. Mater. Chem.* **21**, 5492-5498 (2011).
- 139 Azam, A. *et al.* Two-Dimensional WO₃ Nanosheets Chemically Converted from Layered WS₂ for High-Performance Electrochromic Devices. *Nano Lett.* **18**, 5646-5651 (2018).
- 140 Adhikari, S. & Sarkar, D. High Efficient Electrochromic WO₃ Nanofibers. *Electrochim. Acta* **138**, 115-123 (2014).
- 141 Li, Y. Q., McMaster, W. A., Wei, H., Chen, D. H. & Caruso, R. A. Enhanced Electrochromic Properties of WO₃ Nanotree-like Structures Synthesized via a Two-Step Solvothermal Process Showing Promise for Electrochromic Window Application. *ACS Appl. Nano Mater.* **1**, 2552-2558 (2018).
- 142 Cong, S., Tian, Y. Y., Li, Q. W., Zhao, Z. G. & Geng, F. X. Single-Crystalline Tungsten Oxide Quantum Dots for Fast Pseudocapacitor and Electrochromic Applications. *Adv. Mater.* **26**, 4260-4267 (2014).
- 143 Yao, Y. J. *et al.* WO₃ quantum-dots electrochromism. *Nano Energy* **68**, 104350 (2020).
- 144 Li, H. Z., Shi, G. Y., Wang, H. Z., Zhang, Q. H. & Li, Y. G. Self-seeded growth of nest-like hydrated tungsten trioxide film directly on FTO substrate for highly enhanced electrochromic performance. *J. Mater. Chem. A* **2**, 11305-11310 (2014).
- 145 Bathe, S. R. & Patil, P. S. Influence of Nb doping on the electrochromic properties of

- WO₃ films. *J. Phys. D Appl. Phys.* **40**, 7423-7431 (2007).
- 146 Xie, S. J. *et al.* Electrodeposited Mo-doped WO₃ film with large optical modulation and high areal capacitance toward electrochromic energy-storage applications. *Appl. Surf. Sci.* **459**, 774-781 (2018).
- 147 Koo, B. R., Kim, K. H. & Ahn, H. J. Switching electrochromic performance improvement enabled by highly developed mesopores and oxygen vacancy defects of Fe-doped WO₃ films. *Appl. Surf. Sci.* **453**, 238-244 (2018).
- 148 Zhan, Y. *et al.* Ti-Doped WO₃ synthesized by a facile wet bath method for improved electrochromism. *J. Mater. Chem. C* **5**, 9995-10000 (2017).
- 149 Arvizu, M. A., Niklasson, G. A. & Granqvist, C. G. Electrochromic W_(1-x-y)Ti_(x)Mo_(y)O₍₃₎ Thin Films Made by Sputter Deposition: Large Optical Modulation, Good Cycling Durability, and Approximate Color Neutrality. *Chem. Mater.* **29**, 2246-2253 (2017).
- 150 Arash, A. *et al.* Electrically Activated UV-A Filters Based on Electrochromic MoO_{3-x}. *ACS Appl. Mater. Interfaces* **12**, 16997-17003 (2020).
- 151 Santhosh, S. *et al.* Effect of Ablation Rate on the Microstructure and Electrochromic Properties of Pulsed-Laser-Deposited Molybdenum Oxide Thin Films. *Langmuir* **33**, 19-33 (2017).
- 152 Zheng, L., Xu, Y., Jin, D. & Xie, Y. Novel Metastable Hexagonal MoO₃ Nanobelts: Synthesis, Photochromic, and Electrochromic Properties. *Chem. Mater.* **21**, 5681-5690 (2009).
- 153 Novak, T. G. *et al.* 2D MoO₃ Nanosheets Synthesized by Exfoliation and Oxidation of MoS₂ for High Contrast and Fast Response-Time Electrochromic Devices. *ACS Sustain. Chem. Eng.* **8**, 11276-11282 (2020).
- 154 Dinh, N. N., Oanh, N. T. T., Long, P. D., Bernard, M. C. & Goff, A. H. L. Electrochromic properties of TiO₂ anatase thin films prepared by a dipping sol-gel method. *Thin Solid Films* **423**, 70-76 (2003).
- 155 Silik, E. *et al.* Electrochromic properties of TiO₂ thin films grown by thermionic vacuum arc method. *Thin Solid Films* **640**, 27-32 (2017).
- 156 Tong, Z. *et al.* Achieving rapid Li-ion insertion kinetics in TiO₂ mesoporous nanotube arrays for bifunctional high-rate energy storage smart windows. *Nanoscale* **10**, 3254-3261 (2018).
- 157 Chen, J.-Z., Ko, W.-Y., Yen, Y.-C., Chen, P.-H. & Lin, K.-J. J. A. n. Hydrothermally processed TiO₂ nanowire electrodes with antireflective and electrochromic properties. *ACS Nano* **6**, 6633-6639 (2012).
- 158 De Trizio, L. *et al.* Nb-Doped Colloidal TiO₂ Nanocrystals with Tunable Infrared Absorption. *Chem. Mater.* **25**, 3383-3390 (2013).
- 159 Cao, S., Zhang, S. L., Zhang, T. R. & Lee, J. Y. Fluoride-Assisted Synthesis of Plasmonic Colloidal Ta-Doped TiO₂ Nanocrystals for Near-Infrared and Visible-Light Selective Electrochromic Modulation. *Chem. Mater.* **30**, 4838-4846 (2018).
- 160 Costa, C., Pinheiro, C., Henriques, I. & Laia, C. A. T. Electrochromic Properties of Inkjet Printed Vanadium Oxide Gel on Flexible Polyethylene Terephthalate/Indium Tin Oxide Electrodes. *ACS Appl. Mater. Interfaces* **4**, 5266-5275 (2012).
- 161 Wei, D. *et al.* A Nanostructured Electrochromic Supercapacitor. *Nano Lett.* **12**, 1857-1862 (2012).
- 162 Cui, Y. Y. *et al.* Thermochemical VO₂ for Energy-Efficient Smart Windows. *Joule* **2**, 1707-1746 (2018).

- 163 Mjejri, I., Gaudon, M., Song, G., Labrugere, C. & Rougier, A. Crystallized V₂O₅ as Oxidized Phase for Unexpected Multicolor Electrochromism in V₂O₃ Thick Film. *ACS Appl. Energy Mater.* **1**, 2721-2729 (2018).
- 164 Mjejri, I. & Rougier, A. Color switching in V₃O₇·H₂O films cycled in Li and Na based electrolytes: novel vanadium oxide based electrochromic materials. *J. Mater. Chem. C* **8**, 3631-3638 (2020).
- 165 Margoni, M. M. *et al.* Hydrothermally grown nano and microstructured V₂O₅ thin films for electrochromic application. *Appl. Surf. Sci.* **449**, 193-202 (2018).
- 166 Tong, Z. Q. *et al.* Annealing synthesis of coralline V₂O₅ nanorod architecture for multicolor energy-efficient electrochromic device. *Sol. Energy Mater. Sol. Cells* **146**, 135-143 (2016).
- 167 Zhang, K. *et al.* Building ultrathin polyaniline encapsulated V₂O₅ heterogeneous nanowires and its electrochromic performance. *J. Electroanal. Chem.* **825**, 16-21 (2018).
- 168 Lin, F. *et al.* Hole doping in Al-containing nickel oxide materials to improve electrochromic performance. *ACS Appl. Mater. Interfaces* **5**, 301-309 (2013).
- 169 Liu, Q. R. *et al.* Electrolytes-relevant cyclic durability of nickel oxide thin films as an ion-storage layer in an all-solid-state complementary electrochromic device. *Sol. Energy Mater. Sol. Cells* **157**, 844-852 (2016).
- 170 Purushothaman, K. K. & Muralidharan, G. Nanostructured NiO based all solid state electrochromic device. *J. Sol. Gel Sci. Technol.* **46**, 190-194 (2008).
- 171 Patil, R. A. *et al.* Efficient electrochromic properties of high-density and large-area arrays of one-dimensional NiO nanorods. *Sol. Energy Mater. Sol. Cells* **112**, 91-96 (2013).
- 172 Cai, G. F. *et al.* Inkjet-printed all solid-state electrochromic devices based on NiO/WO₃ nanoparticle complementary electrodes. *Nanoscale* **8**, 348-357 (2016).
- 173 Moghe, S. *et al.* Effect of copper doping on the change in the optical absorption behaviour in NiO thin films. *Renew. Energy* **46**, 43-48 (2012).
- 174 Lin, F. *et al.* Hole Doping in Al-Containing Nickel Oxide Materials To Improve Electrochromic Performance. *ACS Appl. Mater. Interfaces* **5**, 301-309 (2013).
- 175 Zhang, J. H. *et al.* Co-doped NiO nanoflake array films with enhanced electrochromic properties. *J. Mater. Chem. C* **2**, 7013-7021 (2014).
- 176 Dhas, C. R., Venkatesh, R., Sivakumar, R., Raj, A. M. E. & Sanjeeviraja, C. Fast electrochromic response of porous-structured cobalt oxide (Co₃O₄) thin films by novel nebulizer spray pyrolysis technique. *Ionics* **22**, 1911-1926 (2016).
- 177 Shim, H. S., Shinde, V. R., Kim, H. J., Sung, Y. E. & Kim, W. B. Porous cobalt oxide thin films from low temperature solution phase synthesis for electrochromic electrode. *Thin Solid Films* **516**, 8573-8578 (2008).
- 178 Xia, X. H. *et al.* Improved electrochromic performance of hierarchically porous Co₃O₄ array film through self-assembled colloidal crystal template. *Electrochim. Acta* **55**, 989-994, (2010).
- 179 Xia, X. H. *et al.* Cobalt Oxide Ordered Bowl-Like Array Films Prepared by Electrodeposition through Monolayer Polystyrene Sphere Template and Electrochromic Properties. *ACS Appl. Mater. Interfaces* **2**, 186-192 (2010).
- 180 Xie, L. L. *et al.* High Performance and Excellent Stability of All-Solid-State Electrochromic Devices Based on a Li_{1.85}AlO_z Ion Conducting Layer. *ACS Sustainable Chem. Eng.* **7**, 17390-17396 (2019).
- 181 Hopmann, E., Carnio, B. N., Firby, C. J., Shahriar, B. Y. & Elezzabi, A. Y. Nanoscale

- All-Solid-State Plasmochromic Waveguide Nonresonant Modulator. *Nano Lett.* **21**, 1955-1961, (2021).
- 182 Chao, D. L. *et al.* A High-Rate and Stable Quasi-Solid-State Zinc-Ion Battery with Novel
2D Layered Zinc Orthovanadate Array. *Adv. Mater.* **30**, 1803181 (2018).
- 183 Wade, C. R., Li, M. Y. & Dinca, M. Facile Deposition of Multicolored Electrochromic
Metal-Organic Framework Thin Films. *Angew. Chem. Int. Ed.* **52**, 13377-13381 (2013).
- 184 He, P. *et al.* Sodium Ion Stabilized Vanadium Oxide Nanowire Cathode for High-
Performance Zinc-Ion Batteries. *Adv. Energy Mater.* **8**, 1702463 (2018).
- 185 Margoni, M. M. *et al.* Hydrothermally grown nano and microstructured V₂O₅ thin films
for electrochromic application. *Appl. Surf. Sci.* **449**, 193-202 (2018).
- 186 Wan, F. *et al.* Aqueous rechargeable zinc/sodium vanadate batteries with enhanced
performance from simultaneous insertion of dual carriers. *Nat. Commun.* **9**, 1656 (2018).
- 187 Onbattuvelli, V. P. *et al.* Structure and thermal stability of cellulose
nanocrystal/polysulfone nanocomposites. *Mater. Today Commun.* **22**, 100797 (2020).
- 188 Shazali, N. A. H. *et al.* Characterization and Cellular Internalization of Spherical
Cellulose Nanocrystals (CNC) into Normal and Cancerous Fibroblasts. *Materials* **12**,
3251 (2019).
- 189 Jordan, J. H., Easson, M. W., Dien, B., Thompson, S. & Condon, B. D. Extraction and
characterization of nanocellulose crystals from cotton gin motes and cotton gin waste.
Cellulose **26**, 5959-5979 (2019).
- 190 Silversmit, G., Depla, D., Poelman, H., Marin, G. B. & De Gryse, R. Determination of
the V2p XPS binding energies for different vanadium oxidation states (V⁵⁺ to V⁰⁺). *J
Electron Spectrosc* **135**, 167-175 (2004).
- 191 He, P. *et al.* High-Performance Aqueous Zinc-Ion Battery Based on Layered H₂V₃O₈
Nanowire Cathode. *Small* **13**, 1702551 (2017).
- 192 Wen, R. T., Granqvist, C. G. & Niklasson, G. A. Eliminating degradation and uncovering
ion-trapping dynamics in electrochromic WO₃ thin films. *Nat. Mater.* **14**, 996-1001,
(2015).
- 193 Wu, Q. *et al.* Electrochromic Metamaterials of Metal-Dielectric Stacks for Multicolor
Displays with High Color Purity. *Nano Lett.* **21**, 6891-6897 (2021).
- 194 Chen, J., Wang, Z., Chen, Z. G., Cong, S. & Zhao, Z. G. Fabry-Perot Cavity-Type
Electrochromic Supercapacitors with Exceptionally Versatile Color Tunability. *Nano
Lett.* **20**, 1915-1922 (2020).
- 195 Kang, W. B. *et al.* Green synthesis of nanobelt-membrane hybrid structured vanadium
oxide with high electrochromic contrast. *J. Mater. Chem. C* **2**, 4727-4732 (2014).
- 196 Tong, Z. Q. *et al.* Annealing synthesis of coralline V₂O₅ nanorod architecture for
multicolor energy-efficient electrochromic device. *Sol. Energy Mater. Sol. Cells* **146**,
135-143, (2016).
- 197 Cai, G. F. *et al.* One-step fabrication of nanostructured NiO films from deep eutectic
solvent with enhanced electrochromic performance. *J. Mater. Chem. A* **1**, 4286-4292,
(2013).
- 198 Li, H. Z. *et al.* Solution-Processed Porous Tungsten Molybdenum Oxide Electrodes for
Energy Storage Smart Windows. *Adv. Mater. Technol.* **2**, 1700047 (2017).
- 199 Li, H. Z. & Elezzabi, A. Y. Simultaneously enabling dynamic transparency control and
electrical energy storage via electrochromism. *Nanoscale Horiz.* **5**, 691-695 (2020).
- 200 Wang, Y. Y. *et al.* Green revolution in electronic displays expected to ease energy and

- health crises. *Light Sci. Appl.* **10**, 33 (2021).
- 201 Kim, G. W. *et al.* High-Performance Electrochromic Optical Shutter Based on Fluoran Dye for Visibility Enhancement of Augmented Reality Display. *Adv. Opt. Mater.* **6**, 1701382 (2018).
- 202 Zhang, S., Cao, S., Zhang, T. & Lee, J. Y. Plasmonic Oxygen-Deficient TiO_{2-x} Nanocrystals for Dual-Band Electrochromic Smart Windows with Efficient Energy Recycling. *Adv. Mater.* **32**, 2004686 (2020).
- 203 Pan, H. *et al.* Wide gamut, angle-insensitive structural colors based on deep-subwavelength bilayer media. *Nanophotonics* **9**, 3385-3392 (2020).
- 204 Gugole, M., Olsson, O., Rossi, S., Jonsson, M. P. & Dahlin, A. Electrochromic Inorganic Nanostructures with High Chromaticity and Superior Brightness. *Nano Lett.* **21**, 4343-4350 (2021).
- 205 Lee, Y. *et al.* Full-Color-Tunable Nanophotonic Device Using Electrochromic Tungsten Trioxide Thin Film. *Nano Lett.* **20**, 6084-6090 (2020).
- 206 Xiong, K. L. *et al.* Plasmonic Metasurfaces with Conjugated Polymers for Flexible Electronic Paper in Color. *Adv. Mater.* **28**, 9956-9960 (2016).
- 207 Xiong, K. *et al.* Switchable Plasmonic Metasurfaces with High Chromaticity Containing Only Abundant Metals. *Nano Lett.* **17**, 7033-7039 (2017).
- 208 Ke, Y. J. *et al.* Smart Windows: Electro-, Thermo-, Mechano-, Photochromics, and Beyond. *Adv. Energy Mater.* **9**, 1902066 (2019).
- 209 Cai, G. F., Darmawan, P., Cheng, X. & Lee, P. S. Inkjet Printed Large Area Multifunctional Smart Windows. *Adv. Energy Mater.* **7**, 1602598 (2017).
- 210 Zhang, W., Li, H. Z., Hopmann, E. & Elezzabi, A. Y. Nanostructured inorganic electrochromic materials for light applications. *Nanophotonics* **10**, 825-850 (2021).
- 211 Eric, H., Li, H. Z. & Adulhakem, Y. E. Rechargeable Zn²⁺/Al³⁺ dual-ion electrochromic device with long life time utilizing dimethyl sulfoxide (DMSO)-nanocluster modified hydrogel electrolytes. *RSC Adv.* **9**, 32047-32057 (2019).
- 212 Yan, C. Y. *et al.* Stretchable and Wearable Electrochromic Devices. *ACS Nano* **8**, 316-322, (2014).
- 213 Wang, K. *et al.* Long-term-stable WO₃-PB complementary electrochromic devices. *J. Alloy. Compd.* **861**, 158534 (2021).
- 214 Cheng, W. *et al.* Solution-Deposited Solid-State Electrochromic Windows. *Iscience* **10**, 80-86 (2018).
- 215 Rong, K. *et al.* Deep Eutectic Solvent with Prussian Blue and Tungsten Oxide for Green and Low-Cost Electrochromic Devices. *ACS Appl. Electron. Mater.* **1**, 1038-1045 (2019).
- 216 Pan, J. B. *et al.* Directly grown high-performance WO₃ films by a novel one-step hydrothermal method with significantly improved stability for electrochromic applications. *J. Mater. Chem. A* **7**, 13956-13967 (2019).
- 217 Zhao, Q. *et al.* Large-area multifunctional electro-chromic-chemical device made of W₁₇O₄₇ nanowires by Zn²⁺ ion intercalation. *Nano Energy* **89**, 106356 (2021).
- 218 Zhang, W., Li, H., Yu, W. W. & Elezzabi, A. Y. Emerging Zn Anode-Based Electrochromic Devices. *Small Science* **1**, 2100040 (2021).
- 219 Ma, Q., Zhang, H., Chen, J. X., Wu, W. W. & Dong, S. J. Lithium-Ion-Assisted Ultrafast Charging Double-Electrode Smart Windows with Energy Storage and Display Applications. *ACS Cent. Sci.* **6**, 2209-2216 (2020).
- 220 Luo, Y. X. *et al.* Potential Gradient-Driven Fast-Switching Electrochromic Device. *ACS*

- Energy Lett.* **7**, 1880-1887 (2022).
- 221 Vidal-Iglesias, F. J., Solla-Gullon, J., Rodes, A., Herrero, E. & Aldaz, A. Understanding the Nernst Equation and Other Electrochemical Concepts: An Easy Experimental Approach for Students. *J. Chem. Educ.* **89**, 936-939 (2012).
- 222 Archer, M. D. Genesis of the Nernst Equation. *ACS Symp. Ser.* **390**, 115-126 (1989).
- 223 Komayko, A. I. *et al.* The Misconception of Mg^{2+} Insertion into Prussian Blue Analogue Structures from Aqueous Solution. *ChemSuschem* **14**, 1574-1585 (2021).
- 224 Fu, H. Y. *et al.* Enhanced storage of sodium ions in Prussian blue cathode material through nickel doping. *J. Mater. Chem. A* **5**, 9604-9610 (2017).
- 225 Li, H. Z. *et al.* Constructing three-dimensional quasi-vertical nanosheet architectures from self-assemble two-dimensional $WO_3 \cdot 2H_2O$ for efficient electrochromic devices. *Appl. Surf. Sci.* **380**, 281-287 (2016).
- 226 Islam, S. M. & Barile, C. J. Dual Tinting Dynamic Windows Using Reversible Metal Electrodeposition and Prussian Blue. *ACS Appl. Mater. Interfaces* **11**, 40043-40049 (2019).
- 227 Zhang, W., Li, H. Z. & Elezzabi, A. Y. Electrochromic Displays Having Two-Dimensional CIE Color Space Tunability. *Adv. Funct. Mater.* **32**, 2108341 (2022).
- 228 Liang, Y. *et al.* Reversible Zn^{2+} Insertion in Tungsten Ion Activated Titanium Dioxide Nanocrystals for Electrochromic Windows. *Nano Micro Lett.* **13**, 196 (2021).
- 229 Huang, Q. Y. *et al.* Boosting the Zn^{2+} -based electrochromic properties of tungsten oxide through morphology control. *Sol. Energy Mater. Sol. Cells* **220**, 110853 (2021).
- 230 Zhang, S. L. *et al.* Dual-Band Electrochromic Devices with a Transparent Conductive Capacitive Charge-Balancing Anode. *ACS Appl. Mater. Interfaces* **11**, 48062-48070 (2019).
- 231 Zhao, J. X. *et al.* Trace H_2O_2 -Assisted High-Capacity Tungsten Oxide Electrochromic Batteries with Ultrafast Charging in Seconds. *Angew. Chem. Int. Ed.* **55**, 7161-7165 (2016).
- 232 Islam, S. M., Palma, A. A., Gautam, R. P. & Barile, C. J. Hybrid Dynamic Windows with Color Neutrality and Fast Switching Using Reversible Metal Electrodeposition and Cobalt Hexacyanoferrate Electrochromism. *ACS Appl. Mater. Interfaces* **12**, 44874-44882 (2020).
- 233 Zhai, Y. L. *et al.* Recent Advances on Dual-Band Electrochromic Materials and Devices. *Adv. Funct. Mater.* **32**, 2109848 (2022).
- 234 Chua, M. H., Shah, K. W. & Xu, J. W. *Electrochromic smart materials : fabrication and applications*. The Royal Society of Chemistry (2019).
- 235 Jeong, K. R. *et al.* Enhanced black state induced by spatial silver nanoparticles in an electrochromic device. *NPG Asia Mater.* **9**, e362 (2017).
- 236 Feng, Z. Y. *et al.* Widely Adjustable and Quasi-Reversible Electrochromic Device Based on Core-Shell Au-Ag Plasmonic Nanoparticles. *Adv. Opt. Mater.* **2**, 1174-1180 (2014).
- 237 Kim, J. H. *et al.* Nontrivial, Unconventional Electrochromic Behaviors of Plasmonic Nanocubes. *Nano Lett.* **21**, 7512-7518 (2021).
- 238 Tsuboi, A., Nakamura, K. & Kobayashi, N. A Localized Surface Plasmon Resonance-Based Multicolor Electrochromic Device with Electrochemically Size-Controlled Silver Nanoparticles. *Adv. Mater.* **25**, 3197-3201 (2013).
- 239 Kimura, S., Sugita, T., Nakamura, K. & Kobayashi, N. An improvement in the coloration properties of Ag deposition-based plasmonic EC devices by precise control of shape and

- density of deposited Ag nanoparticles. *Nanoscale* **12**, 23975-23983 (2020).
- 240 Agrawal, A. *et al.* An Integrated Electrochromic Nanoplasmonic Optical Switch. *Nano Lett.* **11**, 2774-2778 (2011).
- 241 Tao, X., Liu, D., Yu, J. & Cheng, H. Reversible Metal Electrodeposition Devices: An Emerging Approach to Effective Light Modulation and Thermal Management. *Adv. Opt. Mater.* **9**, 2001847 (2021).
- 242 Stec, G. J., Lauchner, A., Cui, Y., Nordlander, P. & Halas, N. J. Multicolor Electrochromic Devices Based on Molecular Plasmonics. *ACS Nano* **11**, 3254-3261 (2017).
- 243 Christiansen, D. T., Tomlinson, A. L. & Reynolds, J. R. New Design Paradigm for Color Control in Anodically Coloring Electrochromic Molecules. *J. Am. Chem. Soc.* **141**, 3859-3862 (2019).
- 244 Shi, P. J., Amb, C. M., Dyer, A. L. & Reynolds, J. R. Fast Switching Water Processable Electrochromic Polymers. *ACS Appl. Mater. Interfaces* **4**, 6512-6521 (2012).
- 245 Xu, T. *et al.* High-contrast and fast electrochromic switching enabled by plasmonics. *Nat. Commun.*, **7**, 10479 (2016).
- 246 Zhu, T. *et al.* Flexible electrochromic fiber with rapid color switching and high optical modulation. *Nano Research* **16**, 5473-5479 (2023).
- 247 Wu, W. *et al.* Boosting Transport Kinetics of Ions and Electrons Simultaneously by $\text{Ti}_3\text{C}_2\text{T}_x$ (MXene) Addition for Enhanced Electrochromic Performance. *Nano-Micro Lett.* **13**, 20 (2020).
- 248 Strand, M. T. *et al.* Polymer inhibitors enable $>900 \text{ cm}^{(2)}$ dynamic windows based on reversible metal electrodeposition with high solar modulation. *Nat. Energy* **6**, 546-554 (2021).
- 249 Hernandez, T. S. *et al.* Electrolyte for Improved Durability of Dynamic Windows Based on Reversible Metal Electrodeposition. *Joule* **4**, 1501-1513 (2020).
- 250 Islam, S. M. & Barile, C. J. Dynamic Windows Using Reversible Zinc Electrodeposition in Neutral Electrolytes with High Opacity and Excellent Resting Stability. *Adv. Energy Mater.* **11**, 2100417 (2021).
- 251 Xiong, K. *et al.* Switchable Plasmonic Metasurfaces with High Chromaticity Containing Only Abundant Metals. *Nano Lett.* **17**, 7033-7039 (2017).
- 252 Kumar, K. *et al.* Printing colour at the optical diffraction limit. *Nat. Nanotechnol.* **7**, 557-561 (2012).
- 253 Xiong, K., Tordera, D., Jonsson, M. P. & Dahlin, A. B. Active control of plasmonic colors: emerging display technologies. *Rep. Prog. Phys.* **82**, 024501 (2019).
- 254 Li, N. *et al.* Dynamically Switchable Multicolor Electrochromic Films. *Small* **15**, 1804974 (2019).
- 255 Mingyang, L., Dongqing, L., Haifeng, C., Liang, P. & Mei, Z. Manipulating metals for adaptive thermal camouflage. *Sci. Adv.* **6**, eaba3494 (2020).
- 256 Zhang, F. *et al.* Weaker Interactions in Zn^{2+} and Organic Ion-pre-intercalated Vanadium Oxide toward Highly Reversible Zinc-ion Batteries. *Energy Environ. Mater.* **4**, 620-630 (2021).
- 257 Liu, Z., Luo, X., Qin, L., Fang, G. & Liang, S. Progress and prospect of low-temperature zinc metal batteries. *Adv. Powder Mater.* **1**, 100011 (2022).
- 258 Herrero, E., Buller, L. J. & Abruna, H. D. Underpotential deposition at single crystal surfaces of Au, Pt, Ag and other materials. *Chem. Rev.* **101**, 1897-1930 (2001).

- 259 Chirea, M., Collins, S. S., Wei, X. & Mulvaney, P. Spectroelectrochemistry of Silver
Deposition on Single Gold Nanocrystals. *J. Phys. Chem. Lett.* **5**, 4331-4335 (2014).
- 260 Barile, C. J. *et al.* Dynamic Windows with Neutral Color, High Contrast, and Excellent
Durability Using Reversible Metal Electrodeposition. *Joule* **1**, 133-145 (2017).
- 261 Strand, M. T. *et al.* Factors that Determine the Length Scale for Uniform Tinting in
Dynamic Windows Based on Reversible Metal Electrodeposition. *ACS Energy Lett.* **3**,
2823-2828 (2018).
- 262 Bao, H. *et al.* Surface engineering of Rh-modified Pd nanocrystals by colloidal
underpotential deposition for electrocatalytic methanol oxidation. *Nanoscale* **13**, 5284-
5291 (2021).
- 263 Mamme, M. H., Kohn, C., Deconinck, J. & Ustarroz, J. Numerical insights into the early
stages of nanoscale electrodeposition: nanocluster surface diffusion and aggregative
growth. *Nanoscale* **10**, 7194-7209 (2018).
- 264 Plieth, W. *Electrochemistry for Materials Science*, Elsevier, Amsterdam, 2008.
- 265 Syrokostas, G., Siokou, A., Leftheriotis, G. & Yianoulis, P. Degradation mechanisms of
Pt counter electrodes for dye sensitized solar cells. *Sol. Energy Mater. Sol. Cells* **103**,
119-127 (2012).
- 266 Madu, D. C., Islam, S. M., Pan, H. Q. & Barile, C. J. Electrolytes for reversible zinc
electrodeposition for dynamic windows. *J. Mater. Chem. C* **9**, 6297-6307 (2021).
- 267 Miller, D. D., Li, J. Y., Islam, S. M., Jeanetta, J. F. & Barile, C. J. Aqueous alkaline
electrolytes for dynamic windows based on reversible metal electrodeposition with
improved durability. *J. Mater. Chem. C* **8**, 1826-1834 (2020).
- 268 Perez-Lombard, L., Ortiz, J. & Pout, C. A review on buildings energy consumption
information. *Energy Buildings* **40**, 394-398 (2008).
- 269 Rezaei, S. D., Shannigrahi, S. & Ramakrishna, S. A review of conventional, advanced,
and smart glazing technologies and materials for improving indoor environment. *Sol.*
Energy Mater. Sol. Cells **159**, 26-51 (2017).
- 270 Zhao, X. P. *et al.* Dynamic glazing with switchable solar reflectance for radiative cooling
and solar heating. *Cell Rep. Phys. Sci.* **3**, 100853 (2022).
- 271 Strand, M. T. *et al.* Polymer inhibitors enable >900 cm⁽²⁾ dynamic windows based on
reversible metal electrodeposition with high solar modulation. *Nat. Energy* **6**, 546-554
(2021).
- 272 Mandal, J. *et al.* Hierarchically porous polymer coatings for highly efficient passive
daytime radiative cooling. *Science* **362**, 315-318 (2018).
- 273 Raman, A. P., Li, W. & Fan, S. H. Generating Light from Darkness. *Joule* **3**, 2679-2686
(2019).
- 274 Davy, N. C. *et al.* Pairing of near-ultraviolet solar cells with electrochromic windows for
smart management of the solar spectrum. *Nat. Energy* **2**, 17104 (2017).
- 275 Islam, S. M., Hernandez, T. S., McGehee, M. D. & Barile, C. Hybrid dynamic windows
using reversible metal electrodeposition and ion insertion. *Nat. Energy* **4**, 223-229
(2019).
- 276 Llordes, A., Garcia, G., Gazquez, J. & Milliron, D. J. Tunable near-infrared and visible-
light transmittance in nanocrystal-in-glass composites. *Nature* **500**, 323-326 (2013).
- 277 Wang, X. K. *et al.* Mechanical breathing in organic electrochromics. *Nat. Commun.* **11**,
211 (2020).
- 278 Eh, A. L. S., Chen, J. W., Zhou, X. R., Ciou, J. H. & Lee, P. S. Robust Trioptical-State

- Electrochromic Energy Storage Device Enabled by Reversible Metal Electrodeposition. *ACS Energy Lett.* **6**, 4328-4335 (2021).
- 279 Mendelsberg, R. J., Garcia, G. & Milliron, D. J. Extracting reliable electronic properties from transmission spectra of indium tin oxide thin films and nanocrystal films by careful application of the Drude theory. *J. Appl. Phys.* **111**, 063515 (2012).
- 280 Aouaj, M. A., Diaz, R., Belayachi, A., Rueda, F. & Abd-Lefdil, M. Comparative study of ITO and FTO thin films grown by spray pyrolysis. *Mater. Res. Bulltin* **44**, 1458-1461 (2009).
- 281 Rao, Y. F. *et al.* Ultra-Wideband Transparent Conductive Electrode for Electrochromic Synergistic Solar and Radiative Heat Management. *ACS Energy Lett.* **6**, 3906-3915 (2021).
- 282 Poh, W. C., Eh, A. L. S., Wu, W. T., Guo, X. Y. & Lee, P. S. Rapidly Photocurable Solid-State Poly(ionic liquid) Ionogels For Thermally Robust and Flexible Electrochromic Devices. *Adv. Mater.* **34**, 202206952 (2022).
- 283 Kossoy, A. *et al.* Optical and Structural Properties of Ultra-thin Gold Films. *Adv. Opt. Mater.* **3**, 71-77, 1400345 (2015).
- 284 Naik, G. V., Shalaev, V. M. & Boltasseva, A. Alternative Plasmonic Materials: Beyond Gold and Silver. *Adv. Mater.* **25**, 3264-3294, 1205076 (2013).
- 285 Zhang, W., Li, H. Z. & Elezzabi, A. Y. Nanoscale Manipulating Silver Adatoms for Aqueous Plasmonic Electrochromic Devices. *Adv. Mater. Interfaces* **9**, 2200021 (2022).
- 286 Personick, M. L., Langille, M. R., Zhang, J. & Mirkin, C. A. Shape Control of Gold Nanoparticles by Silver Underpotential Deposition. *Nano Lett.* **11**, 3394-3398 (2011).
- 287 Lansaker, P. C., Backholm, J., Niklasson, G. A. & Granqvist, C. G. TiO₂/Au/TiO₂ multilayer thin films: Novel metal-based transparent conductors for electrochromic devices. *Thin Solid Films* **518**, 1225-1229 (2009).

Appendices

Appendix A: Characterization of sodium vanadium nanorod films

Methods of preparation, SEM, CV, and stability test of sodium vanadium nanorod films are included.

Materials and methods

Materials

All the chemicals were of analytical grade and were used without further purification. Zinc sulfate heptahydrate ($\text{ZnSO}_4 \cdot 7\text{H}_2\text{O}$, 99%), zinc foil (Zn, 99.9%), vanadium oxide (V_2O_5 , 99%), sodium chloride (anhydrous, 99%), and polyvinyl alcohol (PVA, $M_w \sim 130,000$) were purchased from Sigma-Aldrich. Cellulose was obtained from Alberta-Pacific Forest Industries Inc.

Synthesis of sodium vanadium nanorods

Briefly, 100 g of commercial V_2O_5 powder was added into 1.5 L of a NaCl aqueous solution (2 M) at room temperature and stirred for 96 h to form a solution with a brownish suspension. Next, purification was conducted by adding distilled water, followed by centrifugation. The centrifugation process was repeated six times. Afterward, the product was diluted with distilled water to form a precursor solution (15 mg mL^{-1}). Next, the precursor solution was sonicated in an ultrasonic bath until a clear SVO colloid was formed.

Fabrication of electrodes

To meet the high viscosity requirement for the bar-coating method, 3 g of cellulose was added to 60 mL of the SVO colloid (15 mg mL^{-1}) at $60 \text{ }^\circ\text{C}$ under stirring for 24 h. Prior to deposition, ITO-coated glass substrates were cleaned with ethanol and deionized (DI) water. Next, the SVO/cellulose paste was bar-coated onto an ITO glass substrate ($2 \text{ cm} \times 5 \text{ cm}$), covering an effective area of $1 \text{ cm} \times 4 \text{ cm}$. The SVO electrodes for the “EE” display were prepared by bar-coating SVO/cellulose paste onto an “EE” shaped cut-out mask on top of an ITO glass substrate ($10 \text{ cm} \times 10 \text{ cm}$). The effective area of one “E” letter is 5 cm^2 , and the total effective area of the whole “EE” display is 10 cm^2 . The SVO electrodes for the display with the color overlay effect were prepared by bar-coating SVO/cellulose paste onto a $2 \text{ cm} \times 2 \text{ cm}$ cut-out square mask on top of an ITO glass substrate ($5 \text{ cm} \times 5 \text{ cm}$). To remove the cellulose, all the bar-coated samples were annealed in air at $200 \text{ }^\circ\text{C}$ for 24 h.

Assembly of electrochromic displays

A PVA-ZnSO₄ gel was prepared by gradually adding 6 g of PVA to 60 mL of a ZnSO₄ solution (0.5 M), which was stirred and heated in a water bath. The Zn-SVO electrochromic displays were constructed by sandwiching a thin Zn square frame between two pieces of SVO electrodes. The PVA-ZnSO₄ gel was used as the electrolyte.

Characterization

To analyze the composition and morphology of the samples, X-ray powder diffraction (XRD) (Bruker D8-Advance) with Cu K α -radiation, X-ray photoelectron spectroscopy (XPS) (Kratos AXIS Ultra), transmission electron microscopy (TEM) (JEM-ARM200CF, JEOL), Fourier transform infrared spectroscopy (FTIR-iS50) and field emission scanning electron microscopy (FESEM) (Zeiss SIGMA FESEM, Germany) were used. Ex situ XPS measurements were conducted immediately after the samples were annealed, colored and bleached. An Alpha-Step

(IQ-W1-040) was used to reveal the thickness of the bar-coated SVO film. All electrochemical measurements were carried out using a Zahner electrochemical workstation (Zennium CIMPS-1). For the CV measurements of the SVO electrode in 1 M LiCl and 0.5 M ZnSO₄, a three-electrode configuration was used with Pt wire and Ag/AgCl as counter and reference electrodes, respectively. Other electrochemical measurements were performed using a two-electrode configuration. The spectroscopy test for visible light transmittance spectra was conducted with an Ocean Optics USB4000 Spectrometer without subtracting the transmittance loss of ITO glass. Dynamic characterization of the SVO electrode was conducted by transmitting a helium-neon laser (632.8 nm) through the samples. A voltage was applied from a Zahner electrochemical workstation, and the photodiode output signal was collected with an oscilloscope. The response times were calculated based on the time required to achieve 90% of the maximum optical contrast. The International Commission on Illumination (CIE) 1931 color space was used to demonstrate chromaticity coordinates.

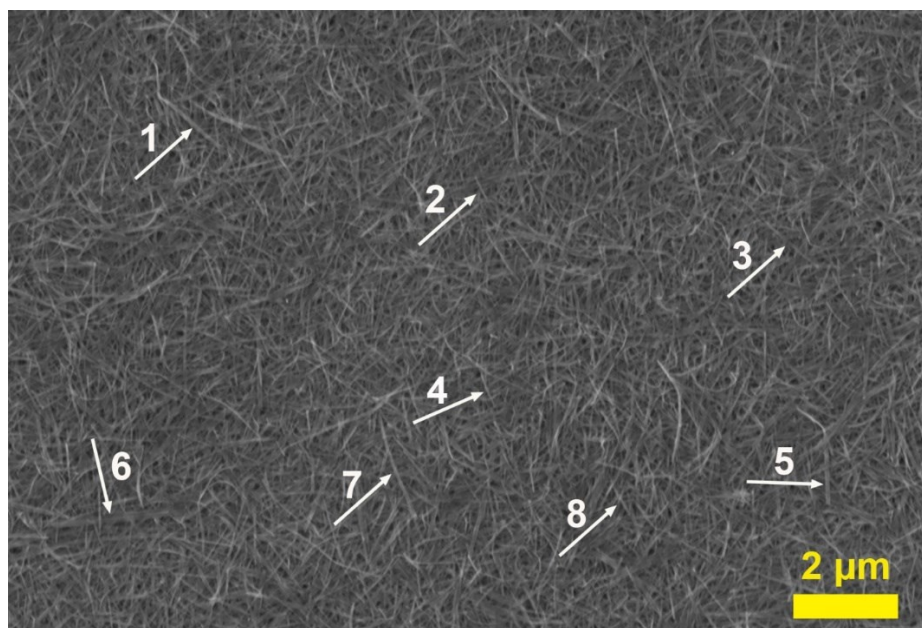


Figure A-1. FESEM image of the SVO nanorods.

Table A-1. Diameter and length of the SVO nanorods.

Sample	Diameter (nm)	Length (μm)
1	50	1.4
2	20	0.5
3	30	1.7
4	20	0.6
5	50	1.3
6	60	2.0
7	40	1.9
8	30	0.8
Range	20-60	0.5-2.0

Figure A-1 shows the FESEM image of the SVO nanorods. Eight SVO nanorods with a specific diameter and length are shown in Table A-1. The SVO nanorods range from 0.5-2.0 μm in length and 20–60 nm in diameter.

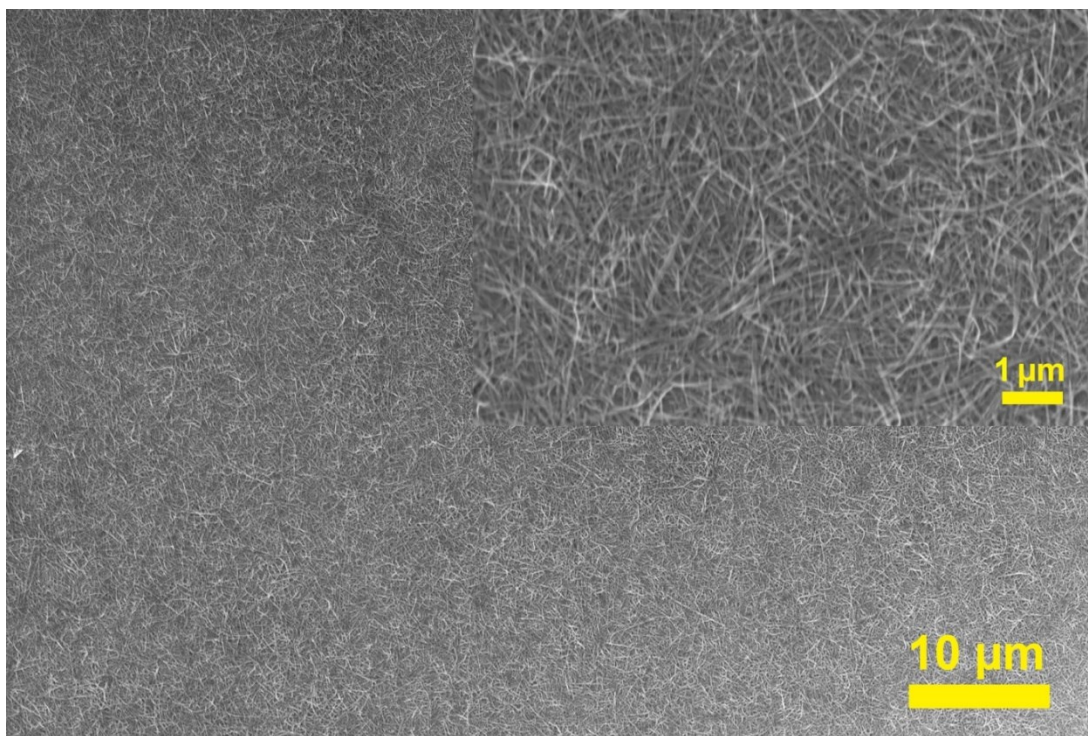


Figure A-2. FESEM images of the bar-coated and annealed SVO films.

Figure A-2 shows FESEM images of the bar-coated SVO films after the annealing process. The homogenous nanorods morphology is consistent with the morphology of SVO nanorods shown in Figs. 3.3c, d.

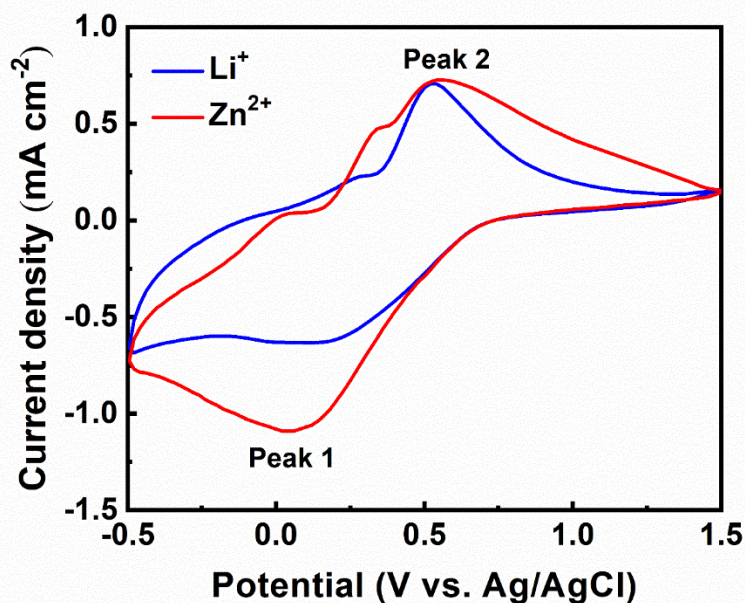


Figure A-3. Cyclic voltammetry (CV) measurement of SVO electrodes performed at 50 mV s^{-1} in 1 M LiCl electrolyte and 0.5 M ZnSO₄ electrolyte.

The CV curves of the SVO electrodes in different electrolytes (1 M LiCl and 0.5 M ZnSO₄) are shown in Fig. A-3. The reduction and oxidation peaks (around 0.10/0.56 V) suggest the intercalation and deintercalation processes. The CV curve of the SVO cathode, measured in the ZnSO₄ electrolyte, exhibits 1.4 times higher capacity compared to that tested in LiCl. This indicates that the SVO cathode is more electrochemically active towards the Zn²⁺. The underlying process may be attributed to the large radius of hydrated sodium ions that enlarge interlayer space and voids.

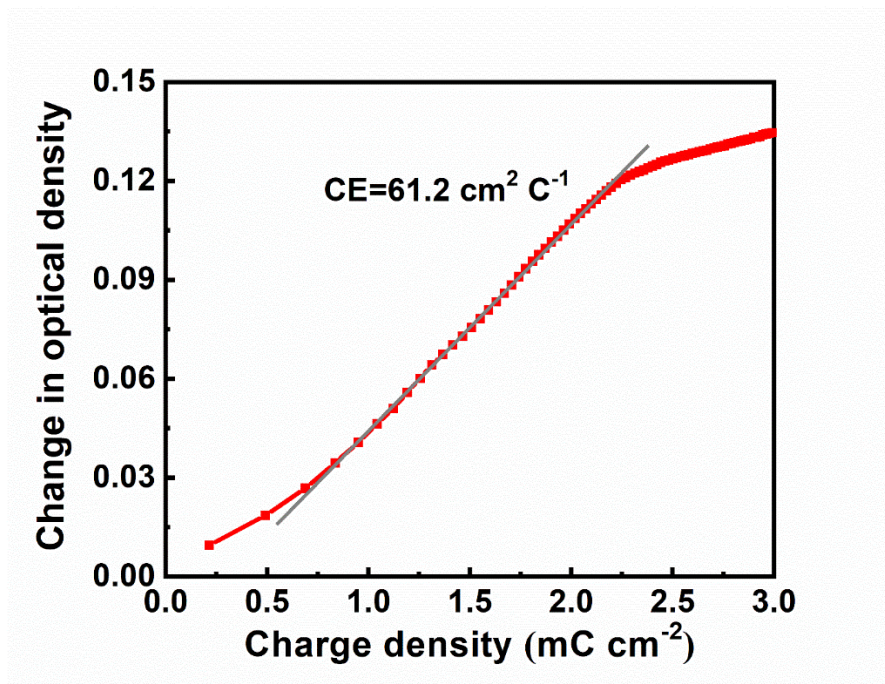


Figure A-4. Coloration Efficiency (CE) of the SVO film.

The coloration efficiency, defined as the change in optical density (ΔOD) per unit of charge intercalated into the electrochromic layer at a particular wavelength, is calculated to be $61.2 \text{ cm}^2 \text{ C}^{-1}$ for the SVO film.

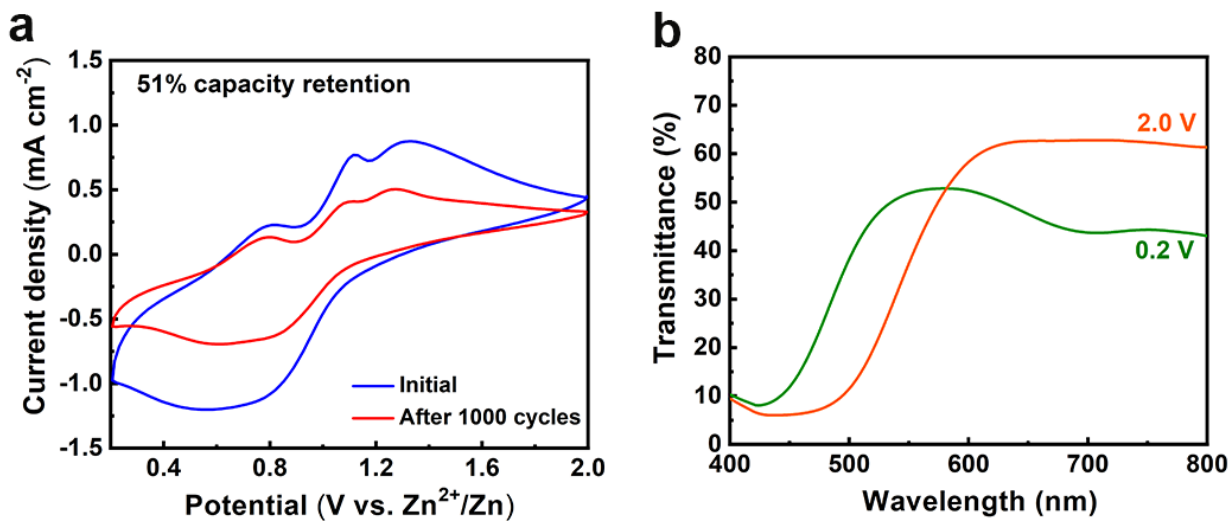


Figure A-5. Cycle performance of the SVO electrode: (a) CV measurement performed at 50 mV s⁻¹, (b) Visible-near infrared transmittance spectra after 1000 cycles measured at 0.2 V and 2.0 V.

The cycling measurements for extended cycles were conducted by the cyclic voltammetric scanning between 0.2 V and 2.0 V at a scan rate of 50 mV s⁻¹. As shown in Fig. A-5, the SVO electrode retains 51% of its initial capacity and has a 13% optical contrast after 1000 CV cycles. This degradation can be attributed to the expansion and exfoliation of the SVO film, and electrochemical grinding phenomena during cycling.

Appendix B: Characterization of tungsten oxide electrochromic electrodes

Methods of preparation, SEM, CV, digital photos and stability test of transmissive-type and Fabry-Perot nanocavity reflective-type WO₃ electrochromic electrodes are included.

Materials and methods

Fabrication of electrodes: The ITO-coated glasses are obtained from eBay (item number: 293148898668). The thickness of the ITO-coated glasses is 1.1mm with an ITO conductive layer of around 220 nm. Prior to the deposition, ITO-coated glass substrates were cleaned with ethanol and deionized (DI) water. Next, WO₃ thin films were sputtered onto ITO glass using DC sputtering at a power of 125 W. Here, the pressure is set at 20 mTorr and gas flow is set to 20 sccm of Ar and 5 sccm of O₂. For SVO electrode fabrication, 100 g of commercial V₂O₅ powder was added into 1.5 L of a NaCl aqueous solution (2 M) at room temperature and stirred for 96 h to form a solution. Next, the solution was purified and diluted with distilled water to form a SVO colloid (15 mg mL⁻¹). Afterward, 3 g of cellulose was added to 60 mL of the SVO colloid at 60 °C under stirring for 24 h. Finally, the SVO electrode was obtained via a bar-coating method. The effective area of all electrochromic electrodes in electrochemical measures was 1 cm × 4 cm. The electrochromic electrodes for the display with color overlay effect were prepared by depositing films through a 2.5 cm × 2.5 cm cut-out square mask placed on top of a 5 cm × 5 cm ITO glass substrate.

Assembly of electrochromic displays: A PVA-ZnSO₄ gel was prepared by gradually adding 6 g of PVA to 60 mL ZnSO₄ solution (0.5 M) which was stirred and heated in a water bath. The electrochromic displays were constructed by sandwiching a thin Zn square frame between one

piece of SVO electrode and one piece of WO_3 or W/WO_3 electrode. The PVA- ZnSO_4 gel was used as electrolyte.

Characterization: To analyze the morphology of the sputtered WO_3 films, field emission scanning electron microscopy (FE-SEM) (Zeiss SIGMA FESEM, Germany) was used. All electrochemical measurements were carried out using a Zahner electrochemical workstation (Zennium CIMPS-1) via a two-electrode configuration. The spectroscopy test for visible light transmittance spectra was conducted with an Ocean Optics USB4000 Spectrometer without subtracting the transmittance loss of ITO glass. The dynamic characterization of the WO_3 electrode was conducted by transmitting a helium-neon laser light (632.8 nm) through the samples. The voltage was applied from Zahner electrochemical workstation and the photodiode output signal was collected with an oscilloscope. The spectroscopy test for optical reflectance spectra was conducted with a Hitachi U-3900H Spectrometer. The International Commission on Illumination (CIE) 1931 color space was used to demonstrate chromaticity coordinates.

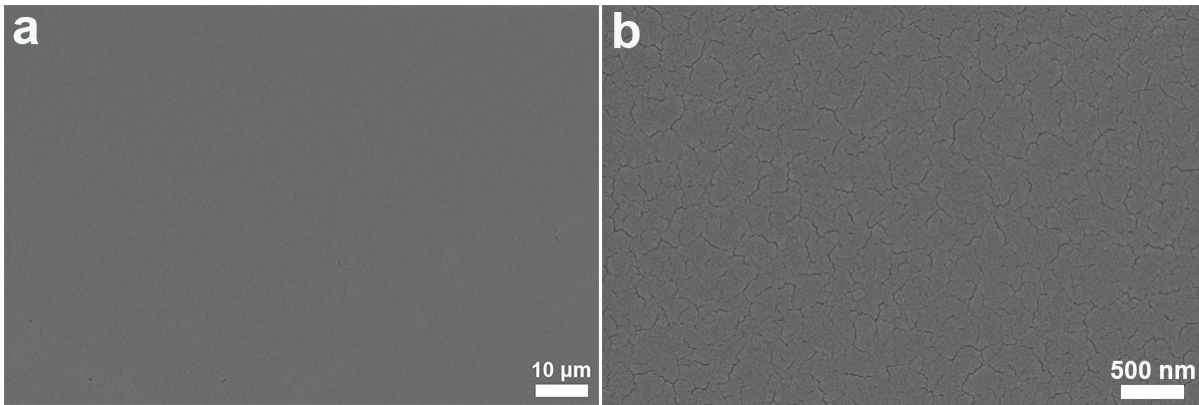


Figure B-1. Field emission scanning electron microscopy (FESEM) images of the sputtered WO_3 films.

Figure B-1 shows FESEM images of the sputtered WO_3 films. The sputtered WO_3 films are dense, smooth, and homogeneous.

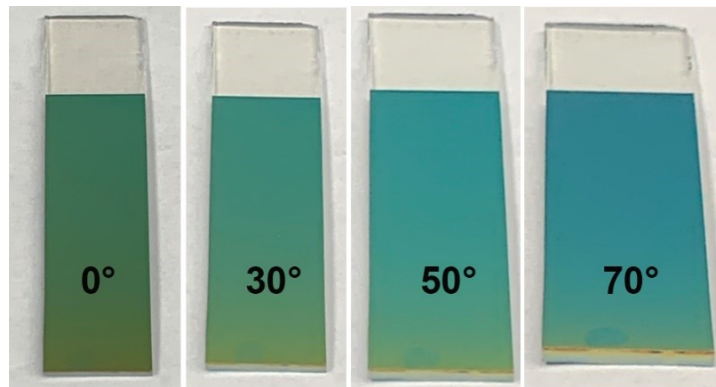


Figure B-2. Digital images of the Fabry-Perot nanocavity W/WO_3 (230 nm) electrode at different viewing angles with respect to the surface normal.

Figure B-2 depicts the digital images of the Fabry-Perot nanocavity W/WO_3 (230 nm) electrode at different viewing angles. There is a slight color change up to a large angle (50°), indicating a good angle-independent reflectance behavior.

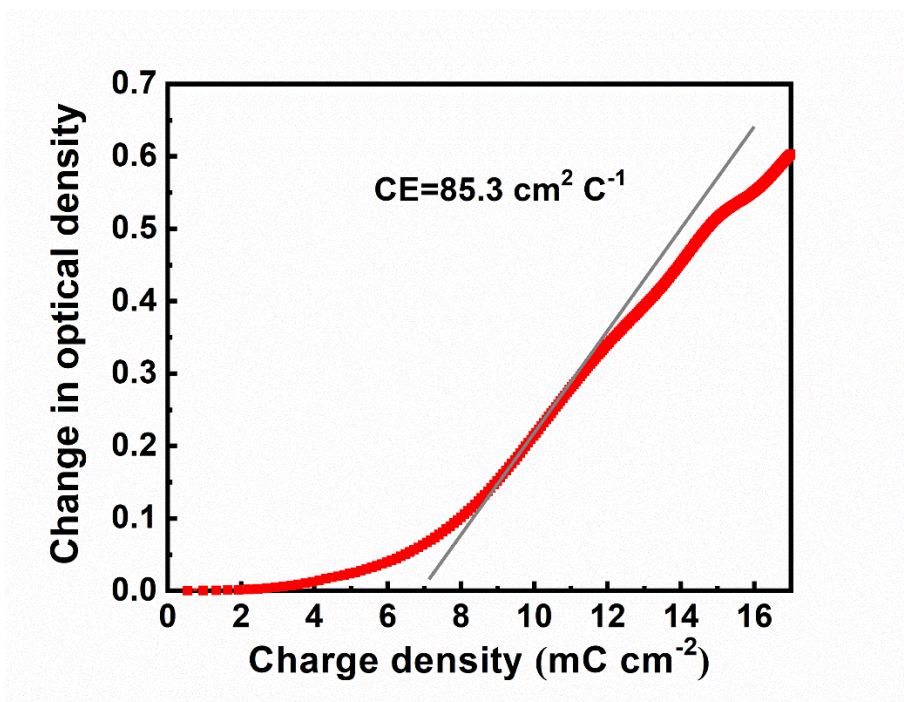


Figure B-3. Coloration Efficiency (CE) of the sputtered WO₃ film.

The coloration efficiency, defined as the change in optical density (ΔOD) per unit of charge intercalated into the electrochromic layer at a particular wavelength, is calculated to be 85.3 cm² C⁻¹ for the sputtered WO₃ film.

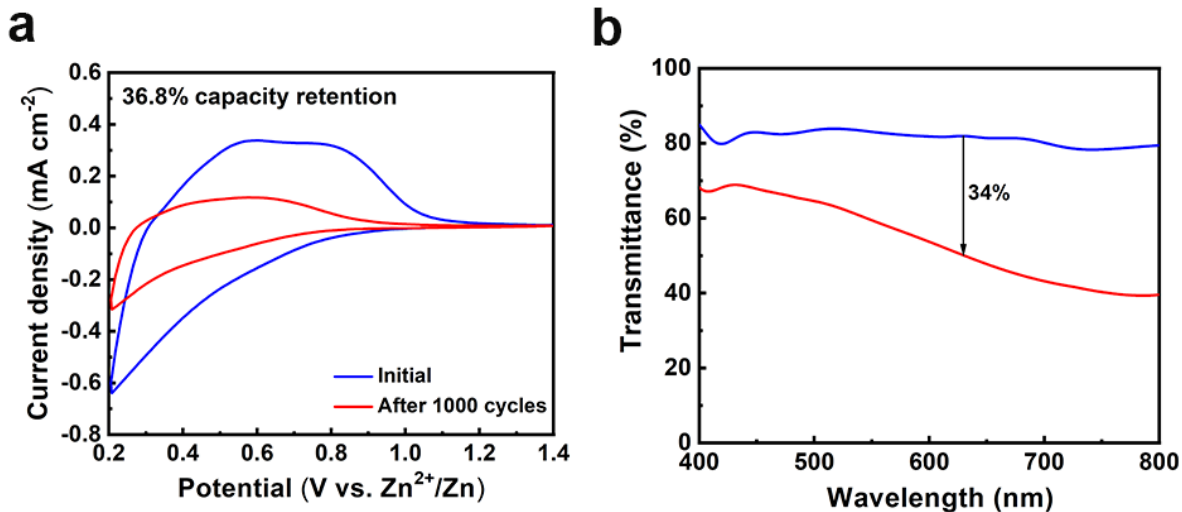


Figure B-4. Cycle performance of the WO₃ electrode: (a) CV measurement performed at 50 mV s⁻¹. (b) Visible-near infrared transmittance spectra after 1000 cycles measured at 0.2 V and 1.4 V.

The cycling measurements for extended cycles were conducted via the cyclic voltammetric (CV) scanning between 0.2 V and 1.4 V at a scan rate of 50 mV s⁻¹. As shown in Figure B-4, the WO₃ electrode retains 36.8% of its initial capacity and has a 34% optical contrast after 1000 CV cycles. This degradation can be attributed to the expansion and exfoliation of the WO₃ film, and the unpreventable trapping of Zn²⁺ ions during cycling.

Appendix C: Characterization of dual-mode electrochromic devices

Methods of preparation, CV, stability test and dynamic test of dual-mode electrochromic devices are included.

Materials and methods

Materials: All solvents and chemicals were of analytical grade and were used without further purification. Zinc sulfate heptahydrate ($\text{ZnSO}_4 \cdot 7\text{H}_2\text{O}$, 99%), Potassium chloride (KCl, 99%), Tungsten powder (W, 99.99%) and Zinc foil (Zn, 99.9%) were purchased from Sigma-Aldrich. Potassium hexacyanoferrate (III) ($\text{K}_3[\text{Fe}(\text{CN})_6]$, 99%) and Iron (III) chloride hexahydrate ($\text{FeCl}_3 \cdot 6\text{H}_2\text{O}$, 97%) were purchased from Alfa Aesar. Hydrogen peroxide (H_2O_2 , 30%) was acquired from ACS reagent.

Preparation of the WO_3 electrode: The W powder (1.8 g) was added to 60 mL of H_2O_2 solution (30%) and stirred for 12 h to form a yellow peroxotungstic acid colloid. Next, the sediments were filtered to obtain a clear colloid. The clear colloid was electrodeposited onto a cleaned ITO glass substrate at -0.3 V for 180 s to obtain a WO_3 electrode. The thickness of the WO_3 film was measured to be 300 nm.

Preparation of the PB electrode: The $\text{K}_3[\text{Fe}(\text{CN})_6]$ (10mM), $\text{FeCl}_3 \cdot 6\text{H}_2\text{O}$ (10 mM), and KCl (50 mM) were dissolved in distilled water under stirring. Next, the electrodeposition was performed at a constant current density (-0.05 mA/cm², 240 s) onto a cleaned ITO glass substrate to obtain a PB electrode. The thickness of the PB film was measured to be 300 nm.

Assembly of the PB-Zn-WO₃ electrochromic device: The PB-Zn-WO₃ electrochromic device (5 cm × 5 cm) was constructed by sandwiching a thin Zn square frame between a PB electrode and a WO₃ electrode. The effective area of the prototype device is 9 cm². The 1M KCl - 0.1M ZnSO₄ solution was used as the electrolyte. For better comparison, 1M ZnSO₄ solution was also used as the electrolyte for the devices.

Electrochemical measurements and materials characterizations: All the electrodeposition, electrochemical and electrochromic measurements were carried out using a Zahner electrochemical workstation (Zennium CIMPS-1). The electrochemical measurements were performed using a three-electrode configuration. The dynamic of 632.8 nm optical transmittance of the electrodes/devices was conducted by directing a helium-neon laser beam onto or through the samples and onto a photodiode and the dynamic data are collected using a storage oscilloscope. The spectroscopic measurements for optical transmittance spectra were conducted using an Ocean Optics USB4000 spectrometer, without subtracting the transmission loss due to the substrate.

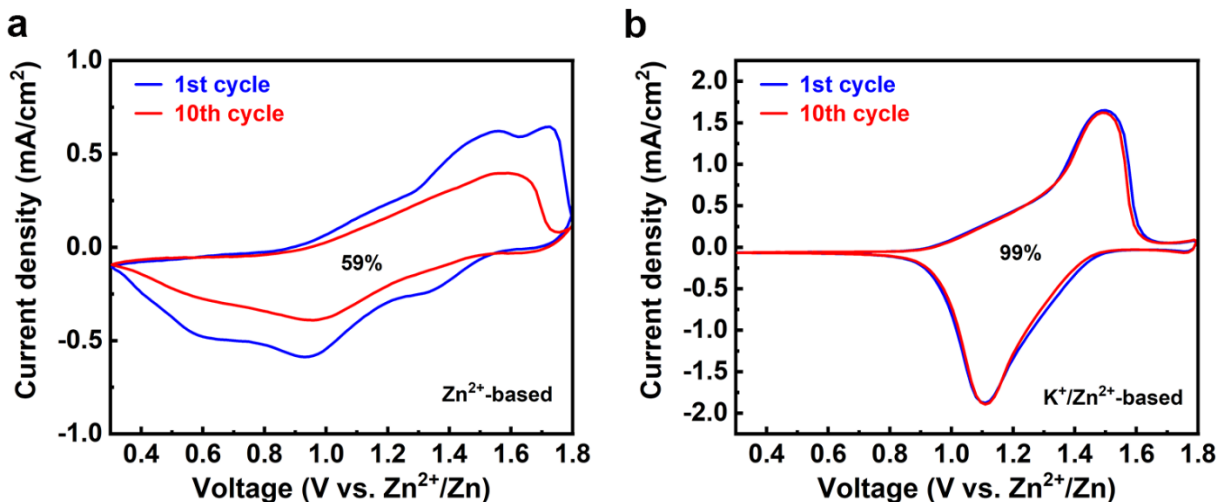


Figure C-1. Cyclic voltammetry (CV) performance of the PB electrode at a scanning rate of 20 mV s⁻¹: a) 1M ZnSO₄ and b) 1M KCl - 0.1M ZnSO₄.

The CV curves of the PB electrode in different electrolytes (1M ZnSO₄ and 1M KCl - 0.1M ZnSO₄) are shown in Figure C-1. While the PB electrode retains 99% of its initial capacity in the KCl - ZnSO₄ electrolyte during successive cycling, only 59% capacity is retained in the ZnSO₄ electrolyte. Remarkably, the hybrid KCl - ZnSO₄ electrolyte is more electrochemical effective, compared to the pure Zn²⁺ electrolyte. This is attributed to the multivalent cations (e.g., Zn²⁺) which lead to a large lattice distortion due to the strong electrostatic interactions. This results in a drastic depreciation in current densities during successive cycling.

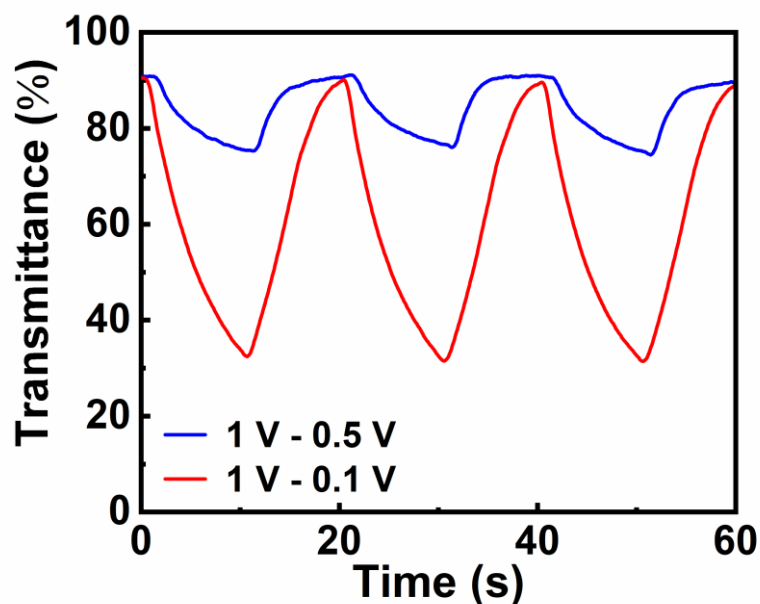


Figure C-2. Dynamic of 632.8 nm optical transmittance of the WO_3 electrode at two voltage ranges of 0.1 V-1.0 V and 0.5 V-1.0 V in a pure 1M ZnSO_4 electrolyte system.

In a pure ZnSO_4 electrolyte system, the response times of the WO_3 electrode are calculated to be 8.5 s for coloration and 7.8 s for bleaching in a voltage range between 0.1 V-1.0 V (Figure C-2). The switching times of 3.2 (for coloration) and 2.6 s (for bleaching) in the hybrid KCl-ZnSO_4 electrolyte system (Figure 3.25c) are much faster than the switching times (8.5/7.8 s) in a pure 1 M ZnSO_4 electrolyte system. This further confirms that the K^+ intercalation/extraction process is more effective compared to that of Zn^{2+} .

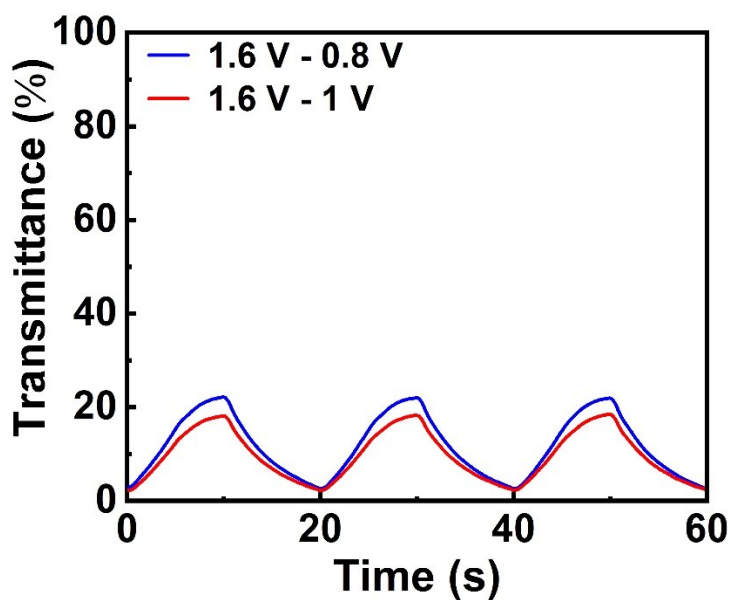


Figure C-3. Dynamic of 632.8 nm optical transmittance of the PB electrode at two voltage ranges of 0.8 V–1.6 V and 1.0 V–1.6 V in a pure 1M ZnSO₄ electrolyte system.

In a pure ZnSO₄ electrolyte system, the response times of the PB electrode are calculated to be 8.2 s for coloration and 7.9 s for bleaching in a voltage range of 0.8 V–1.6 V (Figure C-3). The switching times of 3.6 (for coloration) and 4.3 s (for bleaching) in the hybrid KCl–ZnSO₄ electrolyte system (Figure 3.25d) are much faster than the switching times (8.2/7.9 s) in a pure 1 M ZnSO₄ electrolyte system.

Appendix D: Characterization of silver nanoparticle films

Methods of preparation, CV and SEM of silver nanoparticle films are included.

Materials and methods

Preparation of aqueous silver-based electrolyte: The electrolyte for the underpotential deposition process was prepared by dissolving 1mM AgNO₃ and 50mM LiClO₄ in distilled water. The inclusion of LiClO₄ serves as a supporting electrolyte to enhance the ionic conductivity of the electrolyte. The gel electrolyte was prepared by gradually adding 6 g of polyvinyl alcohol (PVA) to 60 mL of a solution dissolving 1mM AgNO₃ and 50mM LiClO₄ (stirred and heated in a water bath).

Assembly of the transparent-type electrochromic devices: A 1 μm thick Ag anode was prepared on a commercial glass substrate and formed as a square frame around the glass substrate by the sputtering/masking techniques. The transparent-type device was assembled by combining one piece of a flat ITO glass as cathode and one piece of an Ag anode (5 cm × 5 cm). The AgNO₃-LiClO₄ solution was used as the electrolyte.

Assembly of the reflective-type electrochromic devices: The Ag anode was prepared on a commercial glass substrate by sputtering 1 μm thick Ag film. The reflective-type device was assembled by combining one piece of a flat ITO glass as cathode and one piece of an Ag anode (5 cm × 5 cm). The AgNO₃-LiClO₄ solution was used as the electrolyte.

Electrochemical measurements and materials characterizations: All the electrodeposition, electrochemical and electrochromic measurements were carried out using a Zahner

electrochemical workstation (Zennium CIMPS-1). SEM images were obtained using a Zeiss SIGMA FE-SEM microscope. The dynamic test was conducted by directing a helium-neon laser (632.8 nm) onto or through the samples and onto a photodiode. The dynamic test data is collected using a storage oscilloscope. The spectroscopic measurements for optical transmittance spectra were conducted using an Ocean Optics USB4000 spectrometer, without subtracting the transmission loss due to the substrate. The spectroscopic measurements for optical reflectance spectra were conducted using a Hitachi U-3900H spectrometer.

Statistical Analysis: To quantify the size evolution of the Ag nanoparticles, the average diameter distribution (μ) and the standard deviation (σ) of the nanoparticles were evaluated. The sample numbers (n) of Ag nanoparticles were counted in a random $1 \mu\text{m} \times 1 \mu\text{m}$ area of Ag nanoparticle films. The average diameter distribution and the standard deviation of the Ag nanoparticles were evaluated in Excel. Two-sided confidence intervals (CI) of 68.3% were determined by $\mu \pm \sigma$.

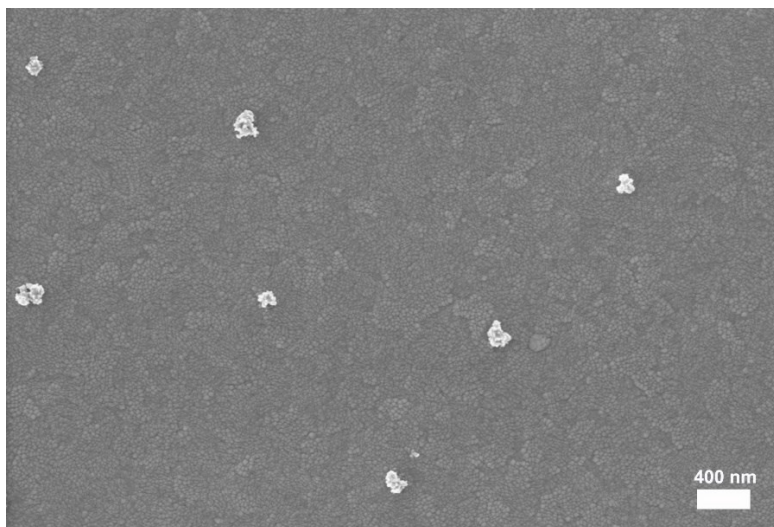


Figure D-1. FE-SEM image of the ITO electrode at 0.5 V.

Figure D-1 demonstrates the FE-SEM image of the ITO electrode at 0.5 V. The dissolving of Ag nanoparticles confirms the recyclability of Ag underpotential deposition.

Appendix E: Characterization of spectral-selective dynamic windows

Methods of preparation, CV and digital photo of spectral-selective dynamic windows are included.

Materials and methods

Preparation of the Au electrodes. Au films were deposited onto clean fused silica (glass) or polyethylene (PE) substrates using a Kurt J. Lesker electron-beam evaporation PVD 75 system. A deposition rate of about 0.2 Å/s and a base pressure of around 2×10^{-6} mbar were used. The thickness during deposition was recorded with a calibrated QCM (quartz crystal microbalance) detector. Postdeposition annealing of Au electrodes was carried out at 100 °C for 12 h and the annealed electrodes were left to cool in air to room temperature.

Preparation of the Ag-coated stainless-steel mesh electrodes. The stainless-steel mesh (50 Mesh, 0.0012" Wire Diameter) was purchased from TWP Inc. The Ag-coated stainless-steel mesh was prepared via an electrodeposition method using a two-electrode configuration, where a piece of Ag foil serves as an anode and the stainless-steel mesh serves as a working electrode. The electroplating solution was prepared by mixing 0.05 M AgNO₃ and 0.25 M LiBr in dimethyl sulfoxide (DMSO). The half-cell was then discharged at a constant voltage of -0.8 V for 3 mins.

Assembly of dynamic windows and thermal-regulated devices. The dynamic windows were assembled using an Au-coated glass electrode as the working and an Ag-coated stainless-steel mesh mounted glass as the counter electrode. The gel electrolyte used in the dynamic window was prepared by adding 10 wt% polyvinyl butyral (PVB) in DMSO solution containing 0.05 M AgNO₃

and 0.25 M LiBr. To avoid short-circuiting between the working and counter electrodes, a 2 mm thick 3M double-sided tape was placed as a spacer. The spacer provides the volume for the gel electrolyte. To assemble the flexible thermal-regulated device, the Au-coated glass electrode was placed with an Au-coated PE electrode.

Measurements and characterizations. All the electrodeposition and electrochemical measurements were carried out using a Zahner electrochemical workstation (Zennium CIMPS-1). SEM images were obtained using a Zeiss Sigma FE-SEM microscope. The sheet resistance of various electrodes was measured by a four-probe resistivity measurement system Pro4 4000. The visible-infrared transmittance spectra within a wavelength range of 0.4 to 2.5 μm were measured using a Perkin-Elmer NIR-UV spectrometer. The mid-infrared spectra within a wavelength range of 2.5 to 20 μm were measured by FTIR-iS50. The reflection spectra were measured using a UV/VIS spectrophotometer (Hitachi U-3900H) equipped with an integrating sphere. In situ spectroelectrochemical properties of the devices were tested by directing a helium–neon laser (632.8 nm) or a fiber laser (1550 nm) through it onto a photodiode and collecting the data with a storage oscilloscope. For thermal characterization, a solar simulator (Ealing Beck Ltd 022/011) simulated solar light, and a FLIR thermal camera (FLIR TG165) monitored temperature changes.

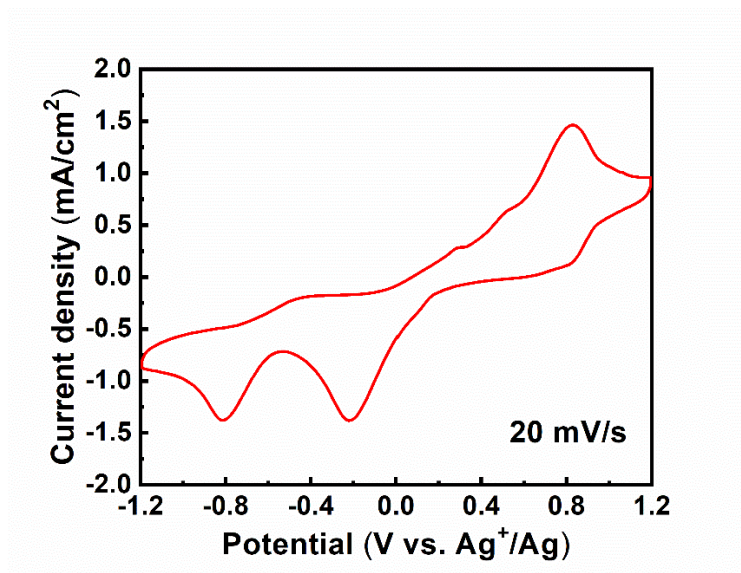


Figure E-1. Cyclic voltammetry (CV) measurement of 5 nm Au/glass electrodes performed at 20 mV s^{-1} in 0.05 M AgNO_3 and 0.25 M LiBr electrolyte.

The CV curve of the 5 nm Au/glass electrodes in 0.05 M AgNO_3 and 0.25 M LiBr electrolyte is shown in Fig. E-1. The reduction and oxidation peaks suggest the growth and dissolution of Ag.



Figure D-2. Digital image of a large-area dynamic window.

Figure D-2 shows the digital images of a large-area dynamic window (30.4 cm × 30.4 cm). This window initially exhibits around 60% transparency across the visible and NIR spectra (Fig. 4.17a, black line).